

X-ray Spectral Study of the Seyfert 1 Galaxy
MCG-6-30-15

Department of Astronomy Graduate School of Science
the University of Tokyo
Takehiro Miyakawa

Contents

Acknowledgement	1
1 Introduction	2
2 Review	4
2.1 Overview of Active Galactic Nuclei (AGN)	4
2.1.1 Discovery of AGNs	4
2.1.2 Hypothesis of super massive black hole	4
2.1.3 Estimation of black hole mass	5
2.1.4 Black hole mass and Eddington luminosity	5
2.1.5 Accretion disks	6
2.1.6 Classification of AGN and the unified model	6
2.2 X-ray Properties of Seyfert 1 Galaxies	7
2.2.1 Light curves	7
2.2.2 Energy spectra	9
2.2.3 “Broad” iron emission line	14
2.3 Motivation of our Study – a case of MCG-6-30-15	19
2.3.1 Narrow iron emission line	19
2.3.2 Invariability of the iron emission line	19
2.3.3 Light bending model	20
2.3.4 Warm absorber model	20
2.3.5 Remaining problems	22
3 Instrumentation	23
3.1 Suzaku	23
3.1.1 Overview of the satellite	23
3.1.2 X-ray Imaging Spectrometer (XIS)	23
3.1.3 X-Ray Telescope (XRT)	29
3.1.4 3-1-4 Hard X-ray Detector (HXD)	31
3.2 RXTE	37
3.2.1 Overview of the satellite	37
3.2.2 Proportional Counter Array (PCA) ¹	38
3.3 Chandra	43
3.3.1 Overview of the satellite	43
3.3.2 High Resolution Mirror Assembly (HRMA)	43
3.3.3 Advanced CCD Imaging Spectrometer (ACIS)	45
3.3.4 High Energy Transmission Grating Spectrometer (HETGS)	48

¹In this thesis, we use only PCA, so we do not explain ASM and HEXTE.

4	Observation and Data Reduction	54
4.1	Suzaku observation and data reduction	54
4.2	RXTE observation and data reduction	55
4.3	Chandra observation and data reduction	55
5	Data analysis and Results	56
5.1	Spectral Variability in a Model Independent Manner – Method 1	56
5.2	Spectral Fitting for the Average Spectrum with Model 1	62
5.3	Variation of Spectral Parameters with Model 1	65
5.3.1	Spectral fitting for the bright and faint spectra made with Method 1 . . .	65
5.3.2	Spectral fitting for the sliced spectra	66
5.4	Evidence of Variation of the Ionization States	66
5.4.1	Variation of oxygen absorption edges below 1 keV	66
5.4.2	Variation of Mg and Si absorption lines	73
5.5	Revisiting the Spectral Model	78
5.5.1	Introducing Spectral Model 2	78
5.5.2	Examination of presence of the “disk line”	81
5.6	Spectral Variability in a model Independent manner – Method 2	83
5.7	Variation of Spectral Parameters with Model 2	88
5.7.1	Spectral fitting for the bright and faint spectra made with Method 2 . . .	88
5.7.2	Spectral fitting for the sliced spectra	95
5.7.3	Spectral fitting for every 20 ksec	98
5.7.4	Spectral fitting for Chandra/HETGS data	98
6	Discussion	109
6.1	Summary of the Results	109
6.2	On the relativistically broadened iron line emission	110
6.3	Interpretation of the Observed Spectral Variability	110
6.3.1	Partial absorption model	110
6.3.2	Variation timescales of spectral parameters	112
6.3.3	Suggestion of the presence of completely blocked component	112
6.4	A Physical Picture	112
6.4.1	Spectral components	112
6.4.2	Parameters of the absorbers	114
6.4.3	Origin of the low-ionized warm absorber	115
6.4.4	Absorbing cloud envelope model	117
7	Conclusion	119
A	Spectral Models	121
B	Decomposition of the Variable Spectral Components	123
C	Robustness of the Spectral Variability Study with Method 2	125

List of Figures

- 2.1 BLR size-luminosity relation. The solid line is the best fit to the data. The dashed line is a fit with a slope of 0.5.
- 2.2 The unified model of Seyfert galaxies (Mushotzky, Done and Pounds 1993). The X-ray source locates close to the black hole, which illuminates the optically thick, geometrically thin accretion disk, giving rise to a Compton reflection spectrum and a fluorescent iron $K\alpha$ line. As the reflection albedo is $< 10\%$, the majority of the X-ray flux incident on the accretion disk is thermalized and reprocessed, enhancing the UV/soft X-ray emission from the disk itself.
- 2.3 EXOSAT 2–10 keV X-ray light curves for NGC 4051, MCG-6-30-15, and NGC4151. Note that NGC 4051 is varying rapidly during the entire observation on timescales of less than 2000 sec (Mchardy 1990), while NGC 4151 is varying rather slowly having an apparent timescale of > 6 hours (Yaqoob 1992).
- 2.4 Suggested geometries for an accretion disk and Comptonizing corona. The top figure is referred to as a “slab” or “sandwich” geometry. The remaining three show “photon starved geometries”. The middle two geometries are often referred to as “sphere + disk geometries”, while the bottom geometry is often referred to as a “patchy corona” or “pill box” model (Reynolds and Nowak 2003).
- 2.5 Left:GINGA MCG 6-30-15 spectrum fitted with a power-law with uniform cold absorber (Matsuoka et al. 1990). Iron K-emission line and K-edge feature are clearly recognized. Middle and Right:Same as in the Left figure with an additional heavily absorbed component (Middle) or a reflection component (Right), respectively.
- 2.6 X-ray reflection spectrum from an illuminated cold slab (Reynolds 1996). Dashed line shows the incident continuum, and solid line shows the reflected spectrum, averaged over all the viewing angles.
- 2.7 Predicted equivalent widths of the iron $K\alpha$ emission line versus viewing angle of the disk (George and Fabian 1991). Curves are shown for incident power-law spectra with $\Gamma = 1.3, 1.5, 1.7, 1.9, 2.1,$ and 2.3 , from the top to the bottom.
- 2.8 Simultaneous fits to the XMM-Newton data split into 5 flux states, 0.55-9.7 keV. The model is shown in units of $Ef(E)$, points with error bars show the ‘unfolded’ data.
- 2.9 EXOSAT GSPC spectrum of Cygnus X-1. The solid line in the top panel is the best-fitting power-law. In the lower panel, residuals from the best-fit power-law are shown.
- 2.10 Profile of the broad iron line caused by the interplay of Doppler shifts, relativistic beaming, and gravitational redshift (Fabian et al. 1989). The top panel shows a systematic double-peaked profiles from two narrow annuli on a non-relativistic disk. In the second panel the effects of transverse Doppler shifting and relativistic beaming is included, and in the third panel gravitational redshift is additionally included. Combining all these effects gives rise to a broad, skewed line profile, as shown in the bottom panel.
- 2.11 GINGA and ASCA spectral fitting of Cyg X-1 with disk reflection and a narrow emission line model (Ebisawa et al. 1996).

- 2.12 The iron $K\alpha$ line profile from MCG-6-30-15 observed with ASCA (Top; Tanaka et al. 1995) and that with Suzaku (Bottom; Miniutti et al. 2007).
- 2.13 Energy dependence of the RMS variability on the time-bin-widths of 2.3×10^4 sec (circles) and 1.8×10^5 sec (squares). The filled and open marks correspond to the SIS and the GIS results, respectively (Matsumoto et al. 2003).
- 2.14 (Left) The iron line EW, the RDC (represented by the iron line) and the direct continuum flux (PLC) as a function of the height h_s of the primary source above the equatorial plane. The variations in the continuum and line flux are obtained by varying the source height between 1 to $20 r_g$ at fixed intrinsic luminosity. The source is located at a distance of r_g from a Kerr black hole rotation axis and it is represented by a ring-like source co-rotating with the accretion flow. The top panel refers to an observer inclination of 30 degree, while the bottom panel is for an inclination of 60 degree. Units are arbitrary. (Right) The iron line flux (RDC) as a function of the direct continuum flux (PLC) for an observer inclination of 30 degree (top panel) and 60 degree (bottom panel). The source configuration is the same as the left panel that the height varies between 1 and $20 r_g$. As a reference, the vertical dotted lines separate different regions of the source heights, $h_s = 1-5, 5-10$ and $10-20 r_g$. Units are arbitrary (Miniutti and Fabian 2004).
- 3.1 (Left) Schematic view of the Suzaku satellite in orbit (Mitsuda et al. 2007). Both solar paddles and the extensible optical bench (EOB) are deployed. On the top, The X-Ray Telescope (XRT-S) for the X-Ray Spectrometer (XRS), and the four X-Ray telescopes (XRT-Is) for the X-ray CCD camera (XIS) can be seen. (Right) Side view of Suzaku with the internal structures after EOB deployment (Mitsuda et al. 2007).
- 3.2 A picture of an XIS sensor (Koyama et al. 2007).
- 3.3 Effective area of a single XRT-XIS system, for the FI (XIS 0,2,3) and BI CCDs (Mitsuda et al. 2007).
- 3.4 (Left) The night Earth spectra with the BI and FI CCDs (Koyama et al. 2007). (Right) XIS background counting rates as a function of energy in comparison of those of ASCA, XMM-Newton, and Chandra (Katayama et al. 2004). The background rates are normalized by the effective area and the field of view, which is a good measure of sensitivity to extended sources.
- 3.5 Time history of the OBF contamination for all the four XIS detectors, measured at the center of the OBF (Koyama et al. 2007).
- 3.6 (Left) Picture of the module XRT-I1 (Serlemitsos et al. 2007). (Right) Schematic view of the Suzaku XRT mounted on the top plate of the Extensible Optical Bench (EOB) (Serlemitsos et al. 2007).
- 3.7 Locations of the optical axis of each XRT-I module in the focal plane determined from the observations of the Crab Nebula in 2005 August–September (Serlemitsos et al. 2007). This figure implies that the image on each XIS detector becomes brightest when a target star is placed at the position of the corresponding cross.
- 3.8 Vignetting of the four XRT-I modules using the data of the Crab Nebula taken during 2005 August 22-27 in the two energy bands 3–6 keV and 8–10 keV (Serlemitsos et al. 2007).
- 3.9 Total effective area of the four XRT-I modules compared with that of XMM-Newton and Chandra (Serlemitsos et al. 2007). Transmissions of the thermal shield and the optical blocking filter, and the quantum efficiency of the CCD are all taken into account.
- 3.10 Image, Point Spread Function (PSF), and Encircled Energy Function (EEF) of the four XRT-I modules in the focal plane (Serlemitsos et al. 2007). All of the images are binned with 2×2 pixels, followed by being smoothed with a Gaussian profile with a sigma of 3

- pixels, where the pixel size is $24 \mu\text{m}$. The EEF is normalized to unity at the edge of the CCD chip (a square of $17'.8$ on a side).
- 3.11 (Left) Hard X-ray Detector (HXD). (Right) Schematic drawing of HXD-S. It consists of 16 well-counter units and 20 anti-counter units (Takahashi et al. 2007).
 - 3.12 Total effective area of the HXD detectors, PIN and GSO, as a function of energy (Takahashi et al. 2007).
 - 3.13 Angular responses of a well-counter unit (Takahashi et al. 2007), measured with radio isotope sources (31 keV from ^{133}Ba , 122 keV from ^{152}Eu , 356 keV from ^{133}Ba , 511 keV from ^{22}Na) placed 280 cm away. The response is consistent with the calculation when the finite distance from the sources to the unit is taken into account.
 - 3.14 (Left) Comparison of four average NXB spectra measured by HXD-PIN, on 4 occasions separated by two months (Kokubun et al. 2007). Each observation has an exposure longer than two days. The Crab spectrum, scaled down by two orders of magnitude, are also shown. (Right) Evolution of the averaged GSO-NXB spectra during the first half year after the launch. Each observation has an exposure longer than a day.
 - 3.15 Background counting rate of Suzaku HXD as a function of energy in comparison of those of RXTE and Beppo-SAX (Mitsuda et al. 2007). The background rate was normalized by the effective area. Background spectra of RXTE and Beppo-SAX are taken from documents for cycle 11 and cycle 5 guest observer programs, respectively. The intensity of the Crab Nebula is also shown.
 - 3.16 RXTE spacecraft viewed from above to reveal the scientific instruments (Rothschild et al. 1998). The five PCA proportional counters and the two HEXTE clusters are shown in relation to the rest of the spacecraft components, such as the two high gain antennae for communications with the ground via the tracking and data relay satellite system, the two solar-power arrays that can rotate to face the Sun, and the ASM on the end with clearance to view the sky.
 - 3.17 Schematic view of PCA counters (Bradt et al. 1993): (Left) Assembly of five PCA counters with total area of 6250 cm^2 . (Right) Schematic view of one PCA unit.
 - 3.18 Effective area of a single PCU.
 - 3.19 A background spectrum for PCU2 calculated for the time of MCG-6-30-15 observation in August, 1997.
 - 3.20 Expanded view of the Chandra flight system, showing several subsystems(Elsner et al. 2000).
 - 3.21 (Left) The four nested HRMA mirror pairs and associated structures. (Right) The HRMA/ACIS and HRMA/HRC effective areas versus X-ray energy in linear-linear scales (Weisskopf et al. 2002). The structure near 2 keV is due to the iridium M-edge. See the main texts for detailed explanation.
 - 3.22 Photograph of the focal plane of ACIS, prior to installation of the optical blocking filters. The ACIS-I is at the bottom; the ACIS-S (the read out for the HETG) is at the top (Weisskopf et al. 2002).
 - 3.23 A schematic drawing of the ACIS focal plane (<http://asc.harvard.edu/proposer/POG/html/HETG.html>) Note the nominal aimpoints: on S3 (the '+') and on I3 (the 'x'). It is standard practice to add an offset to all observations on S3 to move the source away from the node 0-1 boundary. The view is along the optical axis, from the source toward the detectors, (-X). The numerous ways to refer to a particular CCD are indicated: chip letter+number, chip serial number, and ACIS chip number. The node numbering scheme is illustrated lower center.
 - 3.24 The quantum efficiency, convolved with the transmission of the appropriate optional blocking filter, of the FI CCDs and the two BI CCDs as a function of energy. S3 is

- somewhat thicker, hence more efficient than S1. This figure includes the effects of molecular contamination. There is a sharp drop near the Si K-edge at 1.84 keV
- 3.25 A schematic layout of the High Energy Transmission Grating Spectrometer (<http://asc.harvard.edu/prop>)
- 3.26 HETGS observation of Capella (OBSID 1318) (<http://asc.harvard.edu/proporser/POG/html/HETG.htm>)
 The top panel shows an image of detected events on the ACIS-S detector with the image color indicating the ACIS-determined X-ray energy. The bright zeroth-order image is visible on CCD S3 and includes a trailed image (the vertical frame-transfer streak). Diffracted photons are visible forming a shallow “X” pattern; the HEG and MEG spectra are indicated. The images are broad due to dither of the spacecraft. The middle panel shows an image after the data have been aspect corrected and selections applied to include only valid zeroth and first-order events; note that the Y axis has been flipped from the normal Sky view to match the detector coordinates view in the top panel. The lower panel shows an expanded view of the MEG minus-first-order spectrum, where emission lines are clearly visible as bright dots.
- 3.27 (Left) The HETGS MEG effective area, integrated over the PSF is shown with energy and wavelength scales. The $m = +1, +2, +3$ orders (falling on ACIS chips S5, S4, S3; left to right) are displayed in the top panel and the $m = -1, -2, -3$ orders (falling on ACIS chips S0, S1, S2; left to right) are in the bottom panel. The thick solid lines are first order; the thin solid line is third order, and the dotted line is second order. (Right) The HETGS HEG effective area, integrated over the PSF, is shown with energy and wavelength scales. The $m = +1, +2, +3$ orders (falling on ACIS chips S5, S4, S3; left to right) are displayed in the top panel and the $m = -1, -2, -3$ orders (falling on ACIS chips S0, S1, S2; left to right) are in the bottom panel. The thick solid lines are first order; the thin solid line is third order; and the dotted line is second order. Figures are taken from <http://asc.harvard.edu/proporser/POG/html/HETG.html>.
- 3.28 The modelled total first-order (solid curve) and zeroth-order (dotted curve) effective area, integrated over the PSF, of the HRMA-HETG-ACIS-S combination, as a function of energy (<http://asc.harvard.edu/proporser/POG/html/HETG.html>). The first-order data are the same as those plotted in Figure 3.27. The plotted first-order values are the sums of the area at a particular energy from both orders (+/-) of both MEG and HEG spectra. Both a log-log (Top) and a log-linear (Bottom) version are shown.
- 3.29 HEG and MEG resolving power ($E/\Delta E$ or $\lambda/\Delta\lambda$) as a function of energy for the nominal HETGS configuration (<http://asc.harvard.edu/proporser/POG/html/HETG.html>). The resolving power at high energies is dominated by the telescope PSF; at low energies grating effects enter but do not dominate. The “optimistic” dashed curve is calculated from pre-flight models and parameter values. The “conservative” dotted curve is the same except for using plausibly degraded values of aspect, focus, and grating period uniformity. The cutoff at low-energy is determined by the length of the ACIS-S array. Measurements of the HEG and MEG $m = -1$ spectra are shown here by the diamond symbols. The values plotted are the as-measured values and therefore include any natural line width in the lines; for example, the “line” around 12.2 Å is a blend of Fe and Ne lines.
- 5.1 0.2–12 keV XIS light curve of the 2006 observation. The count rate intervals based on which intensity-sliced spectra are made are shown with horizontal red-dotted lines.
- 5.2 Correlation between the flux in 6.0–10 keV and the spectral ratio of 0.5–3.0 keV/6.0–10 keV for the “intensity-sliced spectra” (black), “bright spectra” (red) and “faint spectra” (blue) using the Suzaku XIS data in 2006.
- 5.3 The 6.0 – 10 keV intensity (top) and the spectral hardness ratio (bottom) of the bright (red) and faint (blue) spectra as functions of the time-intervals, T .

- 5.4 Spectral ratios of the bright spectra to the faint spectra for six different timescales.
- 5.5 A 2–30 keV PCA light curve of MCG-6-30-15 with the 2×10^6 sec time-bin from 1996 to 2009, in 6 – 10 keV (middle) and 15 – 30 keV (bottom), as well as the spectral ratio of 2 – 4 keV/6 – 10 keV (top).
- 5.6 Correlation between the 6 – 10 keV flux and the hardness ratio of 2 – 4 keV / 6 – 10 keV from the RXTE PCA data, where time-lengths of each point are 2×10^6 sec (top) and 2×10^7 sec (bottom).
- 5.7 (Top) Spectral fit result for the time-averaged XIS and PIN spectra (1–40 keV) using Model 1 with a *narrow* iron emission line (intrinsic line width is fixed to $1 \sigma = 10$ eV). (Bottom) Spectral fit result for the time-averaged XIS and PIN spectra (1–40 keV) using Model 1 with a *broad* iron emission line (intrinsic line width is allowed to be free and $1 \sigma = 290$ eV).
- 5.8 Ratios of our best-fit model (blue and black) and the observed spectrum (red) to a power-law function. The power-law slope is determined using the data only in 3.0–4.0 keV and 7.5–12 keV. Note that our model includes a moderately broad iron emission line at 6.42 keV ($1\sigma = 290$ eV), but not an extremely distorted one with relativistic effects.
- 5.9 Top: Relation between the variation timescale and ionization degree for the bright and faint spectra in Case 2 (ionization parameter of the low ionized warm absorber varied). Bottom: Relation between the variation timescale and power-law normalization for the bright and faint spectra in Case 2.
- 5.10 Unfolded energy spectra for the eight intensity-sliced spectra calculated from the model only varying the power-law normalization and ionization degree of the lower-ionized warm absorber.
- 5.11 Relation between the ionization degree and power-law normalization for the bright, faint and sliced spectra in Case 2 (ionization parameter of the low ionized warm absorber varied).
- 5.12 Simultaneous fit in the 0.6–1.6 keV band for the twelve spectra (bright and faint spectra for the 6 timescales) with a power-law plus two absorption edge model.
- 5.13 Variation of the power-law normalization and depth of the OVIII edge to describe the spectral variation in 0.6 – 1.6 keV, as functions of the timescales.
- 5.14 (Top) Chandra HETGS simultaneous fit in the 1.15–1.55 keV band for the bright spectrum and faint spectrum with a power-law plus two negative gaussian model. Mg absorption lines are at 1.34 keV and 1.47 keV. (Bottom) Simultaneous fit in the 1.75–2.10 keV band with a power-law plus two negative gaussian model. Si absorption lines are at 1.85 keV and 2.00 keV.
- 5.15 Mg and Si ion fractions of an optically thin low-density photoionized gas, as a function of the ionization parameter, assuming the power-law ionizing spectrum with ϵ^{-1} (Kallman & Bautista 2001).
- 5.16 Spectral fit result for the time-averaged HETGS spectra (5.9–7.1 keV).
- 5.17 Spectral fit result for the 1-40 keV average spectrum for Suzaku XIS/PIN with “Model 2”.
- 5.18 Spectral fit result for the 1-40 keV average spectrum adding Laor’s disk line model to Model 2.
- 5.19 Chi-squares of fitting to the average spectrum, shown as a function of the inner radius of Laor’s disk line model.
- 5.20 A 0.2–12 keV XIS light curve of the 2006 observation (obsID:700007010) to explain the Method 2 of spectral extraction. Top: the case of an interval of 20,000 sec. Bottom: the case of an interval of 40, 000 sec. The periods when the bright spectra and faint spectra are extracted are shown with red and blue, respectively.

- 5.20 (Continued.) The same figure as the previous one, for obsID:700007020.
- 5.20 (Continued.) The same figure as the previous one, for obsID:700007030.
- 5.21 Energy dependence of spectral variability of Suzaku XIS/PIN (defined in eq. 5.1) calculated from the nine sets of the bright and faint spectral pairs, extracted via Method 2.
- 5.22 Spectra variability (defined in 5.1) as functions of the timescales in 1–10 keV (Top), and in 14.8–24.2 keV and 24.2–42.2 keV (Bottom), calculated from the nine sets of the bright and faint spectral pairs, extracted via Method 2.
- 5.23 Spectral variability (defined in eq. 5.1) as functions of the timescales in 1.28–1.40 keV and 1.40–1.52 keV (Top), and in 2.33–2.57 keV and 2.57–2.81 keV (Bottom).
- 5.23 (Continued.) Spectral variability (defined in eq. 5.1) as functions of the timescales in 3.74 – 4.20 keV and 4.68 –5.14 keV (Top), and in 6.08–6.54 keV, 7.01–7.47 keV, and 8.41–9.35 keV (Bottom).
- 5.24 (Top) The fitting results with Model 2, for the bright/faint spectra made with Method 2 on timescales of 256 – 160,000 sec. (Bottom) The unfolded spectral model.
- 5.25 (Top) Relation between the direct power-law normalization and the ionization degree, made by applying Model 2 to the bright and faint spectra created with Method 2. (Bottom) Relation between the direct power-law normalization and the absorbed power-law normalization.
- 5.26 Relation between the spectral model parameters and variation timescales made by applying Model 2 to the bright and faint spectra created with Method 2. Total power-law normalization (Top), covering factor (Middle) and ionization degrees of the low-ionized warm absorber (Bottom).
- 5.27 Spectral fit results with Model 2 for the intensity sliced spectra.
- 5.28 (Top) Relation between the direct power-law normalization and the ionization degree made by applying Model 2 to the intensity sliced spectra. (Bottom) Relation between the direct power-law normalization and absorbed power-law normalization.
- 5.29 Confidence contours between the direct power-law normalization (horizontal axis) and the absorbed power-law normalization (vertical axis).
- 5.30 Spectral fit results with Model 2 for the spectra extracted for every 20 ksec (from top to bottom, obsID:700007010, 700007020 and 700007030). Reduced chi-square is 1.09 ($\chi^2/\text{d.o.f} = 3887/3577$), 1.07 ($\chi^2/\text{d.o.f} = 2253/2100$) and 1.13 ($\chi^2/\text{d.o.f} = 2365/2097$), respectively.
- 5.31 (Top) Relation between the direct power-law normalization and the ionization degree made from the 20 ksec spectra using Model 2. (Bottom) Relation between the direct power-law normalization and the absorbed power-law normalization.
- 5.32 (Top) Relation between time and direct power-law normalization for the spectra made every 20 ksec from obsID:700007010. (Middle) Relation between time and absorbed power-law normalization. (Bottom) Relation between time and the ionization degree.
- 5.32 (Continued.) The same figure with previous one for obsID:700007020.
- 5.32 (Continued.) The same figure with previous one for obsID:700007030.
- 5.33 Spectral fit result for the time-averaged HETGS spectra with Model 2.
- 5.34 Spectral fit result for the bright/faint HETGS spectra with Model 2.

- 6.1 Comparison of the variation amplitude of 20 ksec in 1– 10 keV with a simulated variation amplitude when only the covering factor is variable.
- 6.2 Variability in power-law normalization, covering factor, and ionization degree of low-ionized warm absorber, as functions of the timescales, calculated from Figure 5.26.

- 6.3 A schematic explanation of the absorbing cloud envelop model for MCG-6-30-15 and structure of the low-ionized cloud and the cloud envelope.
- C.1 Spectral ratios of the bright and faint spectra in case of shifting one time-bin to the original spectra. The cases for intervals of 5,000 sec, 10,000 and 20,000 sec, from top to bottom.
- C.1 (Continued) Spectral ratios of the bright and faint spectra in case of shifting one time-bin to the original spectra. The cases for intervals 40,000 sec and 80,000 sec for top and bottom, respectively.

List of Tables

- 3.1 Main XIS Background Emission lines (Tawa et al. 2008). Typical accumulation time are 110–160 ksec.
- 3.2 X-ray Telescope design parameters (Serlemitsos et al. 2007).
- 3.3 Design parameters of the pre-collimator (Serlemitsos et al. 2007).
- 3.4 Design parameters and performance of the RXTE PCA and HEXTE (Bradt et al. 1993, Jahoda et al. 1996, Rothschild et al. 1998).
- 3.5 Design parameters and performance of the HETGS (Canizares et al. 2005).

- 5.1 Results of the average spectral fitting in 1–40 keV
- 5.2 Results of spectral fitting in 1–40 keV for the “bright” and “faint” spectra.
- 5.2 Results of spectral fitting in 1–40 keV for the “bright” and “faint” spectra (continued).
- 5.3 Results of spectral fitting in 1–40 keV for the intensity sliced spectra with Model 1, Case 2 (only the power-law normalization and the ionization degree of the lower-ionized absorber are varied)
- 5.4 Results of spectral fitting in 0.6–1.6 keV for the “bright” and “faint” spectra made with Method 1.
- 5.5 Results of spectral fitting of Chandra/HETGS spectra in 1.15–1.55 keV and 1.75 – 2.10 keV for the intensity sliced spectra when only the power-law normalization and the normalization of absorption lines are varied.
- 5.6 Results of spectral fitting in 5.9–7.1 keV for the average spectra of Chandra/HETG.
- 5.7 Results of spectral fitting in 1–40 keV for the Suzaku XIS/PIN average spectrum with Model 2.
- 5.8 Results of spectral fitting in 1–40 keV for the average spectrum adding Laor’s disk line to Model 2.
- 5.9 Results of spectral fitting of Suzaku in 1–40 keV with Model 2 for the “bright” and “faint” spectra extracted with Method 2.
- 5.9 (Continued)
- 5.10 Results of spectral fitting of Chandra/HETG in 1–7.5 keV with Model 2 for the average spectrum.
- 5.11 Results of spectral fitting in 1–7.5 keV of Chandra/HETG with Model 2 for the intensity sliced spectra

Abstract

The primary question in MCG-6-30-15 is whether the iron line is truly broad and its lack of variability is a result of the general relativistic light bending effects. If the “disk line”, which is a relativistically broadened iron K emission line expected from innermost part of the accretion disk, truly exists in Seyfert 1 galaxies and Galactic black hole binaries, it would provide us with a rare opportunity to measure extremely strong gravities around black holes directly. However, it is still controversial whether the disk line exists or not in Seyfert 1 galaxies and/or the Galactic black hole binaries, since disk line parameters are significantly dependent on the continuum spectral shape, which itself is not fully understood.

In order to constrain the continuum spectral model of MCG-6-30-15, we have studied its spectral variation using Suzaku, RXTE and Chandra. We have calculated spectral hardness ratios between different energy bands observed with Suzaku in 2006 January, and found a clear correlation between the 6 – 10 keV flux and the spectral ratio of 0.5 – 3.0 keV/6.0 – 10 keV. A similar spectral correlation is also found in the RXTE data for over 14 years. Next, we have analyzed the Chandra/HETGS data taken in 2004 May, which requires two warm absorbers with different ionization states ($\log \xi \sim 3.6$ and $\log \xi \sim 2$). We found that the absorption lines of Mg and that of Si are varied with X-ray intensity. The change of the absorption line depths is naturally explained by change of the ionization degree of one of the two photoionized warm absorber ($\log \xi = 1.78 - 1.95$), responding to the incoming flux change. The Suzaku spectral variation is also explained by change of the ionization degree of the low-ionized warm absorber ($\log \xi = 1.2 \sim 3$, $N_H \sim 3.7 \times 10^{21} \text{cm}^{-2}$), while intrinsic spectral slope and high-ionized warm absorber ($\log \xi \sim 3.4$, $N_H \sim 2 \times 10^{23} \text{cm}^{-2}$) are invariable.

Chandra/HETGS spectrum clearly detects a narrow and neutral iron emission line with an equivalent width of ~ 20 eV, which should accompany a cold disk reflection with an amount of $\Omega/2\pi \sim 0.3$. In order to explain the observed energy spectra observed with Suzaku including these components, we need a heavily absorbed spectral component with $N_H \sim 10^{24} \text{cm}^{-2}$ and $\log \xi \sim 1.6$. Using this model, we have studied Suzaku spectral variations at various timescales and intensity ranges. Consequently, we have discovered that the spectral variability is explained sole variations of (1) normalization of the direct power-law, (2) normalization of the absorbed power-law component, and (3) ionization degree of the low-ionized warm absorber. Remarkably, we found a clear anti-correlation between the direct power-law normalization and the absorbed power-law normalization, which suggests a partial covering is taking place. Meanwhile, normalization of the direct power-law and ionization degree of the low-ionized warm absorber indicates a clear correlation.

We have investigated variation timescales of each spectral parameter, and found that the total X-ray normalization (direct component + absorbed one) has the variation timescales of $\sim 1,000$ sec and $\sim 80,000$ sec. The former is understood as due to intrinsic luminosity variation of the black hole. The covering factor (=absorbed power-law normalization/total normalization) and ionization degree of the low-ionized warm absorber are found to have the same variation time scale $\sim 80,000$ sec.

It is difficult to understand that the total normalization and the covering factor vary together, if they are independent. On the other hand, if we assume that intrinsic X-ray luminosity is rather invariable at 80,000 sec, and parts of the X-rays are completely blocked by the partial absorbers which have the variation timescale of 80,000 sec, we may naturally understand the similar variation timescales of the X-ray normalization and the covering factor. In fact, if we consider a situation where numerous, fragmented photoionized absorbers are intervening in the line of

sight of an extended X-ray source, X-ray blocking and partial absorption simultaneously take place depending on various opacities of the absorbers. Hence, we propose such an “absorbing cloud envelope model” that X-ray spectral variation of MCG-6-30-15 is primarily caused by photoionized absorbing clouds, which intermittently intercept the line of sight of an extended X-ray source. Each absorbing cloud has a cold Thomson thick core, which is the X-ray blocker, surrounded by a middle layer (Thomson optical depth ≈ 1 , $\log \xi \sim 1.6$), and an outer envelope (Thomson thin, $\log \xi \sim 1.2 - 3$). The middle layer and the outer envelope correspond to the partial absorber and the low-ionized warm absorber in our spectral model, respectively. The system is surrounded by the high-ionized warm absorber ($\log \xi \sim 3.6$), which is not variable.

Acknowledgement

I am grateful to my supervisor Prof. Ken Ebisawa for his continuous guidance throughout my three years in the doctoral course. He always leads me with enthusiasm from data analysis to writing thesis. I really appreciate plenty of advices he gave me. Owing to him, I was able to have an opportunity to work on a contemporary, very exciting topic in the center of X-ray study of Active Galactic Nuclei. I feel I have become stronger both physically and mentally throughout my research experience. I would not be here without him. Again, I would like to express my deepest gratitude to Prof. Ken Ebisawa.

I convey my sincere thanks to Prof. Hajime Inoue, who was the director of ISAS until September 2009. Throughout my research of black hole candidates even before writing this thesis, he always gave me considerable advice. Despite his extremely tight schedule while he was the director, he kindly spent time with us for scientific discussion from time to time, which I always enjoyed. In the final months of writing this thesis, after he retired from the director, he kindly spent time to discuss this topic with me almost every day. Thanks to him, I believe I could improve my thesis significantly. Again, I would like to express my deepest gratitude to Prof. Hajime Inoue.

I also convey my sincere thanks to Prof. Yuichi Terashima. He gave me considerable advice, especially in publication of papers. Without his help, I could not advance our research. I also would like to thank Mr. Fuminori Tsuchihashi, who was Prof. Terashima's student. We cross-checked our data analysis procedures and results to each other, so that we could be confident with what we have obtained.

I would like to thank Prof. Piotr Życki, who was a visitor at ISAS. He gave me various suggestions from theoretical point of view.

I would like to thank Dr. Aya Bamba and Dr. Yoh Takei, with whom I share office, for giving me considerable advice even when they were very busy, especially in data analysis. I would like to thank Prof. Manabu Ishida. He gave us various comments and advice during the so-called "astro-ph seminar", a student reading group of preprints.

I would like to thank all my friends in the same class, Mr. Toshishige Hagihara, Mr. Shunsuke Kimura, Ms. Ryoko Nakamura, Mr. Masayoshi Ushio, and Mr. Masaki Koshiishi. I suppose we have nurtured kind of "friendly competition", which has kept stimulating us. I had a great time with these friends. I also would like to thank all the members of Ebisawa lab., Mr. Tessei Yoshida, Ms. Kumiko Morihana, Mr. Kei Saitou, Dr. Masahiro Tsujimoto, and Ms. Yumiko Yoshida for making my ISAS life rich and enjoyable. I also appreciate supports from past and present members of ISAS/JAXA.

I acknowledge my family for continuous supports throughout my life.

Finally, I would like to express my deepest gratitude to Ms. Nao Tsuchida for encouragement and understanding.

Chapter 1

Introduction

Iron is the most abundant heavy element in the universe, and its K-shell line and edge energies lie in the range of 6.4 keV to 9.3 keV. Therefore, iron line spectroscopy is a powerful tool in X-ray astronomy to study physical conditions of the objects. In Seyfert galaxies and Galactic black hole binaries, significant iron K-edge and/or K-line feature is observed, which is an evidence of X-ray reprocessing by surrounding matter. Thanks to the combination of large cosmic abundance and high fluorescent yield, the iron $K\alpha$ line at 6.4 keV is the most prominent fluorescent line in the X-ray reflection spectrum. By studying the fluorescent iron line feature of Seyfert galaxies and Galactic black holes in detail, we expect to reveal physical configurations in the vicinity of black holes.

The 6.4 keV iron line detected by EXOSAT from the Galactic black hole binary Cygnus X-1 seemed apparently broadened (Barr, White & Page 1985). This is a motivation of the idea of ‘disk line’, such that the line shape is distorted by the effects of Doppler shift and gravitational redshift, if the iron line originates from the inner part of the accretion disk (Fabian et al. 1989, 2000). Such seemingly broad iron emission lines have been also reported from Seyfert 1 galaxies. The best example is in MCG-6-30-15 (Tanaka et al. 1995): The iron line profile of MCG-6-30-15 seemed broadened and just looked like a disk line in shape. If those ‘disk lines’ are genuine, that provides us with a precious opportunity to constrain black hole parameters from observations of the disk line shapes and intensities..

On the other hand, X-ray energy spectra of Seyfert 1 and Galactic black holes may be interpreted without disk lines. Although EXOSAT GSPC was only sensitive up to ~ 13 keV, GINGA was able to observe up to ~ 30 keV, and detected an iron reprocessing feature in Cyg X-1 above 10 keV, which is considered to be a disk reflection feature (Inoue 1989). Meanwhile, ASCA carried out the first CCD observation of Cyg X-1, and resolved a *narrow* emission line (Ebisawa et al. 1996). In fact, both GINGA and ASCA spectra are explained with a disk reflection component and a narrow iron emission line without an additional broad line (Ebisawa et al. 1996). In the case of MCG-6-30-15 too, the energy spectrum can be interpreted in terms of disk reflection and warm absorbers (Miller et al. 2008) without a broad disk line feature. Thus, it was recognized that parameters of the broad iron emission line are significantly dependent on the continuum spectral modelling.

The primary question is whether or not the iron line in MCG-6-30-15 is truly broad due to relativistic effects in the very vicinity of the black hole. The crucial element to address the problem is to model the underlying continuum spectrum, since the broad iron line parameters are dependent on the choice of the continuum spectral model. However, the spectral modeling is not unique, that is an origin of the controversy. Unless modelling the global continuum energy spectrum correctly, we may not constrain the local iron line feature, and the controversy continues.

In order to tackle this problem, we make use of spectral variations. The broad band continuum of MCG-6-30-15 is complex, with strong modification by warm absorbers, and highly variable. In this thesis, we attempt to comprehensively understand the spectral variability of MCG-6-30-15. Our goal is to find a continuum spectral model of MCG-6-30-15 which is able to explain the observed spectral variation at various timescales with minimum numbers of parameters. If we are successful to construct such a reasonable spectral model, we will see if the relativistically distorted iron emission line is present or not in the energy spectrum of MCG-6-30-15. We believe this is an important step forward to fully understand X-ray energy spectra of not only MCG-6-30-15, but also Seyfert 1 galaxies and black hole binaries in general.

This thesis is organized as follows: In Chapter 2, we briefly review X-ray properties of Seyfert 1 Galaxies, and explain the background of our studying MCG-6-30-15. In Chapter 3, we present scientific instruments on-board Suzaku, RXTE, and Chandra, of which data we used in this thesis. Data reduction is summarized in Chapter 4. Chapter 5 is devoted to data analysis. In Chapter 6, we discuss our results. Finally, Chapter 7 summarizes conclusion of the thesis.

Chapter 2

Review

2.1 Overview of Active Galactic Nuclei (AGN)

2.1.1 Discovery of AGNs

Fath discovered emission lines in the spectrum of NGC 1068 in 1908, which is the beginning of observation of AGNs (Fath 1909). Seyfert is the first scientist to study AGNs systematically (Seyfert 1943), and found that (1) some galaxies contain bright nuclei, (2) emission lines from highly ionized atoms are observed in their spectra, and (3) these emission lines are significantly broadened. The galaxies showing such features are currently called “Seyfert galaxies”.

Importance of AGNs was recognized again in 1950s, when radio telescopes with large enough aperture were built by groups at Cambridge University and Sydney University. The first useful large catalog of radio galaxies was “the third Cambridge catalog” collecting almost 500 sources brighter than 9 Jy at 178 MHz. The Sydney group identified a few radio stars with optical counterparts and found that M 87 and NGC 5128 harbor powerful radio sources Virgo A and Centaurus A, respectively (Bolton, Stanley, & Slee 1954). Baade & Minkowski (1954) also identified Cygnus A with the cD galaxy 3C 405 and measured the redshift of $z = 0.057$. Their emission line spectra were very similar to that of Seyfert Galaxies. However, other 3C radio sources (e.g., 3C 48 and 3C 273) were found to be more difficult to identify, since they appeared to be star-like with no image of host galaxy and furthermore, their spectra were dominated by unidentified broad emission lines without absorption lines.

This mystery was solved by Schmidt in 1963. He found that the emission lines in 3C 273 were able to be identified with the well-known nebular emission lines if the source has an unusually large redshift of $z = 0.158$ (Schmidt 1963). Soon after this discovery, Greenstein & Matthews (1963) identified 3C 48 to be also a galaxy with $z = 0.368$. According to the Hubble law, such large redshift implies that the sources are very distant and thus the absolute magnitude of the source are three orders of magnitude larger than that of normal galaxies. These objects were named “quasi-stellar radio sources”, or quasars. Since then, numerous AGNs have been cataloged, and we currently know presence of many different types of AGNs at various distances.

2.1.2 Hypothesis of super massive black hole

It is now believed that central engine of AGN is a supermassive black hole. Since many observational pieces of evidence inevitably lead to the presence of supermassive black hole, this idea is now widely accepted. The most simple but convincing evidence reaches the very large luminosity, which is 10^{42-46} erg/sec. This indicates that AGN is powered by the mass accretion into a central source since mass accretion can produce very large amount of energy more

efficiently than nuclear fusion. However, the central gravitational source must have a very large mass to sustain the mass accretion against the high radiation pressure. For a typical luminosity of AGNs $L_{bol} \approx 10^{45}$ erg/sec, the central mass in excess of $10^7 M_\odot$ is required. A small size of the emission region is another piece of observational evidence toward black hole. The size can be estimated from a variation timescale of the luminosity. In the X-ray band, the timescale of the variation Δt is known to be less than a few hours. This indicates that the size of the X-ray emission region r is $r \leq \Delta t \times c \approx$ several tens of AU. This compactness as well as the large mass supports the supermassive black hole hypothesis.

2.1.3 Estimation of black hole mass

The “reverberation mapping technique” is the most reliable method of mass estimation (e.g., Kaspi et al. 2000; Nelson et al. 2000). The continuum and broad-line fluxes in AGN show highly correlated variations. However, time variations of the line flux generally lag behind those of continuum over days to months. The lag is the best explained as a light travel time effect and can be used to estimate the size of the Broad Line Region (BLR). If one further assumes that the blobs producing the broad lines take nearly Keplerian orbits, the line widths can be used to estimate velocity of the blobs and in turn the total mass contained within the BLR. The reverberation studies have now provide the mass of numerous Seyfert 1 galaxies and quasars (e.g., Wandel, Peterson, & Malkan 1999). The empirical relationship between the size of BLR and monochromatic continuum luminosity at 5100 Å also has been used to estimate a black hole mass M_{BH} . Kaspi et al. (2000) found the BLR size scales with the rest-frame 5100 Å luminosity as $L^{0.70 \pm 0.03}$, that is to say,

$$R_{BLR} = 32.9_{-1.9}^{+2.0} \left[\frac{\lambda L_\lambda(5100\text{\AA})}{10^{44} \text{ erg/sec}} \right]^{0.700 \pm 0.033} \text{ lt - days.} \quad (2.1)$$

Incidentally, $\lambda L_\lambda(5100 \text{ \AA})$ is estimated from the B -magnitude by adopting an average optical spectral index of -0.5 (See Figure 2.1).

2.1.4 Black hole mass and Eddington luminosity

The central mass of a black hole (M) determines characteristic size of the system. Schwarzschild radius is often used as a scaling factor, which is given as

$$R_S = \frac{2GM}{c^2} \simeq 3 \times 10^{11} \frac{M}{10^6 M_\odot} \text{ [cm].} \quad (2.2)$$

Where, G and M_\odot are gravitational constant (6.67×10^{-11} N m²/kg²), and solar mass ($\sim 2 \times 10^{30}$ kg), respectively. Once scaled by M , characteristics of various black holes from stellar black holes to “monsters” in AGNs may be compared.

AGNs are powered by the gravitational energy release of the accreting matter. Therefore, the gravitational force of the accreting matter needs to be larger than the radiation pressure to sustain the mass accretion. This means presence of the critical luminosity, at which the radiation pressure balances the gravitational force. This is called Eddington luminosity, which is given by

$$L_{Edd} = \frac{4\pi cGMm_p}{\sigma_T} = 1.25 \times 10^{38} \left(\frac{M}{M_\odot} \right) \text{ [erg/sec].} \quad (2.3)$$

Where, m_p is the proton mass, σ_T is the Thomson scattering cross section.

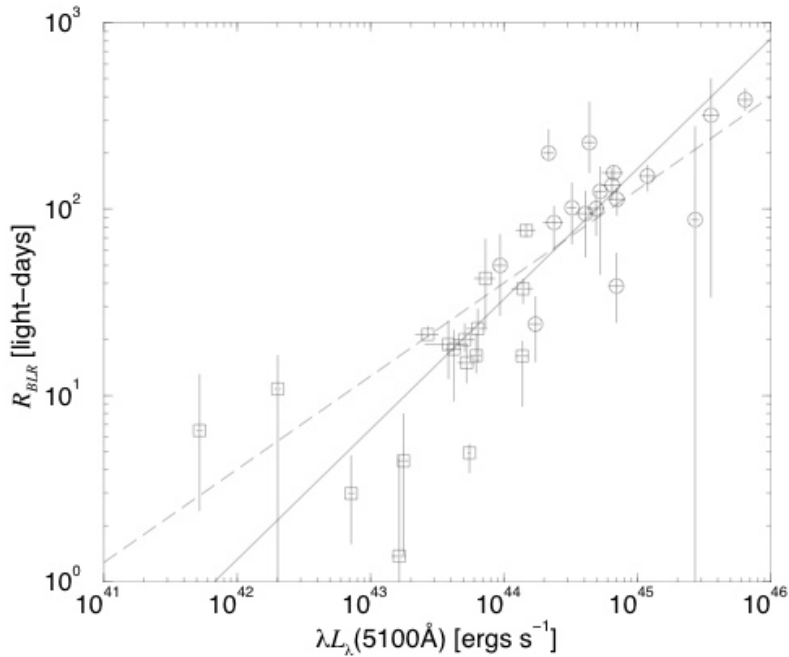


Figure 2.1: BLR size-luminosity relation. The solid line is the best fit to the data. The dashed line is a fit with a slope of 0.5.

2.1.5 Accretion disks

It has been thought that an accretion disk plays a crucial role in conversion of gravitational energy into radiation around compact objects. Shakura & Sunyaev (1973) provides a prototypical description of an accretion disk, which is called “the standard model”. In the case of AGNs, its spectral energy distribution (SED) exhibits a big hump in their optical/UV to soft X-ray band (Koratkar & Blaes 1999). Since most of the energies emitted from AGNs are emerged in that energy band, this spectral component is thought to be a primary emission originated from the standard accretion disk (e.g., Turner et al. 2002).

2.1.6 Classification of AGN and the unified model

Seyfert galaxies are divided into two categories based on their optical spectra; Seyfert 1 (type 1) and Seyfert 2 (type2). Seyfert 1s show both broad (FWHM ≥ 5000 km/sec) permitted lines and narrow (~ 500 km/sec) forbidden lines, which are emitted from a Broad-Line Region (BLR) and Narrow Line Region (NLR), respectively. On the other hand, Seyfert 2 show only narrow lines.

It is generally believed that both types of Seyfert galaxies are intrinsically same, but different viewing angle is cause of the apparent differences (Antonucci et al. 1993, Lawrence 1987). This interpretation is called “a unified model”, which has been a guiding principle in the field of AGN research (see Figure2.2; Mushotzky, Done & Pounds 1993). In this model, a Super Massive Black Hole (SMBH) is present at the center of the AGN, and the standard accretion disk, which is optically thick and geometrically thin, exists around the SMBH. In a quasi-spherical volume surrounding the SMBH, clouds of hot plasma are distributed. Further out from the nucleus, there locates the BLR, and a thick obscuring torus exists even further out. The NLR is located outside the torus. The X-ray source itself resides close to the black hole, and illuminates the accretion disk giving rise to a Compton reflection.

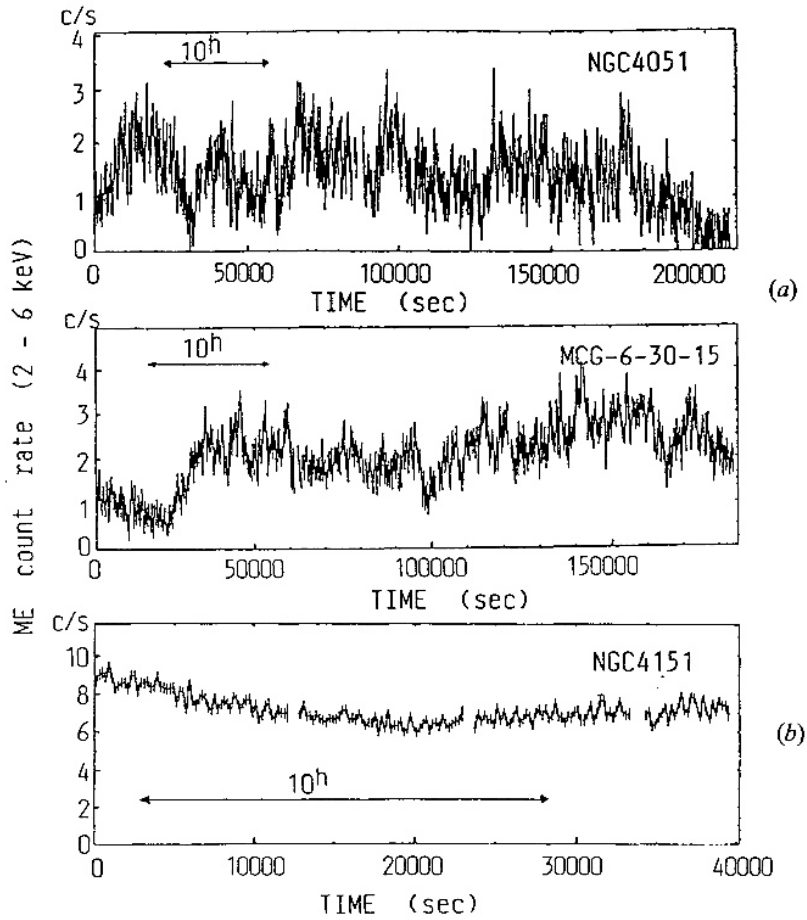


Figure 2.3: EXOSAT 2–10 keV X-ray light curves for NGC 4051, MCG-6-30-15, and NGC4151. Note that NGC 4051 is varying rapidly during the entire observation on timescales of less than 2000 sec (Mchardy 1990), while NGC 4151 is varying rather slowly having an apparent timescale of > 6 hours (Yaqoob 1992).

NGC4051 varied very rapidly through the entire observation on timescales of less than 2000 sec, while NGC4151 varied rather slowly with an apparent time scale of ≥ 6 hours. These rapid variabilities indicate compactness of the X-ray emission region, which is thought to be close to the central black hole. As seen from the Figure2.3, Seyfert 1s are also variable on a long timescales variability. These variability on various timescales is a common feature of Seyfert 1s.

2.2.2 Energy spectra

X-ray energy spectra of Seyfert 1 galaxies have several common components. We explain each component one by one.

Power-law component

While the standard accretion disk (2.1.5) produces a relatively soft, thermal spectrum dominated by optical/UV radiation in AGN, X-ray spectra of AGNs exhibit a power-law component, which has exponential rollover at a few hundreds keV (Maisack et al. 1993, Fabian et al. 1993, Zdziarski et al. 1995). The most promising physical mechanism to produce such a cut-off power-law component is unsaturated inverse Compton scattering (Thorne et al. 1975, Sunyaev et al. 1979). Soft photons from the accretion disk gain energies by inverse Compton scattering by a hot corona above the disk and produce such a power-law spectrum.

If the corona is a thermal plasma whose electron temperature is T_e and the energy of the electron ϵ is non-relativistic ($\ll 4kT_e$), the energy a photon gains after a single scattering is $\Delta E/E_{initial} \approx 4kT_e/m_e c^2$, where m_e is the electron mass and $E_{initial}$ is an initial energy of the photon. Then, after N scatterings, the average final photon energy E_{final} is given by $E_{final} \approx E_{initial} \times \exp(N \times (4kT_e/m_e c^2))$. For a medium with an optical depth of τ , the scattering number N depends on the τ , and N is roughly $\max(\tau, \tau^2)$. If we define the Compton y -parameter as

$$y = \max(\tau, \tau^2)(4kT_e/m_e c^2), \quad (2.4)$$

$E_{final} = E_{initial} \times \exp(y)$. For $y > 1$, the average photon energy increases by an amplification factor of $\exp(y)$. For $y \gg 1$, the average photon energy reaches the thermal energy of the electrons. The former case is referred to as “unsaturated inverse Compton scattering”, while the latter case is referred to as “saturated Compton scattering”. Multiple scatterings lead to exponential energy gain and a power-law spectrum. Photon index of the power-law is determined by the Compton y -parameter as $\Gamma = -1/2 + (9/4 + 4/y)^{0.5}$ (Rybicki and Lightman 1979). X-ray observations of Seyfert 1s generally give photon index $\Gamma \sim 2$, which thus corresponds to $y \sim 1$.

There are two unresolved issues in the unsaturated Comptonization model. First, the mechanism for heating the electrons near to virial temperature is currently unknown. Current hypotheses invoke magnetic processes, perhaps akin to heating solar flare or solar corona (e.g., Di Matteo 1998; Di Matteo, Celotti, and Fabian 1999; Miller and Stone 2000; Machida, Hayashi, and Matsumoto 2000). Liu, Mineshige and Shibata (2002) proposed a self-consistent model based on interaction between the disk and corona, to describe the basic properties of the disk and corona for a given black hole mass and accretion rate.

Second, geometry of the corona and disk is unknown yet. Several suggested geometries for the accretion disk and Comptonizing corona are shown in Figure 2.4. Slab geometry was once suggested (top of Figure 2.4), where both disk and corona exist at the same radii. It was thought early on that a promising source for the necessary coronal energy would be dissipation of magnetic flux tubes as buoyantly rose above the disk into the corona (Galeev, Rosner and Vaiana 1979), and the accretion energy is postulated to be dissipated predominantly within the

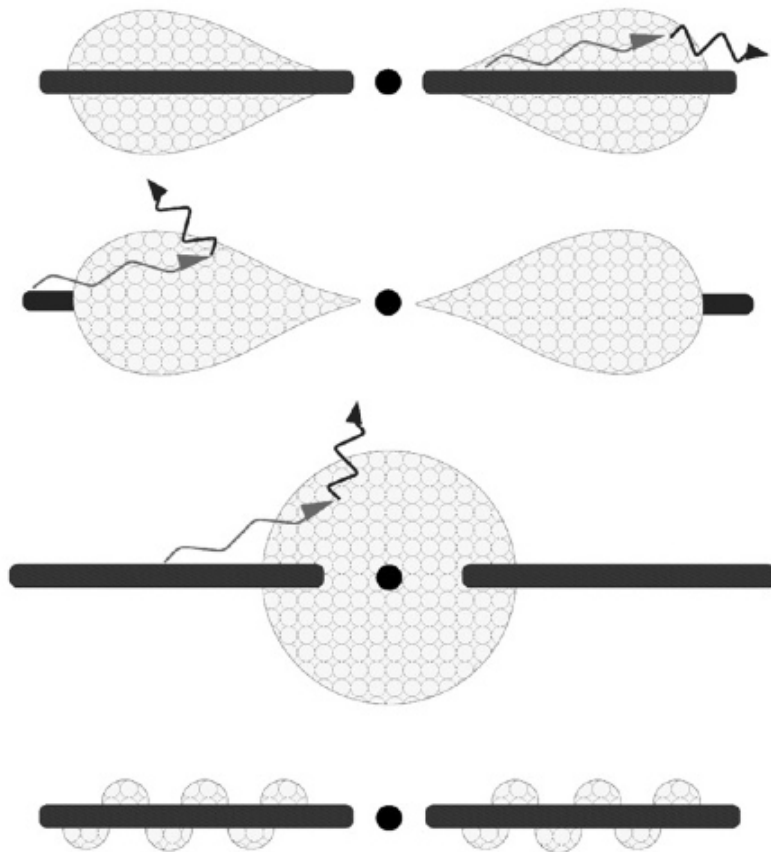


Figure 2.4: Suggested geometries for an accretion disk and Comptonizing corona. The top figure is referred to as a “slab” or “sandwich” geometry. The remaining three show “photon starved geometries”. The middle two geometries are often referred to as “sphere + disk geometries”, while the bottom geometry is often referred to as a “patchy corona” or “pill box” model (Reynolds and Nowak 2003).

corona (Ostriker et al. 1976; Liang and Price 1977). However, the slab corona is easily Compton cooled and it is difficult to reach the high enough temperature to produce the observed hard spectrum (Stern et al. 1995). If the corona locates in the central region and the soft photons come from the outer cool disk, the corona is not strongly Compton cooled and can remain hot enough to produce observed hard spectra (Dove, Wilms and Begelman 1997; middle two figures in Figure 2.4). Alternatively, if the corona is patchy, such that small corona regions sit atop the disk (bottom of Figure 2.4), a relatively small fraction of the reprocessed disk flux is intercepted by the corona. Thus, the coronal patches can also be hot enough to explain the observed spectra (Stern et al. 1995).

Reprocess by surrounding matter

In most Seyfert galaxies, significant iron K-edge and/or K-line feature is observed, which is considered an evidence of reprocessing by surrounding matter, either absorption or reflection, of X-rays from the central engine. If the central source is obscured by an intervening matter, that produces an iron K-edge absorption feature, as long as iron is not fully ionized. Irradiation of the optically thick disk gives rise to a characteristic reflection spectrum, which is the result of Compton scattering and photoelectric absorption. In addition to the reflection continuum, fluorescent emission lines from heavy elements are expected. Thanks to the combination of large cosmic abundance and high fluorescent yield, the iron $K\alpha$ line at 6.4 keV (neutral case) is the most prominent fluorescent line in the X-ray reflection spectrum. Because of the energy dependence of the photoelectric absorption, incident soft X-rays are mostly absorbed, whereas hard photons can be Compton back scattered out of the disk. Above a few tens of keV, energy shift due to the Compton recoil becomes significant and produces a broad hump-like structure around 20–30 keV, which is called “Compton reflection hump”.

While X-ray continuum of Seyfert galaxies in the range 2–30 keV had been described by a single power-law model before the launch of the GINGA satellite (Mushotzky 1984; Turner and Pounds 1989), GINGA has indicated the first observational evidence of the reprocessing feature due to surrounding matter (Matsuoka et al. 1990; Piro et al. 1990). GINGA found that spectra of some Seyfert galaxies flatten above 10 keV, which is explained either due to absorption or reflection by an optically thick matter (Figure 2.5).

Reflection spectrum by cold matter is calculated by considering the X-ray absorption and scattering, and can be compared with observations (e.g., Lightman and White 1988; Guilbert and Rees 1988). An example of the X-ray reflection spectrum from a neutral and uniform density semi-infinite slab of gas is shown in Figure 2.6, where fluorescent emission lines are significant and the reflection hump is seen above 20 keV. Strength, shape, and broadening of this reflected spectrum may be used to diagnose the geometry, ionization state and iron abundance of the reflector, most likely an optically thick accretion disk. George & Fabian (1991) studied the reflection spectra by calculating interaction between X-rays and dense, neutral materials via Monte Carlo simulation, for different viewing angles of the disk. For example, dependence of the iron line equivalent width on the viewing angle is shown in Figure 2.7.

In the case of Seyfert galaxies, accretion disk is not the sole reprocessing site of X-rays. A molecular torus at the parsec scale surrounding the accretion disk, which is required by the unified model (Figure 2.2), also plays an important role. In the case of Seyfert 2s, the outer torus is responsible for the significant absorption (sometimes more than 10^{24} cm⁻²). In the case of Seyfert 1s, the torus works as an additional reflection site to produce a spectrum similar to that from the disk reflection (Figure 2.6).

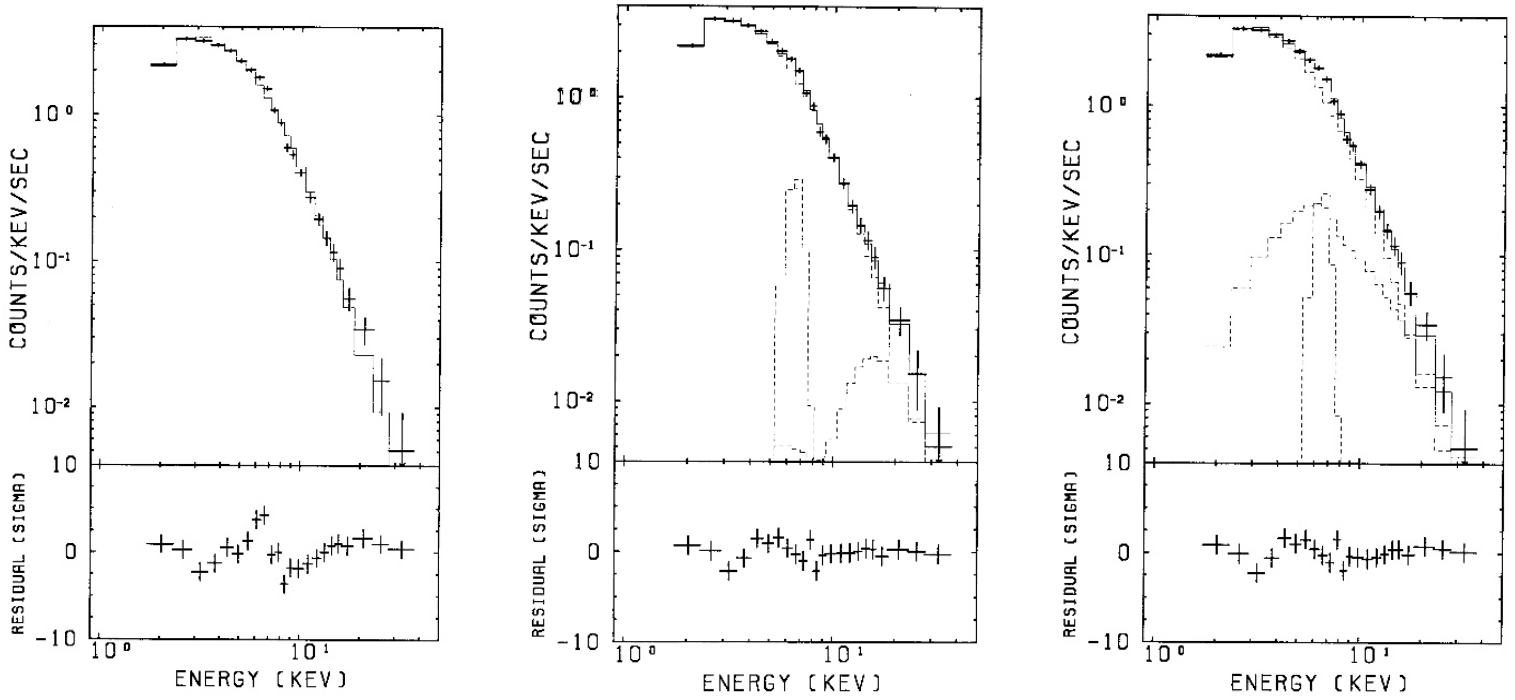


Figure 2.5: Left:GINGA MCG 6-30-15 spectrum fitted with a power-law with uniform cold absorber (Matsuoka et al. 1990). Iron K-emission line and K-edge feature are clearly recognized. Middle and Right:Same as in the Left figure with an additional heavily absorbed component (Middle) or a reflection component (Right), respectively.

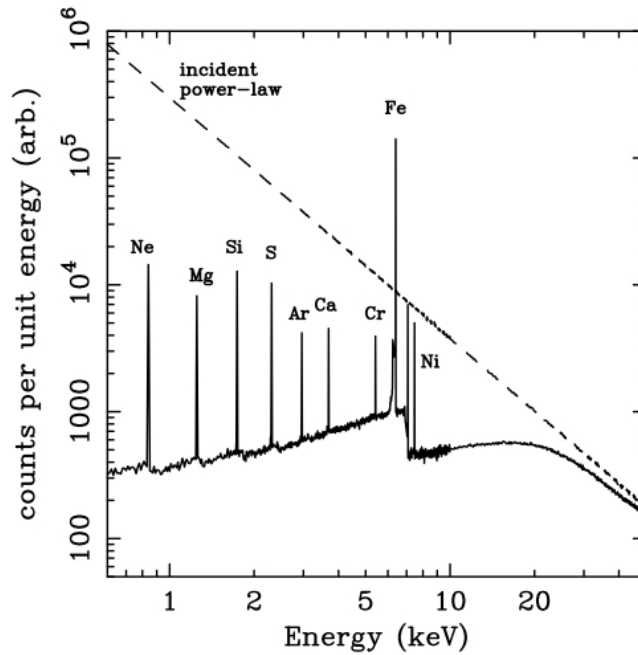


Figure 2.6: X-ray reflection spectrum from an illuminated cold slab (Reynolds 1996). Dashed line shows the incident continuum, and solid line shows the reflected spectrum, averaged over all the viewing angles.

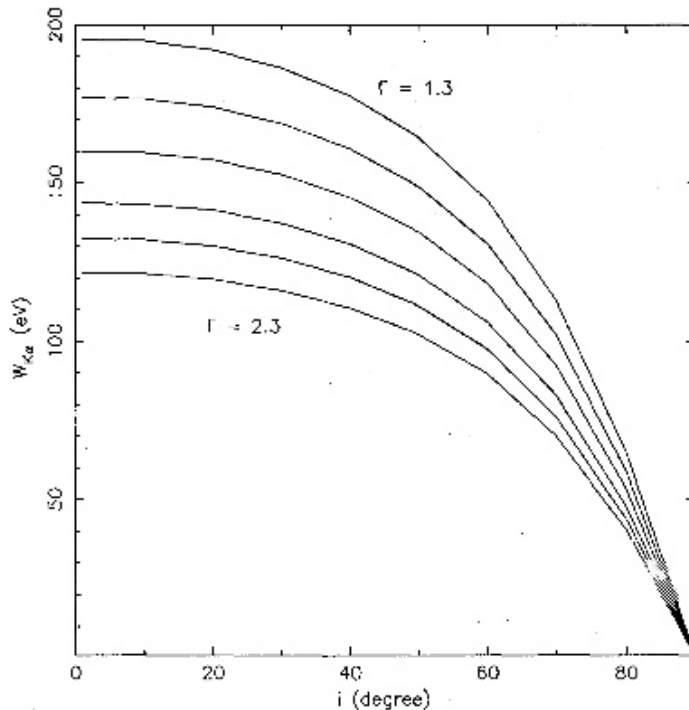


Figure 2.7: Predicted equivalent widths of the iron $K\alpha$ emission line versus viewing angle of the disk (George and Fabian 1991). Curves are shown for incident power-law spectra with $\Gamma = 1.3, 1.5, 1.7, 1.9, 2.1,$ and 2.3 , from the top to the bottom.

Warm absorber

X-ray absorption by partially-ionized, optically thin material in the line-of-sight (so-called “warm absorber”), is a common feature in the X-ray spectra of Seyfert galaxies. Presence of warm absorber was first postulated in order to explain the unusual form of the X-ray spectrum of the QSO MR 2251—178 (Halpern 1984; Pan, Stewart & Pounds 1990). Further evidence for such material came from Ginga observations of nearby Seyfert 1 galaxies, which suggested presence of K-shell absorption edges of highly ionized iron (Nandra, Pounds & Stewart 1990; Nandra et al. 1991; Nandra & Pounds 1994). The ROSAT Position Sensitive Proportional Counter (PSPC) also indicated probable K-shell absorption edges due to OVII and OVIII (Nandra & Pounds 1992; Nandra et al. 1993; Fiore et al. 1992; Turner et al. 1993). However, due to moderate spectral resolution of ROSAT, other explanations besides warm absorber (such as a soft excess or partial covering by a cold absorber) could not be ruled out to explain the observed feature.

ASCA for the first time confirmed presence of the prominent OVII and OVIII edges at 0.74 keV and 0.87 keV respectively in the X-ray spectra of several bright Seyfert 1 galaxies (Fabian et al. 1994). This strongly suggests presence of the photoionized material situated within ~ 10 pc of the primary continuum source. Furthermore, ASCA observations found the warm absorber in MCG-6-30-15 variable on timescales down to several hours (Fabian et al. 1994; Reynolds et al. 1995). In longer time scales, optical depth of the OVII edge remained rather constant on timescales of months to years, whereas depth of the OVIII edge was found to anti-correlate with the primary flux on timescales less than $\sim 10^4$ sec (Otani et al. 1996). These observations lead to a two-zone warm absorber model for MCG-6-30-15.

Recently, Miller et al. (2008) reported that five warm absorbing zones in a wide range of ionization degrees are necessary to fit the observed spectra. Figure 2.8 shows simultaneous fits

to the XMM Newton data split into 5 flux states. They conclude that the five warm absorber model explains the apparent red wing of the iron emission line, its lack of variability, the soft-band “excess” and the high flux seen in the hard X-ray band.

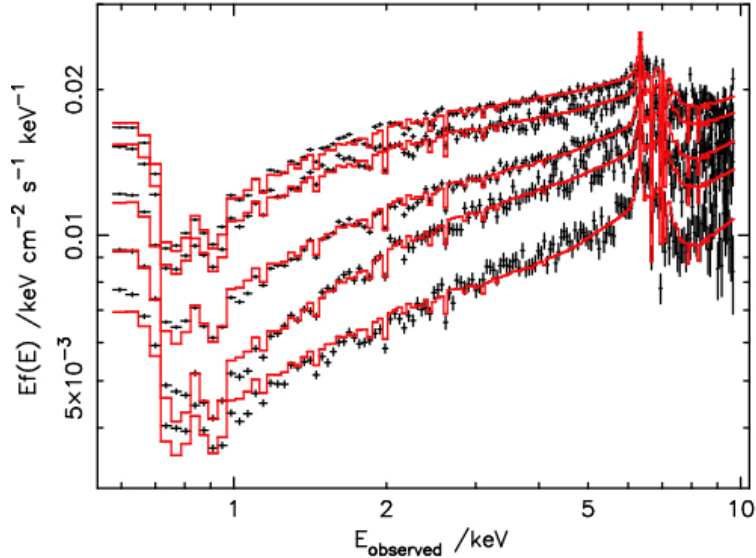


Figure 2.8: Simultaneous fits to the XMM-Newton data split into 5 flux states, 0.55-9.7 keV. The model is shown in units of $Ef(E)$, points with error bars show the ‘unfolded’ data.

2.2.3 “Broad” iron emission line

The 6.4 keV iron line detected by EXOSAT from the Galactic black hole binary Cygnus X-1 looked apparently broadened, if residuals of the power-law fit are observed (Barr, White & Page 1985; Figure 2.9). This is a motivation of the idea of “disk line” by Fabian et al. (1989) as explained below. If the iron line originates from the inner part of the accretion disk, the line shape may be distorted by the effects of Doppler shift and gravitational redshift (Fabian et al. 1989; Fabian et al. 2000). Figure 2.10 demonstrates these effects in a schematic way. In a non-relativistic disk, each radius of the disk produces a symmetric double-horned line profile corresponding to the emission from the material on the approaching (blue-shifted) side and receding (red-shifted) side (first panel of Figure 2.10). The closer to the black hole, where the Keplerian velocity is relativistic, the more relativistic beaming enhances the blue peak of the line (second panel of Figure 2.10). Additional distortions arise from the transverse Doppler effect and the gravitational redshift, both of which reduce the line central energy (third panel of Figure 2.10). Integrating all the line emission from each radius of the relativistic disk produces a highly skewed and broadened emission line profile (fourth panel of Figure 2.10).

Although EXOSAT GSPC was only sensitive up to ~ 13 keV, GINGA was able to obtain high-quality spectrum of Cyg X-1 up to ~ 30 keV, and detected an iron reprocessing feature above 10 keV, which is interpreted as due to disk reflection (Inoue 1989; <http://adsabs.harvard.edu/abs/1989ESASP.296>). Later, ASCA carried out the first CCD spectral observation of Cyg X-1, and resolved a *narrow* emission line (Ebisawa et al. 1996). In fact, both GINGA and ASCA spectra are explained with a disk reflection component and a narrow iron emission line (Figure 2.11), while an additional broad line is not required (Ebisawa et al. 1996). Thus, it was recognized that parameters of the broad iron emission line are significantly dependent on the continuum spectral parameters.

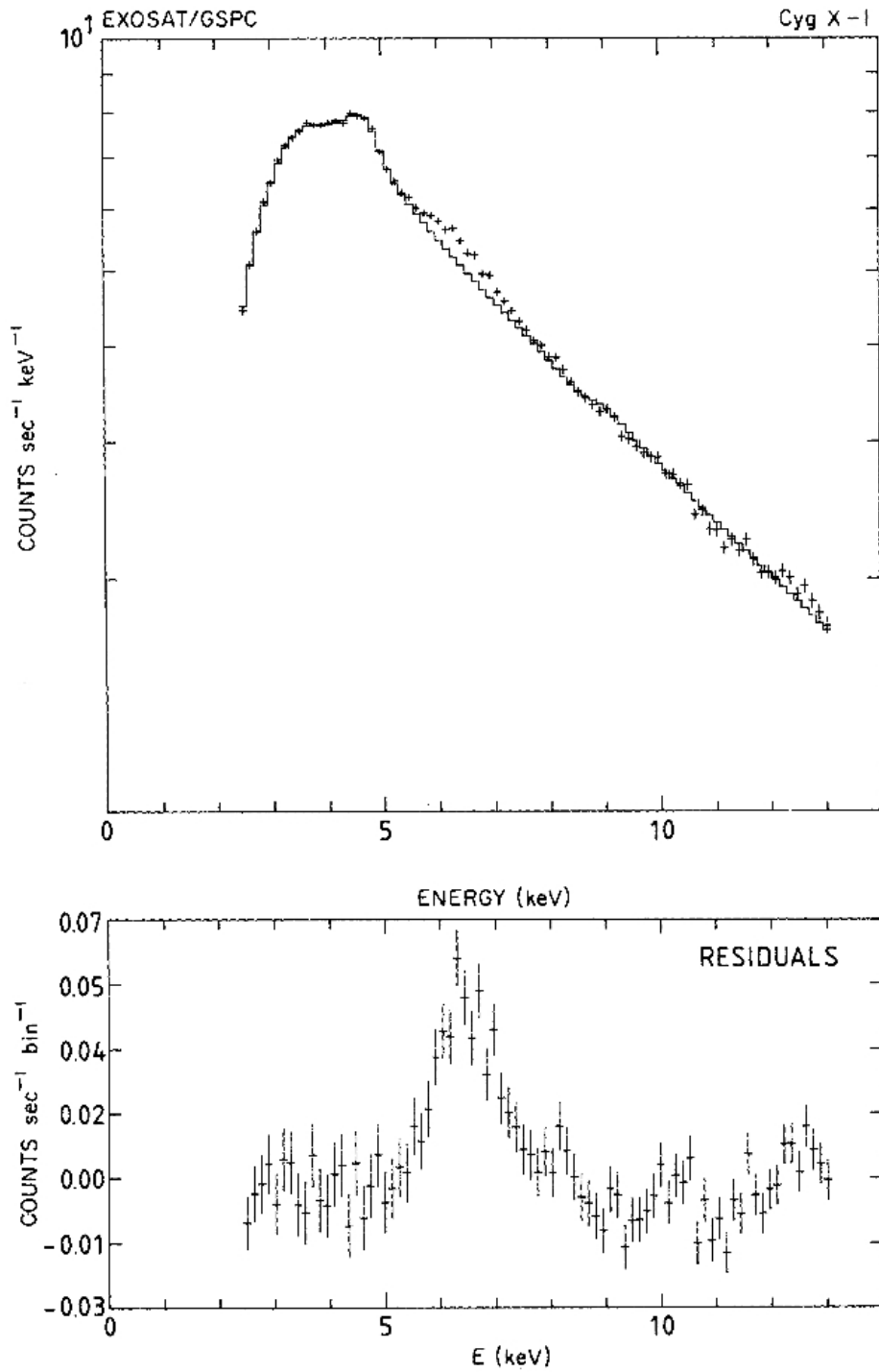


Figure 2.9: EXOSAT GSPC spectrum of Cygnus X-1. The solid line in the top panel is the best-fitting power-law. In the lower panel, residuals from the best-fit power-law are shown.

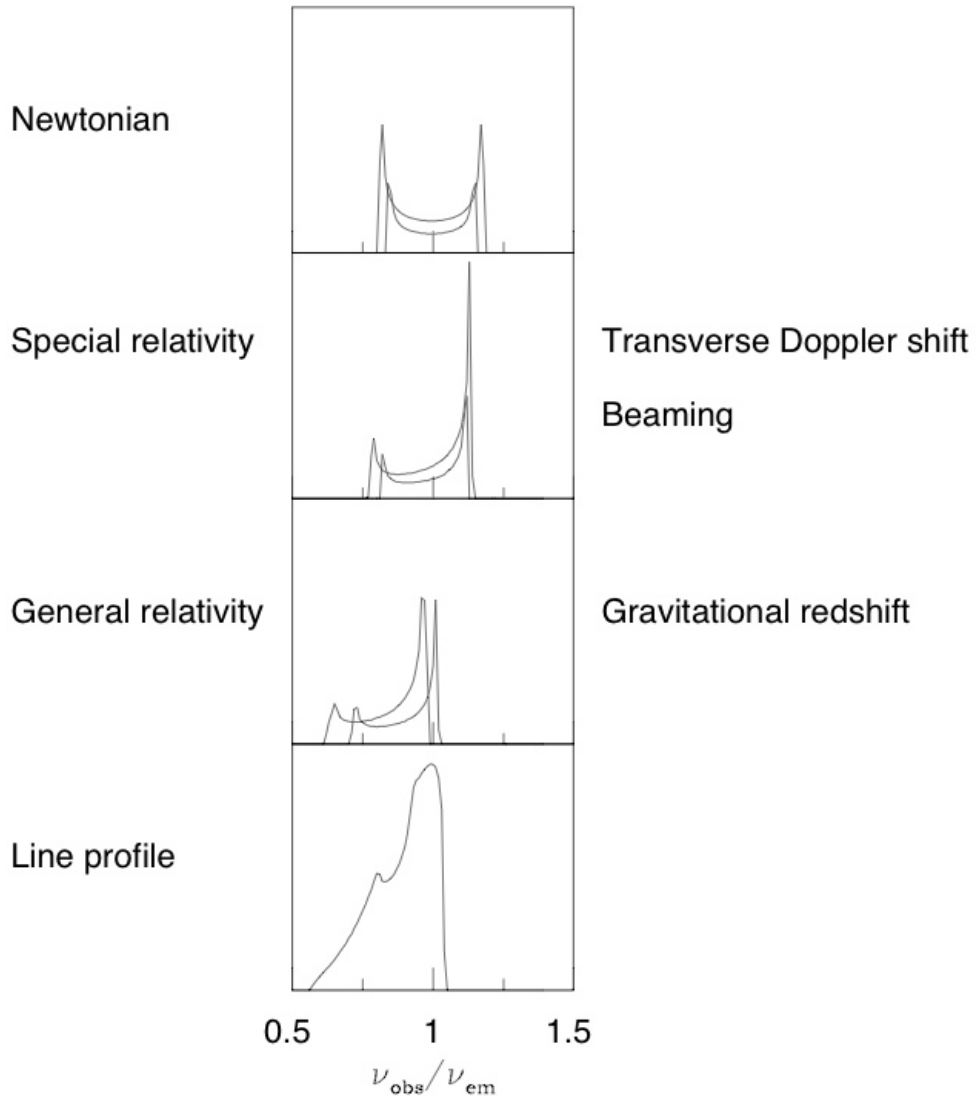


Figure 2.10: Profile of the broad iron line caused by the interplay of Doppler shifts, relativistic beaming, and gravitational redshift (Fabian et al. 1989). The top panel shows a systematic double-peaked profiles from two narrow annuli on a non-relativistic disk. In the second panel the effects of transverse Doppler shifting and relativistic beaming is included, and in the third panel gravitational redshift is additionally included. Combining all these effects gives rise to a broad, skewed line profile, as shown in the bottom panel.

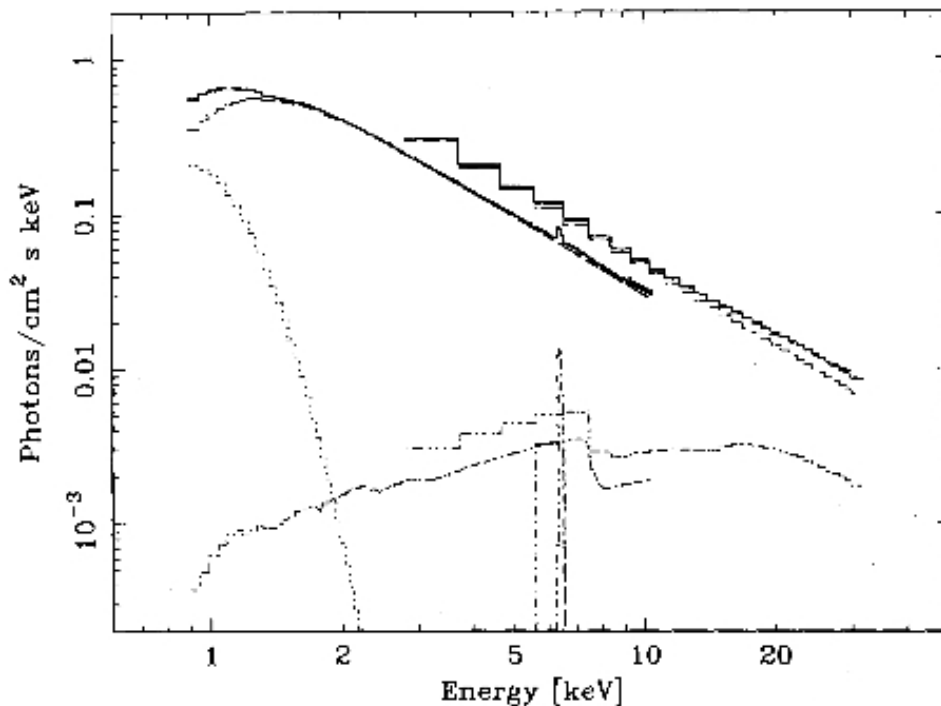


Figure 2.11: GINGA and ASCA spectral fitting of Cyg X-1 with disk reflection and a narrow emission line model (Ebisawa et al. 1996).

In Seyfert 1 galaxies too, broad iron emission lines are reported by many authors. The best example of an apparently skewed and broadened iron line is in MCG-6-30-15 (Tanaka et al. 1995). The iron line profile of MCG-6-30-15 seemed broadened and just looked like a disk line (Figure 2.12), when a particular continuum spectral shape was assumed. Similar broad iron emission lines have been reported in many other Seyfert 1s with ASCA, and thought to be a common spectral feature. Nandra et al. (1997) analyzed X-ray spectra of 18 Seyfert 1 galaxies observed with ASCA and reported that 14 sources show iron lines, which have a mean width of $1\sigma = 0.43 \pm 0.12$ keV with a Gaussian profile.

Meanwhile, recent observations of AGNs with XMM-Newton have shown that the broad iron K line is not so common as previously believed. Although a few Seyfert 1 galaxies (e.g., MCG-6-30-15, Mrk 205, Mrk 509) show clearly broad line features, iron lines in other galaxies are dominated by a relatively narrow feature. From an analysis of 53 Seyfert 1 galaxies observed with XMM-Newton, Page et al. (2004) has shown that 40 sources have a narrow iron K line ($\sigma \leq 0.1$ keV), while broad lines ($\sigma \geq 0.1$ keV) are detected only in the remaining 13 sources. Nandra et al. (2007) analyzed spectra of a sample of 26 Seyfert 1 galaxies observed with XMM-Newton. They reported that relativistic broad lines expected from vicinities of the black holes ($\leq 25 R_s$), are seen in only 30 percent of the sample, though narrow emission at 6.4 keV is nearly universal in the sample.

In a similar study, Yaqoob & Padmanabhan (2004) reported results of the 18 observations of 15 Seyfert 1 galaxies with the Chandra High Energy Transmission Grating Spectrometer (HETGS). They measured width of the line core and obtained a weighted mean of $\text{FWHM} = 2380 \pm 760$ km/sec, which is slightly larger than the instrument resolution ($\text{FWHM} \approx 1860$ km/sec). Evidence of underlying broad-line emission was also found in at least four sources.

If the “disk line”, which is a relativistically broadened iron K emission line expected from

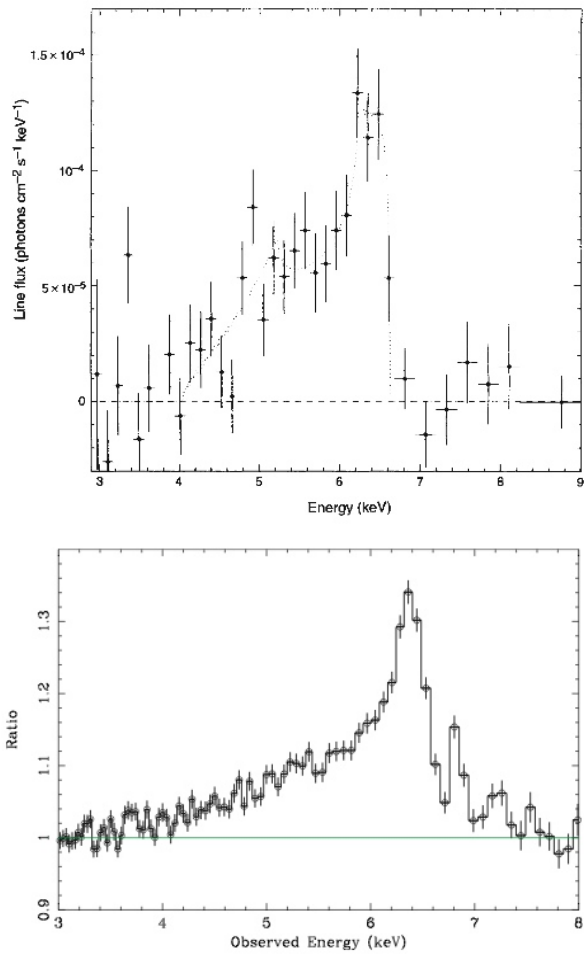


Figure 2.12: The iron $K\alpha$ line profile from MCG-6-30-15 observed with ASCA (Top; Tanaka et al. 1995) and that with Suzaku (Bottom; Miniutti et al. 2007).

innermost part of the accretion disk, truly exists, it would provide us with a rare opportunity to measure extremely strong gravities around the black hole directly. Thus, significant amounts of observational and theoretical works have been made on this subject in recent years. However, it is still controversial whether the disk line exists or not in the Galactic black hole binaries and/or Seyfert 1 galaxies. The primary reason of the difficulty of the problem is that the disk line parameters are dependent on the continuum spectral shape, which itself is not fully understood.

2.3 Motivation of our Study – a case of MCG-6-30-15

As explained in the previous section, the Seyfert 1 galaxy MCG-6-30-15 is famous as the primary “disk line” source. Therefore, the source has been attracting particular attention, and extensively studied with ASCA (Iwasawa et al. 1996,1999; Matsumoto et al. 2003), BeppoSAX (Guainazzi et al. 1999), Rossi X-ray Timing Explorer (Lee et al. 1999, Vaughan & Edelson 2001), Chandra (Lee et al. 2001, Young et al. 2005, Gibson et al. 2007), XMM-Newton (Fabian et al. 2002, Vaughan & Fabian 2004, Ponti et al. 2004), Suzaku (Miniutti et al. 2007), and a combination of Suzaku, Chandra and XMM-Newton (Miller, Turner, and Reeves 2008). In this section, we review observational characteristics of MCG-6-30-15 which have been revealed so far, and summarize remaining problems which we are going to address in the present thesis.

2.3.1 Narrow iron emission line

Using the Chandra HETGS, Young et al. (2005) resolved a narrow emission line at 6.4 keV in MCG-6-30-15, of which equivalent width is ~ 18 eV. This is much weaker than the narrow iron lines in other Seyfert 1 galaxies, for example, NGC 4151 (≤ 2 keV; Takahashi, Inoue and Dotani 2002). In the case of NGC 4151, from a very long RXTE monitoring data, Takahashi, Inoue, and Dotani (2002) obtained an unambiguous evidence that the reverberation of the iron line emission takes place very far from the black hole ($\sim 10^{17}$ cm), presumably the narrow-line region or the pc-scale torus (section 2.2.2). The narrow iron emission line in MCG-6-3-15 indicates that some reprocessing does take place very far from the black hole in MCG-6-3-15 too. However, the narrow and weak iron emission line does not account for the entire observed iron line feature (Figure 2.12). In fact, Young et al. (2005) claim that a broad and strong disk line underlies the weak narrow emission line in MCG-6-3-15.

2.3.2 Invariability of the iron emission line

Fabian et al. (2002) and Matsumoto et al. (2003) reported significant invariability in the iron line energy band of MCG 6-30-15 in XMM-Newton and ASCA observations, respectively. Figure 2.13 shows energy dependence of the Root Mean Square (RMS) variability on the time-bin-widths of 2.3×10^4 sec (circles) and 1.8×10^5 sec (squares) obtained with ASCA (Matsumoto et al. 2003)¹. It is clearly seen that the RMS variability is suppressed at the iron line energy range, in particular, the decrease is more significant in longer timescales.

¹The RMS variability is defined as follows (Ogawara et al. 1997): For a dataset of $\{x_i \pm \delta x_i\}_{i=1,N}$, where $\{x_i\}$ are observed counts per bins, $\{\delta x_i\}$ are their errors and N is number of the data bins, the RMS variability is defined as

$$\text{RMS variability} \equiv \sqrt{\frac{V_{\text{intrinsic}}}{N-1}}/\bar{x} \quad (2.5)$$

Where, $\bar{x} = \Sigma x_i/N$, and $V_{\text{intrinsic}}$ represents the variance arising only from the intrinsic source variability, that is, the variance free from Poisson noise, and is calculated as $V_{\text{intrinsic}} = \Sigma(x_i - \bar{x})^2 - \Sigma\delta x_i^2$.

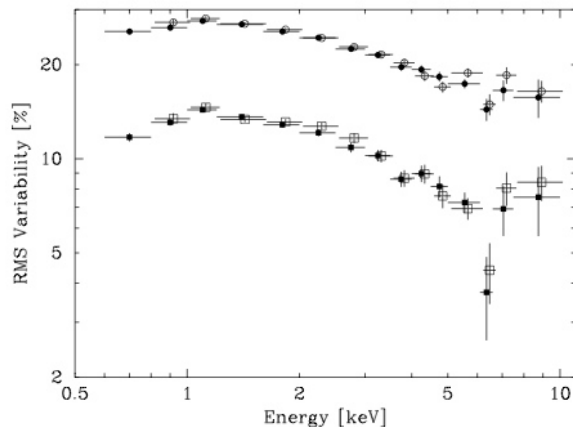


Figure 2.13: Energy dependence of the RMS variability on the time-bin-widths of 2.3×10^4 sec (circles) and 1.8×10^5 sec (squares). The filled and open marks correspond to the SIS and the GIS results, respectively (Matsumoto et al. 2003).

2.3.3 Light bending model

Miniutti and Fabian (2004) proposed that the observed invariability of the iron line may be explained if the disk reflection and line photon production takes place very close to the black hole, such that the apparent invariability of the iron line is caused by general relativistic light-bending effects. The left panel of Figure 2.14 shows the iron line EW, the Reflection-Dominated Component (RDC) and the direct continuum flux (PLC) as a function of the height h_s of the primary source above the equatorial plane, where the source is at a distance of r_g from a Kerr black hole rotation axis and it is represented by a ring-like source co-rotating with the accretion flow. Variations in the continuum and line flux are obtained by varying the source height between 1 and $20 r_g$ at fixed intrinsic luminosity, such that the observed flux variability is induced by light bending effects alone. The right panel of Figure 2.14 shows the iron line flux (RDC) as a function of the direct continuum flux (PLC) for an observer inclination of 30 degree (top panel) and 60 degree (bottom panel), where the source configuration is the same as the left panel.

Miniutti et al. (2007) claim that the strong reflection, the broad iron line (Figure 2.12 bottom) and invariability of the iron line observed with Suzaku may be explained with the light-bending model, and suggest that the innermost disk radius extends down to about as low as two gravitational radii. Niedźwiecki & Życki (2008) independently re-examined the light-bending model and concluded that it is indeed possible that a reflected component is very weakly variable compared to the primary emission, if the illuminating source is moving *radially* in a very vicinity of the rotating black hole.

2.3.4 Warm absorber model

Inoue and Matsumoto (2003) claims that the observed RMS variability of the iron line energy band (Figure 2.13) is less than what is expected when an invariable emission line is superposed on the variable continuum component. Instead, they proposed that the absorbed spectrum due to photoionized warm absorbers (section 2.2.2) mimics the shape of the strongly red-shifted iron line, and variation of the warm absorbers explains apparent invariability in the iron line energy band.

Recently, Miller et al. (2008) analyzed the data of MCG-6-30-15 taken by Suzaku, Chandra, and XMM-Newton. They reported that five warm absorbing zones in a wide range of ionization

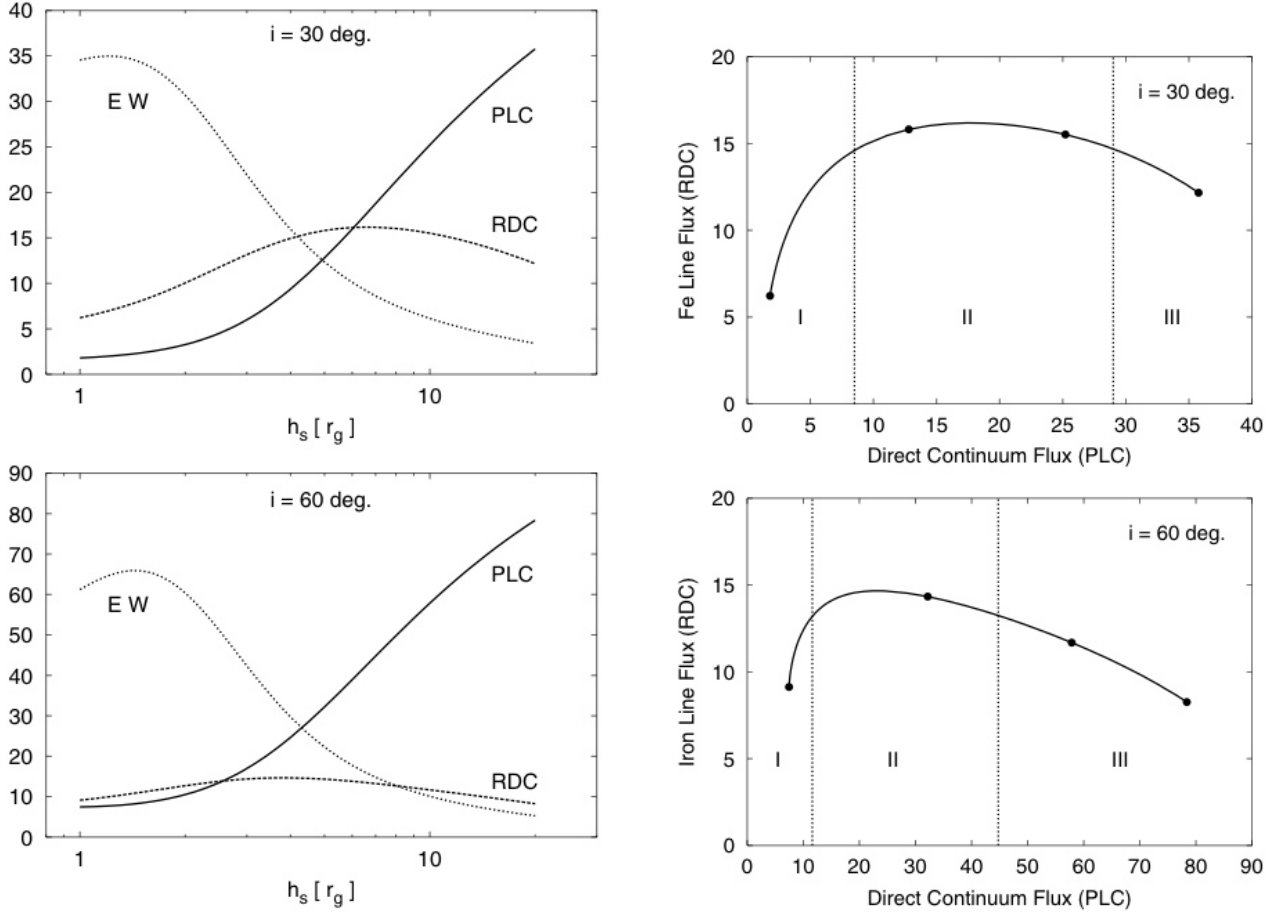


Figure 2.14: (Left) The iron line EW, the RDC (represented by the iron line) and the direct continuum flux (PLC) as a function of the height h_s of the primary source above the equatorial plane. The variations in the continuum and line flux are obtained by varying the source height between 1 to 20 r_g at fixed intrinsic luminosity. The source is located at a distance of r_g from a Kerr black hole rotation axis and it is represented by a ring-like source co-rotating with the accretion flow. The top panel refers to an observer inclination of 30 degree, while the bottom panel is for an inclination of 60 degree. Units are arbitrary. (Right) The iron line flux (RDC) as a function of the direct continuum flux (PLC) for an observer inclination of 30 degree (top panel) and 60 degree (bottom panel). The source configuration is the same as the left panel that the height varies between 1 and 20 r_g . As a reference, the vertical dotted lines separate different regions of the source heights, $h_s = 1-5$, $5-10$ and $10-20 r_g$. Units are arbitrary (Miniutti and Fabian 2004).

degrees are necessary to fit the observed spectra. In addition, a variable partial-covering zone plus absorbed low-ionization reflection provides a complete description of the variable X-ray spectrum. They conclude that the five warm absorber model explains the apparent red wing of the iron emission line, its lack of variability, the soft-band “excess” and the high flux seen in the hard X-ray band. A relativistically-blurred iron line is not required in their model.

2.3.5 Remaining problems

The primary question in MCG-6-30-15 is whether the iron line is truly broad and its lack of variability is a result of the general relativistic light bending effects. The crucial element to address the problem is to model the underlying continuum spectrum and study its variation. The broad band continuum in MCG-6-30-15 is complex, with strong modification by warm absorbers, and highly variable. Unless modelling the global continuum energy spectrum correctly, we may not constrain the local iron line feature, since the broad iron line parameters are dependent on the choice of the continuum spectral model.

In this thesis, we attempt to comprehensively understand the spectral variability of MCG-6-30-15. Our goal is to find a continuum spectral model of MCG-6-30-15 which is able to explain the observed spectral variation at various timescales with minimum numbers of parameters. If we are successful to construct such a reasonable spectral model, we will see if the relativistically distorted iron emission line is present or not in the energy spectrum of MCG-6-30-15. We believe this is an important step forward for us to fully understand X-ray properties of MCG-6-30-15, Seyfert 1 galaxies, and black holes.

Chapter 3

Instrumentation

3.1 Suzaku

3.1.1 Overview of the satellite

Suzaku (Astro-E2) was launched on 12:30 pm JST on July 10, 2005 from the Uchinoura Space Center (USC) in Japan. Suzaku takes a near-Earth circular orbit with an altitude of ~ 570 km and an inclination of 31 degree. The most notable characteristic of Suzaku is a high throughput over the broad energy range from ~ 0.3 keV to ~ 600 keV.

Figure 3.1 shows a schematic view of Suzaku. Suzaku has five X-Ray Telescopes (XRTs), four of which are for the X-ray Imaging Spectrometers (XIS), and one was originally for the X-Ray Spectrometer (XRS); unfortunately, XRS stopped working soon after the launch. The XIS covers the energy range from ~ 0.3 keV to ~ 10 keV. Suzaku also carries the Hard X-ray Detector (HXD), which is non-imaging instrument and can take data from ~ 15 keV to ~ 600 keV.

3.1.2 X-ray Imaging Spectrometer (XIS)

Suzaku has four X-ray Imaging Spectrometers (XISs; Figure 3.2). These employ X-ray sensitive silicon charge-coupled devices (CCDs), which are operated in a photon-counting mode, similar to those used in ASCA SIS, Chandra ACIS, and XMM-Newton EPIC.

Basic components of the XIS

The four Suzaku XISs are named XIS0, XIS1, XIS2, and XIS3, each located on the focal plane of an X-ray Telescope; those telescopes are identical and named respectively as XRT-I0, XRT-I1, XRT-I2, and XRT-I3. Each CCD camera has a single CCD chip with an array of 1024×1024 pixels, and covers an $17.8' \times 17'8$ region on the sky. Each pixel is $24 \mu\text{m}$ square, and the size of the CCD is $25 \text{ mm} \times 25 \text{ mm}$. Unfortunately, XIS2 showed an anomaly on November 9 2006, and has not been available for scientific observation since then.

A CCD has a gate structure on one surface to transfer the charge packets to the readout gates. The surface of the chip with the gate structure is called the "front side". A Front side Illuminated CCD (FI CCD) detects X-ray photons that pass through its gate structure from the front side. Because of the additional photo-electric absorption at the gate structure, the low energy Quantum Detection Efficiency (QDE) of the FI CCD is rather limited. Conversely, a Back-side Illuminated CCD (BI CCD) receives photons from "back", the side without the gate structure. A BI CCD retains a high QDE even in sub-keV energy band because of absence of the gate structure. In Suzaku, XIS1 uses the BI CCDs while the other three use FI CCDs.

In order to reduce contamination of the X-ray signal by optical and UV light, each XIS has

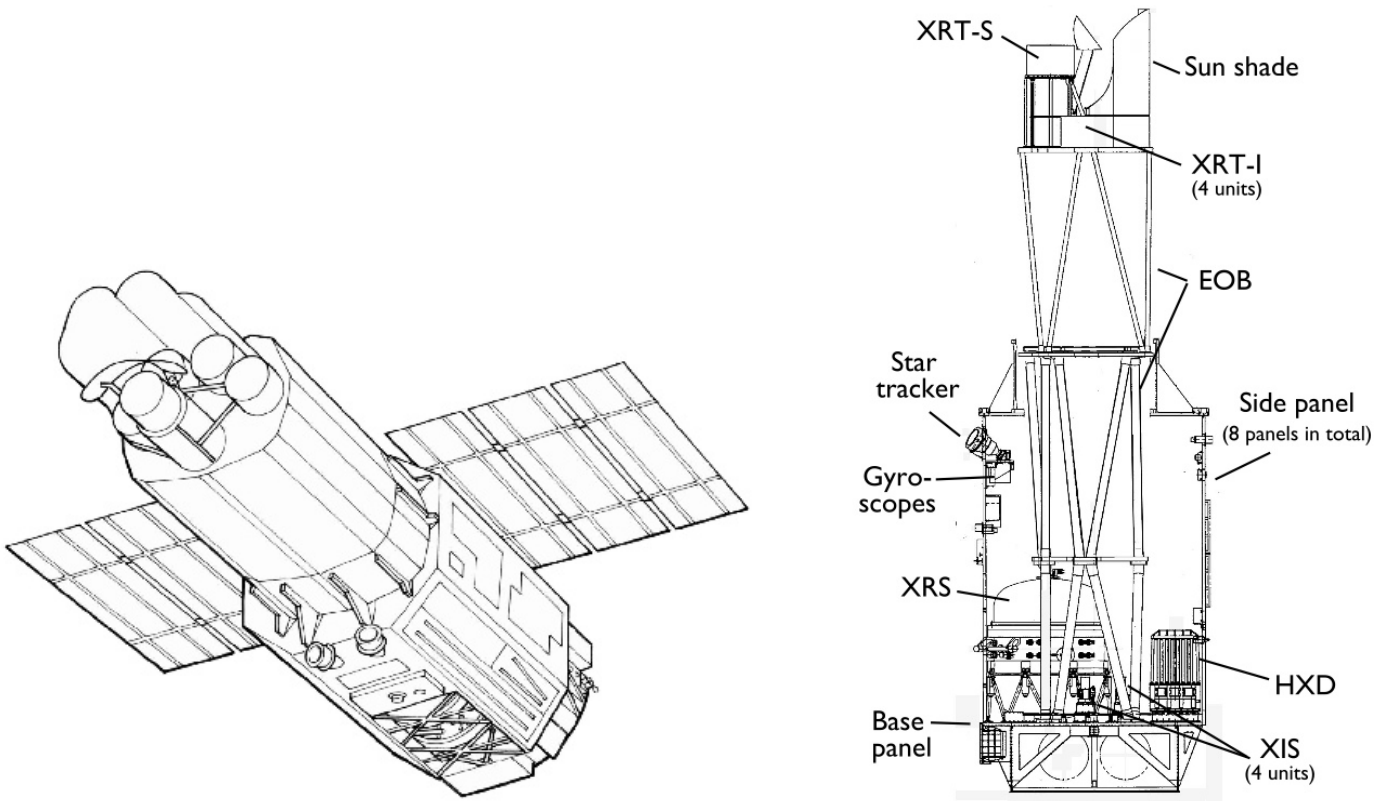


Figure 3.1: (Left) Schematic view of the Suzaku satellite in orbit (Mitsuda et al. 2007). Both solar paddles and the extensible optical bench (EOB) are deployed. On the top, The X-Ray Telescope (XRT-S) for the X-Ray Spectrometer (XRS), and the four X-Ray telescopes (XRT-Is) for the X-ray CCD camera (XIS) can be seen. (Right) Side view of Suzaku with the internal structures after EOB deployment (Mitsuda et al. 2007).

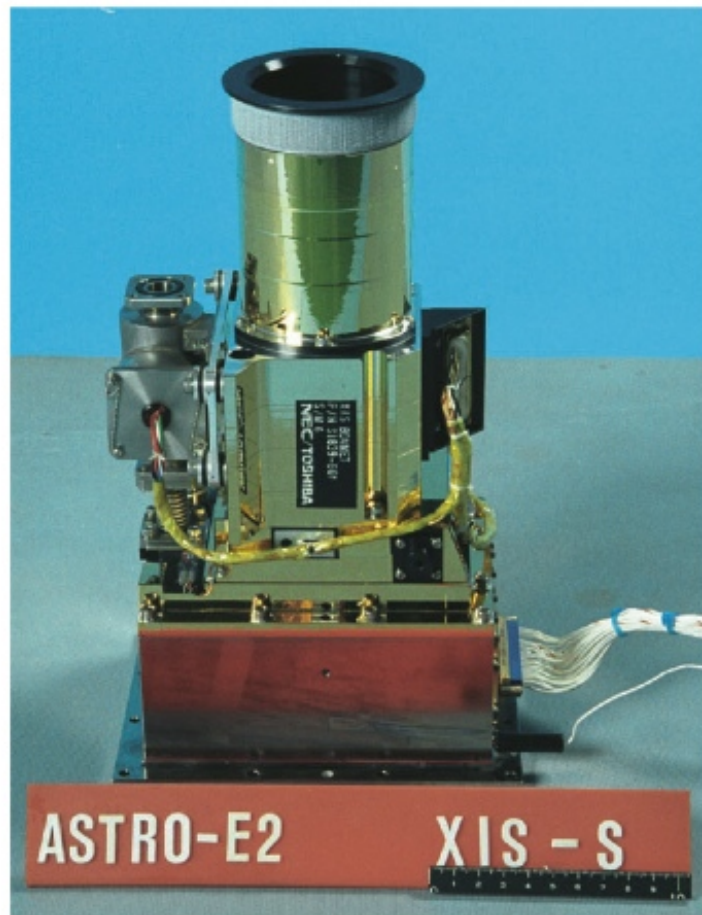


Figure 3.2: A picture of an XIS sensor (Koyama et al. 2007).

an Optical Blocking Filter (OBF) located in front of it. The OBF is made of polyimide with a thickness of 1000 Å, coated with a total of 1200 Å of aluminum (400 Å on one side and 800 Å on the other side). To facilitate the in-flight calibration of the XISs, each CCD sensor has two ^{55}Fe calibration sources.

XIS has a "charge injection capability", which allows an arbitrary amount of charge to be input to the pixels at the top row of the imaging region (exposure area), i.e. the far side from the frame-store region. The charge injection capability may be used to measure the Charge Transfer Inefficiency (CTI) of each column, or to reduce the amount of CTI.

Performance of the XIS

Figure 3.3 shows effective areas of a single BI and FI CCD. The effective area at 0.4 keV of the BI is larger by nearly one order of magnitude than that of the FI CCD. The effective area of the FI becomes larger than BI above 4 keV. The XIS-FI cameras have an effective area of 147 cm² each at 8 keV. Since Suzaku has three identical XIS-FI cameras, the total effective area obtained at 8 keV is ~ 440 cm², which is comparable to that of XMM-Newton EPIC-pn. One of the most remarkable features of XIS is its energy resolution, ~ 60 eV at 1 keV and ~ 130 eV at 6 keV (FWHM). The XIS BI achieves both the good energy resolution and the large effective area simultaneously in soft energy bands. A very thin (~ 1 nm) layer of silver on the backside of XIS-BI improves the energy resolution. The silver catalyzes dissociation of molecular oxygen, leaving negative oxygen ions on the surface (Burke et al. 2004). These ions improve the charge collection efficiency and ensure its superior energy resolution.

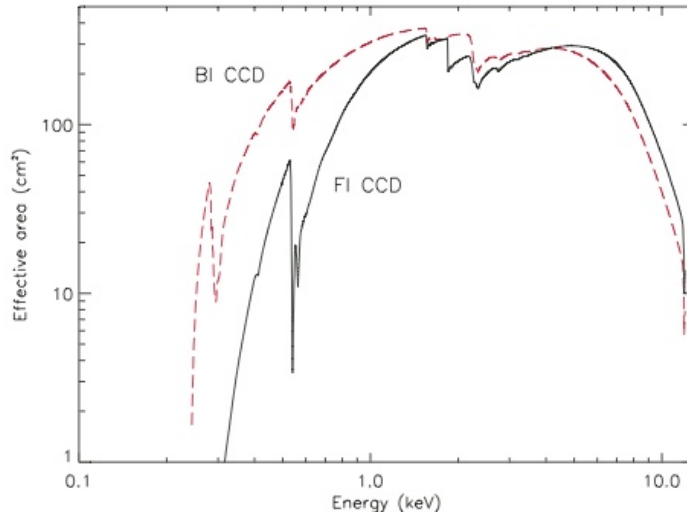


Figure 3.3: Effective area of a single XRT-XIS system, for the FI (XIS 0,2,3) and BI CCDs (Mitsuda et al. 2007).

Low and stable background is one of the advantages of the Suzaku XIS. The background originates from the cosmic X-ray background (CXB) and charged particles (Non X-ray Background, (NXB)). In left hand of Figure 3.4, I show the NXB spectrum obtained by observation of dark earth by XIS. The background rate between 1–12 keV is 0.11 counts s⁻¹ in the XIS-FIs and 0.40 counts s⁻¹ in the XIS-BI (Koyama et al. 2007). There are some fluorescence line features arising from material in the XIS and XRTs. Major lines are summarized in Table 3.1. Mn lines are due to the scattered X-rays from the calibration sources. O lines are mostly contamination from the day earth. Other lines come from material used for the sensor. We compare the background of XISs with that of other CCD cameras used in various missions. Figure 3.4 (Right) shows the

background spectra normalized by effective area and by solid angle of the Field Of View (FOV). This plot demonstrates that Suzaku/XIS and ASCA/SIS have a higher Signal to Noise (S/N) ratio than other instruments. The S/N ratio of Suzaku/XIS-FI at 7 keV is 2–4 times higher than that of XMM-Newton. One of the reasons for the high S/N ratio is the low earth orbit of Suzaku, which makes Suzaku almost free from background flares that often hamper observations by Chandra and XMM-Newton.

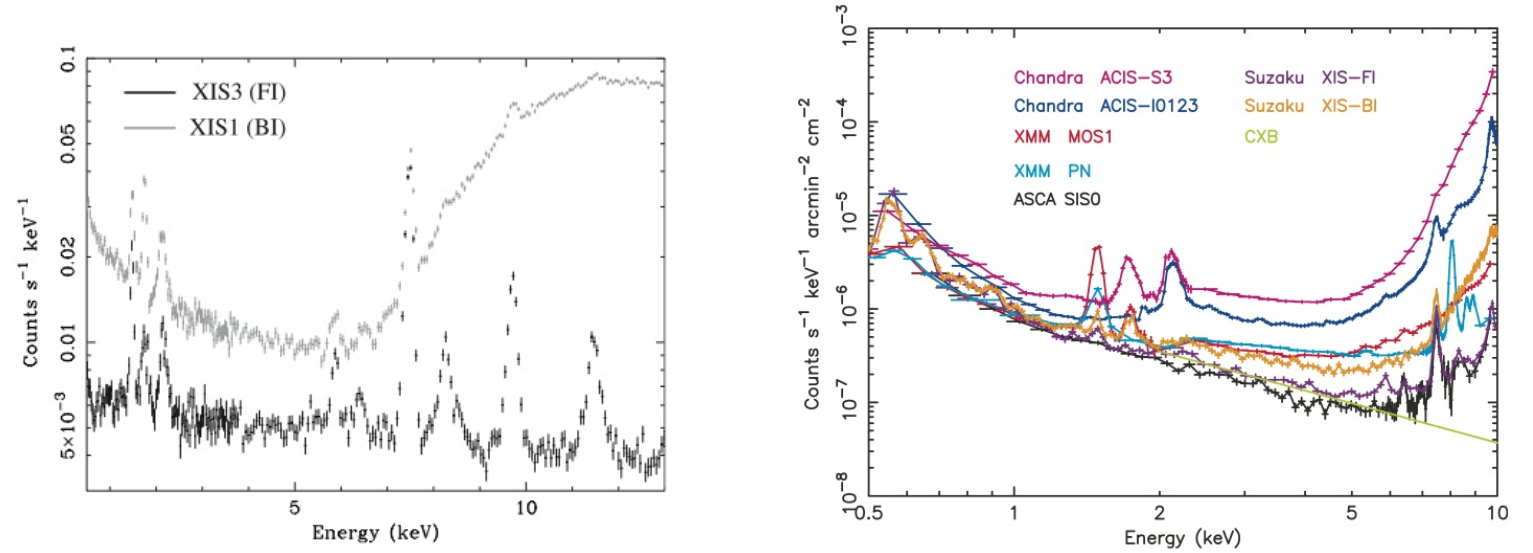


Figure 3.4: (Left) The night Earth spectra with the BI and FI CCDs (Koyama et al. 2007). (Right) XIS background counting rates as a function of energy in comparison of those of ASCA, XMM-Newton, and Chandra (Katayama et al. 2004). The background rates are normalized by the effective area and the field of view, which is a good measure of sensitivity to extended sources.

The OBFs have been gradually contaminated since the the XIS door-open by the out-gas from the satellite, and the rates are different from sensor to sensor. The contamination causes a reduction of low-energy sensitivity, and the corresponding time-varying low energy absorption is additionally included in the response function. For this purpose, the extra absorption due to the OBF contamination is measured by observing the SNR 1E 0102–72 and an isolated neutron star RX J1856.5–3754 regularly. From the overall spectral shape in the low energy absorption, Koyama et al. (2007) assume that the contaminant contains predominantly C and O with the number ratio C/O \sim 6. The time dependence of the contamination thickness is found to be empirically represented by the exponential form, $N_C = a - b \times \exp(-day/c)$, where N_C is the carbon column density in units of 10^{18} cm^{-2} (Figure 3.5).

Capability to conduct Spaced-row Charge Injection (SCI) is another advantage of Suzaku XISs. SCI can mitigate the effects of in-flight radiation damage of XIS, which causes degradation of XIS performance. A sufficient quantity of charges injected periodically during the charge transfer tends to fill radiation-induced traps, and doing so reduces the effects of the traps in the Charge Transfer Efficiency (CTE). Since traps need to be filled quite often, charges injected every 54 rows in every exposure. The charge injected rows are not usable to detect X-ray photons, and become as dead area. This method was successfully implemented in the calibration observations of 1E0102–72 and the Perseus cluster in the end of August 6 2006, and the energy resolution was found to recover to approximately 150 eV at 6 keV (Uchiyama et al. 2009)¹.

¹The SCI has been implemented in regular observations since 2006 October. In this thesis, we

Table 3.1: Main XIS Background Emission lines (Tawa et al. 2008). Typical accumulation time are 110–160 ksec.

Line	Energy keV	XIS-S0	XIS-S1	XIS-S2	XIS-S3
		10^{-9} cnts/sec/pixel	10^{-9} cnts/sec/pixel	10^{-9} cnts/sec/pixel	10^{-9} cnts/sec/pixel
O K	0.523	18.5 ± 0.5	69 ± 3	14 ± 2	14 ± 1
Al K	1.56	2.0 ± 0.2	3.0 ± 0.5	1.5 ± 0.3	1.6 ± 0.3
Si K	1.84	0.3 ± 0.2	2.2 ± 0.5	$0.06 (< 0.28)$	0.5 ± 0.2
Au M	2.31	0.58 ± 0.23	1.1 ± 0.3	0.4 ± 0.2	6.7 ± 2.9
Mn $K\alpha$	5.90	8.4 ± 0.4	0.65 ± 0.29	0.30 ± 0.21	0.39 ± 0.18
Mn $K\beta$	6.49	1.03 ± 0.22	$0.29 (< 0.65)$	$0.00 (< 0.11)$	0.43 ± 0.23
Ni $K\alpha$	7.47	7.2 ± 0.3	6.2 ± 0.5	3.8 ± 0.3	7.1 ± 0.4
Ni $K\beta$	8.27	0.58 ± 0.18	1.2 ± 0.5	0.62 ± 0.21	0.98 ± 0.25
Au $L\alpha$	9.67	3.5 ± 0.3	3.3 ± 1.0	1.9 ± 0.3	3.5 ± 0.4
Au $L\beta$	11.51	$2.3^{+0.7}_{-0.6}$	2.9 ± 1.3	$0.8^{+0.4}_{-0.3}$	$2.7^{+0.6}_{-0.5}$

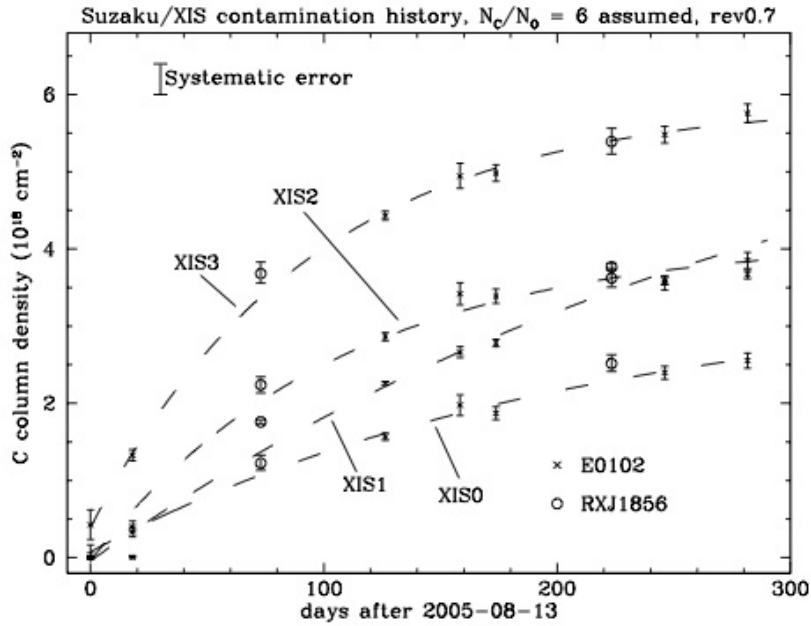


Figure 3.5: Time history of the OBF contamination for all the four XIS detectors, measured at the center of the OBF (Koyama et al. 2007).

Table 3.2: X-ray Telescope design parameters (Serlemitsos et al. 2007).

	XRT-I	ASCA
Focal length	4.75 m	3.50 m
Number of Modules	4	4
Substrate		
Material	Aluminum	Aluminum
Substrate thickness	152 μ m	127 μ m
Axial length	101.6 μ m	101.6 μ m
Reflector		
Material	Au	Au
Number of nested shells	175	120
Diameter of innermost reflector	118 mm	120 mm
Diameter of outermost reflector	399 mm	345 mm
Number of reflectors/telescope	1400	960
Geometrical area/telescope	873 cm ²	558 cm ²
Weight/telescope	19.3 kg	9.84 kg

3.1.3 X-Ray Telescope (XRT)

Basic Components of the XRT

Suzaku has five light-weight thin foil X-ray Telescopes (Serlemitsos et al. 2007; Figure 3.6, Right). Four of them, which are used to focus on the XIS, are called "XRT-I" and the other is called "XRT-S" for the XRS. They are arranged on the Extensible Optical Bench (EOB) as shown in Figure 3.6 (Right). Basic parameters of these two kinds of XRTs are summarized in Table 3.2.

The Suzaku XRT is a thin-foil-nested Wolter-I type telescope. In spite of a severe weight limit imposed by the launch vehicle for Suzaku, maximum possible effective area, particularly at the energy of the Fe K lines, is achieved as shown in the next section. Each mirror consists of thin substrates made of aluminum and a reflecting gold surface, which is attached by an epoxy layer to the substrate. Total thickness of the substrate is 178 μ m. It is 101.6 mm in slant length and with radii extending approximately from 60 mm at the inner part to 200 mm at the outer part. All mirrors are positioned with grooved alignment bars, which hold the foils at their circular edges. A pre-collimator, which blocks off the stray light that would otherwise enter the detector at a larger incident angle than intended, is mounted on each XRT. It is adopted for the first time in the Suzaku satellite. The pre-collimator consists of concentrically nested aluminum foils similar to that of the reflector substrates (Mori et al. 2005). Basic design parameters for the pre-collimator are summarized in Table 3.3. A thermal shield is also installed on top of each pre-collimator in order to isolate the XRT thermally from space, as well as to reflect infrared radiation from the interior of the spacecraft. It is made of an polyethylene terephthalate (PET) film with thickness of 0.24 μ m, coated with aluminum layer with thickness of 30 nm. XRT temperature is controlled within 20 ± 7.5 °C.

Performance of the XRT

Observations of the Crab nebula were carried out in August and September 2005 at various off-axis angles of 0', 3'.5, 7'. The intensity of the Crab is evaluated for each pointing and for each XIS module separately. Serlemitsos et al. (2007) obtained a direction of the optical axis of each telescope by finding the maximum throughput angle. The results are shown in Figure 3.7. The

use Suzaku data taken in January 2006, when SCI was not adopted.

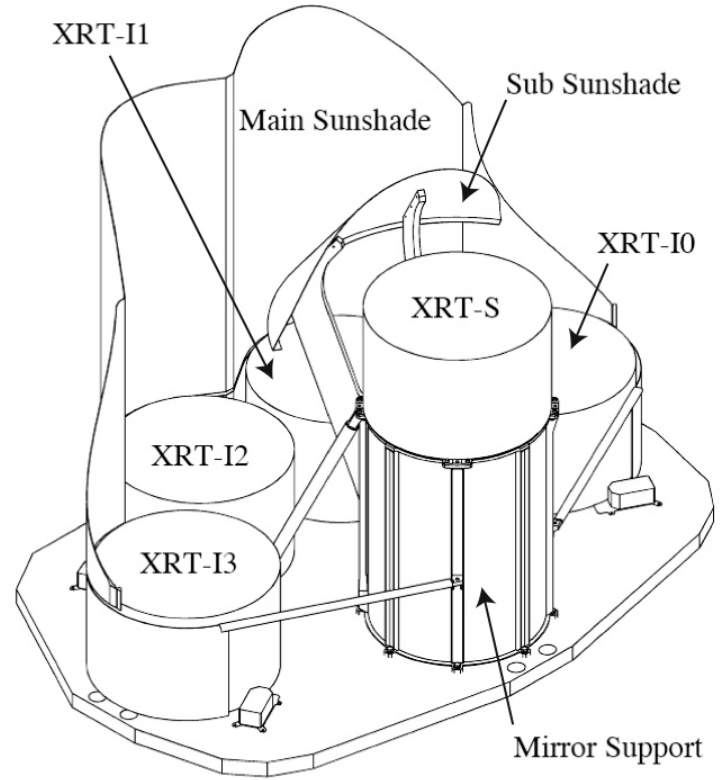
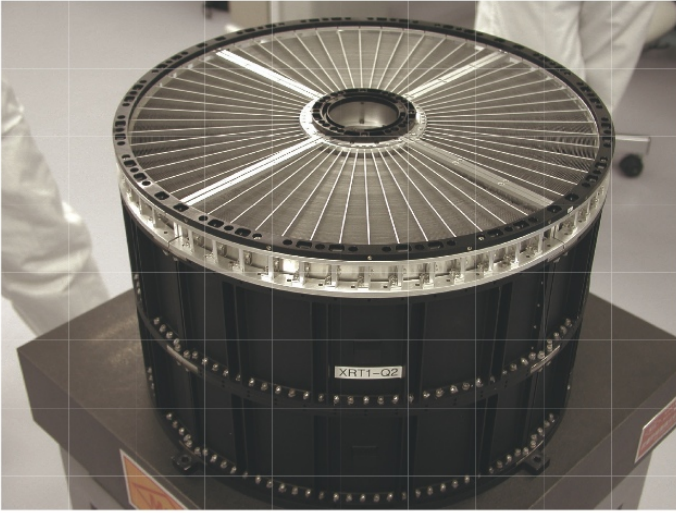


Figure 3.6: (Left) Picture of the module XRT-I1 (Serlemitsos et al. 2007). (Right) Schematic view of the Suzaku XRT mounted on the top plate of the Extensible Optical Bench (EOB) (Serlemitsos et al. 2007).

Table 3.3: Design parameters of the pre-collimator (Serlemitsos et al. 2007).

Parameter	XRT-I
Blade Material	Aluminum
Blade Thickness	120 μm
Blade Height	22 mm
Effective height	30 mm
Number of nesting	175
Housing height	32 mm
Weight/XRT	2.7 kg

optical axes locate roughly within $1'$ from the XIS aim point. This implies that the efficiency of all XRT-Is are more than 97% at 10 keV when we observe a point source on the XIS aim point. The observed intensities of the Crab at various off-axis angles are shown in Figure 3.8 with vignetting curves calculated by the ray-tracing simulator.

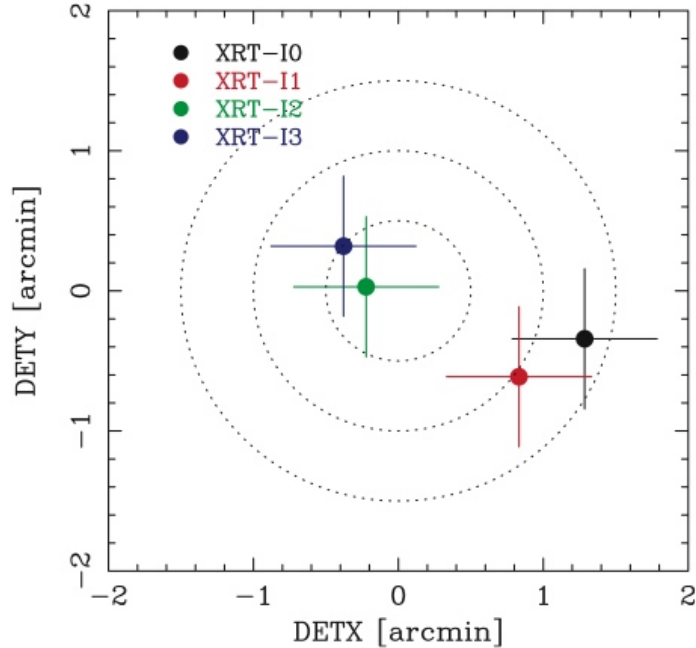


Figure 3.7: Locations of the optical axis of each XRT-I module in the focal plane determined from the observations of the Crab Nebula in 2005 August–September (Serlemitsos et al. 2007). This figure implies that the image on each XIS detector becomes brightest when a target star is placed at the position of the corresponding cross.

Figure 3.9 gives the total effective area of the four XRT-Is including the detector efficiency, compared with that of XMM-Newton (PN + 2MOS) and Chandra (ACIS-I and ACIS-S). The effective area of the four XRT-Is at 7 keV is larger than that of Chandra and comparable to XMM-Newton mirrors. Imaging capability of the XRTs has been verified with data of SS Cyg taken during 2005 November 2. SS Cyg is a point source and moderately bright, and the pile-up is negligible even at the image core. The images, Point Spread Functions (PSFs), and Encircled Energy Functions (EEFs) of all XRT-Is are shown in Figure 3.10. Half Power Diameter (HPD), which is defined as a diameter of a circle that includes 50% of total photons, is obtained as $1'.8, 2'.3, 2'.0$ and $2'.0$ for XRT-I0, 1, 2 and 3, respectively. These values are generally consistent with those obtained from ground-based calibration measurements.

3.1.4 3-1-4 Hard X-ray Detector (HXD)

Basic Component of the HXD

The Hard X-ray Detector (HXD) is a non-imaging, collimated hard X-ray instrument sensitive in 10–600 keV (Figure 3.12). HXD has 16 main detectors called “Well” units arranged in a 4×4 array, surrounded by 20 thick crystal scintillators for active shielding as shown in right hand of Figure 3.11. As illustrated in the bottom panel, each main unit consists of two types of detector; a GSO ($\text{Gd}_2\text{SiO}_5:\text{Ce}$ 0.5% mol) / BGO ($\text{Bi}_4\text{Ge}_3\text{O}_{12}$) phoswich scintillation counter, and four 2 mm thick silicon PIN diodes located inside the BGO shield. Softer photons typically below ~ 40

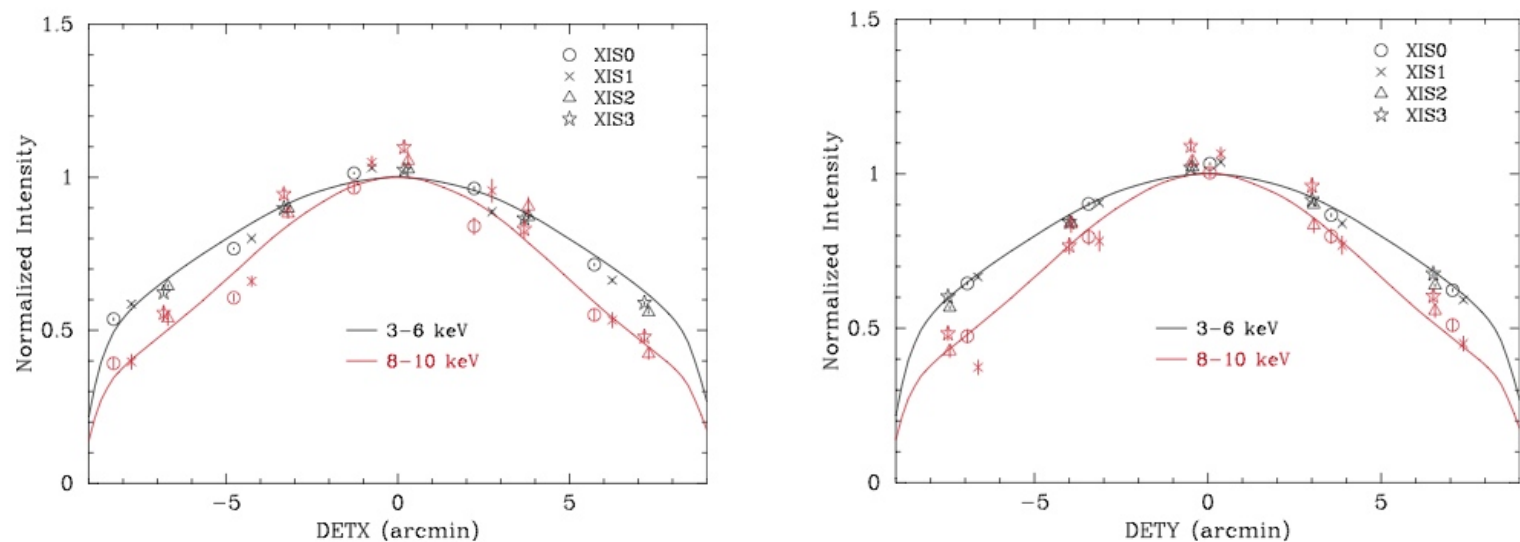


Figure 3.8: Vignetting of the four XRT-I modules using the data of the Crab Nebula taken during 2005 August 22-27 in the two energy bands 3–6 keV and 8–10 keV (Serlemitsos et al. 2007).

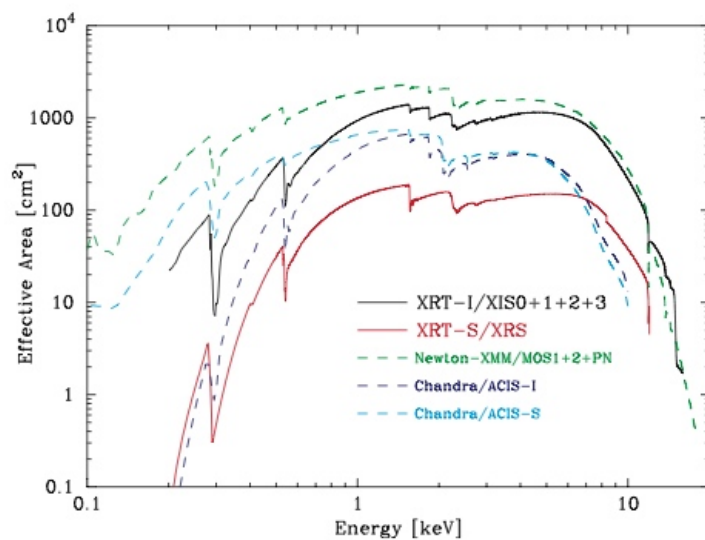


Figure 3.9: Total effective area of the four XRT-I modules compared with that of XMM-Newton and Chandra (Serlemitsos et al. 2007). Transmissions of the thermal shield and the optical blocking filter, and the quantum efficiency of the CCD are all taken into account.

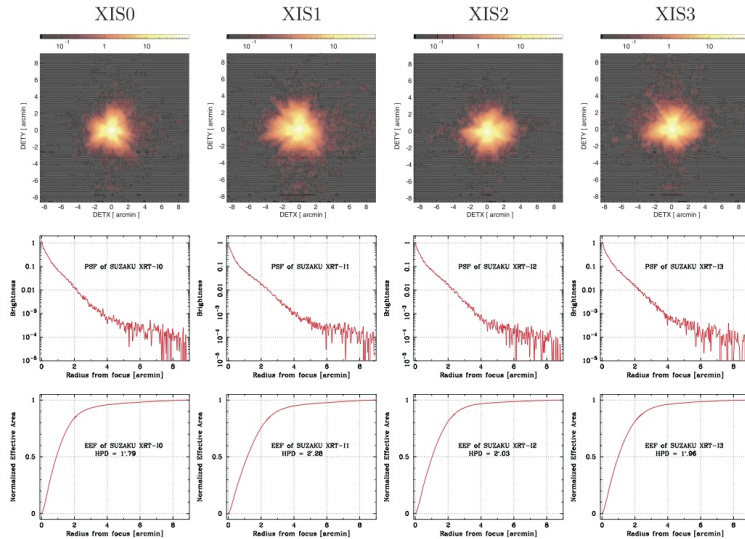


Figure 3.10: Image, Point Spread Function (PSF), and Encircled Energy Function (EEF) of the four XRT-I modules in the focal plane (Serlemitsos et al. 2007). All of the images are binned with 2×2 pixels, followed by being smoothed with a Gaussian profile with a sigma of 3 pixels, where the pixel size is $24 \mu\text{m}$. The EEF is normalized to unity at the edge of the CCD chip (a square of $17'.8$ on a side).

keV are detected mainly by the PIN, while harder photons penetrating the diodes are detected mainly by the GSO².

Performance of the HXD

Figure 3.12 shows effective area of 16 well-counter units, which was based on the photo-peak efficiency calculated by Monte Carlo simulations using EGS4 code (Nelson et al. 1985). The total geometrical area of the PIN diodes is 160 cm^2 , while that of the GSO is 350 cm^2 . There is a large enough overlapping energy region between GSO and PIN 40–70 keV. Angular responses measured with γ -ray lines from the radio isotope are shown in Figure 3.13. Below 100 keV, the passive fine collimators define a $34' \times 34'$ (Full-Width at Half Maximum: FWHM) square FOV. Above ~ 100 keV, the fine collimators become transparent and the BGO active collimator defines a $4^\circ.5 \times 4^\circ.5$ FWHM square opening.

Low background is the most important characteristic of Suzaku HXD. In the hard X-ray and soft γ -ray bands, observations suffer from high backgrounds due to charged particles, cosmic diffuse γ -rays, secondary γ -rays produced in the environment, activation caused by cosmic protons, and so on. In order to reduce the background, the HXD has employed the following five techniques (Takahashi et al. 2007):

- The five-sided tight BGO shielding.
- Use of the 20 shielding counters made of thick BGO crystals which surround the 16 main GSO/BGO counters.
- Sophisticated onboard signal processing and onboard event selection, employing both high speed parallel hardware circuits in the Analog Electronics, and CPU-based signal handing in the Digital Electronics.

²However, MCG-6-3-15 is not bright enough to be detected by GSO above ~ 40 keV. Hence, we use only HXD-PIN in this thesis.

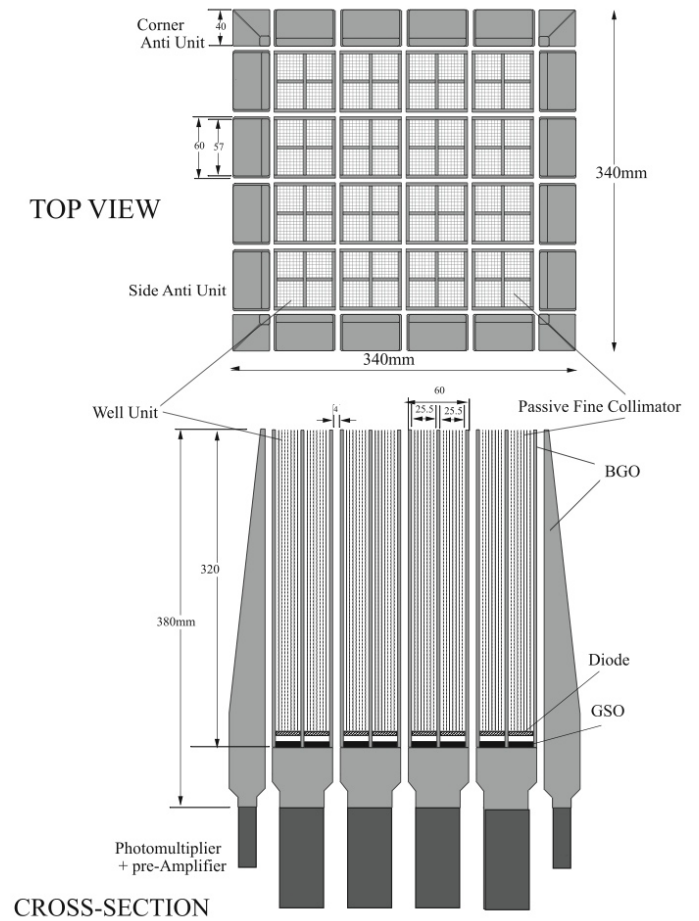


Figure 3.11: (Left) Hard X-ray Detector (HXD). (Right) Schematic drawing of HXD-S. It consists of 16 well-counter units and 20 anti-counter units (Takahashi et al. 2007).

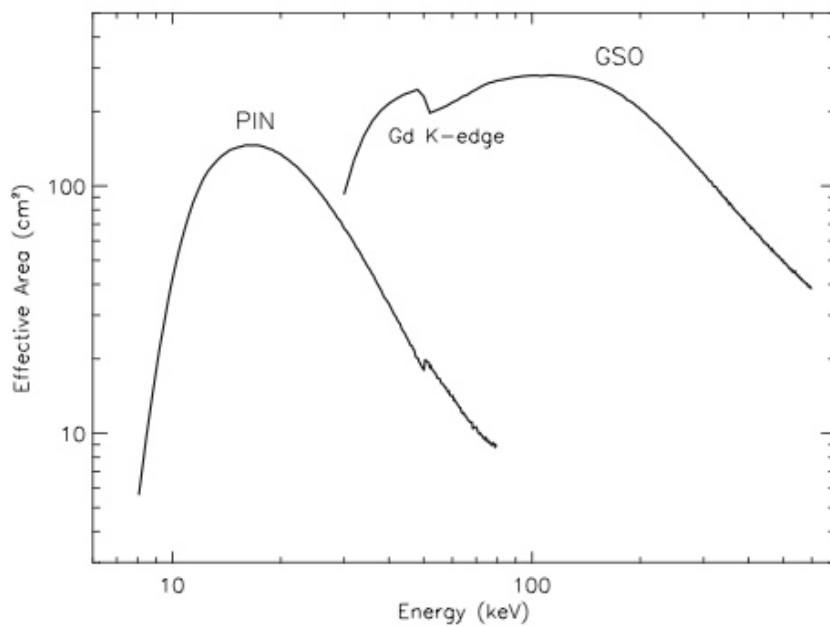


Figure 3.12: Total effective area of the HXD detectors, PIN and GSO, as a function of energy (Takahashi et al. 2007).

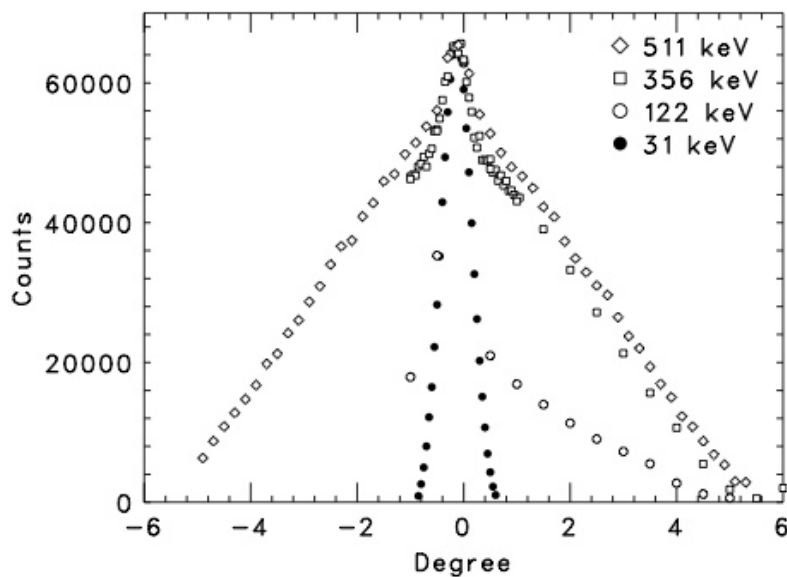


Figure 3.13: Angular responses of a well-counter unit (Takahashi et al. 2007), measured with radio isotope sources (31 keV from ^{133}Ba , 122 keV from ^{152}Eu , 356 keV from ^{133}Ba , 511 keV from ^{22}Na) placed 280 cm away. The response is consistent with the calculation when the finite distance from the sources to the unit is taken into account.

- Careful choice of materials that will not be strongly activated under in-orbit particle bombardment.
- The narrow field of view below ~ 100 keV defined by the fine collimator effectively reduces both the CXB contribution and the source confusion.

The Non X-ray Background (NXB) of PIN diodes, measured in orbit, is plotted in the left panel of Figure 3.14 (Kokubun et al. 2007). The average background counting rate summed over the 64 PIN diodes is ~ 0.6 counts/sec, which is roughly equal to a 10mCrab intensity. In addition, little long-term growth has been observed in the PIN-NXB during the first year of Suzaku, thanks to the small activation effect of silicon. On the contrary, as shown in the right panel of Figure 3.14, a significant long-term accumulation caused by the in-orbit activation has been observed in the GSO-NXB, especially at the early phase of the mission. The background spectrum of GSO contains several activation peaks, whose intensities exponentially increased with individual half-lives.

Figure 3.15 compares the detector backgrounds of hard X-ray missions. The lowest background level per effective area is achieved by the HXD at an energy range of 12–70 keV and 150–500 keV. The in-orbit sensitivity of the experiments can be roughly estimated by comparing the background level with the intensities of celestial source indicated by dotted lines. Below 30 keV, the background level is lower than 10 mCrab, which means a sensitivity better than 0.5 mCrab can be obtained, if an accuracy of 5% is achieved in the background modeling.

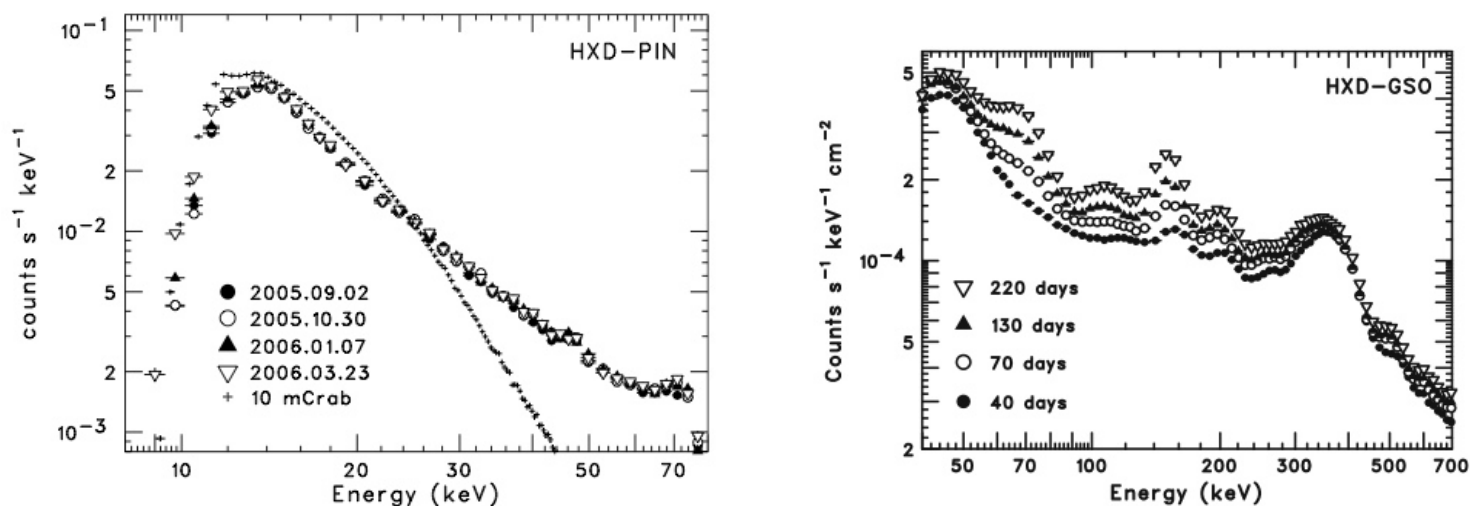


Figure 3.14: (Left) Comparison of four average NXB spectra measured by HXD-PIN, on 4 occasions separated by two months (Kokubun et al. 2007). Each observation has an exposure longer than two days. The Crab spectrum, scaled down by two orders of magnitude, are also shown. (Right) Evolution of the averaged GSO-NXB spectra during the first half year after the launch. Each observation has an exposure longer than a day.

Since there is a strong anti-correlation between the PIN-NXB and magnetic Cut-Off Rigidity (COR), the background modeling of the PIN is primarily based on the counting rate of high-energy charged particles, directly measured by the PIN diodes. Due to large energy depositions inside the silicon, penetrations of cosmic-ray particles cause large signals in the corresponding PIN diodes, and hence activate the Upper Discriminator (UD) in the analog electronics, and then recorded as the PIN-UD monitor count in HK data. Therefore, the PIN-UD rate directly

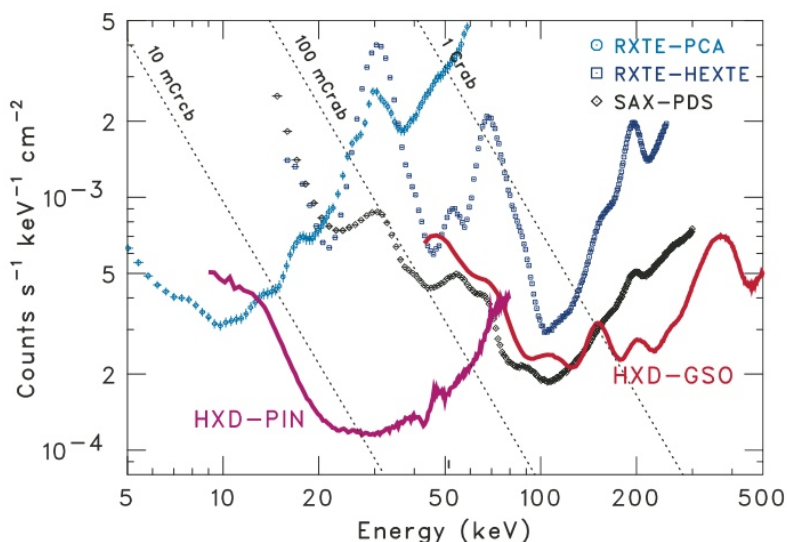


Figure 3.15: Background counting rate of Suzaku HXD as a function of energy in comparison of those of RXTE and Beppo-SAX (Mitsuda et al. 2007). The background rate was normalized by the effective area. Background spectra of RXTE and Beppo-SAX are taken from documents for cycle 11 and cycle 5 guest observer programs, respectively. The intensity of the Crab Nebula is also shown.

indicates the flux of primary cosmic-ray particles, and the background counting rate at any period can be estimated based on the corresponding PIN-UD rate. In the actual modeling procedure, the PIN-NXB rate is described by summation of raw PIN-UD rate and integrated PIN-UD rate with a fixed decaying time constant, to take into account the small effect of the activation during SAA passages. The spectral shape of the PIN-NXB is assumed to depend on the estimated background rate, and is extracted from a database of PIN-NXB spectrum at each estimated rate, which is compiled from the Earth occultation data.

3.2 RXTE

3.2.1 Overview of the satellite

The Rossi X-ray Timing Explorer (RXTE) is a mission organized by NASA Goddard Space Flight Center (GSFC). It was launched on December 30, 1995. The launch vehicle was a Delta II rocket that put RXTE into its intended low-earth circular orbit at an altitude of 580 km, corresponding to an orbital period of about 90 minutes, with an inclination of 23 degrees. Operations are managed at Goddard Space Flight Center.

RXTE is designed to facilitate the study of time variability in the emission of X-ray sources with moderate spectral resolution. Time scales from microseconds to months are covered in an instantaneous spectral range from 2 to 250 keV.

The mission carries two pointed instruments, the Proportional Counter Array (PCA) developed by GSFC to cover the lower part of the energy range, and the High Energy X-ray Timing Experiment (HEXTE) developed by University of California, San Diego (UCSD) covering the upper energy range. These instruments are equipped with collimators yielding a FWHM of one degree. In addition, RXTE carries an All-Sky Monitor (ASM) from MIT that scans about 80 % of the sky every orbit, allowing monitoring at time scales of 90 minutes or longer. Data

Table 3.4: Design parameters and performance of the RXTE PCA and HEXTE (Bradt et al. 1993, Jahoda et al. 1996, Rothschild et al. 1998).

	PCA	HEXTE
Energy range	2 – 60 keV	15 – 250 keV
Energy resolution	< 18% at 6 keV	15 % at 60 keV
Time resolution	1 μ sec	8 μ sec
Spatial resolution	collimator with 1 degree FWHM	1 degree FWHM
Detectors	5 proportional counters	2 clusters of 4 NaI/CsI scintillation counters
Collecting area	6500 cm ²	2 \times 800 cm ²

from PCA and ASM are processed on board by the Experiment Data System (EDS), also built by MIT, while HEXTE is equipped with its own data processing system. Figure 3.16 shows a schematic view of RXTE satellite in orbit.

The PCA is an array of five proportional counters with a total collecting area of 6500 square cm. Events detected by the PCA will be processed on board by the EDS before insertion into the telemetry stream. The instrumental properties of PCA are summarized in Table 3.4.

The HEXTE consists of two clusters each containing four photoswitch NaI (TI) / CSI (Na) scintillation detectors. Each cluster can "rock" (beamswitch) along mutually orthogonal directions to provide background measurements 1.5 or 3.0 degrees away from the source every 16 to 128 sec. The instrumental properties of HEXTE are also summarized in Table 3.4.

The ASM consists of three wide-angle shadow cameras equipped with position-sensitive Xenon proportional counters with a total collecting area of 90 cm². ASM observes 80 % of the sky every 90 minutes in the energy band of 2–10 keV and detects sources brighter than 30 mCrab. Each camera has the field of view of 6° \times 90° and the spatial resolution of 3' \times 15'. Events detected by the ASM will be processed on board by the EDS before insertion into the telemetry stream.

The EDS consists of eight Event Analyzers (EA), of which six are dedicated to the PCA and two to the ASM. Each EA contains an Intel 80286 processor and associated memory. The EAs can be programmed independently to process incoming events from the instruments.

3.2.2 Proportional Counter Array (PCA)³

System Description

The RXTE PCA (Proportional Counter Array) consists of five large proportional counters (PCUs) with anti-coincidence (hereafter "veto") features which provide a very low background. A mechanical hexagonal collimator is carried on each proportional counter, which provides an angular resolution of 1 degree (FWHM). Because of the large effective area, sources as faint as 1 mCrab can be detected only in a few seconds. The detailed descriptions on the PCA design, as well as the orbit performances are given in Jahoda et al. (1996).

The total geometrical area of 5 PCUs is 6250 cm². The schematic view of an assembly of five units and each proportional counter are given in Figure 3.17. We summarize the design parameters and performance of PCA in Table 3.4. The PCA is effective over the range 2–60 keV with 18 % energy resolution at 6 keV. PCA units are filled with Xe gas and achieve low background through efficient veto schemes including side and rear chambers and a propane top layer.

³In this thesis, we use only PCA, so we do not explain ASM and HEXTE.

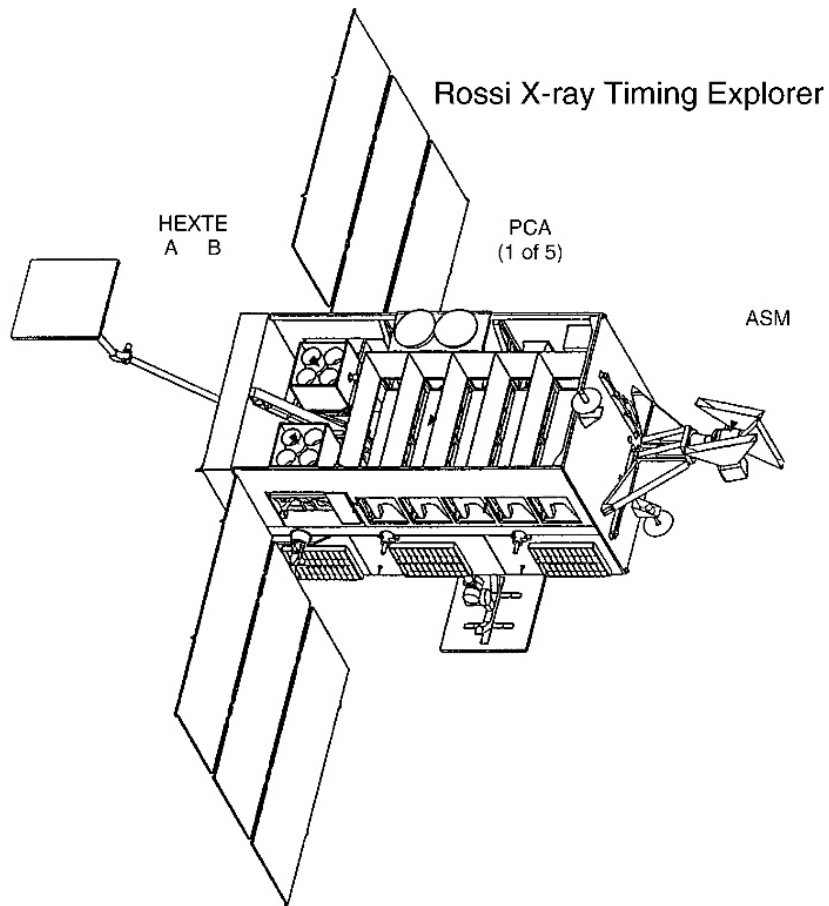


Figure 3.16: RXTE spacecraft viewed from above to reveal the scientific instruments (Rothschild et al. 1998). The five PCA proportional counters and the two HEXTE clusters are shown in relation to the rest of the spacecraft components, such as the two high gain antennae for communications with the ground via the tracking and data relay satellite system, the two solar-power arrays that can rotate to face the Sun, and the ASM on the end with clearance to view the sky.

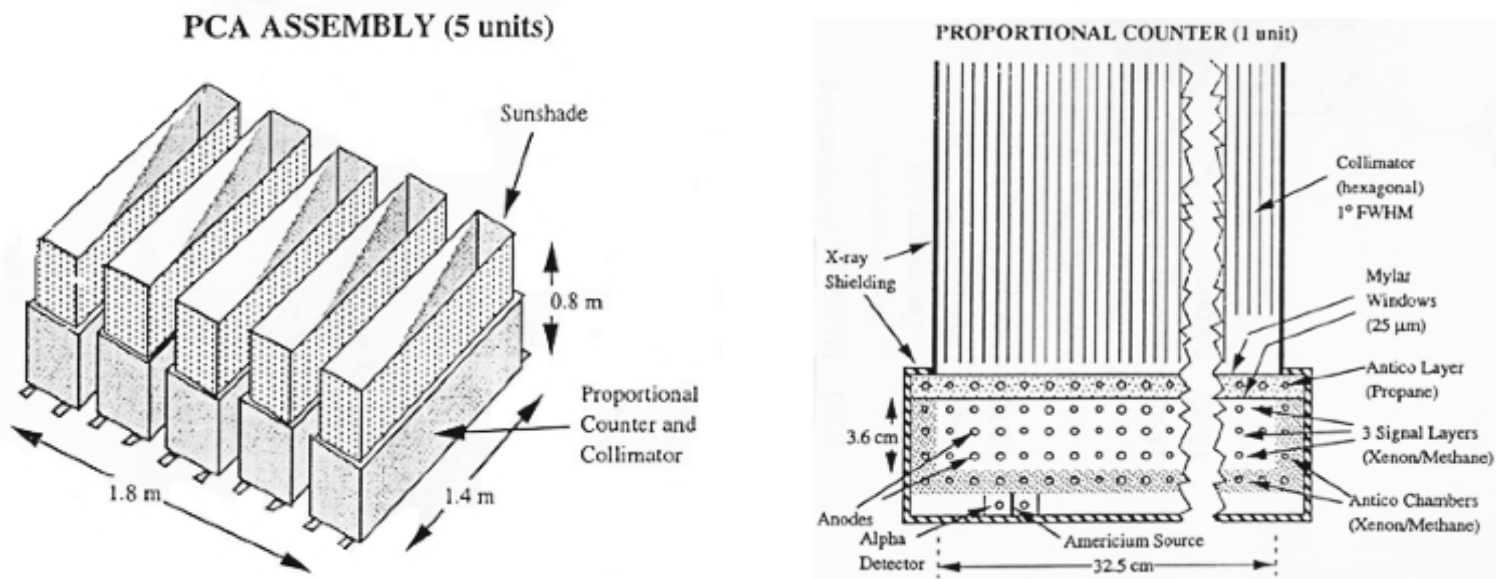


Figure 3.17: Schematic view of PCA counters (Bradt et al. 1993): (Left) Assembly of five PCA counters with total area of 6250 cm^2 . (Right) Schematic view of one PCA unit.

The PCA composes of five, nearly identical aligned gas-filled proportional counter modules. Each module is referred to as a PCU (Proportional Counter Unit) numbered 0–4. Each PCU is equipped with a hexagonal collimator of beryllium copper. The nominal thickness of each sheet of the collimator is $69 \mu\text{m}$; the depth of the collimator is 21 cm and dimension of each cell is 0.32 cm measured flat to flat. Beyond the collimator there are two aluminized mylar windows. Each window is $25 \mu\text{m}$ thick, coated on both sides with 70 nm of aluminium, and separated by 1.3 cm. Behind second window the main volume is filled with a Xenon/Methane (90/10) mixture nominally filled to 840 torr. Each PCU is split into two volumes by a mylar window, the upper propane veto volume and the main xenon volume. Through these volumes run five layers of anode-wire grids (1 propane veto; 3 xenon, each split into two; 1 xenon veto layer). Below the xenon volume the calibration source (^{241}Am) is mounted.

The 1 degree FOV (FWHM) of the tubular (hexagonal) collimators yields a source confusion limit at $\sim 0.1 \text{ mCrab}$. The Crab nebula will yield 8700 counts/sec (2–10 keV) and 1200 counts/sec (10–30 keV) in the PCA. The background in these two bands are 20 and 24 counts/sec, respectively. With these backgrounds, an AGN source of intensity 1.3 mCrab and photon index 1.7 will be detected at $\geq 2 \sigma$ in only 1 sec at 2–10 keV and at 3σ in 10 sec at 10–30 keV. Monitored veto rates will provide a measure of the background to at least 10 % of its value.

The PCUs were operated flawlessly for the first 70 days in orbit. PCUs 3 and 4 showed evidence of occasional breakdown in mid March 1996. Since then these units have been regularly turned off to avoid breakdowns. Furthermore, PCU 1 has begun to suffer the same types of problems since mid March 1999. In this thesis, we use the PCU 2 only.

On-board Data Processing

The system will process count rates from the PCA up to 5×10^5 counts/sec (only 6 % deadtime for the Crab) and will be able to determine photon arrival time with an accuracy of $\sim 1 \mu\text{sec}$. The PCA data stream can be binned and telemetered in 6 different modes simultaneously by 6 independent Event Analyzers (EA) which operate in parallel, each analyzing the total PCA data stream. Two other EAs will process the ASM data and control its rotation.

Two of the 6 PCA EAs are intended to be reserved for two standard PCA modes with timing and spectral parameters that will remain unchanged throughout the mission to provide a uniform mission data bank. For the remaining 4 PCA EAs, however, processing modes are flexibly selected by guest observers to accommodate the scientific requirements. The standard modes consists of Standard-1 and Standard-2. Standard-1 contains 8 rates sampled at 0.125 sec; the total good event rate from each individual counter, propane event rates summed over the PCA, and the rate of all other events. Standard-1 also contains calibration spectra which are stored and telemetered separately for each detector and each layer once every 128 seconds. Standard-2 contains 129 channel pulse height spectra for each signal layer of each detector, 33 channel propane layer spectra for each detector, and 29 rates of various combinations of coincidences for each detector read out every 16 seconds. To obtain faster time resolution than 16 seconds, we need to use other mode data instead of the standard mode data, e.g. Generic Event mode, Generic Binned mode, Single Bit mode and so on. In this thesis, we use only the Standard-2 mode data.

Energy Response

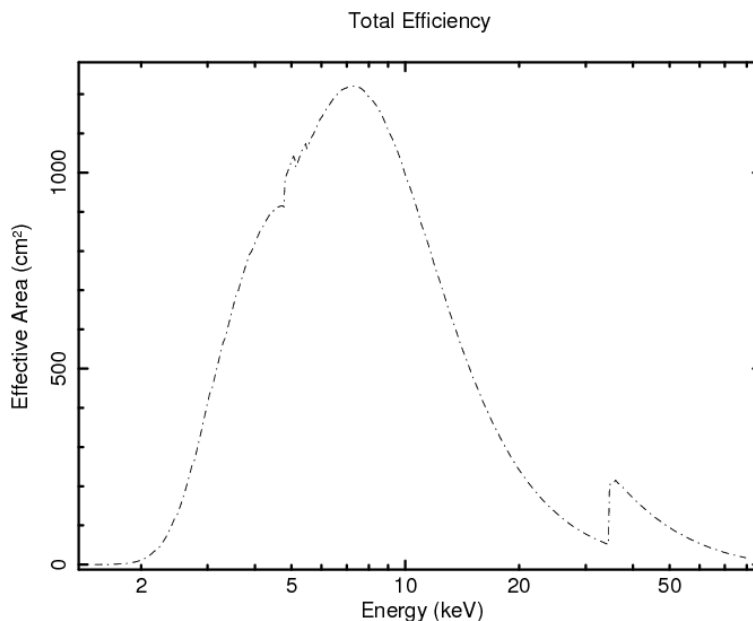


Figure 3.18: Effective area of a single PCU.

As seen from Figure 3.17, each PCU detector, from the top, consists of a thermal shield, a collimator, an aluminized mylar window, a propane volumes, and a detector body. The low energy threshold of the PCA is determined by the transmission of the mylar windows (1 mm each) and the propane volume. For generating the response matrix, the important quantity is the photo-electric stopping power of each layer and all exterior layers. Figure 3.18 shows the effective area of a single PCU.

The gain of the counter is monitored continuously with an ^{241}Am radioactive source for which detection of the α particle identifies the calibration X-rays. Additional information about the energy scale has been obtained from measurements of the iron line in the super nova remnant Cassiopeia A, and the Xe-L escape peak which is collected in a special mode that keeps all events with a calibration flag.

PCA response matrices map 900 energies from 0.023 to 100 keV to 256 PHA channels. Half of the energy channels are equally spaced below 10 keV, except that the three channels which

include one of the Xe-L edges are split into two channels with channel boundary matching the atomic edge. The remaining channels are also equally divided except that the channel including the Xe-K edge is again split into two channels.

Background Estimation

The detector background mainly consists of two components, the diffuse sky background which enters through the collimator as X-rays, and the internal background which arises from interactions between radiation or particles in orbital environment with the detector or spacecraft. Since PCA does not produce continuous measurements of the background, it relies on a model background.

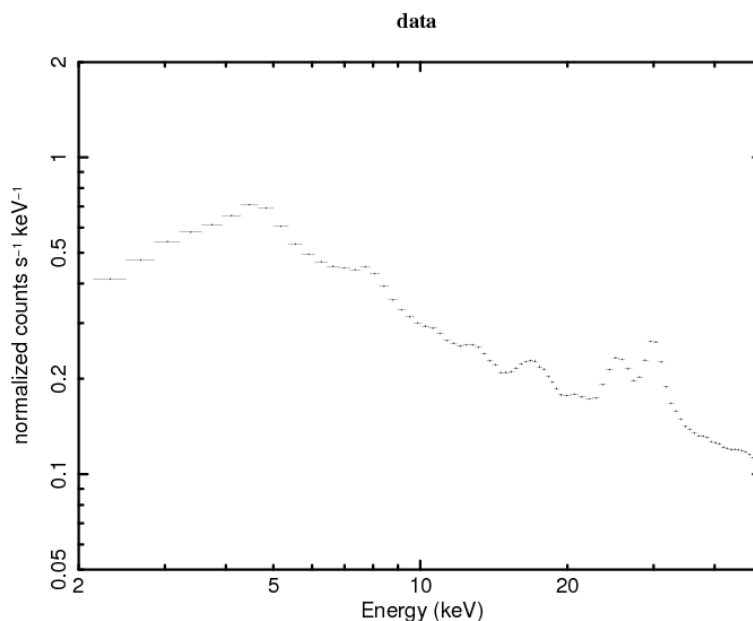


Figure 3.19: A background spectrum for PCU2 calculated for the time of MCG-6-30-15 observation in August, 1997.

Figure 3.19 shows the total background only PCU2 detectors during the RXTE observation of MCG-6-30-15, taken in 1997 August. The upper line includes photon counts from the source, from comparison. Line features are present due to Xe-L escape photons, copper fluorescence (primarily from the back plane and concentrated in the third layer), un-flagged calibration events, and a contribution which appears to come from residual activity in the collimator. The background typically varies between 18-24 counts/sec/PCU. In practice, the most significant contributions to the background are dependent on the local particle environment of the satellite and the recent history of passage through SAA, the presence of background components after passage through the SAA indicates that some of the detector or spacecraft becomes activated.

To model the background, it is assumed that the internal background varies on a time scale which is long compared to the natural timescale of the PCA Standard-2 data (16 sec). The design is such that the model can be evaluated once every 16 seconds, and that the equivalent of a Standard-2 data file can be created with separate information for each detector and each anode chain.

The modeled background spectrum can be based on parameters measured at the time of the observation, parameters describing the condition and position of the spacecraft, and parameters describing the evolution of the spacecraft. PCA background models based on these parameters have been constructed in two ways: using data from blank-sky observations and using data

from periods of Earth occultation. The models based on the local particle parameters are constructed using data from only those spacecraft orbits in which the SAA-induced activation is small. Some of these data are still significantly contaminated by SAA-induced activation but this contamination can be later removed by an appropriately constructed model of the activation component of the background.

3.3 Chandra

3.3.1 Overview of the satellite

The Chandra X-ray observatory was launched on July 23, 1999 as the X-ray component of NASA's four Great Observatories (HST, CGRO, SST). The Chandra orbit is highly elliptical with apogee height ~ 122500 km and perigee height of ~ 26300 km at December 2006, and varies with time. Thanks to this orbit, reasonably high observing efficiency ($\sim 75\%$) is allowed. A long continuous observation (~ 160 ksec) is possible by virtue of the long time orbital period of ~ 64 h. Chandra has a remarkable characteristic in angular resolution of $0''.5$ which is superior to those of other previous satellite. Main instruments on board Chandra are the follows: the High Resolution Mirror Assembly (HRMA), the Advanced CCD Imaging Spectrometer (ACIS), the High Resolution Camera (HRC), and the High and Low Energy Transmission Grating (HETG and LETG). In this thesis, we use HETG in combination of ACIS. Figure 3.20 shows a schematic view of the satellite including these detector system.

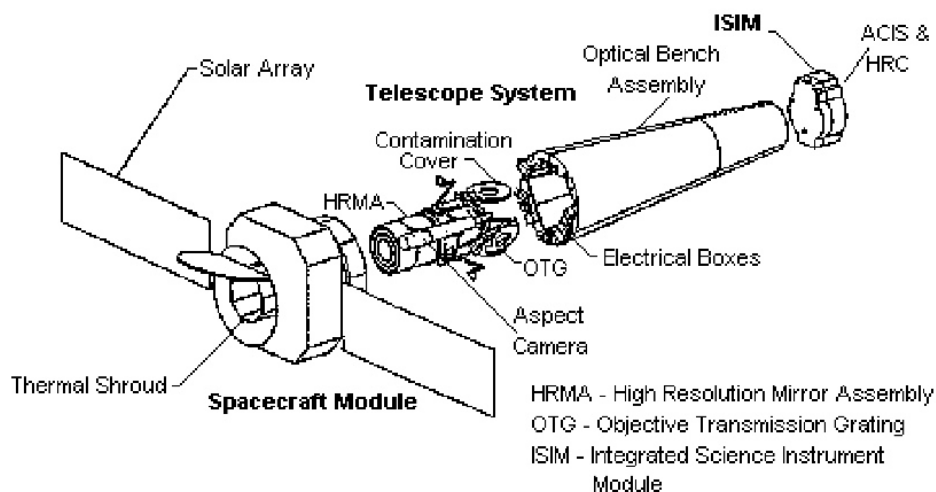


Figure 3.20: Expanded view of the Chandra flight system, showing several subsystems (Elsner et al. 2000).

3.3.2 High Resolution Mirror Assembly (HRMA)

The HRMA consists of four pairs of coaxially nested Walter Type-I thin-mirrors that adopts a grazing-incident optics as shown in left hand of Figure 3.21. These eight mirrors were fabricated from Zerodur glass after the substrate of the mirrors were coated with iridium and polished. The outermost diameter of this telescope is 1.23 m and focal length is about 10 m.

In Figure 3.21(Right), the HRMA effective area is calculated by the raytrace simulation based on the HRMA model and scaled by the XRCF calibration data. The HRMA/ACIS effective area

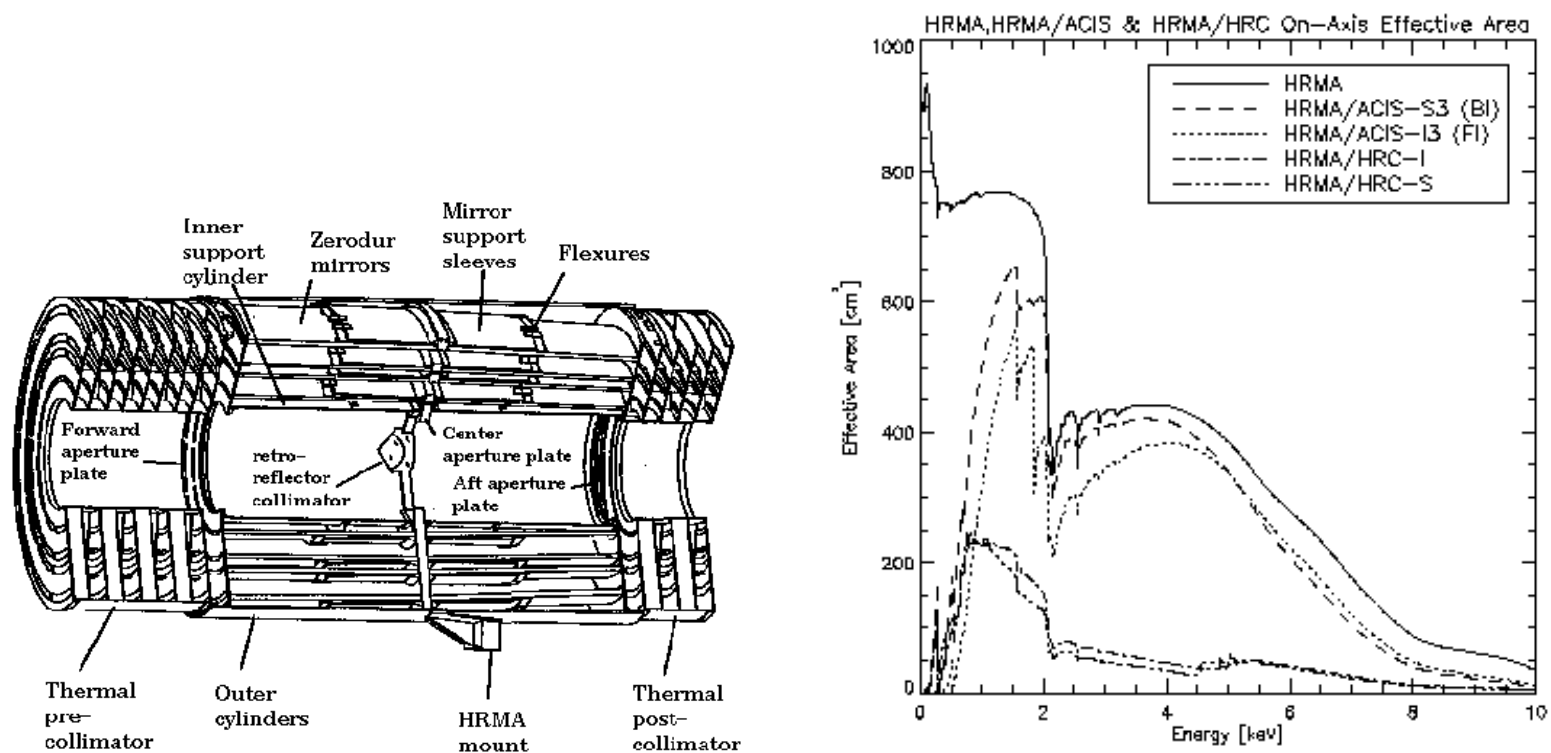


Figure 3.21: (Left) The four nested HRMA mirror pairs and associated structures. (Right) The HRMA/ACIS and HRMA/HRC effective areas versus X-ray energy in linear-linear scales (Weisskopf et al. 2002). The structure near 2 keV is due to the iridium M-edge. See the main texts for detailed explanation.

is the products of the HRMA effective area and the Quantum Efficiency (QE) of ACIS-I3 (front illuminated) or ACIS-S3 (back illuminated). The HRMA/HRC effective area is the product of HRMA effective area and the QE of HRC-I or HRC-S at their aimpoints, including the effect of UV/Ion Shields (UVIS). The effective area of the telescope has a dependence on the X-ray energy since the X-ray reflectivity exponentially drops down to $\sim 0\%$ above the critical energy for total reflection. Especially, the effective area shows sharp drop at ~ 2 keV due to M-edge of iridium. Above an X-ray energy of ~ 10 keV, no X-ray photons can be reflected by the mirrors. On-axis effective area is about 800 cm^2 at 0.25 keV, and declines to 400 cm^2 at 5.0 keV, 100 cm^2 at 8.0 keV.

3.3.3 Advanced CCD Imaging Spectrometer (ACIS)

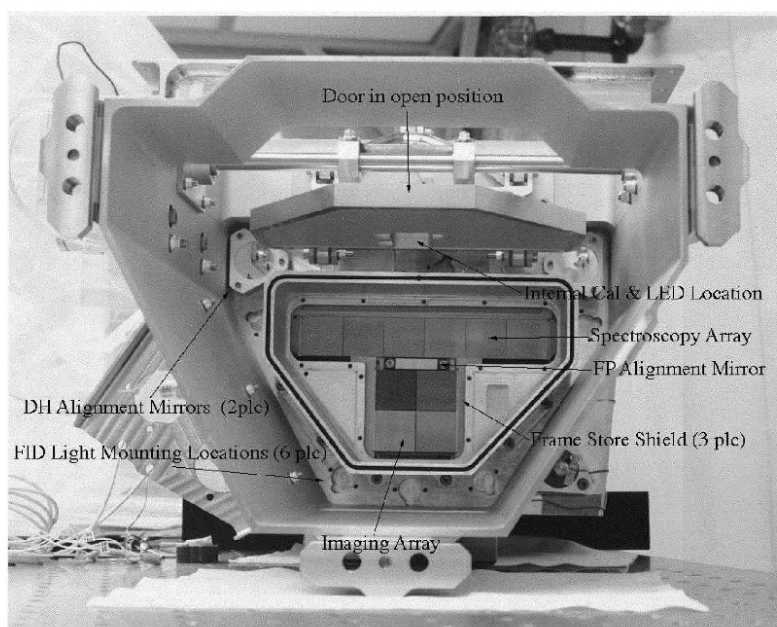


Figure 3.22: Photograph of the focal plane of ACIS, prior to installation of the optical blocking filters. The ACIS-I is at the bottom; the ACIS-S (the read out for the HETG) is at the top (Weisskopf et al. 2002).

The Advanced CCD Imaging Spectrometer (ACIS) is comprised of ten 1024×1024 pixel CCDs; 2×2 array of ACIS-I (I0-I3) and 1×6 array of ACIS-S (S0-S5). The physical size of CCD pixels is $24.0\ \mu\text{m}$ square (~ 0.492 arcsec) so that the spacial resolution for on-axis imaging with HRMA/ACIS detector system is limited not by HRMA but by the pixel size. The CCDs are used for taking high angular-resolution images and obtaining moderate energy-resolution spectra of the images. The ACIS-S can also be used in conjunction with the High or Low Energy Transmission Grating (HETG or LETG) to obtain the high energy-resolution spectra of point-like sources. Figure 3.22 and Figure 3.23 shows a photograph and a schematic layout of CCD chips, respectively. These CCD chips are slightly titled to follow the HRMA focal surface and the focal surface of the gratings, respectively. ACIS provides many observing mode to accommodate variety of observational objectives. Since we analyzed the data of HETGS only in this thesis, only Timed Exposure (TE) mode of ACIS-S with the readout time of 3.24 sec was utilized. The quantum efficiency (QE) of ACIS is shown in Figure 3.24. The QE below 1.0 keV exponentially decreases due to the absorption by Optical Blocking Filter (OBF) and by the gate

ACIS FLIGHT FOCAL PLANE

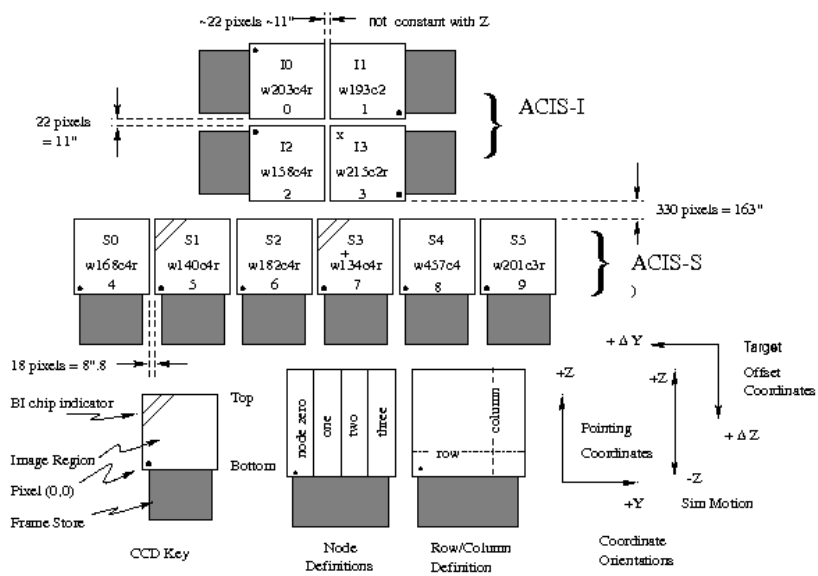


Figure 3.23: A schematic drawing of the ACIS focal plane (<http://asc.harvard.edu/proposer/POG/html/HETG.html>). Note the nominal aimpoints: on S3 (the '+') and on I3 (the 'x'). It is standard practice to add an offset to all observations on S3 to move the source away from the node 0-1 boundary. The view is along the optical axis, from the source toward the detectors, (-X). The numerous ways to refer to a particular CCD are indicated: chip letter+number, chip serial number, and ACIS chip number. The node numbering scheme is illustrated lower center.

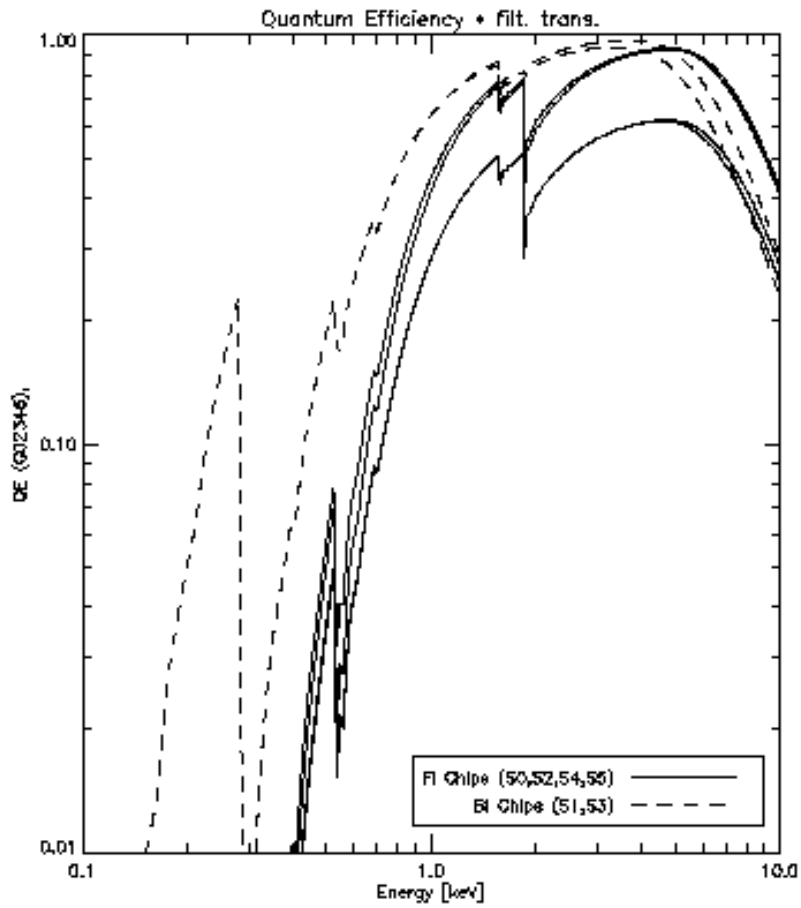


Figure 3.24: The quantum efficiency, convolved with the transmission of the appropriate optional blocking filter, of the FI CCDs and the two BI CCDs as a function of energy. S3 is somewhat thicker, hence more efficient than S1. This figure includes the effects of molecular contamination. There is a sharp drop near the Si K-edge at 1.84 keV

Table 3.5: Design parameters and performance of the HETGS (Canizares et al. 2005).

Grating Facet Average Parameters	
HEG/MEG period	2000.81 Å / 4001.95 Å
HEG/MEG Bar thickness	5100 Å / 3600 Å
HEG/MEG Bar width	1200 Å / 2080 Å
HEG and MEG bar material	Gold
Performance	
HETGS Range	0.4–10 keV (31–12 Å)
HEG Range	0.8–10 keV (15–1.2 Å)
MEG Range	0.4–5 keV (31–2.5 Å)
Effective area	7 cm ² at 0.5 keV
	59 cm ² at 1.0 keV
	200 cm ² at 1.5 keV
	28 cm ² at 6.5 keV
Resolving Power ($E/\Delta E$, $\lambda/\Delta\lambda$)	
HEG	1070–65 (1000 at 1 keV (12.4 Å))
MEG	970–80 (660 at 0.826 keV (15 Å))
Resolution (ΔE)	0.4–77 eV (FWHM)
HEG ($\Delta\lambda$)	0.012 Å (FWHM)
MEG ($\Delta\lambda$)	0.023 Å (FWHM)
Absolute Wavelength Accuracy	
HEG	± 0.006 Å
MEG	± 0.011 Å

structure of the CCD chips. Since BI chips have the gate at the opposite side to HRMA, the quantum efficiency of BI CCDs are larger than those of FI CCDs in low-energy band. Owing to the increase of the Charge Transfer Inefficiency (CTI) effect, the QE becomes smaller at the further side from the readout. The total effective area of combination with the HRMA and ACIS is shown in right hand of Figure 3.21.

3.3.4 High Energy Transmission Grating Spectrometer (HETGS)

HETGS overview

The data we analyze in this thesis are obtained with the HETGS, which is composed of High Energy Grating (HEG) and Medium Energy Grating (MEG). The MEG and HEG provide high resolution spectra (with $E/\Delta E \sim 1000$) from 0.4 keV to 5 keV and from 0.8 to 8 keV, respectively, for point sources and slightly extended (a few src seconds) sources. Design parameters and performance of the HETGS are summarized in Table 3.5.

A schematic layout of the HRMA-HETG-ACIS-S system is shown in Figure 3.25. The HETGS consists of 336 gold grating facets mounted on an assembly which can be swung into position behind the Chandra mirrors. When the HETGS intercepts the X-ray reflected from the mirrors, the X-rays are diffracted and form one-dimensional images in the focal plane detectors (see Figure 3.26). As the amount of the diffraction depends sensitively on the X-ray energy, the location of the diffracted X-rays directly becomes the information of their energies. A diffraction angle β is given according to the grating equation,

$$\sin \beta = \frac{m\lambda}{p} \quad (3.1)$$

where m is the integer order number, λ is the photon wavelength in angstroms, p is the spatial period of the grating lines, and β is the dispersion angle. A un-dispersed image is formed by the zeroth-order events, $m = 0$, while dispersed images are formed by the higher orders, primarily the first-order, $m = 1$. Spatial period between the gold gratings, p , is 4001.95 \AA for MEG and 2000.81 \AA for HEG.

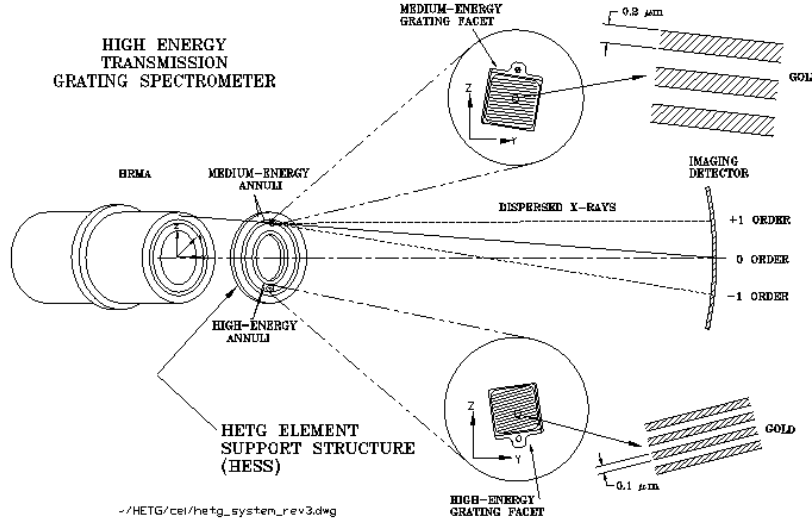


Figure 3.25: A schematic layout of the High Energy Transmission Grating Spectrometer (<http://asc.harvard.edu/proposers/POG/html/HETG.html>).

HETGS performance

The HETGS performance is characterized by its effective area and resolution. The HETGS effective area depends not only on the HRMA effective area and the ACIS efficiency, but also on the process of selecting events, effect of chip gaps, and use of “ACIS ENERGY” to do order sorting. Combining the HETG diffraction efficiencies with the HRMA effective area and ACIS-S detection efficiency produces the system effective area as a function of energy, described as an “ancillary response file” or ARF. Standard HETGS ARFs corresponding to individual orders are shown in Figure 3.27. The MEG covers an energy band of $0.4\text{--}5 \text{ keV}$ ($31\text{--}2.5 \text{ \AA}$), while the HEG covers that of $0.8\text{--}10 \text{ keV}$ ($15\text{--}1.2 \text{ \AA}$). Figure 3.28 shows the total HETGS effective area combined the plus and minus first-order areas of both HEG and MEG, which is 7 cm^2 at 0.5 keV , 59 cm^2 at 1.0 keV , 200 cm^2 at 1.5 keV , and 28 cm^2 at 6.5 keV , respectively. In combination of MEG and HEG, the covered energy range by HETGS is $0.4\text{--}10 \text{ keV}$ ($31\text{--}0.2 \text{ \AA}$).

As mentioned above, the profile in the dispersion direction defines the instrument spectral resolution, ΔE or $\Delta \lambda$. Note that the resolutions, ΔE or $\Delta \lambda$, are defined as the full-width at half-maximum of the Gaussian by which a core of the line profile is modeled. A high-resolution spectrum is created by projecting the events along with the dispersion axis and binning the events into energy or wavelength bins. The HETGS line response function (LRF) at a given wavelength is encoded in the grating RMF files. According to the grating equation (3.1), the wavelength resolution $\Delta \lambda$ is given in the following equation,

$$\Delta \lambda = \frac{p \cos \beta \Delta \beta}{m} + \frac{\Delta p \sin \beta}{m}. \quad (3.2)$$

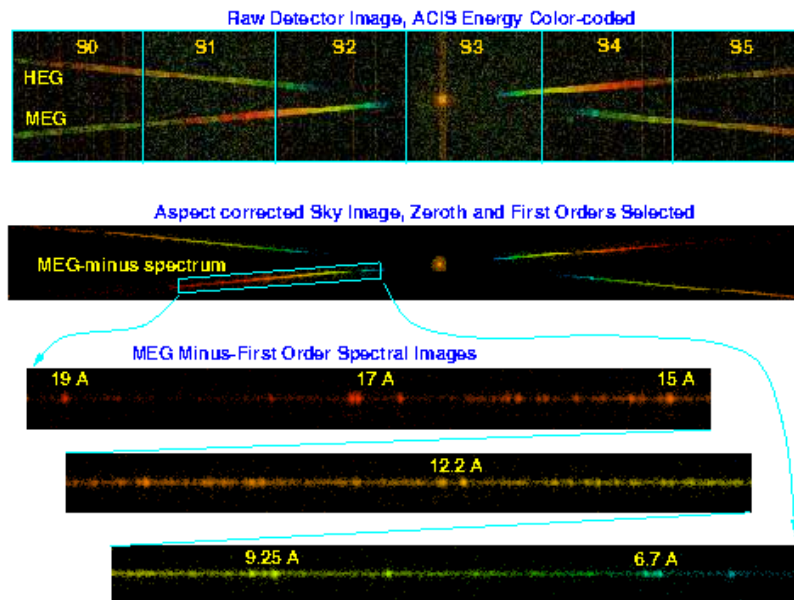


Figure 3.26: HETGS observation of Capella (OBSID 1318) (<http://asc.harvard.edu/proposer/POG/html/HETG.html>). The top panel shows an image of detected events on the ACIS-S detector with the image color indicating the ACIS-determined X-ray energy. The bright zeroth-order image is visible on CCD S3 and includes a trailed image (the vertical frame-transfer streak). Diffracted photons are visible forming a shallow “X” pattern; the HEG and MEG spectra are indicated. The images are broad due to dither of the spacecraft. The middle panel shows an image after the data have been aspect corrected and selections applied to include only valid zeroth and first-order events; note that the Y axis has been flipped from the normal Sky view to match the detector coordinates view in the top panel. The lower panel shows an expanded view of the MEG minus-first-order spectrum, where emission lines are clearly visible as bright dots.

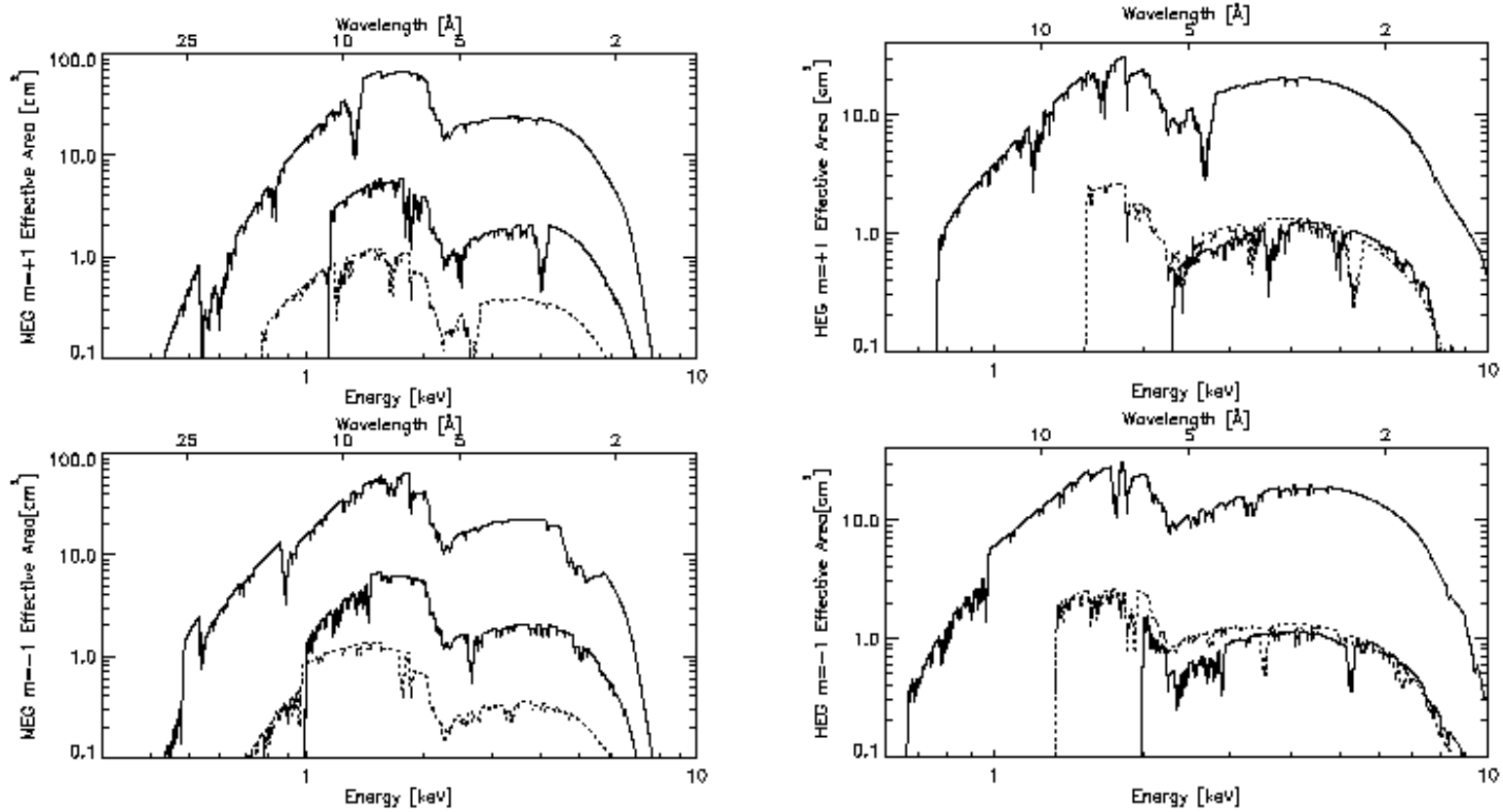


Figure 3.27: (Left) The HETGS MEG effective area, integrated over the PSF is shown with energy and wavelength scales. The $m = +1, +2, +3$ orders (falling on ACIS chips S5, S4, S3; left to right) are displayed in the top panel and the $m = -1, -2, -3$ orders (falling on ACIS chips S0, S1, S2; left to right) are in the bottom panel. The thick solid lines are first order; the thin solid line is third order, and the dotted line is second order. (Right) The HETGS HEG effective area, integrated over the PSF, is shown with energy and wavelength scales. The $m = +1, +2, +3$ orders (falling on ACIS chips S5, S4, S3; left to right) are displayed in the top panel and the $m = -1, -2, -3$ orders (falling on ACIS chips S0, S1, S2; left to right) are in the bottom panel. The thick solid lines are first order; the thin solid line is third order; and the dotted line is second order. Figures are taken from <http://asc.harvard.edu/proposers/POG/html/HETG.html>.

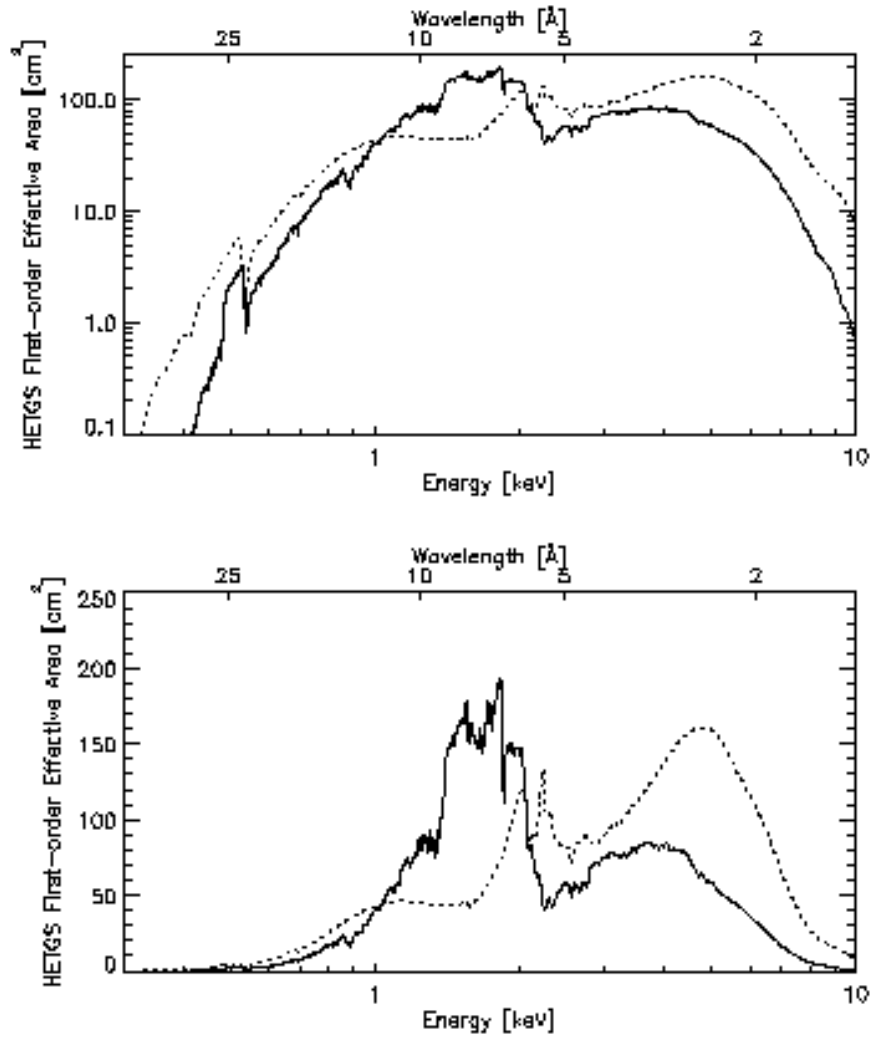


Figure 3.28: The modelled total first-order (solid curve) and zeroth-order (dotted curve) effective area, integrated over the PSF, of the HRMA-HETG-ACIS-S combination, as a function of energy (<http://asc.harvard.edu/proposer/POG/html/HETG.html>). The first-order data are the same as those plotted in Figure 3.27. The plotted first-order values are the sums of the area at a particular energy from both orders (+/-) of both MEG and HEG spectra. Both a log-log (Top) and a log-linear (Bottom) version are shown.

The resolving power, $E/\Delta E = \lambda/\Delta\lambda$, of HETGS is represented as a function of energy in Figure 3.29. The resolution when expressed as a wavelength, $\Delta\lambda$, is roughly constant at 0.012 \AA and 0.023 \AA for HEG and MEG, respectively. Thus, the energy resolution are 1 eV at 1 keV for HEG and 1.25 eV at 0.826 keV for MEG. The absolute wavelength is estimated by comparing the measured emission line wavelengths with the expected ones. Systematic wavelength errors is less than 100 km/sec in Doppler velocities: $\pm 0.006 \text{ \AA}$ and 0.011 \AA for HEG and MEG, respectively.

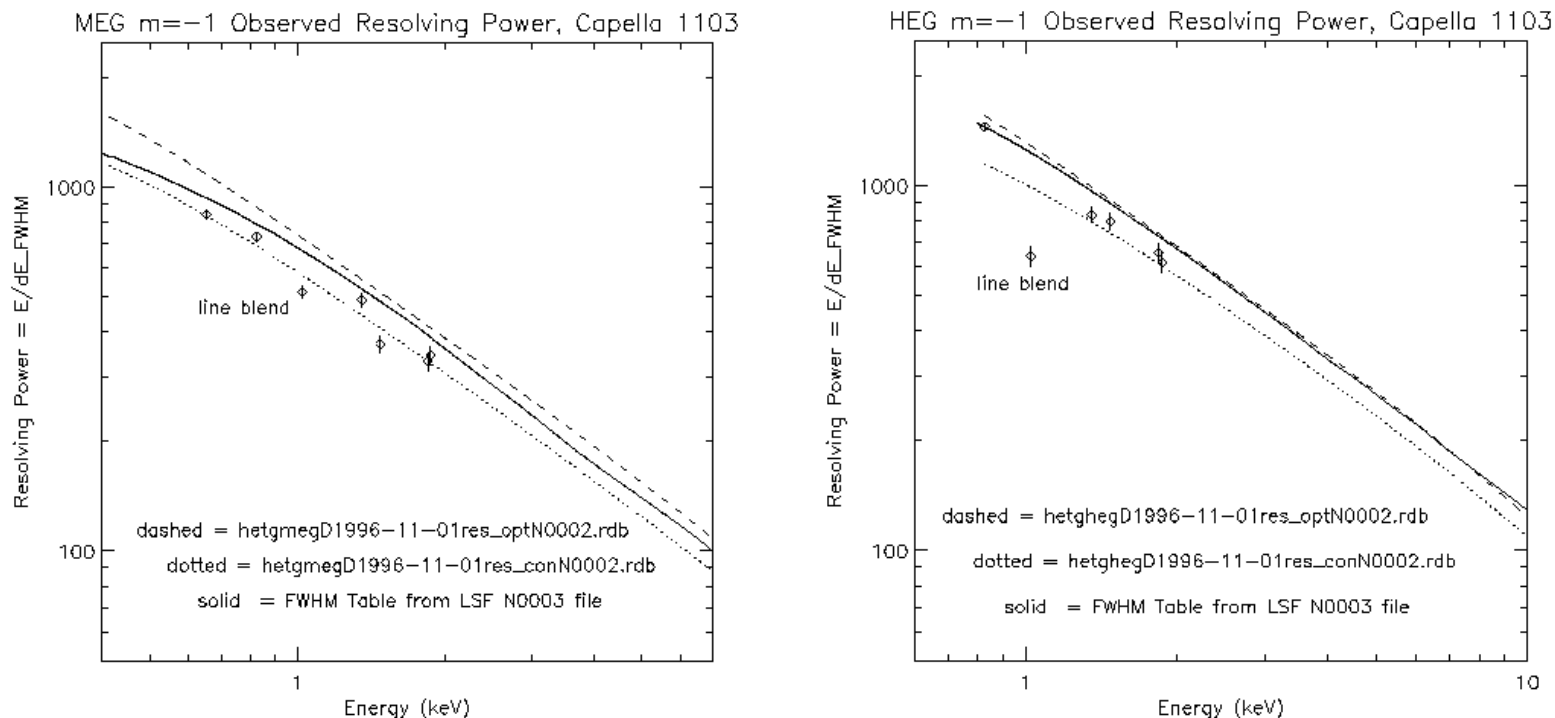


Figure 3.29: HEG and MEG resolving power ($E/\Delta E$ or $\lambda/\Delta\lambda$) as a function of energy for the nominal HETGS configuration (<http://asc.harvard.edu/proposer/POG/html/HETG.html>). The resolving power at high energies is dominated by the telescope PSF; at low energies grating effects enter but do not dominate. The “optimistic” dashed curve is calculated from pre-flight models and parameter values. The “conservative” dotted curve is the same except for using plausibly degraded values of aspect, focus, and grating period uniformity. The cutoff at low-energy is determined by the length of the ACIS-S array. Measurements of the HEG and MEG $m = -1$ spectra are shown here by the diamond symbols. The values plotted are the as-measured values and therefore include any natural line width in the lines; for example, the “line” around 12.2 \AA is a blend of Fe and Ne lines.

Chapter 4

Observation and Data Reduction

4.1 Suzaku observation and data reduction

The Suzaku satellite (Mitsuda et al. 2007) has observed MCG-6-30-15 ($z = 0.00775$; Fisher et al. 1995) four times. The first observation was performed between August 17–19 in 2005 for about 45 ksec. In 2006 January, the source was observed three times, between 9–14 (143 ksec exposure), 23–26 (99 ksec), and 27–30 (97ksec). In this paper, we use the data taken in 2006 January.

For data reduction we used the HEADAS 6.5 software package, provided by NASA/GSFC. The XIS data were screened with XSELECT using the standard criterion (Koyama et al. 2007). The screening criteria were as follows: grade 0, 2, 3, 4, and 6 events were used, data collected within 436 sec of passage through the South Atlantic Anomaly (SAA) were discarded, data were selected to be elevation from sunlit Earth rim ≥ 20 degree and elevation from dark Earth rim ≥ 5 degree. The XIS pulse-height data were converted to PI (Pulse Invariant) channels using the xispi software and charge transfer inefficiency (CTI) parameters.

The XIS spectra and light-curves were extracted from the cleaned event files (both 3×3 and 5×5 edit mode data) with XSELECT. The XIS source spectra were extracted from a circular regions of 3.82 arcmin radius centred on the source, while background products were extracted from the outer annulus region with a total area being equal to that of the source region. The spectra were binned at least 30 counts in order to apply a χ^2 minimization technique.

We generated XIS response matrices using xisrmfgen, which takes into account the time-variation of the energy response. As for generating ancillary response files (ARFs), we used xissimarfgen (Ishisaki et al. 2007). This tool calculates ARFs through ray-tracing, and we selected the number of input photons as 400000, with the “estepfile” parameter “full”.

After extracting the products for the back-illuminated CCD (XIS1) and for the three front-illuminated CCD XIS detectors (XIS0, XIS2, XIS3) separately, we found the XIS0, XIS2, and XIS3 products are almost identical to each other. So we combined the XIS0, XIS2, and XIS3 products in our analysis. We used the addascaspec ftool to combine the XIS spectra and responses.

As for HXD/PIN (Takahashi et al. 2007), spectra and light curves were extracted from the cleaned HXD/PIN event files. The data were processed based on the standard criteria: data collected within 500 sec of passage through the South Atlantic Anomaly (SAA) were discarded, data were selected to be elevation from the dark Earth rim ≥ 5 degree, and Cut-off rigidity ≥ 8 GeV.

Instrumental background model is provided by the HXD instrument team, as simulated PIN event files. Event spectra were extracted with XSELECT after the dead-time correction, using the tool hxddtcor. The HXD/PIN non-X-ray background (NXB) spectra were made from

a time dependent model provided by the HXD team for each observation. We increased the exposure time of the NXB spectra by a factor of 10 since the NXB event files are simulated with a ten times scaled level than the actual background to avoid large statistical error. These background event files do not contain the cosmic X-ray background (CXB) component, which we estimated separately using the PIN response for flat emission distribution (ae_hxd_pinflat1_20080129.rsp), and assuming a CXB spectrum as $9.0 \times 10^9 (E/3 \text{ keV})^{-0.29} \times \exp(-E/40 \text{ keV})$ (ergs/s/cm²/keV/str) measured by HEAO-1 (Boldt 1987). Both NXB and CXB spectra were subtracted from the event spectra, and the spectra were binned at least 30 counts to apply a χ^2 minimization technique.

4.2 RXTE observation and data reduction

MCG-6-30-15 has also been observed for over 14 years with the Rossi X-ray Timing Explorer (RXTE: Bradt et al. 1993). RXTE carries three scientific instruments: the Proportional Counter Array (PCA: Jahoda et al. 1996), the High Energy X-ray Timing Experiment (HEXTE: Rothschild et al. 1998), and the All-Sky Monitor (ASM: Levine et al. 1996). We have used PCA only. We obtained 1341 RXTE observations.

For spectral data reduction, we used the HEADAS 6.5 software package, provided by NASA/GSFC. Additional selection criteria for PCA was as follows: 1) elevation angle from the Earth was larger than 10 degree, and 2) the offset angle was smaller than 0.02 degree. PCA spectra were only extracted from Proportional Counter Unit 2 (PCU2), since it was the only PCU that was active in all of the selected observations. We used Standard 2 mode data, which has a time resolution of 16 sec and 129 channels covering the full PCA (2 – 60 keV) energy range. The background spectra were estimated by the background model for faint sources.

We added 1 % systematic errors to each PCA spectral bin so as to obtain $\chi_\nu^2 \sim 1$ for the spectrum of the Crab. The PCA energy range was limited to 2 – 30 keV.

4.3 Chandra observation and data reduction

The Chandra satellite has observed MCG-6-30-15 five times. The first observation was performed between April 5 to 6 and August 21 to 22 in 2000 for about 128 ksec. In 2004 May, the source was observed four times between May 19 and 27 in 2004, resulting in a good exposure time of 522 ksec. In this paper, we use the data taken in 2004 May.

As for average spectrum, we used the data provided by the Chandra Grating Data Archive and Catalog (TGCat). The TGCat is a browsable interface to analysis-quality spectral products (binned spectra and corresponding response files). TGCat makes it easy to find observations of a particular object, type of object, or type of observation, to quickly assess the quality and potential usefulness of the spectra with pre-computed graphics or custom-generated plots of binned spectra. Spectra, responses, event files, and summary products may be downloaded as a package.

For data reduction we used the CIAO 4.0 software package. We used tgextract, which is the CIAO tool, to produce a PHA2 spectrum file from the Level2 event file.

The +1 and –1 orders of the HEG were combined, the +1 and –1 orders of the MEG were combined. The HEG and MEG spectra were modeled separately. The spectra were binned at least 30 counts in order to apply a χ^2 minimization technique.

Chapter 5

Data analysis and Results

5.1 Spectral Variability in a Model Independent Manner – Method 1

First, we study spectral variation of the source in a model-independent manner using Suzaku and RXTE data. We make the ‘intensity-sliced energy spectra’ from the Suzaku XIS data as follows:

1) Create a light curve (the average of XIS0, XIS2, and XIS3), with a bin-width of 128 sec in the 0.2 – 12 keV band. We found that the count rate varies from ~ 1 to ~ 7 cts/sec. Figure 5.1 shows the 0.2–12 keV XIS light curve used in the present data analysis.

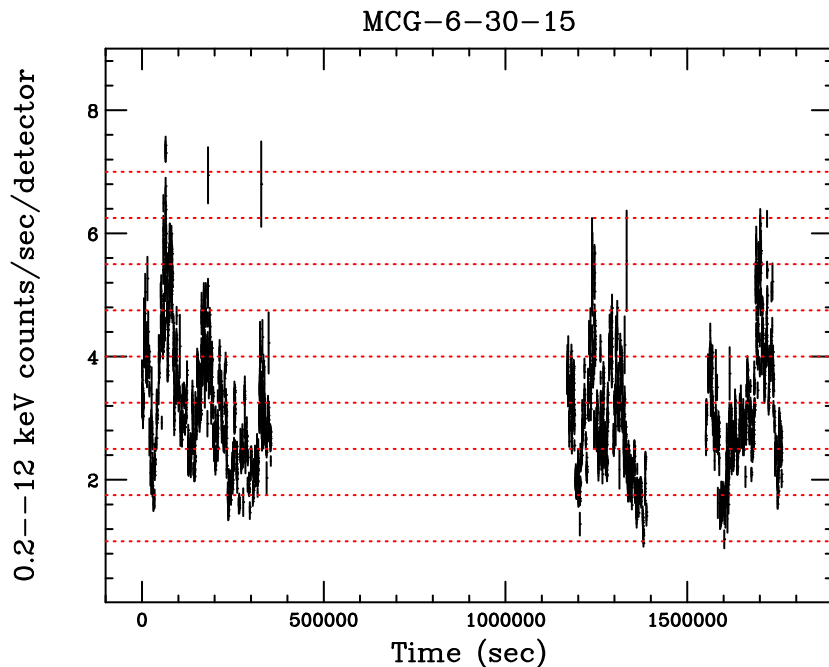


Figure 5.1: 0.2–12 keV XIS light curve of the 2006 observation. The count rate intervals based on which intensity-sliced spectra are made are shown with horizontal red-dotted lines.

2) Choose time periods when the source intensity is in the ranges of 1–1.75, 1.75–2.50, 2.50–3.25, 3.25–4.00, 4.00–4.75, 4.75–5.50, 5.50–6.25, 6.25–7.00 cts/sec. These intensity ranges are chosen so that the exposure times for individual intensity bins are approximately equal.

3) From the eight intervals corresponding to the different source flux levels, we create eight intensity-sliced energy spectra (the sum of XIS0, XIS2, and XIS3).

In the “sliced spectral method” above, we cannot study spectral variations at different timescales. Therefore, we extract another spectral dataset to study energy spectral variations in various timescales. This method is called “Method 1” throughout this thesis in order to distinguish from another method of spectral extraction we introduce later to further study energy spectral variation (“Method 2”; section 5.6). We define and extract the “bright spectra” and the “faint spectra” as follows from the Suzaku XIS data:

- 1) Divide the entire observation period into a series of the time-interval of which length is T .
- 2) Create light curves for individual intervals with a time-bin-width of 128 sec, and calculate the average count rate for each interval T .
- 3) For each interval, create the “bright spectrum” from the period when the XIS count rates (0.2 – 12 keV) are higher than the average, and the “faint spectrum” when the count rates are lower than the average.
- 4) Average the bright spectra and faint spectra for all the intervals.
- 5) Thus, for a given T , we have one bright spectrum and one faint spectrum.
- 6) Repeat the procedure for different time-intervals of T . As for T , we chose 5,000, 9,000, 15,000, 40,000, 75,000 and 200,000 sec.

Thus, we have six “bright spectra” and six “faint spectra” corresponding to the six timescales. Note that there may be data gaps within a single time interval, T , since Suzaku has a low-earth orbit and the observation is intermittent every $\sim 3,000$ seconds or so. Typical exposure is $\sim 50\%$ of T .

From the eight “intensity-sliced spectra”, six “bright spectra” and six “faint spectra” thus created from the Suzaku XIS data, we studied spectral variations in a model independent manner by calculating spectral hardness ratios between different energy bands. Consequently, we have discovered a significant correlation between the intensity in the 6.0 – 10 keV and the spectral ratio of 0.5 – 3.0 keV / 6.0 – 10 keV. This correlation is shown in Figure 5.2.

Figure 5.3 gives the 6.0 – 10 keV intensity and the 0.5 – 3.0 / 6.0 – 10 keV spectral-ratio as functions of the time-interval T . From these figures, it is obvious that the intensity and spectral variations are more prominent with increasing timescales. In fact, Figure 5.4 shows ratios of the bright spectra to the faint spectra for different time-intervals. It is obvious that the “bright” spectra are steeper than the “faint” spectra below ~ 10 keV for all the timescales, and that the bright spectra get more steepened with increasing timescales. We emphasize that the spectral variation we found here is *model independent*.

Next, we use the RXTE/PCA data sets and carry out similar analysis. Figure 5.5 shows a 2 – 30 keV PCA light curve from 1996 to 2009. We use these datasets to search for characteristic spectral variations in typical timescales of $\sim 10^6$ sec and $\sim 10^7$ sec, which are too long to study with Suzaku observations. We make light curves in several different energy bands with the time bin-widths of 2×10^6 sec and 2×10^7 sec, and investigate intensity versus spectral hardness correlations in these timescales. Consequently, we have found there is a significant correlation between the intensity in the 6 – 10 keV band and the spectral ratio of 2 – 4 keV / 6 – 10 keV in both timescales (Figure 5.6). This is very similar to the spectral correlation found in the Suzaku data in 2006 in timescales of $\sim 10^3$ to $\sim 10^5$ sec (Figure 5.2). Therefore, we confirm that MCG-6-30-15 maintains the characteristic spectral hardness correlation in a wide range of timescales from some thousand seconds to ~ 10 years. It would be natural to assume that the similar spectral variations found in the RXTE data and Suzaku data at different timescales have the same origin. We are going to investigate for the origin of this characteristic spectral variation in the following.

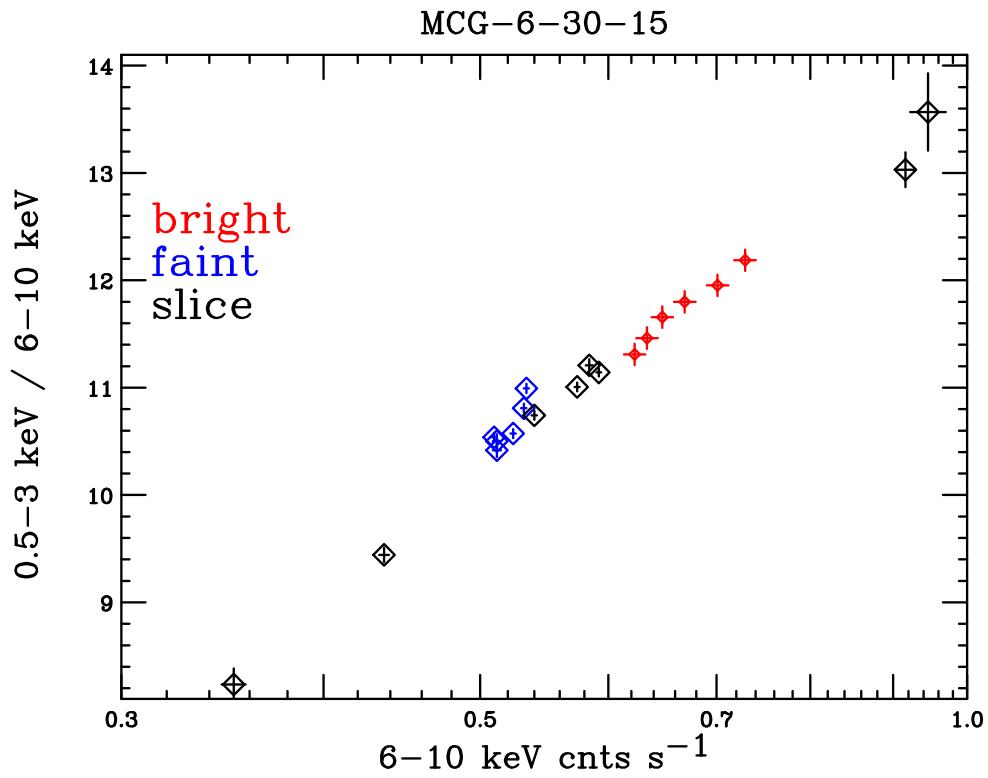


Figure 5.2: Correlation between the flux in 6.0–10 keV and the spectral ratio of 0.5–3.0 keV/6.0–10 keV for the “intensity-sliced spectra” (black), “bright spectra” (red) and “faint spectra” (blue) using the Suzaku XIS data in 2006.

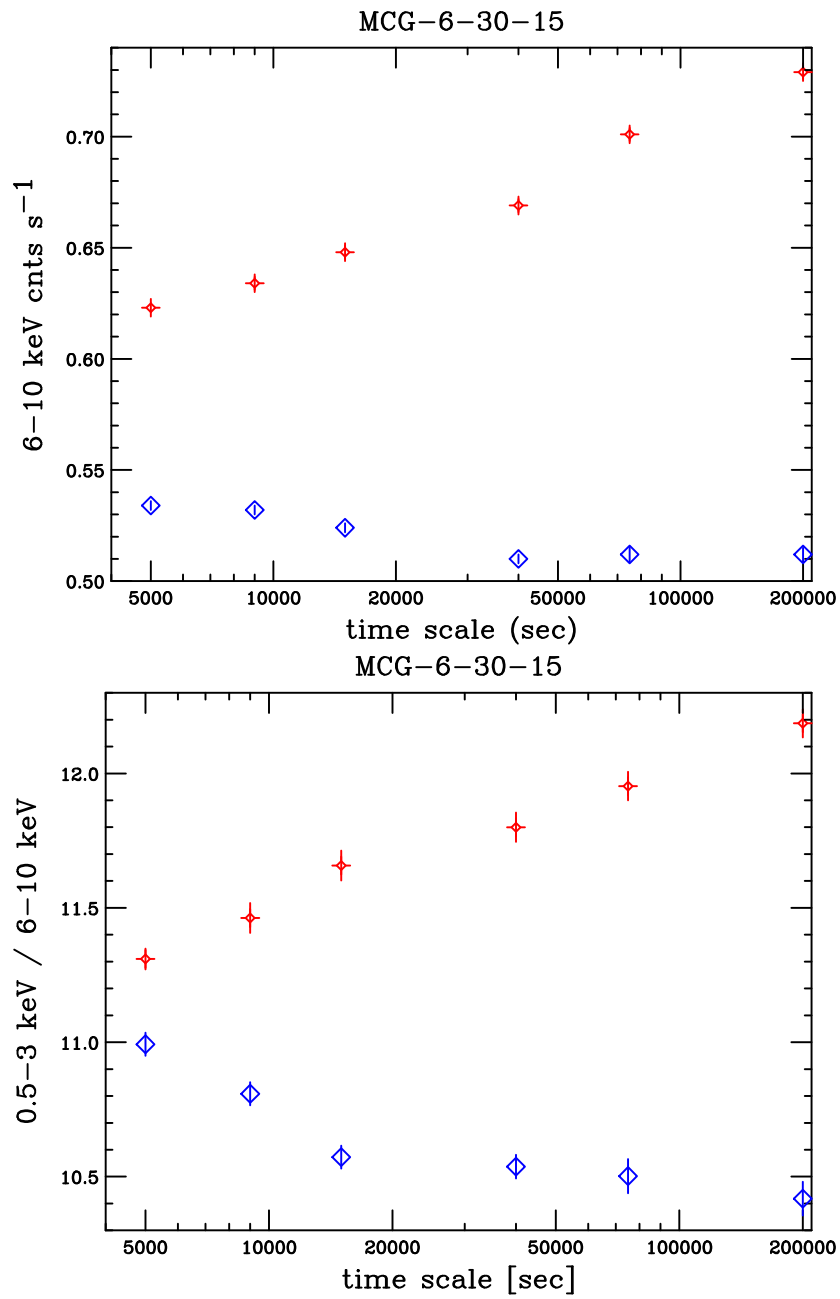


Figure 5.3: The 6.0 – 10 keV intensity (top) and the spectral hardness ratio (bottom) of the bright (red) and faint (blue) spectra as functions of the time-intervals, T .

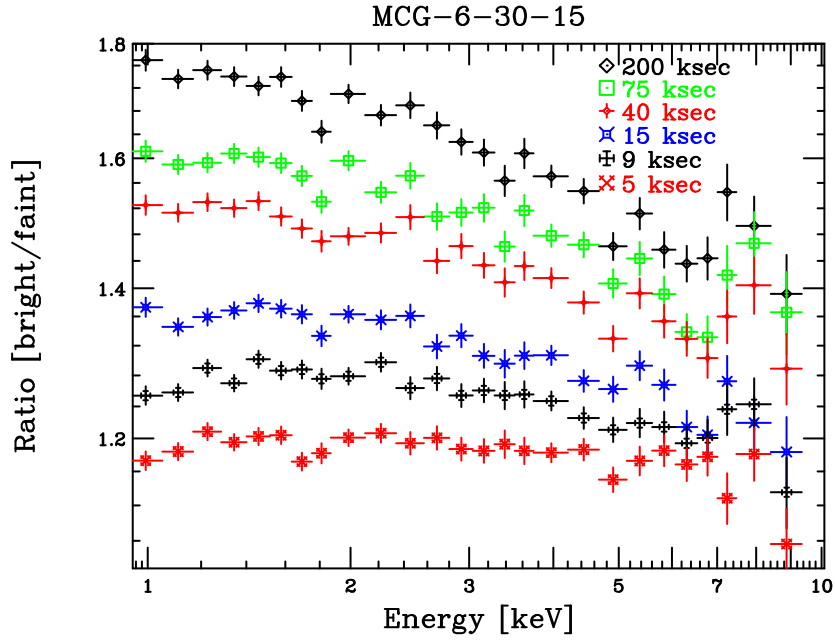


Figure 5.4: Spectral ratios of the bright spectra to the faint spectra for six different timescales.

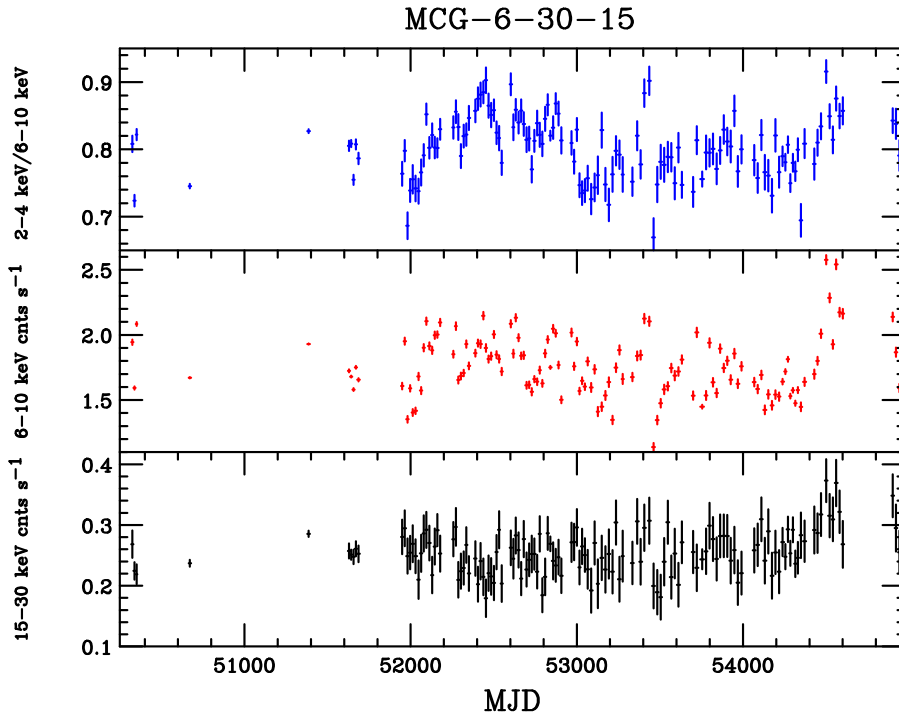


Figure 5.5: A 2–30 keV PCA light curve of MCG-6-30-15 with the 2×10^6 sec time-bin from 1996 to 2009, in 6 – 10 keV (middle) and 15 – 30 keV (bottom), as well as the spectral ratio of 2 – 4 keV/6 – 10 keV (top).

5.2 Spectral Fitting for the Average Spectrum with Model 1

In order to study origin of the spectral variation found in the previous section, we assume a spectral model and investigate variation of the spectral parameters. First, we fit the time-average spectrum of MCG-6-30-15 with a simple, but physically reasonable spectral model. Note that the model we adopt here is not our “final” model, but rather a “working” model introduced in order to interpret and quantify the energy spectral variations. We call this model “Model 1” in order to distinguish a more reasonable spectral model we introduce later (“Model 2”; section 5.5.1).

The spectral model we adopt here, Model 1, has the following components; (1) power-law with an exponential cut-off, (2) disk reflection component from neutral matter (“pexrav”; Magdziarz & Zdziarski 1995), (3) iron emission line at ~ 6.4 keV either narrow or broad, (4) two warm absorbers with different ionization states, and (5) neutral photoelectric absorption (“phabs”; Balucinska-Church & McCammon 1992). (6) a narrow gaussian absorption line to account for the instrumental feature around the Au M-edge. Spectral models are explained in detail in appendix A.

We use XSTAR Version 2.1kn8 (Kallman et al. 2004) to model the warm absorbers, assuming the solar abundance and the photon index of the ionizing spectrum 2.0. The temperature, pressure and density of the warm absorbers are assumed to be 10^5 K, 0.03 dyne/cm² and 10^{12} cm⁻³, respectively. We made a grid model by running XSTAR for different values of ξ and N_H ; the log ξ values are from 0.1 to 5 (erg cm s⁻¹) and N_H values are from 10^{20} to 10^{24} (cm⁻²). The number of steps for log ξ and N_H are both 20, thus our grid model has 20×20 grid-points.

All the fits were made with XSPEC v11 (Arnaud 1996). In Fig.5.7 (Top), we show the fitting result for total average spectrum with a *narrow* iron emission line (line width is fixed at $1\sigma = 10$ eV), where reduced chi-square is 1.51 ($\chi^2/\text{d.o.f} = 339.3/224$). The broadband 1–40 keV spectrum was fitted reasonably well, while there remain some residuals in the energy range of 5–7 keV (within ± 5 %) for putatively broad iron emission line. If we allow the intrinsic line width to be free, the fit significantly improved, where reduced chi-square is 1.20 ($\chi^2/\text{d.o.f} = 267.4/222$). Central energy of the line is 6.42 ± 0.06 keV, the intrinsic line width is $1\sigma = 290 \pm 60$ eV, and the equivalent width is 100 ± 20 eV (Figure 5.7, Bottom). The best-fit parameters for the average spectra are shown in Table 5.1 for both the narrow line model and the broad line model. Note that the XSTAR warm absorber model includes the absorption lines, and in fact the observed FeXXV and FeXXVI absorption line features at 6.67 keV and 6.97 keV are successfully modeled. Although the model is successful above 1 keV, we found this spectral model fails to fit the data below 1 keV; this issue is discussed in section 5.4.1.

Note that the current model does not require an extremely broadened iron emission line, which may be expected from very vicinity of a fast rotating black hole. With the combination of the cold reflection, mildly broad emission line and two warm absorbers, this model can successfully fit the seemingly broad iron line feature. In Figure 5.8, we show the ratio of our best-fit model to a power-law function, as well as the ratio of the observed spectrum to the same power-law function. A seemingly broad-line like structure down to ~ 4 keV is recognized both in the model and data, but this is explained by combination of the disk reflection, warm absorbers and a mildly broad gaussian line that is not significantly red-shifted.

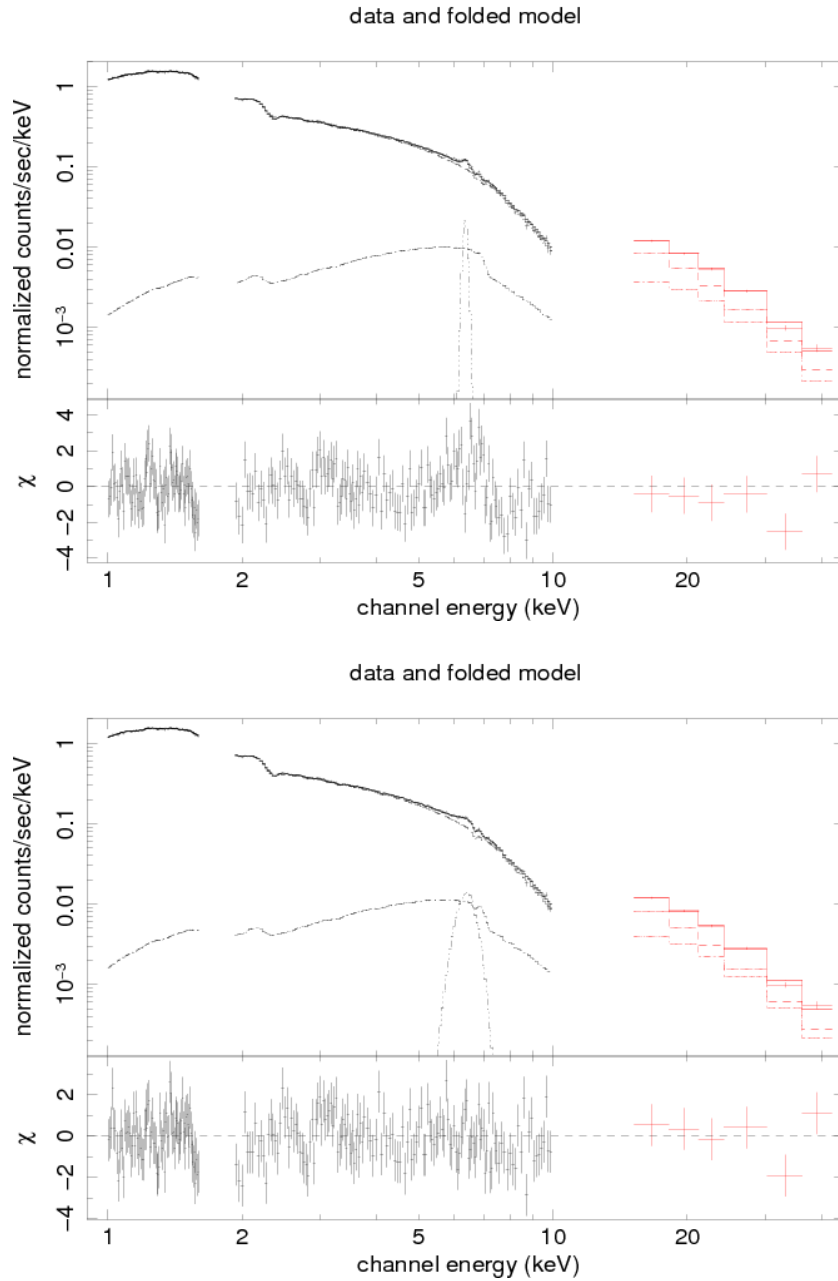


Figure 5.7: (Top) Spectral fit result for the time-averaged XIS and PIN spectra (1–40 keV) using Model 1 with a *narrow* iron emission line (intrinsic line width is fixed to $1 \sigma = 10$ eV). (Bottom) Spectral fit result for the time-averaged XIS and PIN spectra (1–40 keV) using Model 1 with a *broad* iron emission line (intrinsic line width is allowed to be free and $1 \sigma = 290$ eV).

Table 5.1: Results of the average spectral fitting in 1–40 keV

	broad line	narrow line
N_H (10^{21} cm $^{-2}$)	2.2 ± 0.2	1.7 ± 0.2
N_H (10^{22} cm $^{-2}$)	6_{-2}^{+3}	10_{-4}^{+6}
log ξ	3.3 ± 0.1	3.6 ± 0.2
N_H (10^{21} cm $^{-2}$)	2.4 ± 0.8	1.5 ± 0.4
log ξ	$1.7_{-0.3}^{+0.1}$	$1.0_{-0.4}^{+0.2}$
Line E (keV)	6.42 ± 0.06	6.35 (fix)
sigma (keV)	0.29 ± 0.06	0.01 (fix)
norm (10^{-5})	4.4 ± 0.7	1.7 ± 0.3
EW (eV)	100 ± 20	38 ± 6
cutoffpl K (10^{-2})	1.47 ± 0.05	1.38 ± 0.03
photon index	1.95 ± 0.02	1.90 ± 0.02
E_{cut} (keV)	160 (fix)	160 (fix)
cosIncl	0.866 (fix)	0.866 (fix)
$\Omega/2\pi$	1.0 ± 0.2	0.8 ± 0.2
Line E (keV)	2.35 ± 0.02	2.35 ± 0.02
sigma (keV)	0.01 (fix)	0.01 (fix)
norm (10^{-5})	-2.2 ± 0.5	-2.2 ± 0.5
reduced chi-square (d.o.f)	1.20 (222)	1.51 (224)

Errors are quoted at statistical 90% level. Constant factor to adjust normalizations between XIS and PIN is 1:1.086 (Ishida, Suzuki, and Someya 2007). Units of the cutoff power-law and pexrav normalization are photons/s/cm 2 /keV at 1 keV. Ω is solid angle of the reflector seen from the central source, and $\Omega/2\pi$ is defined as the ratio of the normalization of the reflection component to that of the cutoff power-law component. Unit of the line normalization is photons/s/cm 2 . Redshift of warm absorber and objects are 0.001 and 0.00775, respectively (Young et al. 2005, Fisher et al. 1995). Energy cutoff (E_{cut}) is fixed to 160 keV (Guainazzi et al. 1999). The solar abundances are defined in Greeves, Noels and Sauval (1996) for the warm absorbers and in Anders & Ebihara (1982) for the reflection component (pexrav).

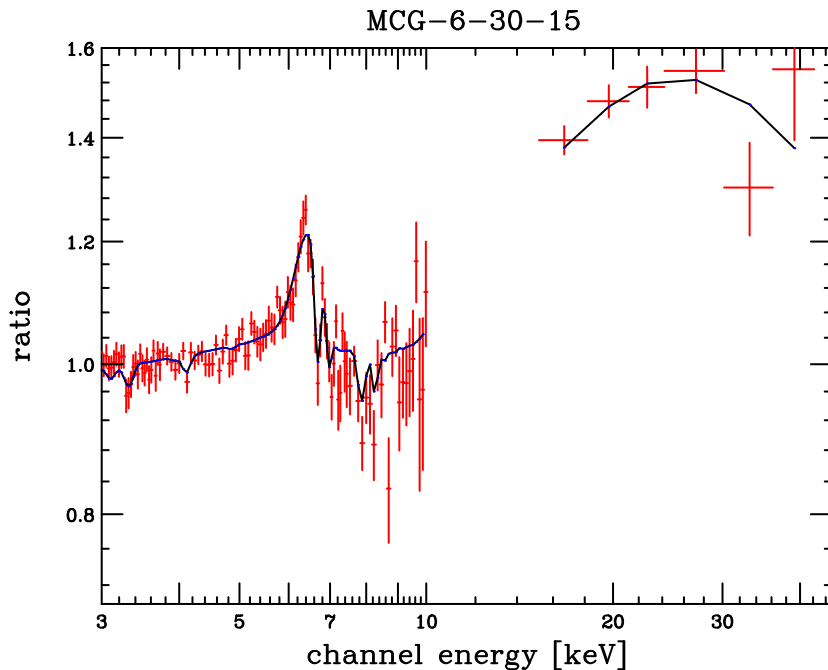


Figure 5.8: Ratios of our best-fit model (blue and black) and the observed spectrum (red) to a power-law function. The power-law slope is determined using the data only in 3.0–4.0 keV and 7.5–12 keV. Note that our model includes a moderately broad iron emission line at 6.42 keV ($1\sigma = 290$ eV), but not an extremely distorted one with relativistic effects.

5.3 Variation of Spectral Parameters with Model 1

5.3.1 Spectral fitting for the bright and faint spectra made with Method 1

Next, we quantify the observed spectral variation on different timescales. We try to fit the six “bright” spectra and the six “faint” spectra simultaneously (both XIS and PIN in 1 – 40 keV) with minimum numbers of variable parameters. As a result, we found that the twelve spectra are fitted reasonably well with keeping the reflection component constant, and only varying normalization of the direct component and another parameter to describe its apparent spectral slope, such that the direct component spectrum steepens as the flux increases (corresponding to Figures 5.2 and 5.4). Namely, we found *only two parameters are required* to describe continuum spectral variations of the twelve data-sets, whereas all the other spectral parameters are constant. Iron line flux is slightly variable, but it hardly affects the overall spectral shape.

We found that either power-law photon index, ionization parameter or column density of the lower-ionized warm absorber can almost equally reproduce the observed spectral change of the direct component. The best-fit parameters are shown in Table 5.2 for the twelve spectra, when the power-law index, ionization parameter and column density is varied (Case 1, 2 and 3, respectively, in Table 5.2), besides the power-law normalization.

In Fig 5.9, we show relations between the variation timescales and ionization degrees of the low-ionized warm absorber in Case 2 (Top) and relations between the variation timescales and the power-law normalizations (Bottom). It is obvious that both the ionization degree and the power-law normalization for the bright state increases with the variation timescale, while those for the faint state decreases with the variation timescale. These figures correspond to Figure 5.3, such that the spectral steepening below 10 keV with increasing timescales may be interpreted

as increase of the ionization parameter and power-law normalization with variation timescales.

5.3.2 Spectral fitting for the sliced spectra

We can also successfully fit the eight intensity-sliced spectra with Case 2, namely only varying the power-law normalization and the ionization parameter (Table 5.3). In Figure 5.10, we show the incident spectral changes for the intensity sliced spectra calculated from the best-fit parameters. Figure 5.11 shows correlation between the power-law normalization and ionization parameter of the lower ionized warm absorber in Case 2 for the sliced spectra, as well as for the bright and faint spectra. We can see a clear correlation as $\log \xi = (1.7 \pm 0.2) \times \log K + (4.7 \pm 0.3)$.

Figure 5.10 and Figure 5.11 are considered to correspond to Figure 5.4 and Figure 5.2 respectively, indicating that the observed spectral variation may be naturally interpreted as variation of ionization degree of the warm absorber accompanying the source luminosity variation, while the intrinsic power-law index and column density of the warm absorber is invariable.

5.4 Evidence of Variation of the Ionization States

Using a simple model (“Model 1”), we have found the observed characteristic spectral variation of MCG-6-30-15 may be explained by the change of only two spectral parameters, the power-law normalization and another parameter to describe the apparent spectral slope change. For the latter parameter, we could not distinguish three possibilities from the model fitting, power-law index, ionization degree of the warm absorber, or column density of the warm absorber. We have suggested that change of the ionization parameter with the power-law flux is likely, since the warm absorber is photoionized by the illuminating source. If this is the case, there should be local spectral features in absorption edges or lines due to change of the ionization degree. We will search for these spectral features as an evidence of variation of the ionization state of the warm absorber.

5.4.1 Variation of oxygen absorption edges below 1 keV

We found our “Model 1”, including two warm absorbers, fails to explain the energy spectra below 1 keV in Suzaku XIS. In fact, strong oxygen absorption lines have been observed with grating instruments below 1 keV (e.g., Lee et al. 2001), which suggests that there is another warm absorber responsible for the oxygen features below 1 keV. In any case, in order to quantify the observed spectral variation with a simple model, we fit the 0.6–1.6 keV spectra using a power-law model with two absorption edges. The twelve spectra bright and faint spectra are fitted simultaneously.

The best-fit absorption edge energies are 0.706 keV and 0.855 keV, which are considered to be primarily due to absorption edges of OVII and OVIII, respectively. We could fit all the twelve spectra with common photon index and the common 0.706 keV edge optical depth, while only the power-law normalization and the optical depth of the 0.855 keV edge are variable (Fig. 5.12). The best-fit parameters are shown in Table 5.4.

Optical depth of the OVIII edge becomes deeper and shallower for the faint state and the bright state, respectively, as the variation timescale increases (Fig. 5.13). This result suggests that the oxygen gets more highly ionized and the OVIII edge depth becomes shallower, as the source brightens and the warm absorber gets more highly ionized. This is consistent with what was observed with ASCA (Otani et al. 1996). The invariable OVII depth regardless of the flux variation, which was also observed with ASCA (Otani et al. 1996), may suggest that the OVII edge originate from a rather extended area in the line of sight, so that the OVII edge depth does

Table 5.2: Results of spectral fitting in 1–40 keV for the “bright” and “faint” spectra.

timescale	5 ksec	9 ksec	15 ksec	40 ksec	75ksec	200 ksec
state	bright	faint	bright	faint	bright	faint
<i>Case 1: power-law normalization and its index are variable</i>						
N_H (10^{21} cm $^{-2}$)				1.7±0.1		
N_H (10^{22} cm $^{-2}$)				10±2		
log ξ				3.56±0.05		
N_H (10^{21} cm $^{-2}$)				1.4±0.2		
log ξ				1.03 $^{+0.03}_{-0.11}$		
Line E (keV)				6.35 (fix)		
sigma (keV)				0.01 (fix)		
norm (10^{-5})				1.7±0.1		
EW (eV)	35±2	41±3	35±2	42±3	33±2	44±3
cutoffpl K (10^{-2})	1.51 $^{+0.01}_{-0.02}$	1.26 $^{+0.01}_{-0.02}$	1.57 $^{+0.01}_{-0.02}$	1.22 $^{+0.01}_{-0.02}$	1.64 $^{+0.01}_{-0.02}$	1.18 $^{+0.01}_{-0.02}$
photon index	1.91±0.01	1.90±0.01	1.91±0.01	1.89±0.01	1.92±0.01	1.88±0.01
E_{cut} (keV)				160 (fix)		
cosIncl				0.866 (fix)		
pextrav K (10^{-2})				1.07±0.08		
Line E (keV)				2.35±0.01		
sigma (keV)				0.01 (fix)		
norm (10^{-5})				-2.12±0.22		
reduced chi-square (d.o.f)				1.30 (2786)		
<i>Case 2: power-law normalization and ionization degree of the lower-ionized warm absorber are variable</i>						
N_H (10^{21} cm $^{-2}$)				2.14±0.05		
N_H (10^{22} cm $^{-2}$)				3.2 $^{+0.8}_{-0.6}$		
log ξ				3.29±0.04		
N_H (10^{21} cm $^{-2}$)				2.5±0.3		
log ξ	1.57±0.05	1.56 $^{+0.05}_{-0.06}$	1.60±0.05	1.46 $^{+0.05}_{-0.09}$	1.74 $^{+0.05}_{-0.06}$	1.41±0.06
Line E (keV)				6.35 (fix)		
sigma (keV)				0.01 (fix)		
norm (10^{-5})				1.7±0.1		
EW (eV)	36±2	42±3	35±2	43±3	33±2	45±3
cutoffpl K (10^{-2})	1.64±0.02	1.37±0.02	1.68 $^{+0.02}_{-0.01}$	1.33±0.02	1.73±0.02	1.25±0.01
photon index				1.96±0.01		
E_{cut} (keV)				160 (fix)		
cosIncl				0.866 (fix)		
pextrav K (10^{-2})				1.7±0.1		
Line E (keV)				2.35±0.01		
sigma (keV)				0.01 (fix)		
norm (10^{-5})				-2.3±0.2		
reduced chi-square (d.o.f)				1.41 (2787)		

See the footnote of Table 5.1.

Table 5.2: Results of spectral fitting in 1–40 keV for the “bright” and “faint” spectra (continued).

state	5 ksec		9 ksec		15 ksec		40 ksec		75ksec		200 ksec	
	bright	faint	bright	faint								
<i>Case 3: power-law normalization and column density of the lower-ionized warm absorber are variable</i>												
N_H (10^{21} cm $^{-2}$)												
N_H (10^{22} cm $^{-2}$)												
log ξ												
N_H (10^{21} cm $^{-2}$)	2.8±0.4	3.0±0.4	2.5±0.4	3.2±0.4	2.1±0.4	3.7±0.4	1.8±0.3	4.0±0.5	1.4±0.4	3.9 $^{+0.5}_{-0.4}$	1.1±0.3	4.2 $^{+0.5}_{-0.4}$
log ξ												
Line E (keV)												
sigma (keV)												
norm (10^{-5})												
EW (eV)	36±2	42±3	35±2	43±3	34±2	43±3	33±2	45±3	32±2	45±3	30±2	46±3
cutoffpl K (10^{-2})	1.63 $^{+0.03}_{-0.02}$	1.37±0.02	1.67 $^{+0.03}_{-0.02}$	1.33±0.02	1.71 $^{+0.03}_{-0.02}$	1.31±0.02	1.77 $^{+0.03}_{-0.02}$	1.25±0.02	1.87 $^{+0.03}_{-0.02}$	1.26 $^{+0.02}_{-0.01}$	1.96 $^{+0.03}_{-0.02}$	1.24±0.02
photon index												
E_{cut} (keV)												
cosincl												
pextrav K (10^{-2})												
Line E (keV)												
sigma (keV)												
norm (10^{-5})												
reduced chi-square (d.o.f)												

See the footnote of Table 5.1.

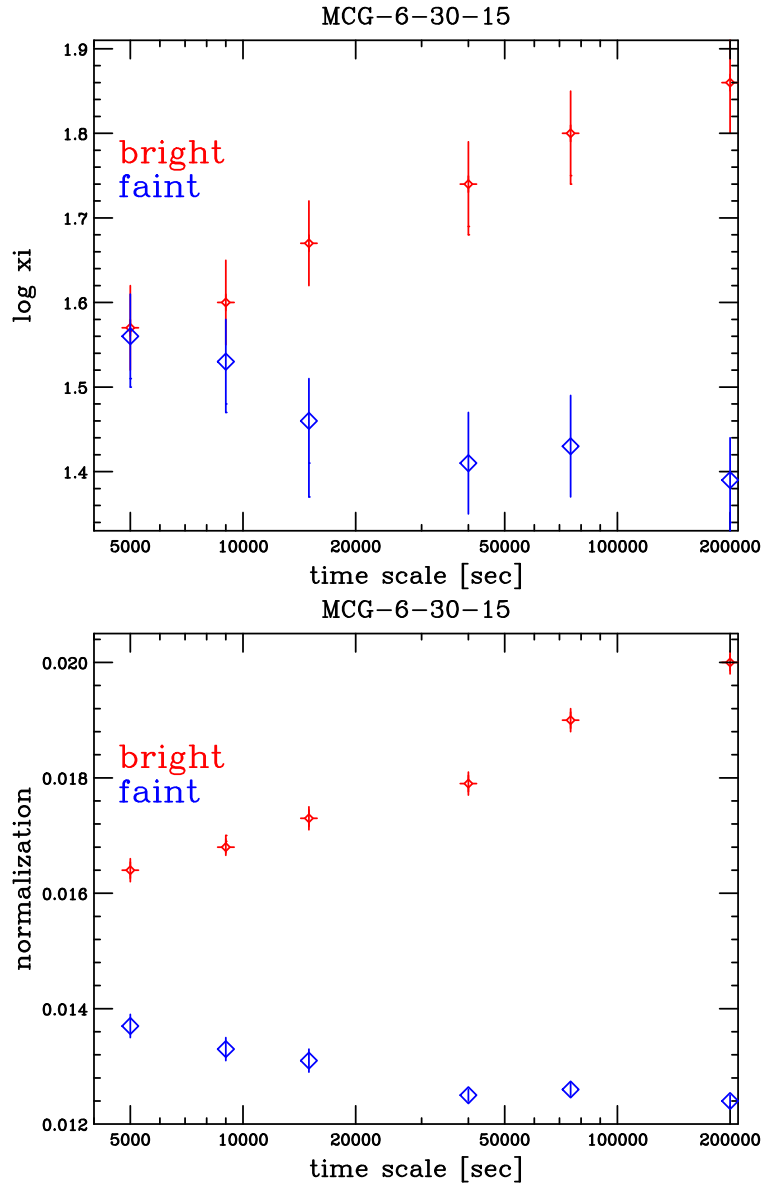


Figure 5.9: Top: Relation between the variation timescale and ionization degree for the bright and faint spectra in Case 2 (ionization parameter of the low ionized warm absorber varied). Bottom: Relation between the variation timescale and power-law normalization for the bright and faint spectra in Case 2.

Table 5.3: Results of spectral fitting in 1–40 keV for the intensity sliced spectra with Model 1, Case 2 (only the power-law normalization and the ionization degree of the lower-ionized absorber are varied)

state	slice 1	slice 2	slice 3	slice 4	slice 5	slice 6	slice 7	slice 8
N_H (10^{21} cm $^{-2}$)				2.3 \pm 0.1				
N_H (10^{22} cm $^{-2}$)				3.3 \pm 0.9				
$\log \xi$				3.27 $^{+0.04}_{-0.06}$				
N_H (10^{21} cm $^{-2}$)				4.1 \pm 0.3				
$\log \xi$	1.24 $^{+0.12}_{-0.10}$	1.57 \pm 0.06	1.69 $^{+0.06}_{-0.03}$	1.70 \pm 0.06	1.74 $^{+0.05}_{-0.06}$	1.86 $^{+0.05}_{-0.06}$	1.75 \pm 0.06	2.05 \pm 0.12
Line E (keV)				6.35 (fix)				
sigma (keV)				0.01 (fix)				
norm (10^{-5})				1.7 \pm 0.2				
EW (eV)	68 \pm 6	44 \pm 4	40 \pm 4	36 \pm 3	36 \pm 3	35 \pm 3	33 \pm 3	21 \pm 2
cutoffpl K (10^{-2})	0.75 \pm 0.02	1.35 \pm 0.03	1.54 \pm 0.04	1.72 \pm 0.04	1.75 \pm 0.04	1.77 \pm 0.04	1.89 \pm 0.05	3.23 \pm 0.12
photon index				2.04 \pm 0.02				
E_{cut} (keV)				160 (fix)				
cosIncl				0.866 (fix)				
pextrav K (10^{-2})				2.8 $^{+0.5}_{-0.3}$				
Line E (keV)				2.35 \pm 0.01				
sigma (keV)				0.01 (fix)				
norm (10^{-5})				-2.4 \pm 0.3				
reduced chi-square (d.o.f)				1.24 (1143)				

See the footnote of Table 5.1.

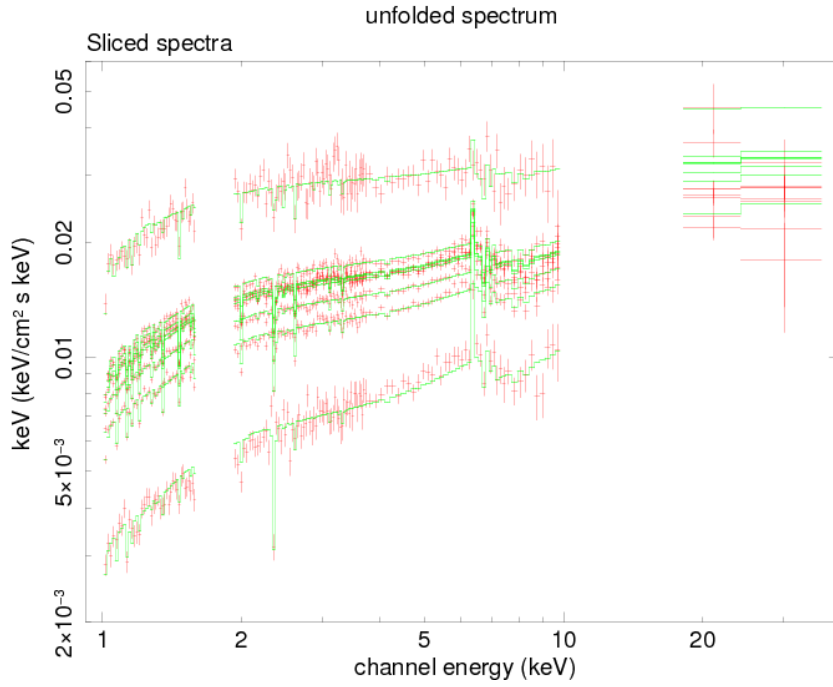


Figure 5.10: Unfolded energy spectra for the eight intensity-sliced spectra calculated from the model only varying the power-law normalization and ionization degree of the lower-ionized warm absorber.

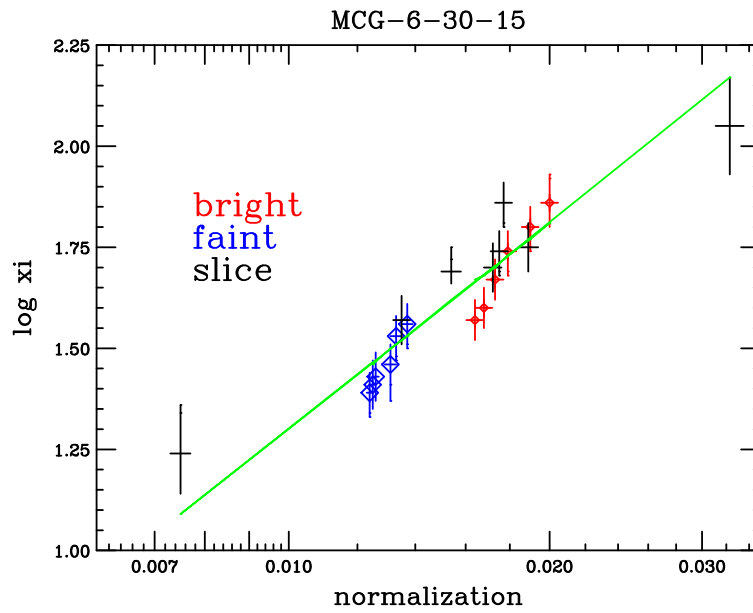


Figure 5.11: Relation between the ionization degree and power-law normalization for the bright, faint and sliced spectra in Case 2 (ionization parameter of the low ionized warm absorber varied).

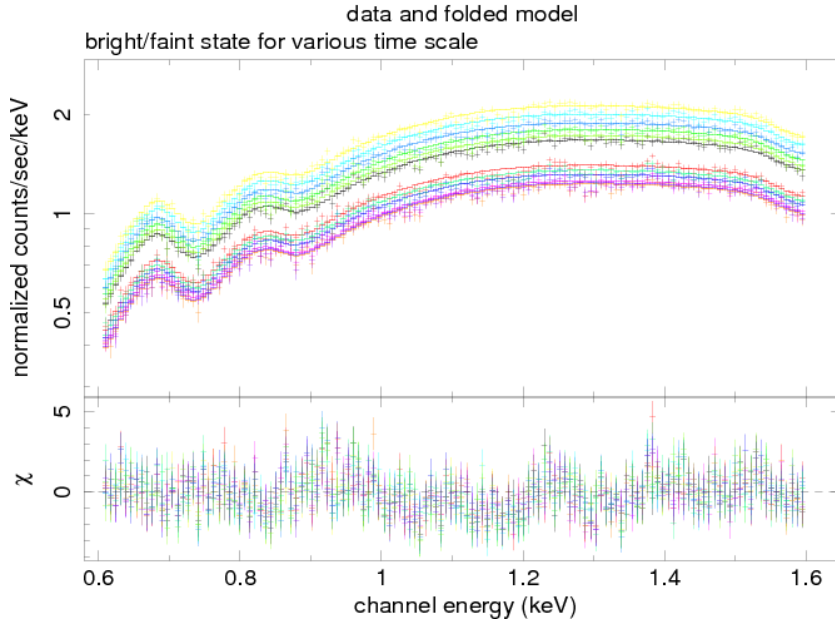


Figure 5.12: Simultaneous fit in the 0.6–1.6 keV band for the twelve spectra (bright and faint spectra for the 6 timescales) with a power-law plus two absorption edge model.

not respond to the flux variation instantaneously. The current results suggest that the spectral variation below 1.6 keV is mainly due to variation of the photoionization as a consequence of the intrinsic flux changes, while the photon index is invariable.

5.4.2 Variation of Mg and Si absorption lines

Next, we investigate for variation of absorption lines observed in Chandra/HETGS spectra to search for evidence of the ionization state variation accompanying the flux variations. To do that, we extract the “bright spectrum” and “faint spectrum” from Chandra/HETGS data as follows: 1) Create a light curve with a time-bin-width of 128 sec, and calculate the average count rate. 2) Create the “bright spectrum” from the period when the MEG and HEG count rates (0.4–10 keV) are higher than the average, and the “faint spectrum” when the count rates are lower than the average.

We fit the bright/faint spectra in the 1.15–1.55 keV band with a single power-law and two negative gaussian model to investigate for the MgXI (He-like 1.34 keV) and MgXII (H-like 1.47 keV) lines. We also fit the bright/faint spectra in the 1.75–2.10 keV band separately with a single power-law and **two** negative gaussian model to investigate for the SiXIII (He-like 1.85–1.86 keV) and SiXIV (H-like 2.00 keV) lines.

In Figure 5.14, we show the fitting result for the bright/faint spectra in both energy bands. We found that we can fit the bright and faint spectra with common photon index, while only the power-law normalization and the normalization of absorption lines are varied in both energy ranges. The best fit parameters are shown in Table 5.5.

We notice that the MgXI absorption line equivalent width is larger in the faint state, while that of the MgXII line is larger in the bright state. This is understood as due to change of the ionization state of the warm absorber, such that MgXI is more abundant in the faint state, while MgXII is more abundant in the bright state. According to Kallman & Bautista (2001), ion fraction of MgXI and that of MgXII are equal at $\log \xi \simeq 2$ (see the top of Figure 5.15). Thus,

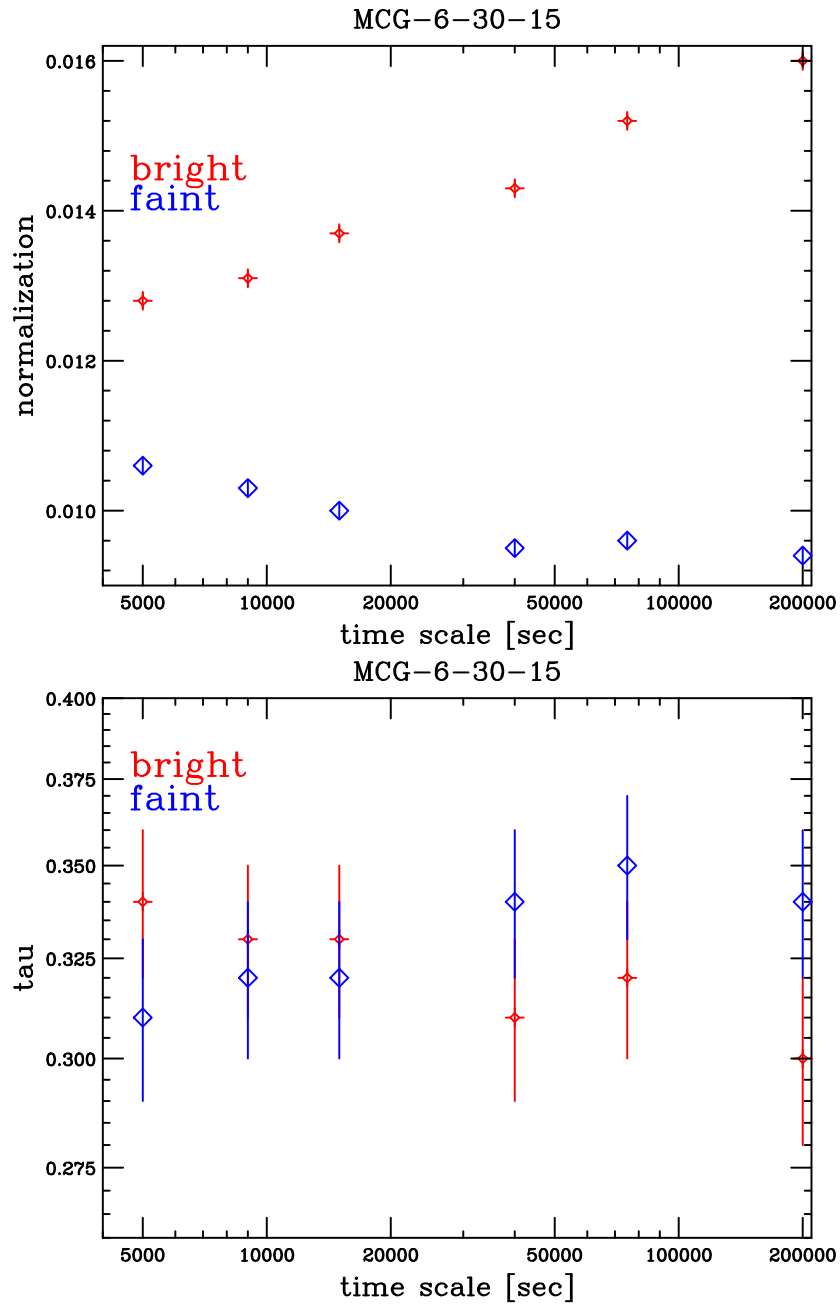


Figure 5.13: Variation of the power-law normalization and depth of the OVIII edge to describe the spectral variation in 0.6 – 1.6 keV, as functions of the timescales.

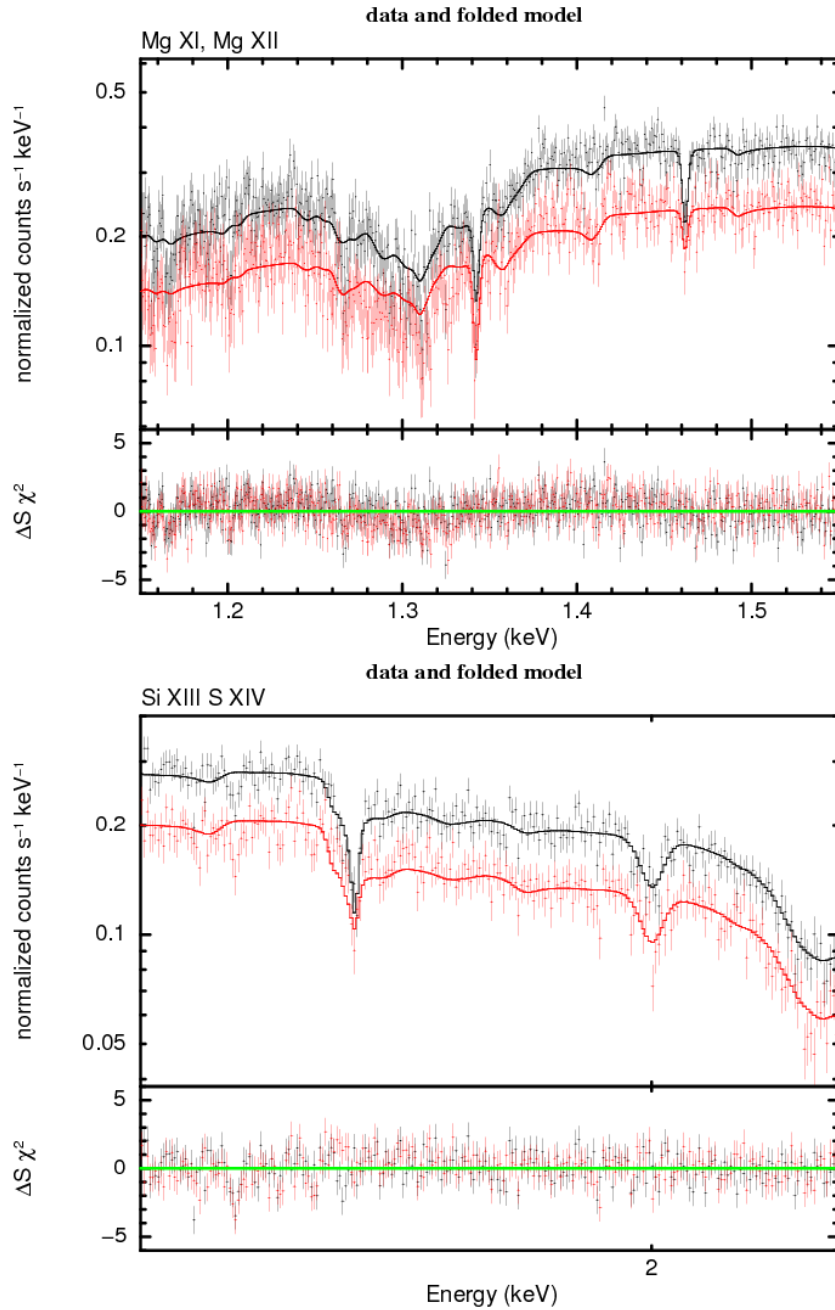


Figure 5.14: (Top) Chandra HETGS simultaneous fit in the 1.15–1.55 keV band for the bright spectrum and faint spectrum with a power-law plus two negative gaussian model. Mg absorption lines are at 1.34 keV and 1.47 keV. (Bottom) Simultaneous fit in the 1.75–2.10 keV band with a power-law plus two negative gaussian model. Si absorption lines are at 1.85 keV and 2.00 keV.

Table 5.5: Results of spectral fitting of Chandra/HETGS spectra in 1.15–1.55 keV and 1.75 – 2.10 keV for the intensity sliced spectra when only the power-law normalization and the normalization of absorption lines are varied.

	bright	faint
Mg XI absorption line		
line E (keV)	1.3424±0.0004	
sigma (10 ⁻³ keV)	1.4±0.5	
norm (10 ⁻⁵)	-1.2±0.3	-1.0±0.2
EW (eV)	-1.9±0.5	-2.2±0.4
Mg XII absorption line		
line E (keV)	1.4621±0.0004	
sigma (10 ⁻³ keV)	1.2±0.6	
norm (10 ⁻⁵)	-1.0±0.2	-0.4±0.2
EW (eV)	-1.7±0.3	-1.0±0.5
photon index	0.95±0.07	
norm (10 ⁻³)	8.6±0.2	6.0±0.2
reduced chi-square	1.21 ($\chi^2/\text{d.o.f} = 1329/1096$)	
	bright	faint
Si XIII absorption line		
line E (keV)	1.8515±0.0005	
sigma (10 ⁻³ keV)	< 1.7	
norm (10 ⁻⁵)	-1.0±0.2	0.4±0.2
EW (eV)	-2.4±0.5	-1.4±0.7
Si XIV absorption line		
line E (keV)	2.000±0.002	
sigma (10 ⁻³ keV)	5.5 ^{+1.9} _{-2.1}	
norm (10 ⁻⁵)	-1.5±0.4	-1.1±0.4
EW (eV)	-3.8±1.0	-3.9±1.4
photon index	0.97±0.15	
norm (10 ⁻³)	7.7±0.8	5.7±0.6
reduced chi-square	1.17 ($\chi^2/\text{d.o.f} = 539/459$)	

the present result suggests presence of a warm absorber with $\log \xi \simeq 2$, such that change of the ionization degree causes the transition between the He-like Mg dominant state and H-like Mg dominant state. This is consistent with the Suzaku result that ionization state variation of the low-ionized warm absorber (Table 5.3, Figures 5.10 and 5.11) is suggested from continuum spectral variations.

As for variation of the Si absorption line equivalent width, the SiXIII line equivalent width is larger for the bright spectrum, while that of the SiXIV line is not much different. Variation of the SiXIII line equivalent width is consistent with the presence of the warm absorber with $\log \xi \simeq 2$, since ion fraction of SiXIII increases when $\log \xi$ varies from ~ 1.5 to ~ 2 (see the bottom of Figure 5.15). However, ion fraction of SiXIV should increase more dramatically when $\log \xi$ increases accordingly (Figure 5.15, bottom), which is not seen in the SiXIV absorption line depth. This result may be understood if there is another higher ionized warm absorber at $\log \xi \geq 3$, which produces a significant amount of SiXIV but not SiXIII (Figure 5.15, bottom).

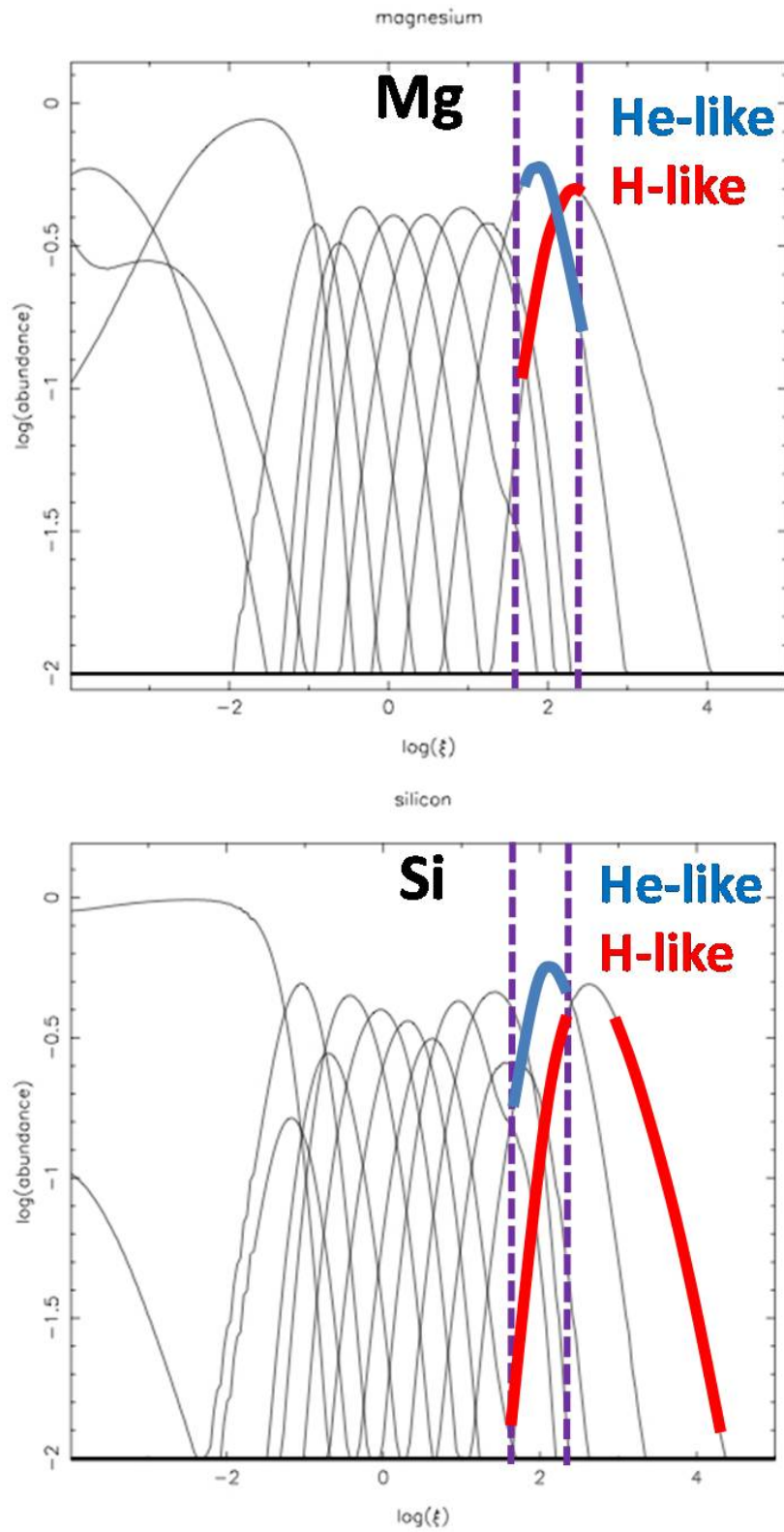


Figure 5.15: Mg and Si ion fractions of an optically thin low-density photoionized gas, as a function of the ionization parameter, assuming the power-law ionizing spectrum with ϵ^{-1} (Kallman & Bautista 2001).

Table 5.6: Results of spectral fitting in 5.9–7.1 keV for the average spectra of Chandra/HETG.

Iron line E (keV)	6.34 ± 0.01
sigma (keV)	$1.8_{-1.3}^{+2.2} \times 10^{-2}$
norm (10^{-5})	$1.1_{-0.5}^{+0.8}$
EW (eV)	23_{-10}^{+16}
Fe XXV (keV)	6.69 ± 0.01
sigma (keV)	0.01 (fixed)
norm (10^{-6})	-9.2 ± 3.3
EW (eV)	-21 ± 8
Fe XXVI (keV)	6.96 ± 0.02
sigma (keV)	0.01 (fixed)
norm (10^{-6})	-9.2 ± 3.9
EW (eV)	-23 ± 10
cutoffpl K (10^{-2})	$1.6_{-1.0}^{+2.6}$
photon index	1.88 ± 0.53
reduced chi-square (d.o.f)	0.58 (111)

Presence of such a highly ionized warm absorber is, again, consistent with the Suzaku spectral results ($\log \xi \sim 3.3$; Tables 5.1, 5.2 and 5.3).

In summary, characteristic continuum spectral variation observed with Suzaku and XTE (Figures 5.2 and 5.6), is explained as due to variation of ionization state of a warm absorber (Figure 5.11), which is confirmed by changes of the absorption edge depths (Figure 5.12) and absorption line equivalent widths (Figure 5.14).

5.5 Revisiting the Spectral Model

So far, we have studied spectral variations of MCG-6-30-15 using Suzaku, RXTE and Chandra data, assuming a simple spectral model (“Model 1”; section 5.2), and indicated that the spectral variation at various timescales is successfully explained by variation of ionization state of the low-ionized ($\log \xi \approx 2$) warm absorber. In this section, we scrutinize the observed energy spectra more carefully, and introduce a slightly more elaborated model, “Model 2”, which shall become our next working model.

5.5.1 Introducing Spectral Model 2

As already mentioned in section 2.3.1, using the Chandra HETGS, Young et al. (2005) resolved a narrow emission line at 6.4 keV in MCG-6-30-15. In order to confirm the result independently, we fit the 5.9–7.1 keV average spectrum of Chandra/HETGS. In Figure 5.33, we show the fitting result using a power-law component and three gaussian component to account for a narrow iron emission line, He-like iron absorption line, and H-line iron absorption line. The best fit parameters are shown in Table 5.6. We detected the narrow iron emission line at 6.34 ± 0.01 keV with the equivalent width of 23_{-10}^{+16} eV, which is consistent with Young et al. (2005).

The narrow-line fluorescence emission is an evidence of the reprocessing far from the black hole, which should accompany the continuum disk reflection. Corresponding to the ~ 20 eV equivalent width, solid angle of the reflector is $\Omega/2\pi \sim 0.3$ (e.g., George and Fabian 1991; Figure 2.7), which is much smaller than what we have obtained from Model 1 ($\Omega/2\pi \approx 1$; Table

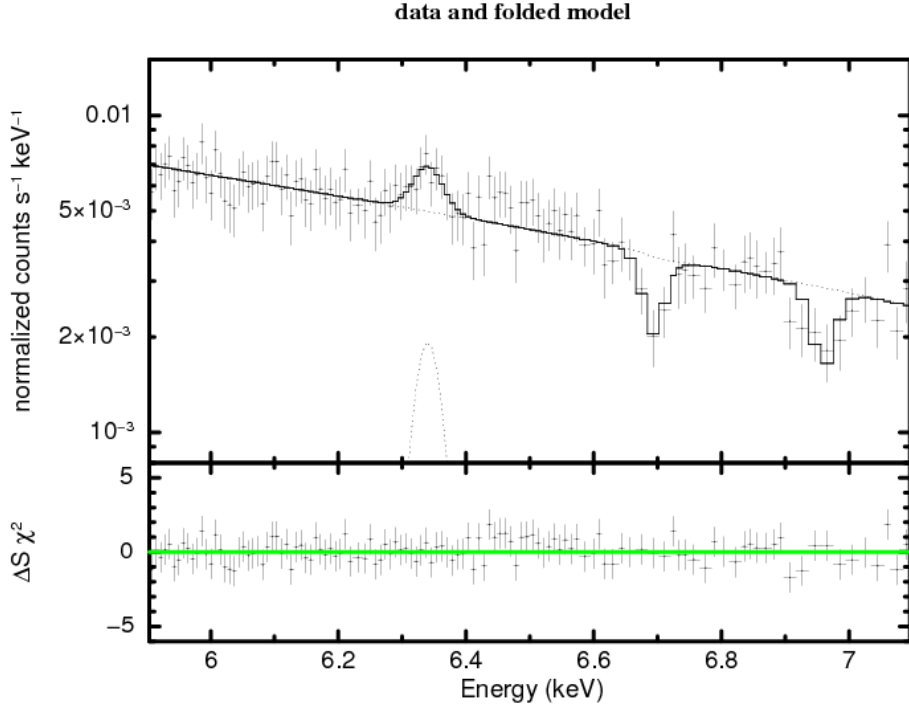


Figure 5.16: Spectral fit result for the time-averaged HETGS spectra (5.9–7.1 keV).

5.1). Consequently, in order to explain the observed energy spectrum including the outer disk reflection ($\Omega/2\pi \sim 0.3$) and the narrow iron line with an equivalent width of ~ 20 eV, we need another disk reflection component corresponding to an amount of $\Omega/2\pi \sim 0.7$.

The disk reflection spectrum and a heavily absorbed component by optically thick matter have similar spectral shape, so we may approximate the disk reflection spectrum by an heavily absorbed spectrum. In fact, from spectral fitting, the disk reflection component and a heavily absorbed component are difficult to distinguish (Figure 2.5). Also, the reflecting disk or the absorbing matter in the vicinity of the black hole are considered to be ionized. Therefore, we introduce an additional spectral component heavily absorbed by a warm absorber. The following is our “Model 2”, which shall be a new working model to study spectral variation:

interstellar absorption \times {high-ionized warm absorber \times low-ionized warm absorber \times (A \times cutoff power-law + B \times warm absorber \times cutoff power-law) + outer disk reflection component + narrow iron emission line)}

Here, outer disk reflection component is neutral, and its normalization is fixed at $\Omega/2\pi \sim 0.3$. The term with A is the direct component, and the term with B is considered to be either disk reflection component or heavily absorbed component, presumably from vicinity of the black hole. Photon indexes of the direct component and the heavily absorbed component are made equal, since their origins are the same.

We try Model 2 to the Suzaku average spectrum. We found the fit improves if we additionally put a weak iron neutral edge at 7.11 keV and an absorption line at 7.0 keV. The latter may suggest deficiency of the H-like iron absorption line equivalent-width already included in the high-ionized warm absorber (calculated with XSTAR; section 5.2). Figure 5.17 shows the fitting result for the Suzaku average spectrum with Model 2. Parameters of the high-ionized and low-

Table 5.7: Results of spectral fitting in 1–40 keV for the Suzaku XIS/PIN average spectrum with Model 2.

state	average
N_H (10^{21} cm $^{-2}$)	$1.5^{+0.4}_{-0.2}$
N_H (10^{23} cm $^{-2}$)	$2.4^{+1.8}_{-1.6}$
log ξ	3.37 ± 0.04
N_H (10^{21} cm $^{-2}$)	3.7 ± 1.3
log ξ	$1.54^{+0.25}_{-0.13}$
N_H (10^{24} cm $^{-2}$)	$1.6^{+0.6}_{-0.1}$
log ξ	$1.57^{+0.21}_{-0.19}$
direct cutoffpl K (10^{-2})	1.44 ± 0.03
absorbed cutoffpl K (10^{-2})	0.60 ± 0.09
photon index	$1.91^{+0.02}_{-0.01}$
E_{cut} (keV)	160(fix)
cosIncl	0.866(fix)
pextrav K (10^{-2})	direct cutoffpl K $\times 0.3$
Line E (keV)	6.35 (fix)
sigma (keV)	0.01 (fix)
norm (10^{-5})	1.2 ± 0.3
EW (eV)	27 ± 7
edge E (keV)	7.11 (fix)
MaxTau	0.05 ± 0.02
Line E (keV)	7.0 (fix)
sigma (keV)	0.01(fix)
norm (10^{-6})	-6.8 ± 2.4
Line E (keV)	2.35 ± 0.02
sigma (keV)	0.01(fix)
norm (10^{-5})	-2.3 ± 0.5
reduced chi-square (d.o.f)	1.12 (203)

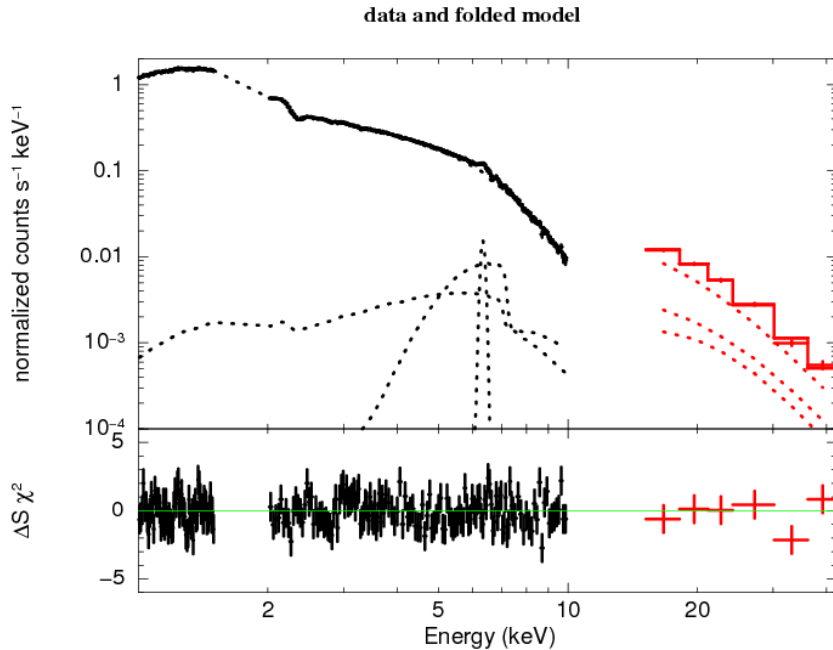


Figure 5.17: Spectral fit result for the 1-40 keV average spectrum for Suzaku XIS/PIN with “Model 2”.

ionized warm absorbers are similar to those of Model 1 (Table 5.1). For the newly introduced heavily absorbed component, we obtain $N_H \sim 1.6 \times 10^{24} \text{ cm}^{-2}$ and $\log \xi = 1.57$. For the time being, we leave its interpretation as either disk reflection component or heavily absorbed component. Ratio of the normalization of the heavily absorbed component to the direct component is $0.60/1.44 \approx 0.4$. If interpreted as disk reflection this suggests $\Omega/2\pi \sim 0.4$. Or, in the absorption interpretation, the source is partially absorbed by the ionized thick matter by $\sim 40\%$.

5.5.2 Examination of presence of the “disk line”

Many authors claim presence of the “disk line” in the energy spectrum of MCG-6-30-15 (section 2.2.3). Therefore, we examine if presence of the disk line may be reconciled with our Model 2. We analyze the time-average spectrum of MCG-6-30-15 adding a disk line model from a fast-rotating Kerr black hole (Laor 1991). Parameters of “Laor’s disk line” model are explained in appendix A. Note that Model 2 already includes a narrow iron emission line, so the new model we adopt here has both the narrow line from very far from the black hole, and a putative broad line which may be from a region closer to the black hole.

We try to fit the spectrum with Laor’s disk line model with varying the inner disk radius, r_{in} . Figure 5.18 and Table 5.8 show the best-fitting result for the Suzaku average spectrum adding Laor’s model to Model 2, where $r_{in} \approx 200 r_g$ and the reduced chi-square is 1.07 ($\chi^2/\text{d.o.f} = 214/200$). Compared to the case without the disk line ($\chi^2/\text{d.o.f} = 227/203$), the F -value is $((227 - 214)/3) / (214/200) = 4.05$, which gives the upper-probability 0.008 of F -distribution of the degrees of freedom (3,200). Namely, presence of the disk line is significant with a confidence greater than 99 %.

The line is only mildly broadened, and the equivalent width of the broad disk line is $40 \pm 20 \text{ eV}$. Figure 5.19 shows the chi-squares of fitting to the average spectrum as a function of the inner disk radius. As seen from this figure, $\approx 200 r_g$ is the best fitting value, and Δ chi-squares

Table 5.8: Results of spectral fitting in 1–40 keV for the average spectrum adding Laor’s disk line to Model 2.

state	average
laor line E (keV)	6.40±0.06
Index	−3 (fix)
r_{in} (R_g)	216 $^{+184}_{-207}$
r_{out} (R_g)	400 (fix)
inclination (deg)	30 (fix)
norm (10^{-5})	1.3 $^{+0.4}_{-0.6}$
EW (eV)	40±20
N_H (10^{21} cm $^{-2}$)	3.5 $^{+1.4}_{-0.5}$
N_H (10^{23} cm $^{-2}$)	2.9 $^{+0.9}_{-0.4}$
log ξ	3.35±0.04
N_H (10^{21} cm $^{-2}$)	3.7 $^{+1.4}_{-0.8}$
log ξ	1.52 $^{+0.21}_{-0.12}$
N_H (10^{24} cm $^{-2}$)	1.7 $^{+1.3}_{-0.2}$
log ξ	1.65 $^{+0.08}_{-0.16}$
direct cutoffpl K (10^{-2})	1.44 $^{+0.04}_{-0.02}$
absorbed cutoffpl K (10^{-2})	0.55 $^{+0.05}_{-0.07}$
photon index	1.91 $^{+0.02}_{-0.01}$
E_{cut} (keV)	160(fix)
cosIncl	0.866(fix)
pextrav K (10^{-2})	direct cutoffpl K ×0.3
Line E (keV)	6.35 (fix)
sigma (keV)	0.01 (fix)
norm (10^{-6})	5.4 $^{+2.4}_{-4.5}$
EW (eV)	12 $^{+5}_{-10}$
edge E (keV)	7.11 (fix)
MaxTau	0.04±0.02
Line E (keV)	7.0 (fix)
sigma (keV)	0.01(fix)
norm (10^{-6})	−6.1 $^{+2.1}_{-2.3}$
Line E (keV)	2.35±0.02
sigma (keV)	0.01(fix)
norm (10^{-5})	−2.3±0.5
reduced chi-square (d.o.f)	1.07 (200)

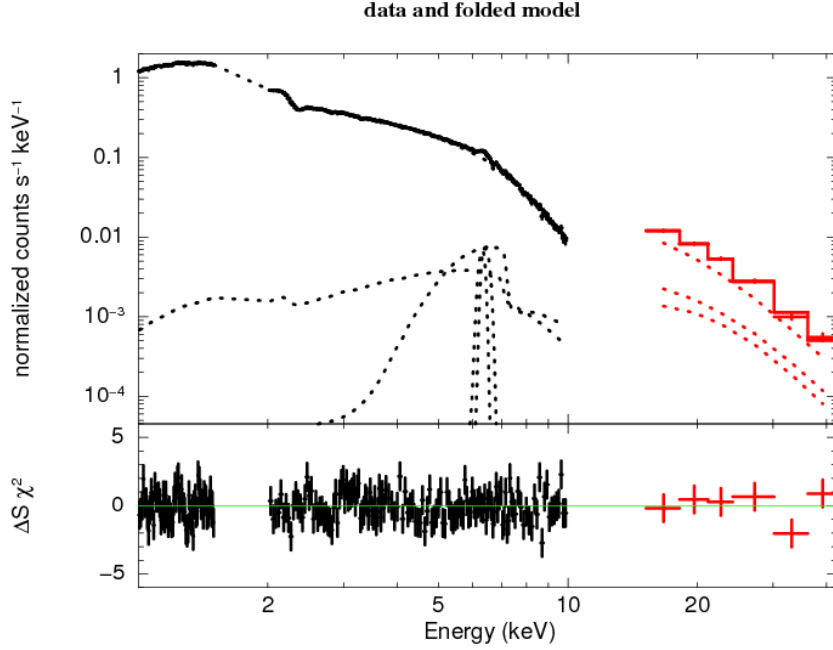


Figure 5.18: Spectral fit result for the 1-40 keV average spectrum adding Laor’s disk line model to Model 2.

become greater than 2.71 when r_{in} is less than $9 r_g$. This indicates that our Model 2 is only reconciled with a broad disk line from the region $r_{in} > 9r_g$ (90 % confidence).

The reason we do not require an extremely distorted disk line as opposed to Miniutti et al. (2007) and others (Figure 2.12) is primarily that the newly introduced heavily absorbed component in Model 2 has an ionized edge feature which looks like a disk line (Figure 5.17), and secondly that the warm absorbers which are already included in Model 1 have spectral curvature below 4 keV without which the residual may look like a low-energy tail of the disk line. In other words, we are demonstrating that the disk line feature is dependent on the choice of spectral models, as we have already explained in the review (Section 2.3.3).

Also, we have seen that the spectral model fitting alone does not tell if the heavily absorbed component we introduced here is really an absorbed component or due to disk reflection. To answer this question, we will further study spectral variations observed with Suzaku, using Model 2 as a new working model.

5.6 Spectral Variability in a model Independent manner – Method 2

Before applying Model 2 to the Suzaku spectra, we introduce a new method to study spectral variations in a model independent manner. In contrast to Method 1 introduced in section 5.1, we call the new method as Method 2.

In Method 2, we extract the “bright spectra” and “faint spectra” as follows:

- 1) Create a light curve (the average of XIS0, XIS2, and XIS3), with a bin-width of T sec in the 0.2 – 12 keV band.

- 2) Create the “bright spectrum” and the “faint spectrum” from every two adjacent bins, such that the average count of the former is brighter than the other.

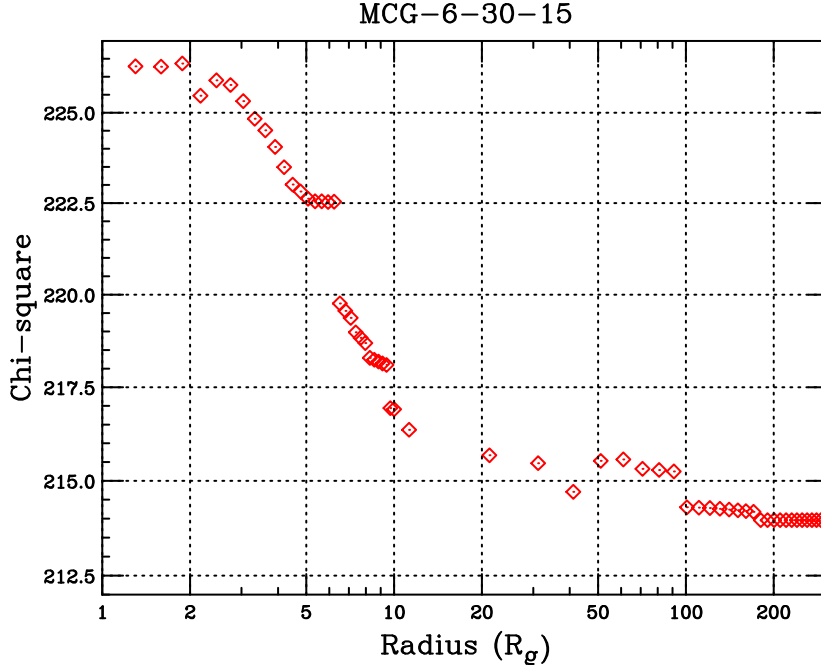


Figure 5.19: Chi-squares of fitting to the average spectrum, shown as a function of the inner radius of Laor’s disk line model.

3) Average the bright spectra and faint spectra from all the samples of the bright and faint spectra pairs.

4) Thus, for a given T , we have one bright spectrum and one faint spectrum.

5) Repeat the procedure for different intervals of T . As for T , we chose 128, 256, 512, 1,024, 5,000, 10,000, 20,000, 40,000, and 80,000 sec.

Figure 5.20 demonstrates how the bright and faint spectra are extracted with Method 2 corresponding to $T = 20,000$ sec (top) and 40,000 sec (bottom) based on the 0.2–12 keV XIS light curve. In Method 2, as opposed to Method 1, we can cancel variations shorter than T . Therefore, Method 2 would be more appropriate to investigate spectral variation just around the timescale T . Each adjacent 2 bins correspond a single Fourier component with the period $2T$. In the following, when we mention variation timescales, we mean $2T$, from 256 sec to 160,000 sec.

In order to quantify the degree of time variability, we define the variation amplitude

$$\frac{(C_b - C_f)}{(C_b + C_f)/2} \quad (5.1)$$

where, C_b and C_f are count rates of the bright state and faint state thus defined, respectively¹. Figure 5.21 gives energy dependence of the spectral variation amplitude for the nine different timescales. It is remarkable that variation amplitude below 3 keV is almost constant between the timescales of 256 and 2048 sec, while energy dependence gets more significant for longer time scales.

¹The error is given as $4 \sqrt{C_b^2 \delta C_f^2 + C_f^2 \delta C_b^2} / (C_b + C_f)^2$, as shown in the following. If we consider $f(A, B) = (A - B)/(A + B)$, $\delta f(A, B) = \frac{\delta A - \delta B}{A + B} - \frac{(A - B)}{(A + B)^2} (\delta A + \delta B) = \frac{(A + B) - (A - B)}{(A + B)^2} \delta A + \frac{-(A + B) - (A - B)}{(A + B)^2} \delta B = \frac{2B}{(A + B)^2} \delta A - \frac{2A}{(A + B)^2} \delta B$. Hence, $\delta f(A, B)^2 = \frac{4B^2}{(A + B)^4} \delta A^2 + \frac{4A^2}{(A + B)^4} \delta B^2$ (we assume $\delta A \delta B = 0$).

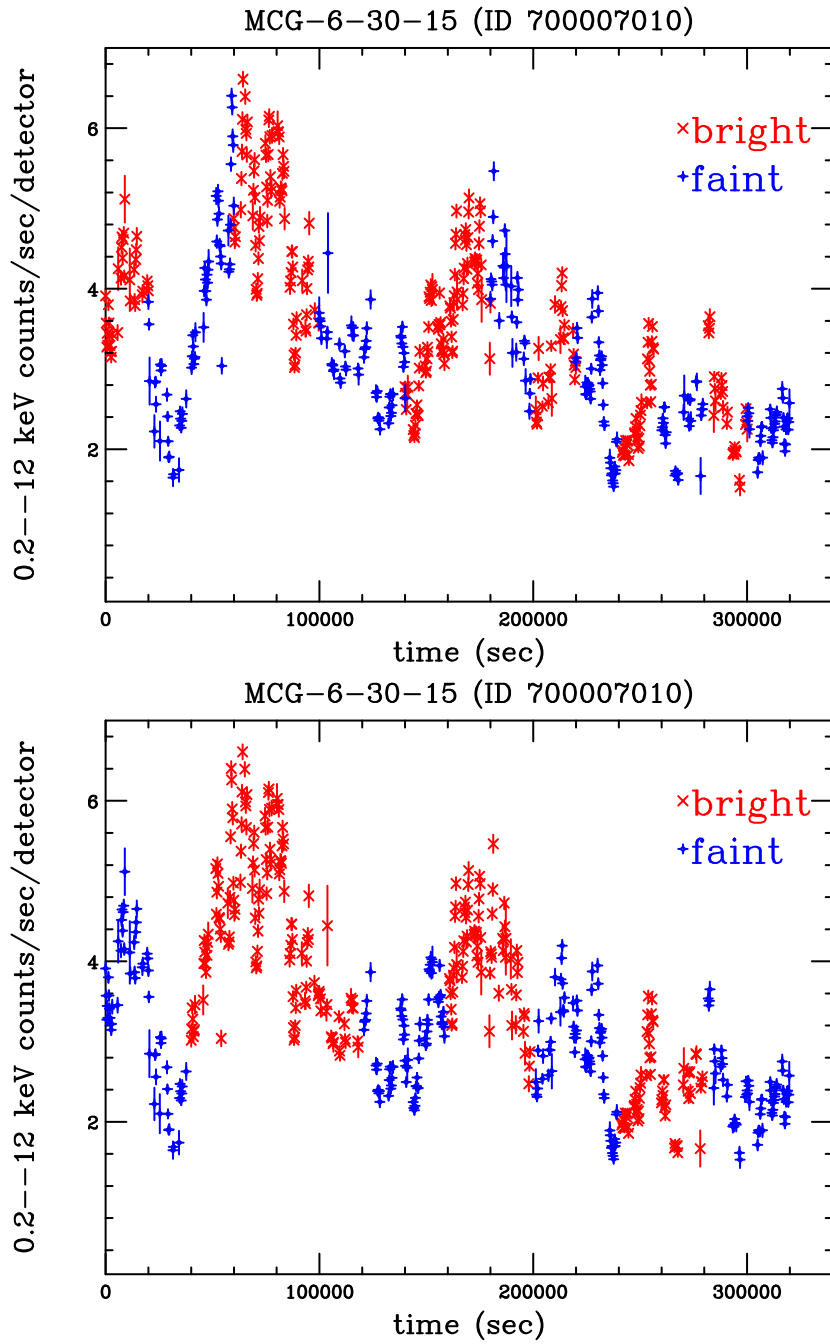


Figure 5.20: A 0.2–12 keV XIS light curve of the 2006 observation (obsID:700007010) to explain the Method 2 of spectral extraction. Top: the case of an interval of 20,000 sec. Bottom: the case of an interval of 40,000 sec. The periods when the bright spectra and faint spectra are extracted are shown with red and blue, respectively.

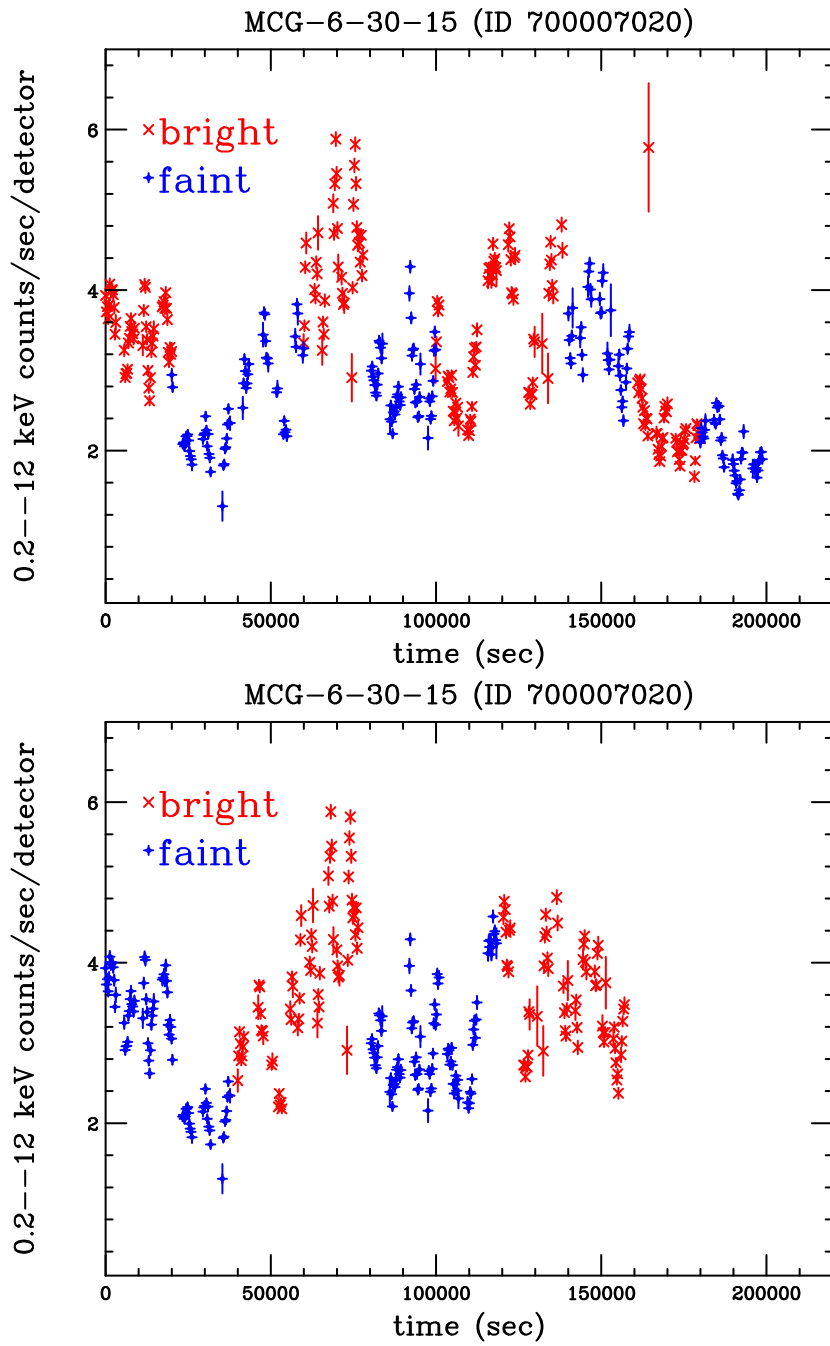


Figure 5.20: (Continued.) The same figure as the previous one, for obsID:700007020.

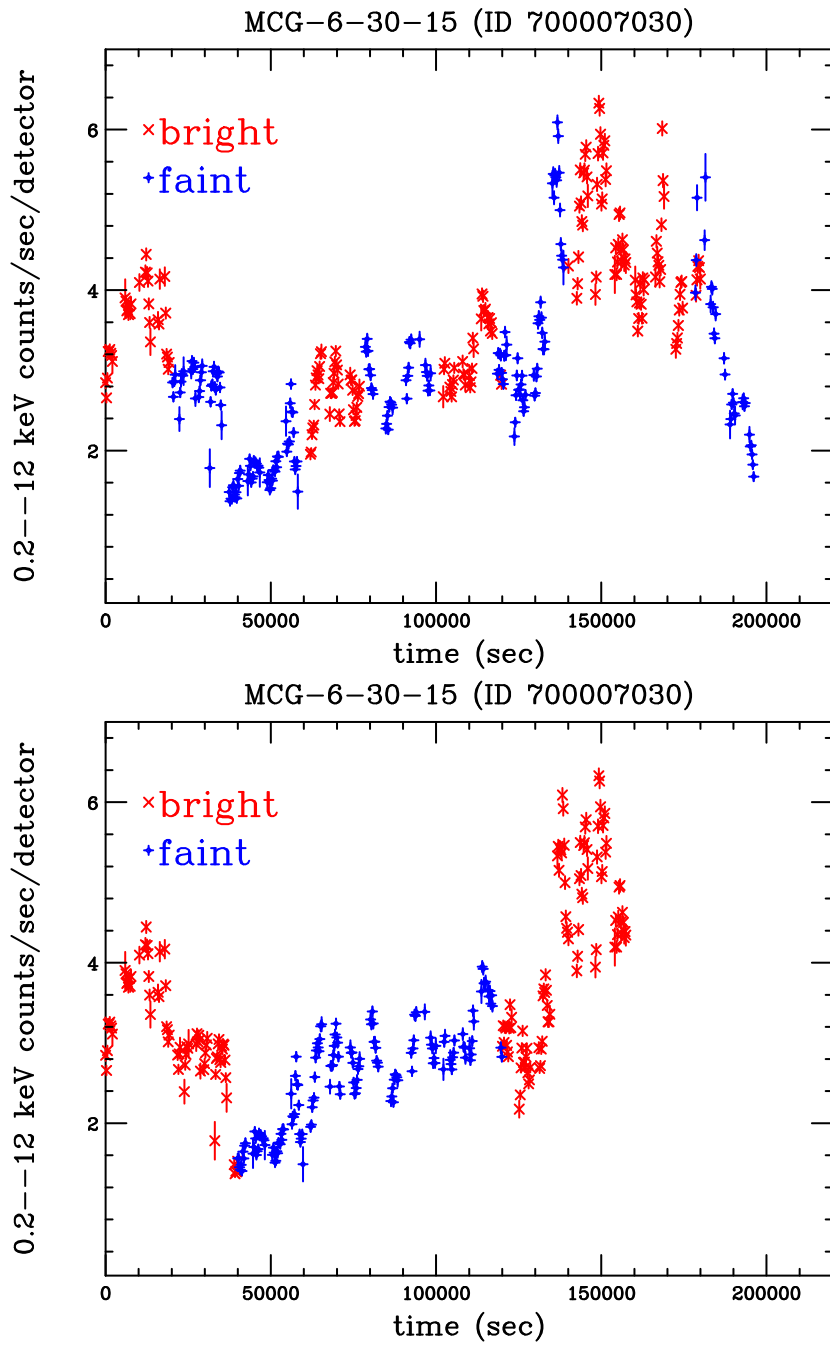


Figure 5.20: (Continued.) The same figure as the previous one, for obsID:700007030.

Figure 5.22 shows variation amplitudes in wide energy ranges, in 1–10 keV, 14.8 – 24.2 and 24.2 – 42.2 keV. As for PIN energy band, we calculated the variation amplitude between 10,000 sec and 160,000 sec because the sensitivity of PIN is much smaller than that of XIS. In general, if there is a characteristic timescale of the variation T_0 in the data, the variability defined here should have a timescale dependence of $\propto T$ when $T \ll T_0$, and $\propto T^{-1/2}$ when $T \gg T_0$, where T is the time-interval to study the variability within². Hence, the shape of variability is convex upward around T_0 . As seen from Figure 5.22, MCG-6-30-15 seems to have two characteristic timescales of variability at $\sim 10,000$ sec and $\sim 80,000$ sec. Similarly, Figure 5.23 shows variation amplitude in several narrow energy ranges from 1.28–1.40 keV to 8.41 – 9.35 keV, as functions of the timescales. Presence of the two characteristic timescales are also recognized in the individual narrow energy ranges.

Also, as seen from Figure 5.23, the variation amplitude below 3 keV is much larger than that above 3 keV when variation timescale is between 40,000 and 160,000 sec. This corresponds to the steepening of the variation amplitude below ~ 7 keV in Figure 5.21 as the variation timescale increases.

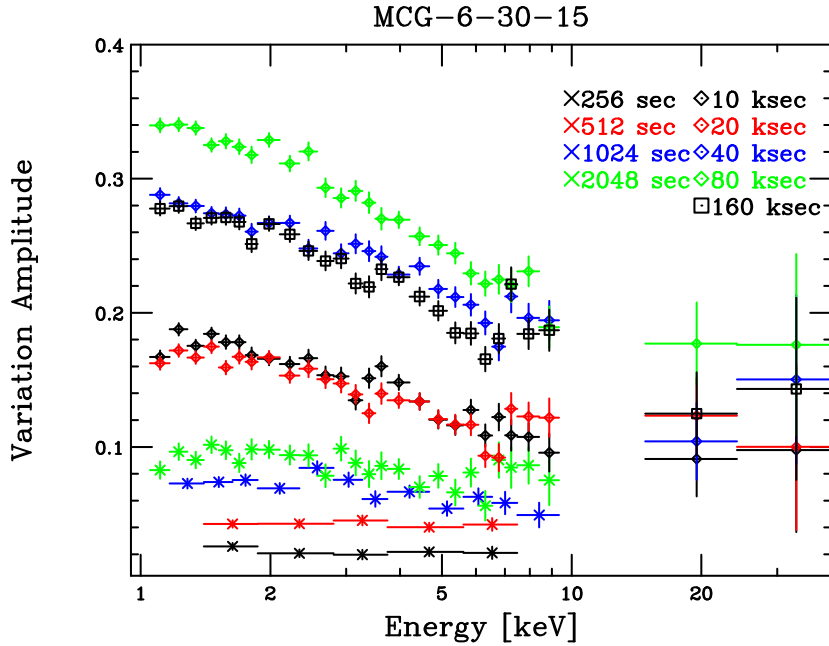


Figure 5.21: Energy dependence of spectral variability of Suzaku XIS/PIN (defined in eq. 5.1) calculated from the nine sets of the bright and faint spectral pairs, extracted via Method 2.

5.7 Variation of Spectral Parameters with Model 2

5.7.1 Spectral fitting for the bright and faint spectra made with Method 2

Next, we apply Model 2 to the bright and faint spectra at various timescales extracted with Method 2. We do not include the disk line, since it is minor in our model even if exists (Figure

²Let's put the typical counts F and its variation amplitude ΔF corresponding to T_0 , and those corresponding to T as f and Δf . Then the variability for T_0 is $\Delta F/F$, and we need to obtain $\Delta f/f$. For $T \ll T_0$, if we put $N = T_0/T$, $\Delta f/f = (1/N)\Delta F/F = (T/T_0)\Delta F/F$. For $T \gg T_0$, if we put $N = T/T_0$, $\Delta f^2/f^2 = (\sum \Delta F)^2 / (\sum F)^2 = \sum \Delta F^2 / (NF)^2 = N\Delta F^2 / N^2 F^2 = (1/N) \Delta F^2 / F^2$. Therefore, $\Delta f/f = (T/T_0)^{-0.5} \Delta F/F$.

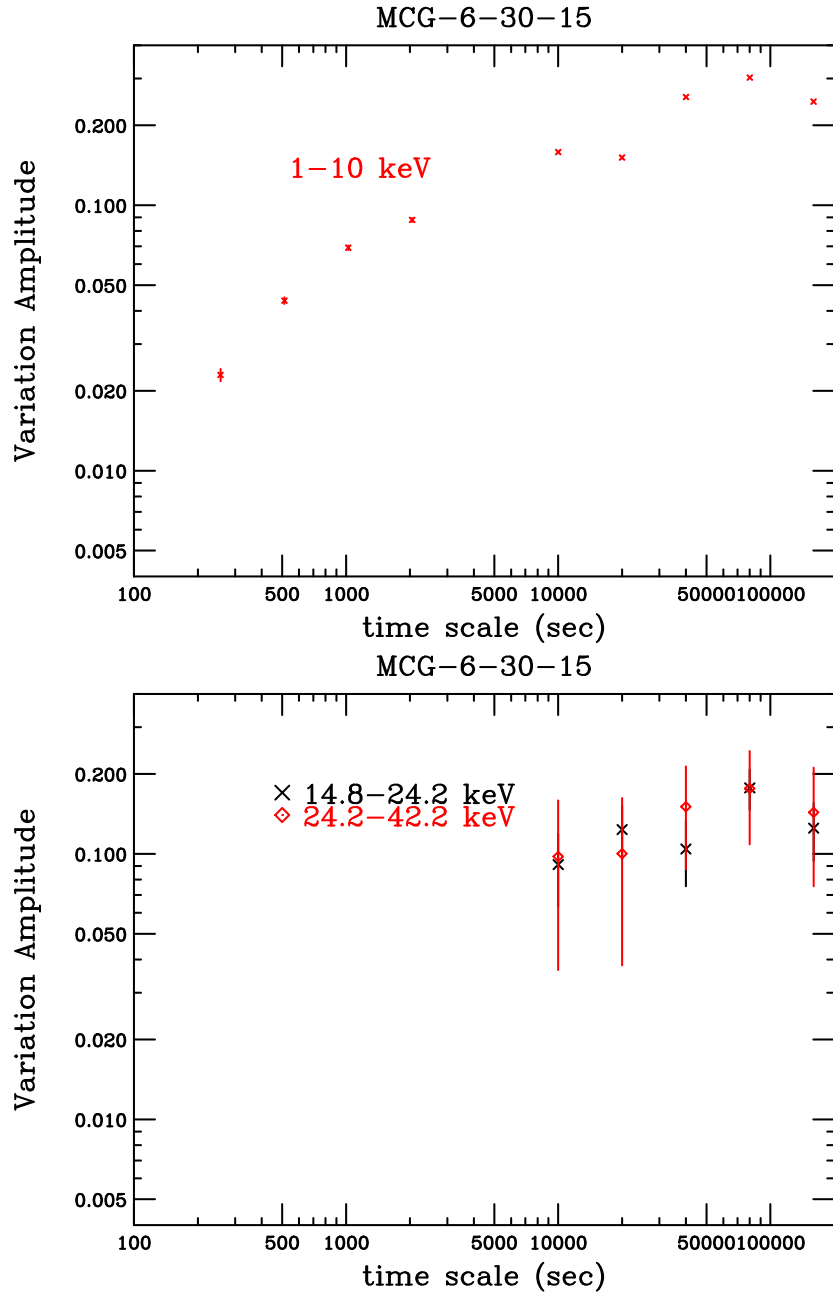


Figure 5.22: Spectra variability (defined in 5.1) as functions of the timescales in 1–10 keV (Top), and in 14.8–24.2 keV and 24.2–42.2 keV (Bottom), calculated from the nine sets of the bright and faint spectral pairs, extracted via Method 2.

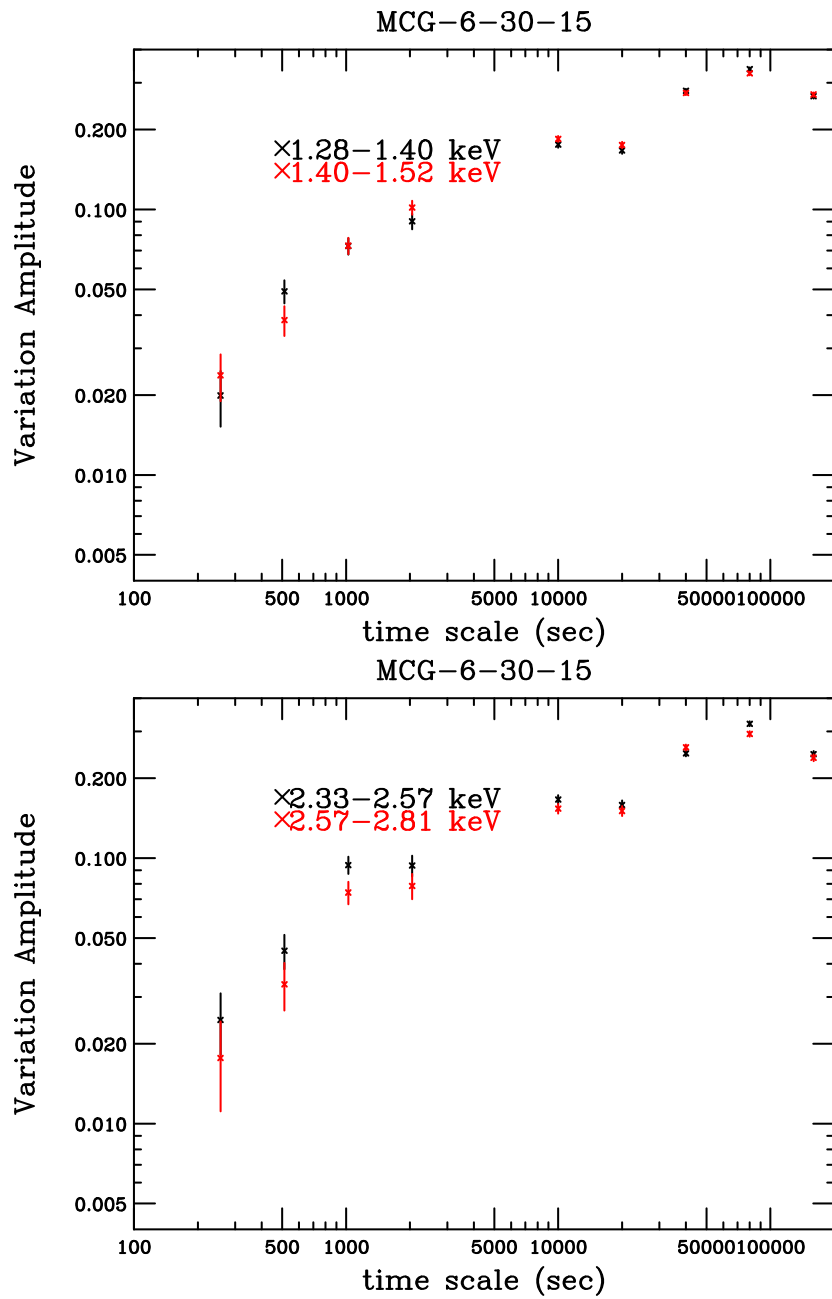


Figure 5.23: Spectral variability (defined in eq. 5.1) as functions of the timescales in 1.28–1.40 keV and 1.40–1.52 keV (Top), and in 2.33–2.57 keV and 2.57–2.81 keV (Bottom).

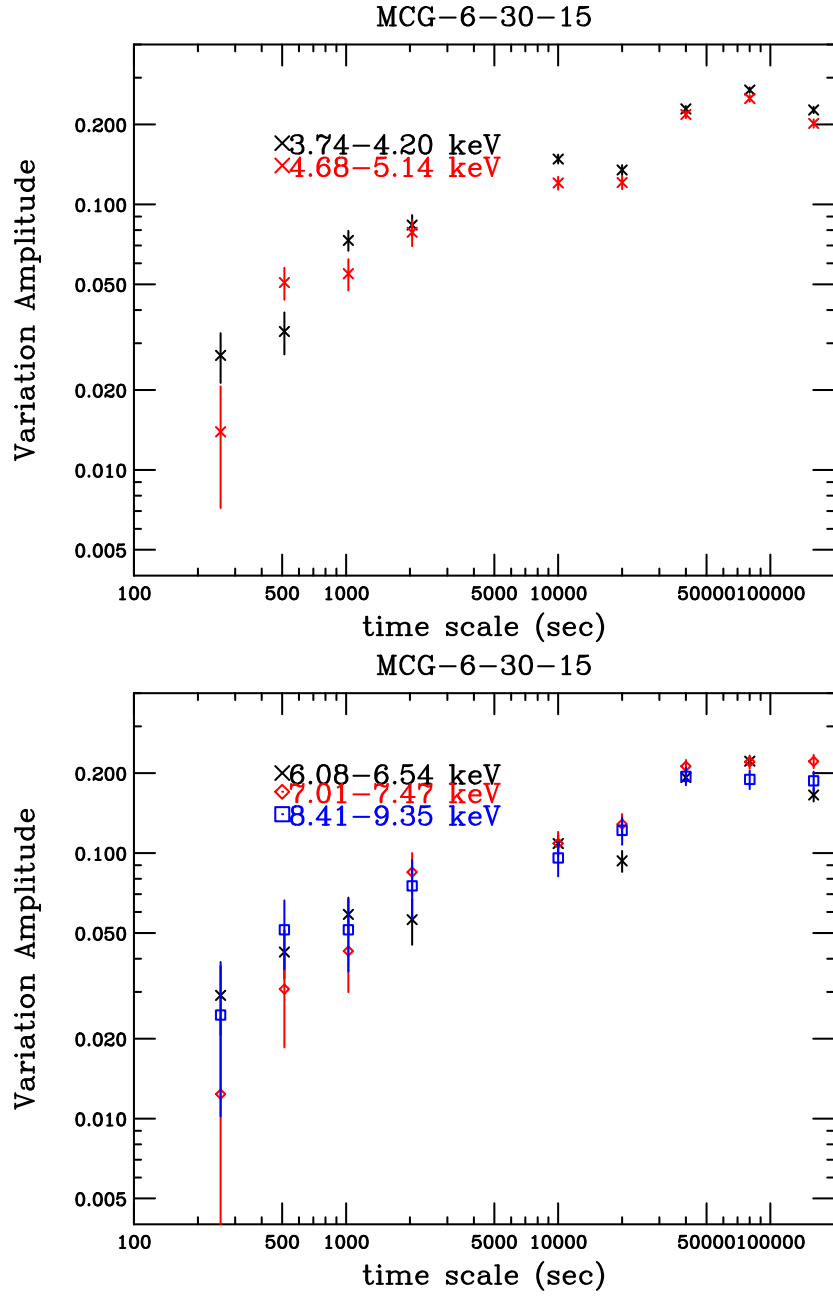


Figure 5.23: (Continued.) Spectral variability (defined in eq. 5.1) as functions of the timescales in 3.74 – 4.20 keV and 4.68 – 5.14 keV (Top), and in 6.08–6.54 keV, 7.01–7.47 keV, and 8.41–9.35 keV (Bottom).

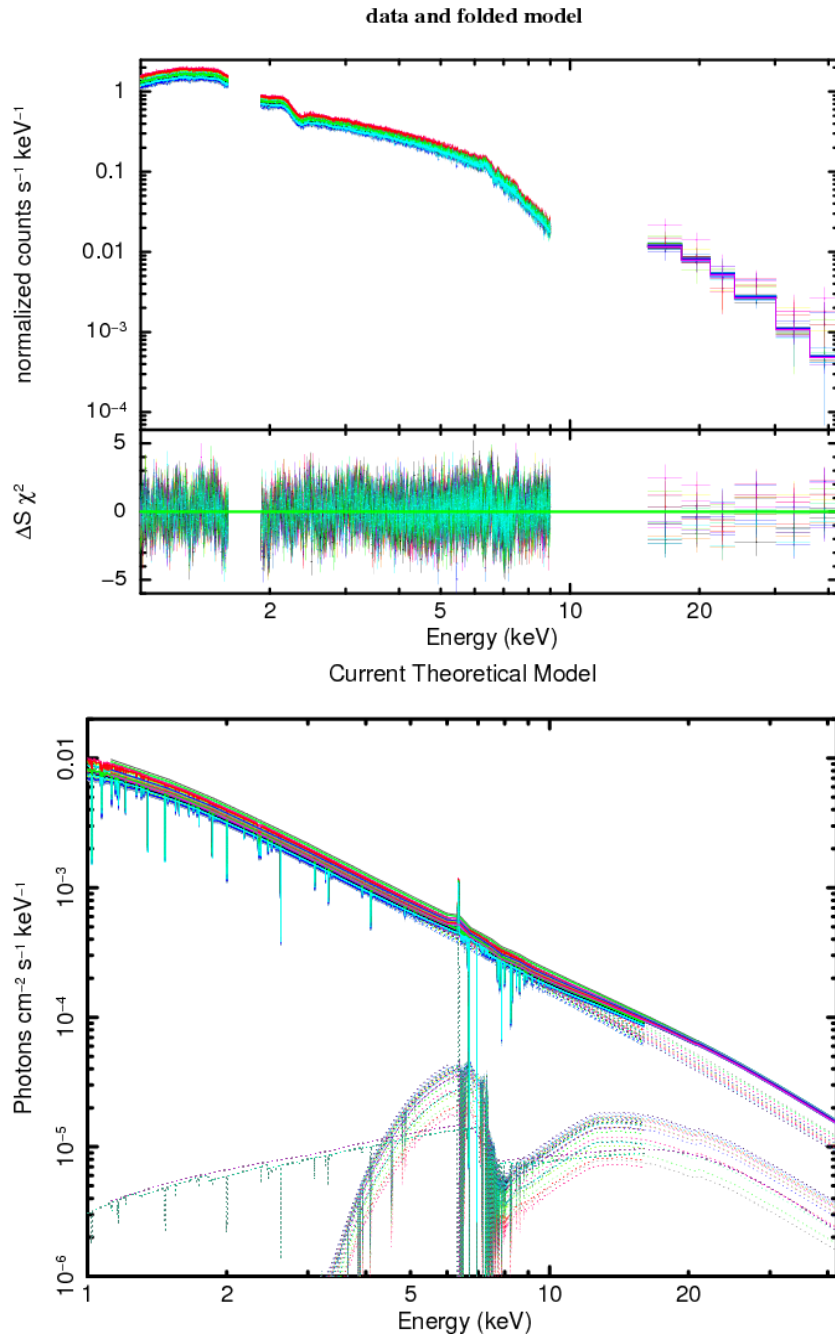


Figure 5.24: (Top) The fitting results with Model 2, for the bright/faint spectra made with Method 2 on timescales of 256 – 160,000 sec. (Bottom) The unfolded spectral model.

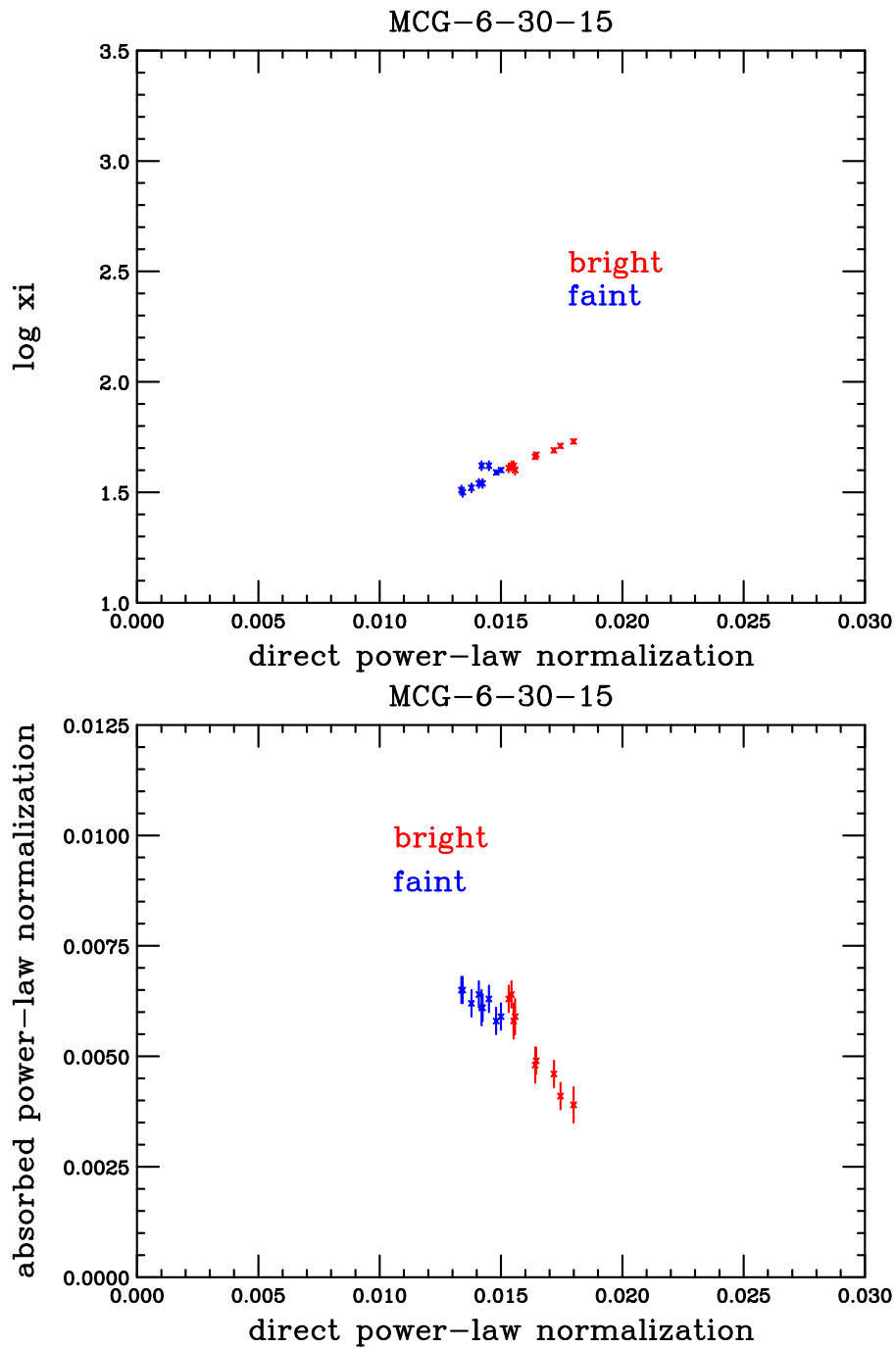


Figure 5.25: (Top) Relation between the direct power-law normalization and the ionization degree, made by applying Model 2 to the bright and faint spectra created with Method 2. (Bottom) Relation between the direct power-law normalization and the absorbed power-law normalization.

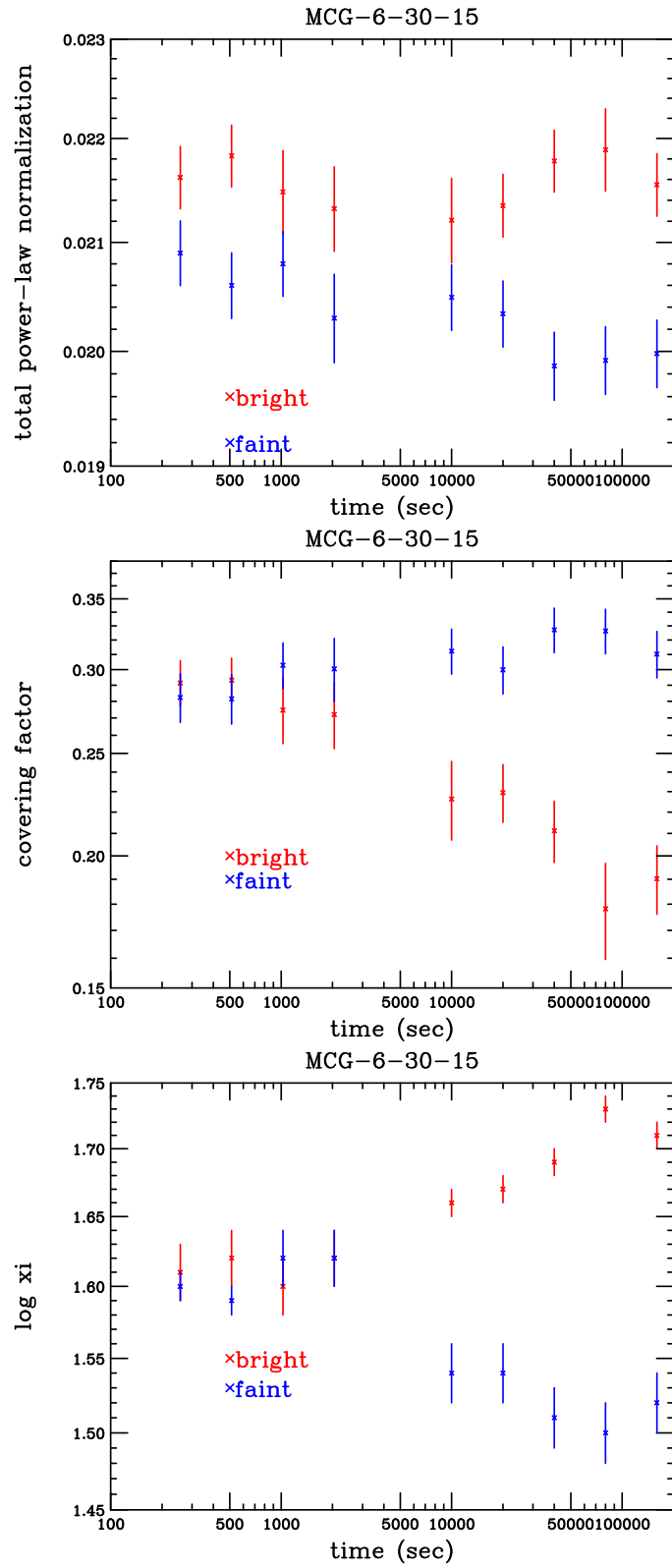


Figure 5.26: Relation between the spectral model parameters and variation timescales made by applying Model 2 to the bright and faint spectra created with Method 2. Total power-law normalization (Top), covering factor (Middle) and ionization degrees of the low-ionized warm absorber (Bottom).

5.18), and hardly affects the amount of spectral variation.

We try to fit the 18 spectra (bright and faint spectra for each of the nine timescales) simultaneously, with a minimum number of free parameters. The out disk reflection component is fixed at $\Omega/2\pi \sim 0.3$ as before. Photon indexes of the direct component and absorbed power-law component are linked. Consequently, we found the spectral variability is explained only variation of normalization of the direct power-law, ionization degree of the lower-ionized warm absorber, and normalization of the absorbed power-law component.

Figure 5.24 shows the simultaneous fitting result for the 18 bright/faint spectra. The best-fit parameters are shown in Table 5.9 for the 18 spectra. Note that only the three parameters are variable to describe the spectral variations.

We found some interesting correlations between the variable parameters. The top panel of Figure 5.25 shows a correlation between the direct power-law normalization and ionization degree of the low-ionized warm absorber, which is confirming the previous result already obtained with Model 1 (Figure 5.11). The bottom panel of Figure 5.25 shows a remarkable anti-relation between normalization of the direct power-law component and that of the absorbed power-law component. This anti-correlation corresponds to the fact obtained via Model 1 that the reflection component (with $\Omega/2\pi \approx 1$) was constant and the spectral variation was described by changes of only two parameters, normalization of the power-law component and ionization of the low-ionized warm absorber (section 5.4.2). In Model 2, we have three free parameters, but since there is a strong correlation between the direct power-law normalization and absorbed power-law normalization, there are effectively two independent parameters which describe the observed spectral variations.

We study variation timescales of the three variable spectral parameters. In top of Figure 5.26, we show timescale dependence of the variation of the total power-law (i.e., summation of the direct power-law normalization and absorbed power-law normalization). We see the total normalization is variable in all the timescales, and differences between the two states seem to have two peaks (or bottoms) at 512 sec and 80,000 sec. In the middle panel, we show timescale dependence of the “covering factor”, which is absorbed power-law normalization divided by the total power-law normalization. It is found that the covering factor for the bright and faint state is almost the same and constant up to 2,048 sec. Above 10,000 sec, the covering factor for the bright state and the faint state decreases and increases, respectively, and seems to have a peak (or bottom) at 80,000 sec. In the bottom of Figure 5.26, we show relation between the variation timescales and the ionization degrees of the low-ionized warm absorber, which indicates a very similar timescale dependence as the covering factor. Note that timescale dependences of the three parameters above 10,000 sec are very similar to each other.

5.7.2 Spectral fitting for the sliced spectra

We also apply Model 2 to the eight intensity sliced spectra made in section 5.3.2. Again, we only allow three spectral parameters to be variable, the direct power-law normalization, absorbed power-law normalization, and ionization degree of the low-ionized warm absorber. In Figure 5.27, we show the simultaneous fitting result of the eight spectra with Model 2, where the reduced chi-square is 1.01 ($\chi^2/\text{d.o.f} = 1145/1135$).

The top panel of Figure 5.28 shows relation between the direct power-law normalization and ionization degree. The bottom panel of Figure 5.28 shows relation between direct power-law normalization and partial absorbed power-law normalization. These correlations correspond to those found in Figure 5.25 for the bright and faint spectral analysis, while amplitudes of the parameter variation are larger for the intensity sliced spectra.

Then, we plot a two-dimensional fit-static contour plot of a steppar run. Figure 5.29 shows

Table 5.9: Results of spectral fitting of Suzaku in 1–40 keV with Model 2 for the “bright” and “faint” spectra extracted with Method 2.

state	128 sec		256 sec		512 sec		1024 sec	
	bright	faint	bright	faint	bright	faint	bright	faint
N_H (10^{21} cm $^{-2}$)				1.6 \pm 0.1				
N_H (10^{23} cm $^{-2}$)				2.4(fix)				
log ξ				3.40 \pm 0.01				
Line E (keV)				7.0(fix)				
sigma (keV)				0.01 (fix)				
norm (10^{-6})				-7.0 $^{+0.4}_{-0.5}$				
N_H (10^{21} cm $^{-2}$)				3.7(fix)				
log ξ	1.61 \pm 0.02	1.60 $^{+0.01}_{-0.02}$	1.62 \pm 0.02	1.59 $^{+0.01}_{-0.02}$	1.60 \pm 0.02	1.62 \pm 0.02	1.62 \pm 0.02	1.62 \pm 0.02
N_H (10^{24} cm $^{-2}$)				1.6(fix)				
log ξ				1.90 \pm 0.01				
Line E (keV)				6.35 (fix)				
sigma (keV)				0.01 (fix)				
norm (10^{-5})				1.37 \pm 0.05				
EW (eV)								
cutoffpl K (10^{-2})	1.532 \pm 0.004	1.500 \pm 0.004	1.543 \pm 0.004	1.480 \pm 0.004	1.558 \pm 0.004	1.450 $^{+0.003}_{-0.002}$	1.552 \pm 0.005	1.420 \pm 0.004
absorbed cutoffpl K (10^{-3})	6.3 $^{+0.4}_{-0.3}$	5.9 \pm 0.3	6.4 $^{+0.3}_{-0.4}$	5.8 \pm 0.3	5.9 \pm 0.4	6.3 $^{+0.4}_{-0.3}$	5.8 \pm 0.4	6.1 \pm 0.4
photon index				1.92 \pm 0.01				
E_{cut} (keV)				160 (fix)				
cosIncl				0.866 (fix)				
pexrav K (10^{-2})				cutoffpl K (256 sec bright) \times 0.3				
edge E (keV)				7.11 (fix)				
MaxTau				0.003 $^{+0.004}_{-0.002}$				
Line E (keV)				2.35 \pm 0.0				
sigma (keV)				0.01 (fix)				
norm (10^{-5})				-2.1 \pm 0.1				
reduced chi-square (d.o.f)				1.15 (19086)				

See the footnote of Table 5.1.

Table 5.9: (Continued)

binsize	5 ksec		10 ksec		20 ksec		40 ksec		80 ksec	
	bright	faint	bright	faint	bright	faint	bright	faint	bright	faint
N_H (10^{21} cm $^{-2}$)										
N_H (10^{23} cm $^{-2}$)										
log ξ										
Line E (keV)										
sigma (keV)										
norm (10^{-6})										
N_H (10^{21} cm $^{-2}$)										
log ξ										
N_H (10^{24} cm $^{-2}$)										
log ξ										
Line E (keV)										
sigma (keV)										
norm (10^{-5})										
EW (eV)										
cutoffpl K (10^{-2})	1.641±0.004	1.409±0.002	1.645 $^{+0.003}_{-0.005}$	1.424±0.003	1.718 $^{+0.004}_{-0.006}$	1.337±0.004	1.799±0.005	1.342±0.004	1.745±0.004	1.378±0.003
absorbed cutoffpl K (10^{-3})	4.8±0.4	6.4±0.3	4.9±0.3	6.1±0.3	4.6 $^{+0.4}_{-0.3}$	6.5±0.3	3.9±0.4	6.5±0.3	4.1 $^{+0.4}_{-0.3}$	6.2±0.3
photon index										
E_{cut} (keV)										
cosIncl										
pexrav K (10^{-2})										
edge E (keV)										
MaxTau										
Line E (keV)										
sigma (keV)										
norm (10^{-5})										
reduced chi-square (d.o.f)										

See the footnote of Table 5.1.

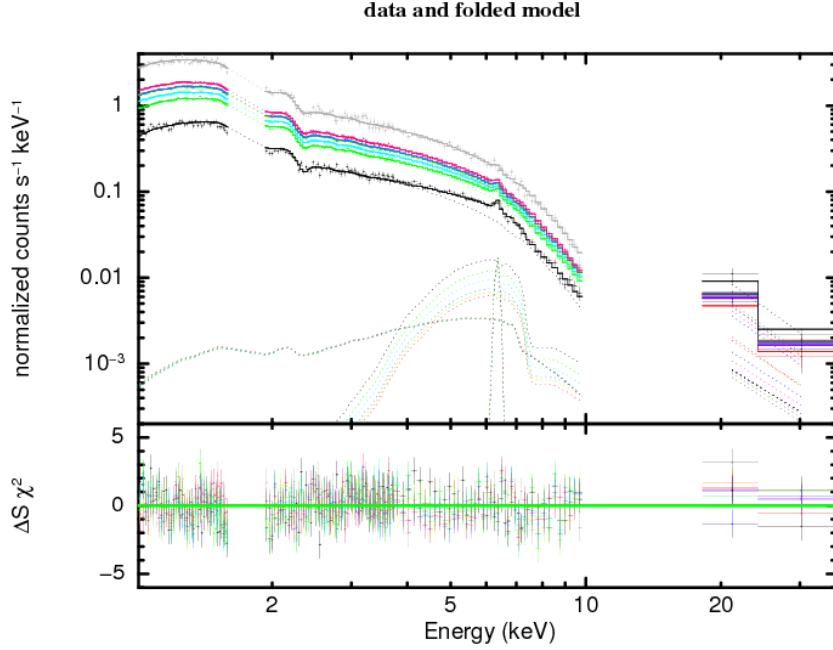


Figure 5.27: Spectral fit results with Model 2 for the intensity sliced spectra.

confidence contours between the direct power-law normalization (horizontal axis) and the absorbed power-law normalization (vertical axis).

5.7.3 Spectral fitting for every 20 ksec

Next, we create a time-sequence of the energy spectra from Suzaku data, and apply Model 2. We see that variation amplitude in 1–10 keV is dominant around 20–80 ksec in the top panel of Figure 5.22. So, we made energy spectra every 20 ksec, and investigate time variation of spectral parameters.

In Figure 5.30, we show the fitting result for the 20 ksec spectra with Model 2. Model fit is made for the three observation sequences separately (obsID:700007010, 700007020 and 700007030). For each sequence, all the spectra extracted every 20 ksec are fitted simultaneously, only varying the three model parameters, direct power-law normalization, absorption power-law normalization, and ionization state of the low-ionized warm absorber.

Figure 5.31 shows relation between the direct power-law normalization and ionization degree, and that between the direct power-law normalization and the absorbed power-law normalization. Although scattering of individual observations is more significant than in the cases of the bright/faint analysis (Figure 5.25) or the intensity-slice analysis (Figure 5.28), correlation or anti-correlation between these parameters are obvious.

Figure 5.32 shows time histories of the direct power-law normalization, the absorbed power-law normalization and ionization degree of the low-ionized warm absorber.

5.7.4 Spectral fitting for Chandra/HETGS data

Finally we fit the Chandra/HETGS spectra with Model 2. In Figure 5.33 and Table 5.10, we show the fitting result for the average spectrum. We also fit the bright/faint spectra (section 5.4.2) in the 1.0–7.5 keV band with Model 2 (Figure 5.34, Table 5.11). In stead of allowing

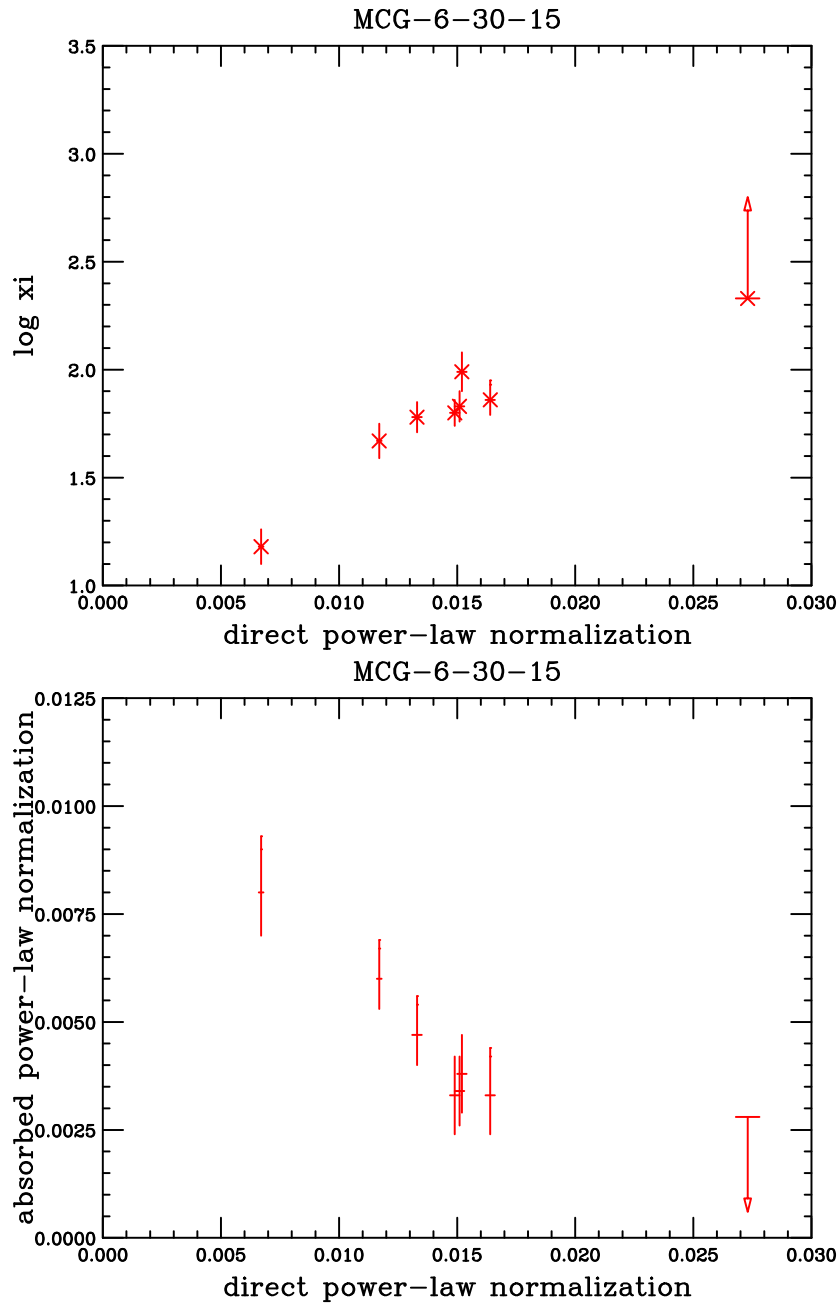


Figure 5.28: (Top) Relation between the direct power-law normalization and the ionization degree made by applying Model 2 to the intensity sliced spectra. (Bottom) Relation between the direct power-law normalization and absorbed power-law normalization.

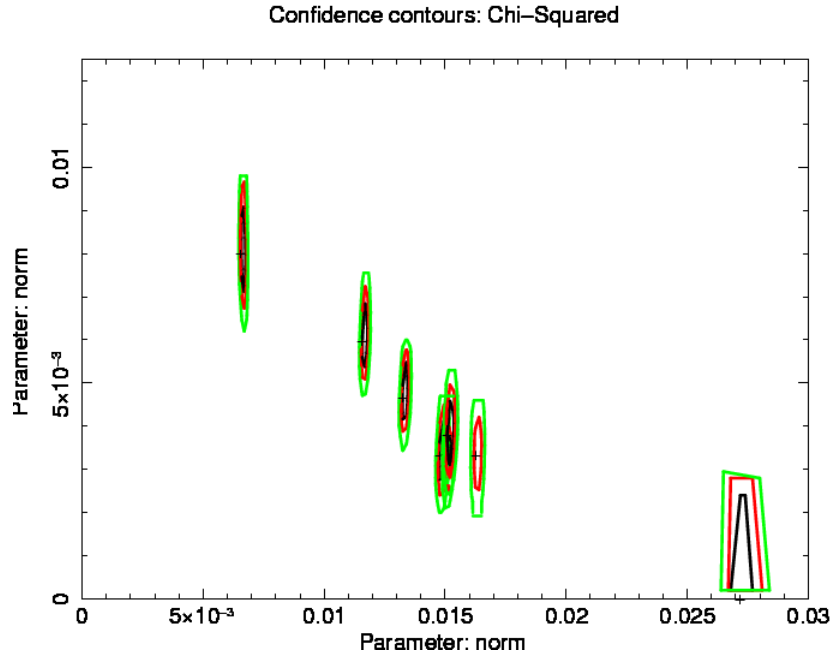


Figure 5.29: Confidence contours between the direct power-law normalization (horizontal axis) and the absorbed power-law normalization (vertical axis).

the normalization of the absorbed power-law component to be free, we fixed it to the total power-law normalization minus the direct power-law normalization. The fit is successful, indicating the anti-correlation between the direct power-law normalization and absorbed power-law normalization, which is consistent with the Suzaku results. In addition to the ionization degree of the low-ionized component, which is significantly variable as expected ($\log \xi = 1.95 \pm 0.04$ and 1.78 ± 0.04), ionization degree of the high-ionized warm absorber is made a free parameter, expecting to see any differences. However, these values are almost the same for bright and faint state ($\log \xi = 3.64 \pm 0.05$ and 3.62 ± 0.06). In summary, Chandra/HETGS spectral variation between the bright state and faint state is described by the change of only two spectral parameters, normalization of the direct component and ionization degree of the low-ionized warm absorber.

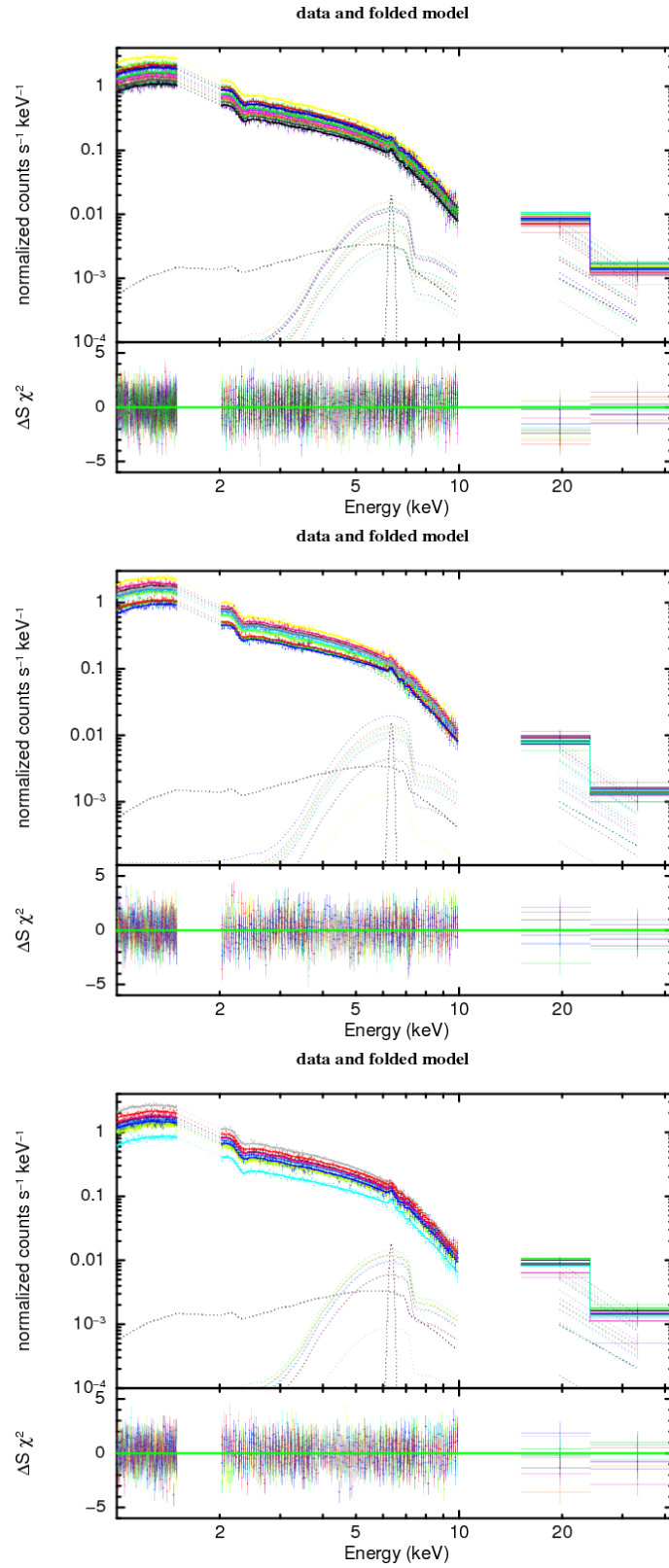


Figure 5.30: Spectral fit results with Model 2 for the spectra extracted for every 20 ksec (from top to bottom, obsID:700007010, 700007020 and 700007030). Reduced chi-square is 1.09 ($\chi^2/\text{d.o.f} = 3887/3577$), 1.07 ($\chi^2/\text{d.o.f} = 2253/2100$) and 1.13 ($\chi^2/\text{d.o.f} = 2365/2097$), respectively.

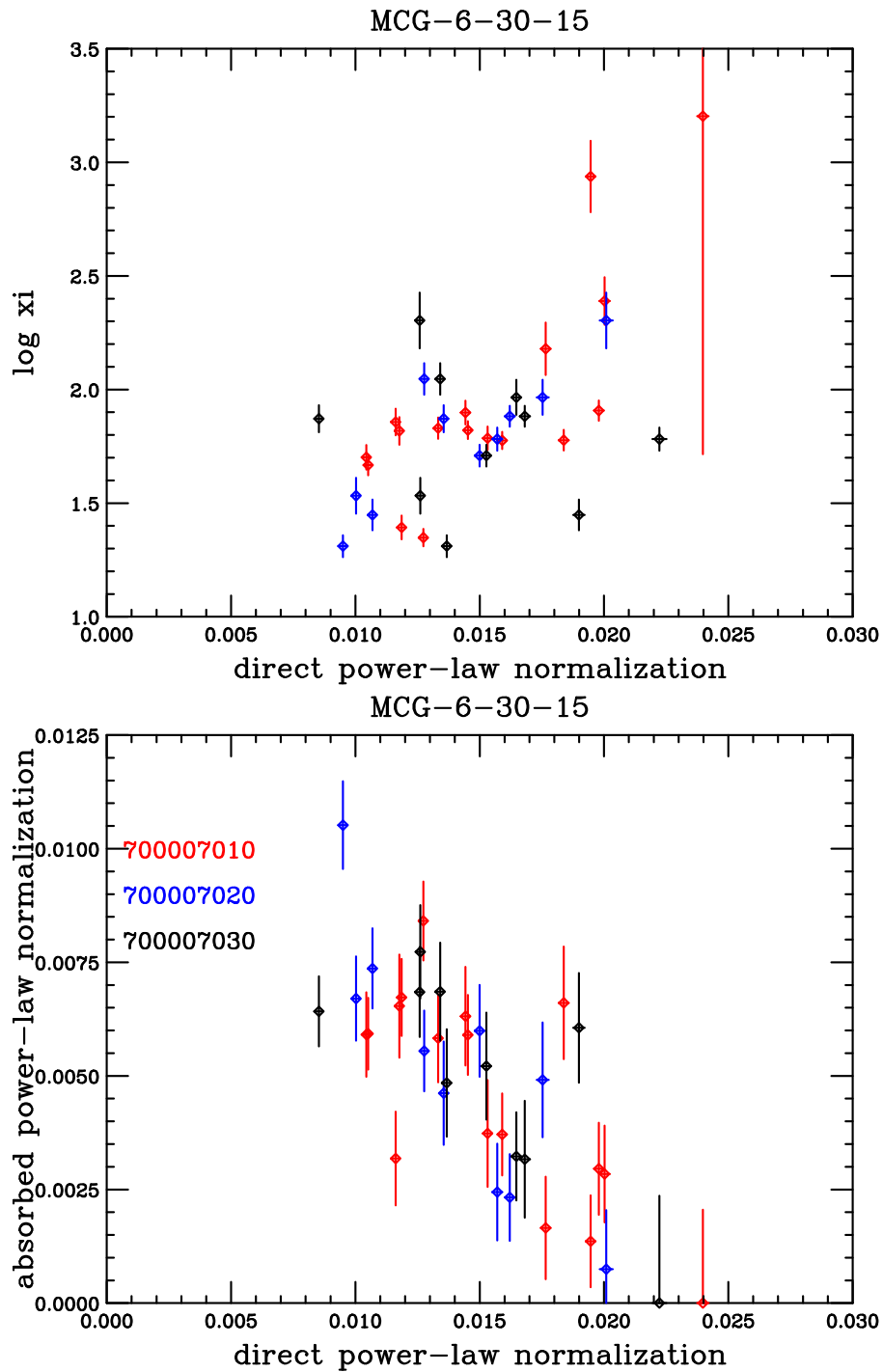


Figure 5.31: (Top) Relation between the direct power-law normalization and the ionization degree made from the 20 ksec spectra using Model 2. (Bottom) Relation between the direct power-law normalization and the absorbed power-law normalization.

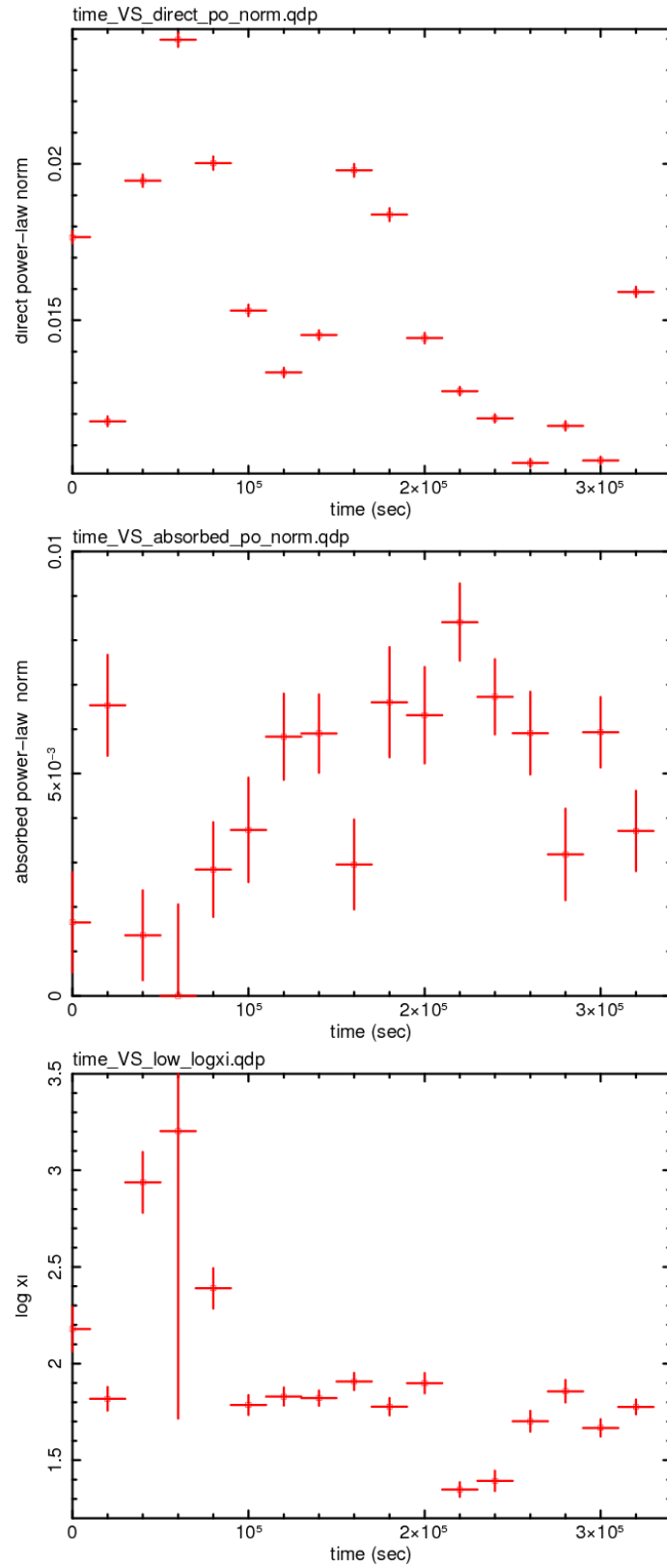


Figure 5.32: (Top) Relation between time and direct power-law normalization for the spectra made every 20 ksec from obsID:700007010. (Middle) Relation between time and absorbed power-law normalization. (Bottom) Relation between time and the ionization degree.

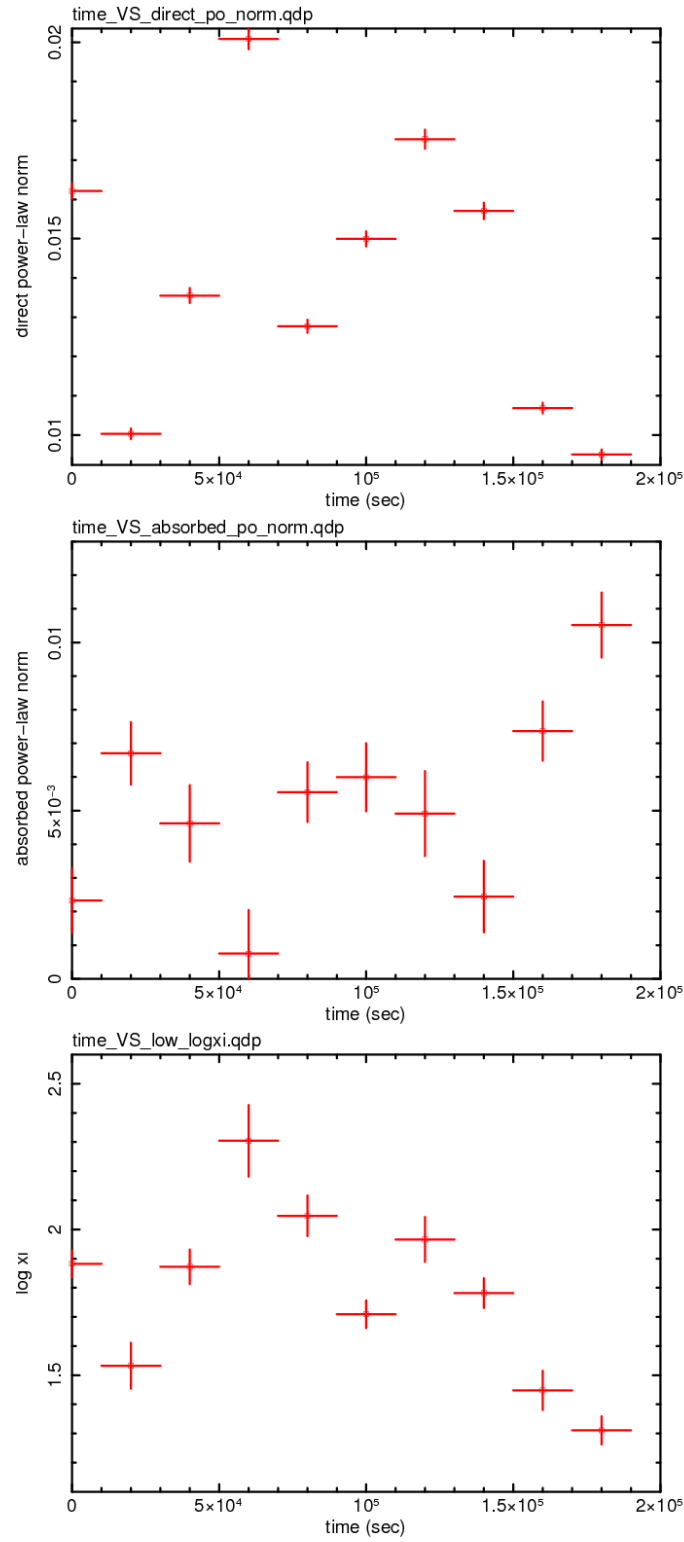


Figure 5.32: (Continued.) The same figure with previous one for obsID:700007020.

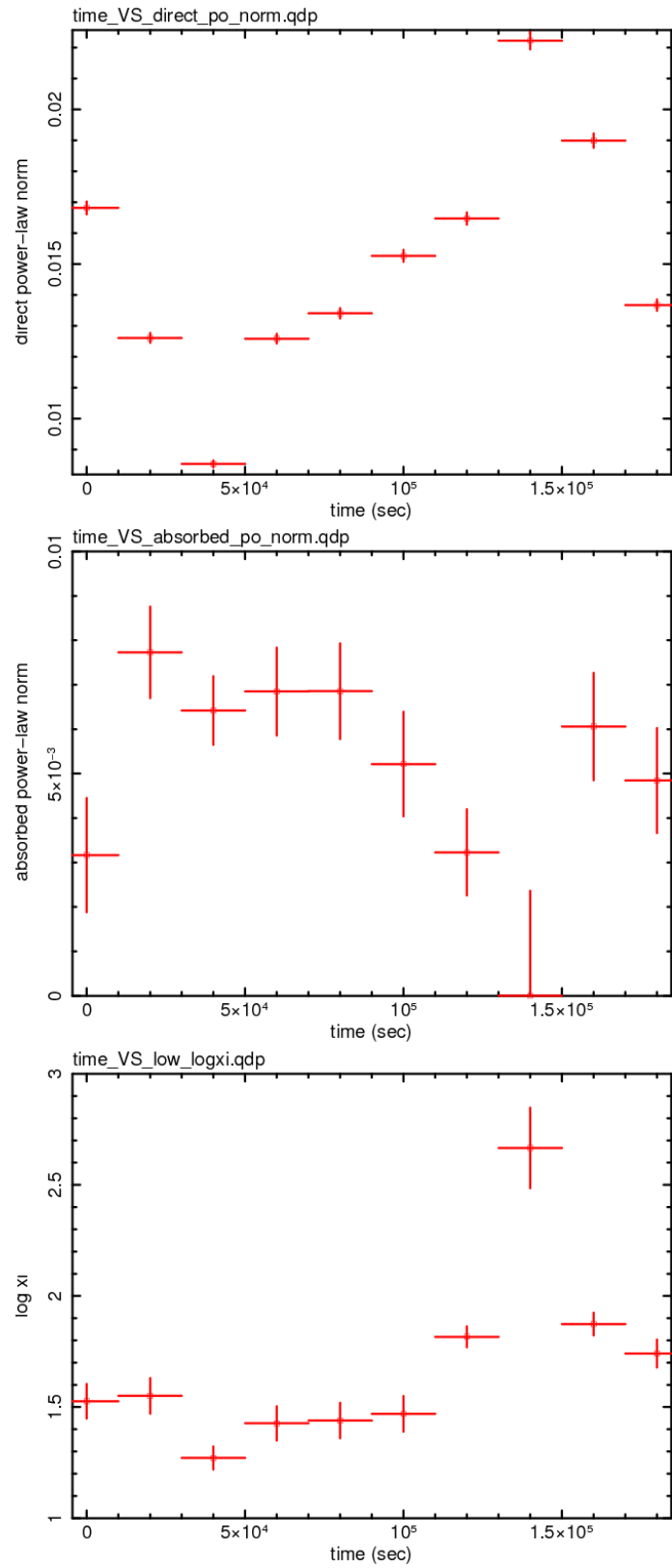


Figure 5.32: (Continued.) The same figure with previous one for obsID:700007030.

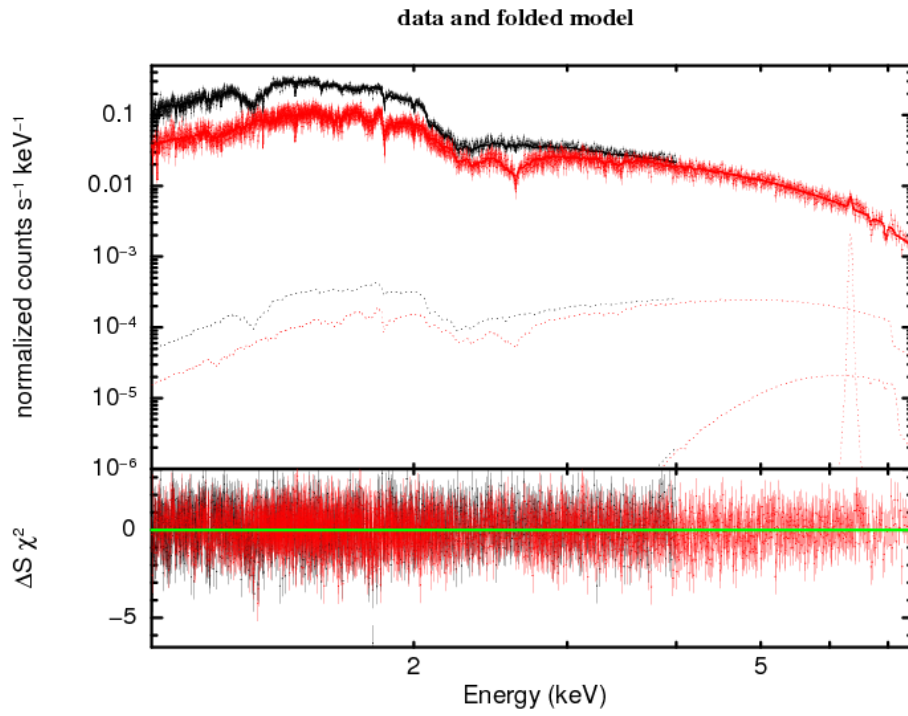


Figure 5.33: Spectral fit result for the time-averaged HETGS spectra with Model 2.

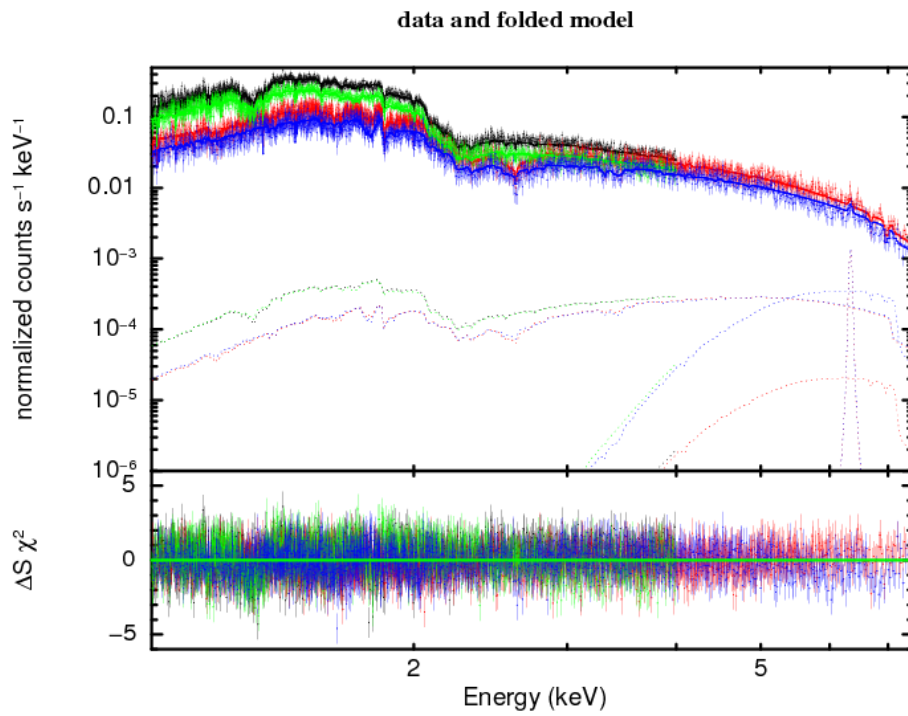


Figure 5.34: Spectral fit result for the bright/faint HETGS spectra with Model 2.

Table 5.10: Results of spectral fitting of Chandra/HETG in 1–7.5 keV with Model 2 for the average spectrum.

N_H (10^{21} cm $^{-2}$)	1.5(fixed)
N_H (10^{23} cm $^{-2}$)	2.4(fixed)
log ξ	3.64 \pm 0.04
redshift (10^{-3})	1.8 $^{+0.2}_{-0.5}$
Line E (keV)	6.98 $^{+0.03}_{-0.06}$
sigma (keV)	0.01(fix)
norm (10^{-6})	-5.0 $^{+3.9}_{-7.6}$
N_H (10^{21} cm $^{-2}$)	3.7(fixed)
log ξ	2.04 \pm 0.03
redshift (10^{-3})	7.4 \pm 0.1
N_H (10^{24} cm $^{-2}$)	1.6(fixed)
log ξ	1.57(fixed)
redshift (10^{-3})	1(fixed)
Line E (keV)	6.34 (fix)
sigma (keV)	0.018 (fix)
norm (10^{-5})	1.2 \pm 0.4
EW (eV)	25 \pm 8
direct cutoffpl K (10^{-2})	1.23 \pm 0.01
absorbed cutoffpl K (10^{-2})	<0.2
photon index	1.76 \pm 0.01
E_{cut} (keV)	160(fix)
cosIncl	0.866(fix)
pextrav K (10^{-2})	direct cutoffpl K \times 0.3
edge E (keV)	7.11 (fix)
MaxTau	0.13 $^{+0.10}_{-0.09}$
reduced chi-square (d.o.f)	0.92 (5099)

Table 5.11: Results of spectral fitting in 1–7.5 keV of Chandra/HETG with Model 2 for the intensity sliced spectra

	bright	faint
N_H (10^{21} cm $^{-2}$)		1.5 (fix)
N_H (10^{23} cm $^{-2}$)		2.4(fixed)
log ξ	3.64 \pm 0.05	3.62 \pm 0.06
redshift (10^{-3})		1.82 $^{+0.24}_{-0.29}$
N_H (10^{21} cm $^{-2}$)		3.7(fixed)
log ξ	1.95 \pm 0.04	1.78 \pm 0.04
redshift (10^{-3})		7.4 $^{+0.2}_{-0.1}$
N_H (10^{24} cm $^{-2}$)		1.6(fixed)
log ξ		1.57 (fix)
redshift (10^{-3})		1 (fix)
Line E (keV)		6.34(fix)
sigma (keV)		0.018 (fix)
norm (10^{-6})		7.8 \pm 4.3
EW (eV)	14 \pm 8	18 \pm 10
direct cutoffpl K (10^{-2})	1.47 \pm 0.01	1.05 \pm 0.01
absorbed cutoffpl K (10^{-2})	1.5 - direct cutoffpl K	1.5 - direct cutoffpl K
photon index		1.78 \pm 0.04
E_{cut} (keV)		160 (fix)
cosIncl		0.866 (fix)
pexrav K (10^{-2})	direct cutoffpl K (bright) \times 0.3	
reduced chi-square (d.o.f)		0.89 (7505)

Chapter 6

Discussion

We have analyzed Suzaku, RXTE, and Chandra data of MCG-6-30-15 in order to study its spectral variations. In this chapter, firstly we summarize important results obtained from the data analysis. Then we will interpret these results phenomenologically. Finally, we propose a physical picture to explain these observational facts.

6.1 Summary of the Results

First, we summarize spectral model independent results as follows:

1. We have studied spectral variations of MCG-6-30-15 in a model independent manner using Suzaku data, and found a clear correlation between the 6 – 10 keV flux and the spectral ratio of 0.5 – 3.0 keV/6.0 – 10 keV in the variation timescales between 5 ksec to 200 ksec. (Figure 5.2). A very similar correlation between the 6 - 10 keV flux and the spectral ratio of 2 – 4 keV / 6 – 10 keV is found in the RXTE data in the variation timescales between 2×10^6 sec and 2×10^7 sec (Figure 5.6).
2. We studied spectral variation amplitude of the source in various timescales comparing energy spectra extracted from the two adjacent time-bins at various lengths (Method 2). In this manner, we have studied spectral variation amplitude in the timescales between 256 and 160,000 sec. We found the variation amplitude below ~ 4 keV does not show energy dependence between the timescales of 256 and 2048 sec, while energy dependence gets more significant (greater variability for lower energies) for longer time scales (Figure 5.21).

The following results are model dependent:

1. We have introduced a spectral model to include a narrow and weak fluorescent iron emission line (equivalent width ~ 23 eV; Table 5.6), which is confirmed with Chandra HETG (Figure 5.16), the corresponding cold disk reflection with $\Omega/2\pi = 0.3$, a heavily absorbed component by an ionized matter, and two warm absorbers with different ionization states (Model 2; Table 5.7, Figure 5.17).
2. The ionized iron K-edge of the heavily absorbed component and the spectral curvature due to warm absorbers explain the seemingly broad “disk line” spectral feature. Even if we put an additional “disk line”, the fit hardly improves and its equivalent width is only 40 eV (Table 5.8, Figure 5.18).

3. The Suzaku and Chandra spectral variations are described by change of the three spectral parameters, normalization of the direct power-law component, that of the absorbed power-law component, and ionization degree of the low-ionized warm absorber (Figures 5.24, 5.27, 5.30 and 5.34). Variation of the ionization degree of the low-ionized warm absorber and invariability of that of the high-ionized warm absorber are confirmed by observations of absorption lines by Chandra/HETG (Figure 5.14, Tables 5.5 and 5.11).
4. We searched for correlations among three variable spectral parameters. We found the normalizations of the direct power-law component and the absorbed power-law component are anti-correlated, and the normalization of the direct power-law component and ionization degree of the low-ionized warm absorber are correlated (Figures 5.25, 5.28 and 5.31).
5. We have studied timescale dependency of the three variable spectral parameters (Figure 5.26). We see the total normalization (sum of the direct power-law normalization and the absorbed power-law normalization) is variable in all the timescales, and differences of those between the bright state and the faint state have two peaks (or bottoms) at 512 sec and 80,000 sec. Timescale dependence of the “covering factor”, which is absorbed power-law normalization divided by the total power-law normalization, is almost constant up to 2,048 sec. Above 10,000 sec, the covering factor for the bright state and the faint state decreases and increases, respectively, and seems to have a peak (or bottom) at 80,000 sec. The ionization degrees of the low-ionized warm absorber indicates a very similar timescale dependence as the covering factor. We found the timescale dependences of the three parameters above 10,000 sec are similar to each other.

6.2 On the relativistically broadened iron line emission

We have analyzed the time-average spectrum of MCG-6-30-15 adding the disk line model expected from a fast-rotating Kerr black hole (Laor 1991). We fitted the data with varying the inner disk radius, r_{in} of the disk line model, and found that the best-fit value $\approx 200 r_g$ and the equivalent-width 40 ± 20 eV. The lower limit of r_{in} is $9 r_g$ at 90 % confidence level (Figure 5.19). The extremely broadened iron emission line with a large equivalent width, which some authors claim to be emitted in the very vicinity of an extremely fast-rotating black hole (e.g., $r_{in} = 1.6 r_g$, Miniutti et al. 2007), is obviously inconsistent with our model. The primary reason that we do not require an extremely distorted disk line is that the newly introduced heavily absorbed component has an ionized edge feature which has a similar spectral shape to the disk line (Figure 5.17). In addition, the warm absorbers produce spectral curvatures below 4 keV without which the residual may look like a low-energy tail of the disk line. Therefore, the claim that MCG-6-30-15 harbors a Kerr BH with nearly extreme rotation, based on the observed iron line feature, is model dependent, and not robust.

6.3 Interpretation of the Observed Spectral Variability

6.3.1 Partial absorption model

If we introduce a heavily absorbed spectral component, the observed energy spectrum was fitted successfully (#2 in section 6.2), while spectral fitting alone may not distinguish an absorbed spectral component and a reflected spectrum by optically thick matter (Figure 2.5). If there is a disk reflection close to the central X-ray source, there should be some correlation between the direct component and the reflected component. On the other hand, if a relatively stable X-ray source is partially absorbed, the direct component and the absorbed component should

anti-correlate. In fact, this is the very fact we have discovered from the data (#4 in section 6.2). Therefore, in the following, we will take the “partial absorption model” to interpret the energy spectrum of MCG-6-30-15.

Also, we found variation of three spectral parameters are necessary and sufficient to describe the observed spectral variations (#4 in section 6.2); they are normalization of the direct power-law component (N_1), that of the absorbed component (N_2) and ionization degree of the low-ionized warm absorber (or the corresponding attenuation factor W_L). Instead, we may take the total normalization $N(= N_1 + N_2)$, partial covering factor $\alpha(= N_2/N)$ and W_L . If we take this model, observed spectral variability, $\delta F/F$, may be calculated from variations of the N, α and W_L , namely $\delta N/N, \delta \alpha/\alpha$ and $\delta W_L/W_L$ (Appendix B). Now, we pay attention to the spectral variation caused by change of the amount of partial absorption. The coefficient is given with Equation B.8. For the sake of the simplicity, we ignore the minor term to originate in the reflection from the outer-part. Then,

$$\frac{\delta F}{F} = \frac{(W_2 - W_L)\alpha}{(W_L(1 - \alpha) + W_2\alpha)N} \frac{\delta \alpha}{\alpha}, \quad (6.1)$$

where W_2 is the attenuation factor of the partially absorbed component. The value in the left-hand side is identified with the variability defined in Equation 5.1. The right-hand side value may be calculated using the best-fit parameters for the Suzaku average spectrum.

We compare the observed variation amplitude in 20 ksec and the calculated variation amplitude when only the covering fraction is varied (Fig 6.1). It is remarkable that the broad iron edge feature is explained well by this model. The remarkable invariability in the iron energy band, which has been known for years (section 2.3.2), is explained by this model. We suppose this is another evidence that the partial absorption is taking place in MCG-6-30-15.

In Figure 6.1, significant excess variation amplitude is seen below 3 keV. This is due to variation of the warm absorber, $\delta W_L/W_L$, which is more significant for lower energies.

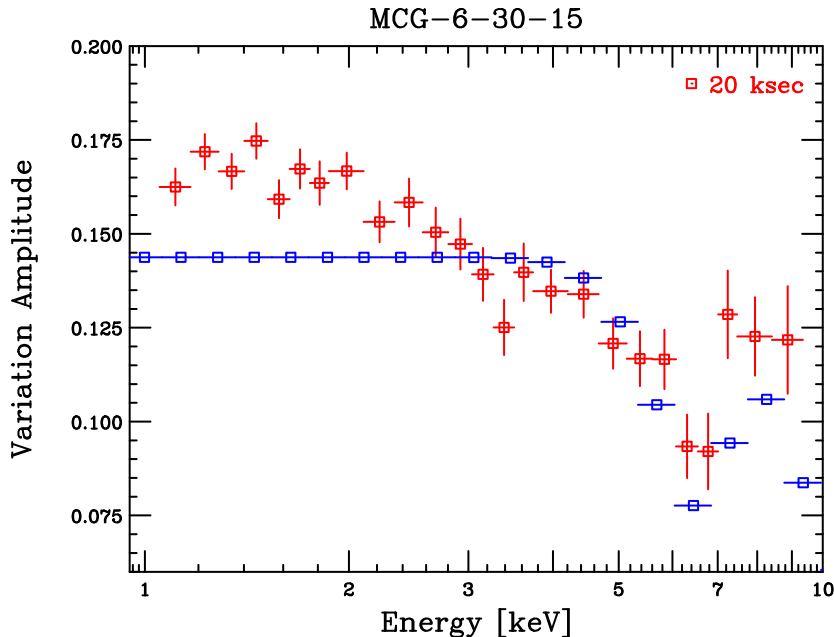


Figure 6.1: Comparison of the variation amplitude of 20 ksec in 1– 10 keV with a simulated variation amplitude when only the covering factor is variable.

6.3.2 Variation timescales of spectral parameters

We have studied variation timescales of the best-fit spectral parameters (#5 in section 6.2). Here, following equation 5.1, we define variation amplitude of the parameters as $|P_b - P_f| / ((P_b + P_f)/2)$, where P_b and P_f are best-fit parameters in the bright spectrum and faint spectrum, respectively, taken from Figure 5.26. In Figure 6.2 we show variation amplitude of the parameters for the total power-law normalization N , ionization degree of the low-ionized warm absorber $\log \xi$, and the covering factor α . We see there are short timescale variations at and below 2048 sec only in N , but not in $\log \xi$ and α . It is natural to assume that this variation is due to intrinsic variation of the X-ray source luminosity. For longer timescales, all the three parameters seem to have similar timescale dependences, such that they tend to increase from 1024 sec to 80,000 sec and decrease toward 160,000 sec. We can easily understand that $\log \xi$ is related to N due to photoionization. On the other hand, it is rather difficult to imagine origin of the relation between N and α , since they are considered to be independent.

6.3.3 Suggestion of the presence of completely blocked component

As mentioned, timescale dependence of the variability of the total normalization, N , is similar to that of the covering factor for timescales $\geq 10,000$ sec. There will be two possibilities to explain this. The first possibility is that the variability of N reflects variation of the original X-ray luminosity, and by some reason it affects variation of the partial absorbers surrounding the black hole. The second possibility is that there are undetectable X-rays being completely blocked by some “X-ray blockers”, where variability of N is caused by the X-ray blockers. Now, let’s define $N_T = N + N_3$, where N_T is the total amount of X-rays from the X-ray source, and N_3 is the fully blocked X-rays which do not reach us. Since $N = N_T - N_3$, N should have the same variation as N_3 , if N_T is rather invariable. Simply considering that the X-ray blocker and the partially absorber have the same origin, we can thus explain the correlation between the total X-ray flux N and the covering fraction.

We would suggest that the second possibility more naturally explains the observation. If there are such X-ray blockers, they must be Thomson thick and their column densities must be much greater than $1/\tau_T = 1.5 \times 10^{24} \text{ cm}^{-2}$, where τ_T is the Thomson cross-section. Coincidentally, observed column density of the partial warm absorber is $\sim 1.6 \times 10^{24} \text{ cm}^{-2}$ (Table 5.7). Presumably, the partial absorbers are fast moving clouds, and each cloud has density gradient such that the very thick central core ($N_H \gg 1/\tau_T$) completely blocks the X-rays, and the moderately thick surrounding layer ($N_H \approx 1/\tau_T$) is seen as the partial observer.

6.4 A Physical Picture

6.4.1 Spectral components

We have shown that the energy spectrum of MCG-6-30-15 at least has the following components (1) X-ray luminosity source, (2) mostly invariable high-ionized warm absorber, (3) variable low-ionized warm absorber, (4) ionized partial absorber whose column density is about reciprocal of the Thomson scattering cross section. In addition, the cold reflection continuum component with $\Omega/2\pi \sim 0.3$, narrow iron emission line, and interstellar absorber are necessary, which originate in the regions far from the black hole, but we do not mention these components in the following discussion.

Among the three variable components, (1), (3), and (4), the variation of (1) has two components; (1-1) the component whose variation has a typical timescale of ~ 1 ksec, and (1-2) the component whose variation has a typical timescale of ~ 100 ksec. As explained in section

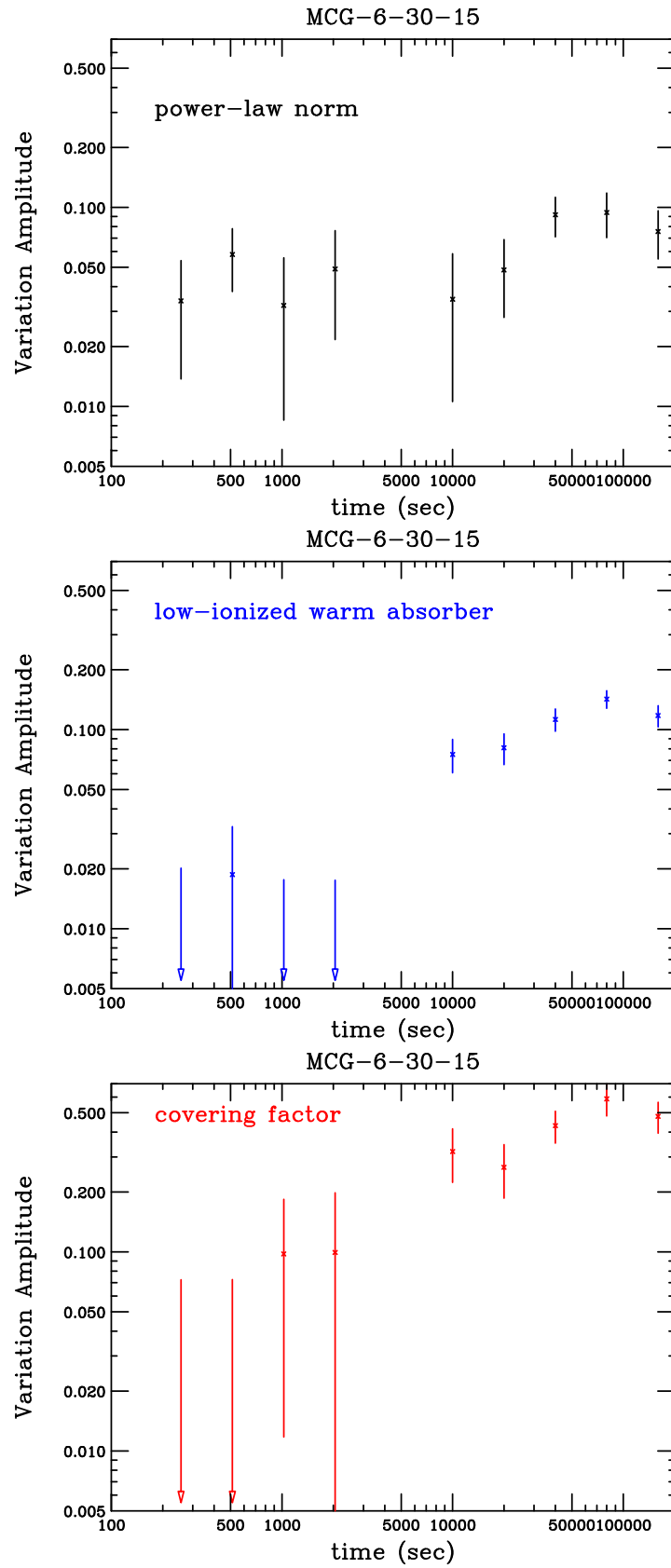


Figure 6.2: Variability in power-law normalization, covering factor, and ionization degree of low-ionized warm absorber, as functions of the timescales, calculated from Figure 5.26.

6.3.3, (1-2) share the typical variation timescale as (3) and (4), which is explained if we assume Thomson thick absorbers that completely block the incoming X-rays. Therefore, in addition to the four components above, we consider (5) the Thomson thick ($N_H \geq 10^{24.2} \text{ cm}^{-2}$) absorber, which varies simultaneously with (3) and (4). Hereafter, we discuss physical situation of the X-ray emitting and absorption regions around the black hole based on these five components.

In the following discussion, we assume the X-ray luminosity $L = 10^{43} \text{ erg/sec}$, others parameter values are taken from best-fit values for the Suzaku spectra.

6.4.2 Parameters of the absorbers

We consider physical conditions of the spectra components (2) to (5), namely four absorbers surrounding the central X-ray source. In the following, r is distance from the central X-ray source to the absorber, h is a typical thickness of the absorbing region along the line of sight, n is density. We provide suffixes to distinguish different absorbed components.

First, in general, we note the following relations hold:

$$\xi \equiv L/nr^2 = \frac{L}{N_H r} \left(\frac{h}{r} \right), \text{ where } N_H = nh, \quad (6.2)$$

$$r = \frac{L}{N_H \xi} \left(\frac{h}{r} \right) \leq \frac{L}{N_H \xi}. \quad (6.3)$$

1. Constant high-ionized warm absorber (suffix H)

From model fitting, $\xi_H \simeq 10^{3.4} \text{ erg cm/s}$, $N_{H,H} \simeq 10^{23.4} \text{ cm}^{-2}$. Hence,

$$r_H = \frac{L}{N_{H,H} \xi_H} \left(\frac{h_H}{r_H} \right) \leq \frac{L}{N_{H,H} \xi_H} \simeq 10^{16.2} \text{ cm}. \quad (6.4)$$

If we assume $h_H \sim r_H$, $r_H \sim 10^{16} \text{ cm}$ and $n_H \sim 10^7 \text{ cm}^{-3}$.

2. Variable low-ionized warm absorber (suffix L)

From model fitting, $\xi_L \simeq 10^{1.5} \text{ erg cm/s}$ and $N_{H,L} \simeq 10^{21.6} \text{ cm}^{-2}$. Hence,

$$r_L \simeq \frac{L}{N_{H,L} \xi_L} \left(\frac{h_L}{r_L} \right) \leq 10^{19.9} \text{ cm}. \quad (6.5)$$

If we assume $h_L \sim r_L$, $r_L \sim 10^{20} \text{ cm}$ and $n_L \sim 10^2 \text{ cm}^{-3}$.

3. Variable partial absorber (suffix 2)

From model fitting, $\xi_2 \simeq 10^{1.6} \text{ erg cm/s}$, $N_{H,2} \simeq 10^{24.2} \text{ cm}^{-2}$. Hence,

$$r_2 \simeq \frac{L}{N_{H,2} \xi_2} \left(\frac{h_2}{r_2} \right) \leq \frac{L}{N_{H,2} \xi_2} \simeq 10^{17.2} \text{ cm}. \quad (6.6)$$

Here, we may further constrain the parameters of the partial absorber from variation timescale of the partially absorbed component. The variation timescale, $\sim 10^5 \text{ sec}$, corresponds to the crossing time of the partial absorbers in front of the X-ray source. Assuming the size of the X-ray source and that of a partial absorber have similar dimensions, the crossing time is expressed as $\sim h_2/V$. Where V is the velocity of a partial absorber. Hence,

$$h_2 \sim V \times 10^5 \sim 10^{14} \left(\frac{V}{10^9 \text{ cm/s}} \right) \text{ cm}. \quad (6.7)$$

Where V is normalized to a typical velocity of the broad line region. Combining h_2 and $N_{H,2} \approx 10^{24} \text{ cm}^{-2}$, we estimate as follows:

$$n_2 \sim 10^{10} \text{ cm}^{-3}, \quad (6.8)$$

$$r_2 \simeq \left(\frac{L}{\xi_2 N_{H,2}} h \right)^{1/2} \simeq 10^{15.6} \text{ cm}. \quad (6.9)$$

4. Variable X-ray blocker

Variable partial absorbers are likely to be fast-moving blobs, which may naturally have central, cold Thomson thick cores ($N_H \geq 10^{24.2} \text{ cm}^{-2}$), which are completely opaque to incoming X-rays and considered to be the X-ray blocker.

Since we consider the partial absorber and the X-ray blocker as different parts of the same entity, we call them “low-ionized clouds”, hereafter.

6.4.3 Origin of the low-ionized warm absorber

Next, we discuss origin of the variable low-ionized warm absorber.

Constraint from thermal condition

In general, recombination timescale of the plasma is written as (e.g., Shull & Steenberg 1982),

$$t_r \simeq 200 (n/10^9 \text{ cm}^{-3})^{-1} (T/10^5 \text{ K})^{3/2} \text{ sec}. \quad (6.10)$$

Using Equation 6.5, order of n_L as estimated as 10^2 cm^{-3} assuming $h_L \sim r_L$, which gives too long a recombination time compared to the typical timescale of $\sim 10^5 \text{ sec}$. Instead, since we see instantaneous change of ξ_L corresponding to a flux change of $\sim 10^5 \text{ sec}$, we need

$$n_L \geq 10^{6.3} \left(\frac{T}{10^5 \text{ K}} \right)^{3/2} \text{ cm}^{-3}. \quad (6.11)$$

Since $N_{H,L} = n_L h_L \simeq 10^{21.6}$,

$$h_L \leq 10^{15.3} \left(\frac{T}{10^5 \text{ K}} \right)^{-3/2}. \quad (6.12)$$

Combining Equations 6.5 and 6.12, we obtain,

$$\frac{h_L}{r_L} \leq 10^{-1.7} \left(\frac{T}{10^5 \text{ K}} \right)^{-3/4}. \quad (6.13)$$

Namely, if we assume a “static shell” structure of the low-ionized warm absorber, we need to consider an extremely thin layer. Obviously, this is physically unlikely, and we need to consider other possibilities.

Examination of a transient model

Next, we consider a possibility that the low-ionized warm absorber is not static, but rather transient. We have seen that the high-ionized warm absorber is constant, within which the low-ionized warm absorber may appear temporarily behind the low-ionized clouds, such that X-ray flux from the central source is blocked and the ionization degree of the blocked region is lowered until the clouds are moving away. Let’s assume that the X-ray is turned off for a period

of t_{off} . When X-ray is turned on again, the low-ionized warm absorber goes back to the original on-state with a timescale of t_r .

In the case of $t_{rec} \gg t_{off}$, this outer region can not follow the X-ray off and on. Therefore, this outer region keeps the same ionization state, and we will not see variation of the ionization degree. Oppositely, in the case of $t_{rec} \ll t_{off}$, this outer region quickly switches between the two ionization states, and we will never see the situation that the region is low-ionized and the incoming X-ray is on, which we are looking for.

Consequently, only possibility of observing the transient low-ionized warm absorber behind the low-ionized clouds is when $t_{rec} \simeq t_{off}$. However, in the high-ionized warm absorber region, $\xi_H \simeq 10^{3.4}$ gives a temperature of $T \simeq 10^{6.5}$ K (Kallman & McCray 1982). Using Equation 6.10, we estimate

$$t_{r,H} \simeq 3.6 \times 10^6 (n/10^7 \text{ cm}^{-3})^{-1} (T/10^{6.5} \text{ K})^{3/2} \text{ sec.} \quad (6.14)$$

is much larger than $t_{off} \sim 10^5$ sec. Therefore, we conclude $t_{rec} \simeq t_{off}$ is not realized, and the transient low-ionized absorber region does not appear within the high-ionized warm absorber region.

Possibility of low-ionized cloud envelope

Next, we consider a possibility that the low-ionized warm absorber is associated with the low-ionized clouds. As estimated in Equation 6.8, density of the partial absorber in the low-ionized cloud is $n_2 \sim 10^{10} \text{ cm}^{-3}$, where the ionization degree is $\xi_2 \sim 10^{1.6}$ erg cm/s. On the other hand, density of the surrounding high-ionized warm absorber is estimated as $n_H \sim 10^7 \text{ cm}^{-3}$, with $\xi_H \sim 10^{3.4}$ erg cm/s. Therefore, it is expected that there is a medium-ionized and medium density layer in the boundary between the low-ionized clouds and the high-ionized warm absorber. We call this putative layer as the ‘‘cloud envelope’’. We assume its density, n_{ENV} , as an intermediate value, $\sim 10^9 \text{ cm}^{-3}$. Corresponding to $\xi_2 \sim 10^{1.5}$ erg cm/s and $n_2 \sim 10^{10} \text{ cm}^{-3}$, the average ξ_{ENV} of the cloud envelope is expected as $\sim 10^{2.5}$ erg cm/s since ξ is inverse proportion to the density.

Meanwhile, it is known that there takes place thermal instability in the range of $\xi = 10^2 \sim 10^3$ erg cm/s (Reynolds & Fabian 1995). Therefore, it is expected that ionization state of this region is fluctuated between ξ_H and ξ_2 , such that the cloud envelop continuously connects the variable partial absorber in the low-ionized clouds and the surrounding constant high-ionized warm absorber.

We estimate column density of the cloud envelope as $N_{H,ENV} \sim n_{ENV} h_2 \sim 10^{23} \text{ cm}^{-2}$. If $\sim 10\%$ of the field of view is occupied by the cloud envelop, observable column density is effectively $N_H \sim 10^{22} \text{ cm}^{-2}$, which agrees with the observed value, $N_{H,L} \simeq 10^{21.6} \text{ cm}^{-2}$.

This model can explain the following observational facts well:

- The low-ionized warm absorber has a similar variation timescale as the partial absorber and the X-ray blocker.
- In the Suzaku spectra made for every 20 ksec (Figure 5.31), when there are hardly low-ionized clouds in the field of view (=absorbed power-law normalization is null), $\log \xi_L$ is the largest at $\simeq 3.2$, which approach to the value of $\log \xi_H \simeq 3.4$.
- In the same figure, when there are many low-ionized clouds in the field of view (=absorbed power-law normalization is large), $\log \xi_L$ is in the range of ~ 1.3 to ~ 1.9 , close to the value of $\log \xi_2 \simeq 1.6$.

6.4.4 Absorbing cloud envelope model

Finally, we present a picture surrounding the X-ray source to explain the observations. We call our model “absorbing cloud envelope model”. Basic points of our model are the following:

1. Observed X-ray flux and spectral variability is primarily caused by the random motion of low-ionized clouds, size of each $h_2 \sim 10^{14}$ cm and a typical velocity of $V \sim 10^9$ cm/s (Equation 6.7), in front of the central X-ray source.
2. Central X-ray source is not fully blocked, but not fully exposed. Typically, 20–50 % of the source is covered, and ~ 20 –25 % of the flux is varied.

Assuming that amplitude of the observed flux variation is determined by statistical fluctuation of the number of clouds in the field of view, N_{cloud} , the average number of N_{cloud} is estimated as $\sim 4 - 5$ since $\Delta N_{cloud}/N_{cloud} \approx 0.5$.

Assuming the size of X-ray source $r_x \sim 10^{0.5} h_2 \sim 10^{14.5}$ cm, then, the covering fraction is $\sim N_{cloud}(\pi h_2^2/\pi r_x^2) \sim 10^{-1} N_{cloud} \approx 0.5$.

We note that the solid angle of the absorption region relative to the X-ray source should be much smaller than 4π , otherwise we will have to see strong fluorescent lines. The low-ionized clouds may be located near the equatorial plane of the accretion disk, assuming that origin of the low-ionized clouds be related to the accretion flow. We may be observing MCG-6-30-15 close to the edge-on angle.

We may calculate the average covering factor C_{ave} from intensity-sliced spectra as $C_{ave} = \sum_{i=1}^8 C_i \times t_i/T$, where t_i and T are exposure time for each spectrum and the total observation, respectively. We thus obtain $C_{ave} \sim 0.3$, which agrees with the estimate above. According to Blandford et al. (1991), the integrated covering factor is about 0.1 for the Broad Line Region (BLR). Our results suggest that the partial absorption takes place in the BLR, and the low-ionized clouds corresponds to the BLR blobs.

Typically, BLR blobs have a velocity of $V \sim 10^9$ cm/sec. If this is considered as a Kepler velocity, $r \sim 1000 r_s$, where r_s is the Schwarzschild radius¹. If an absorber with $N_H \sim 10^{24}$ cm⁻² covers the power-law component completely ($\Omega \sim 4\pi$), equivalent width of the iron line to the scattering (reflection) component is ~ 1 keV. Considering $C_{ave} \sim 0.3$ and ratio of the direct component to the reflection continuum, 10 to 1, the expected iron line equivalent width is ~ 30 eV. It is thought that the accretion disk covers the lower-half of the line emission region. Hence, the expected line equivalent width is $15 \approx 30$ eV. As mentioned in subsection 5.5.2, we fit the spectrum with Laor’s disk line model, where the best-fit inner radius and the equivalent width of the disk line are $\approx 200 r_g$ and 40 ± 20 eV, respectively (Table 5.8). These mildly broadened, weak line parameters are not inconsistent with those expected from the BLR.

Identifying this with $r_2 \sim 10^{15.6}$ (Equation 6.9), the central black hole mass of MCG-6-30-15 is $\sim 10^7 M_\odot$. If M_{BH} is $\sim 10^7 M_\odot$, size of the central X-ray source ($r_x \sim 10^{14.5}$ cm) corresponds to $\sim 10^2 r_s$. Central X-ray source is variable on a timescale of ~ 1 ksec from variability analysis, which may be compared with the free fall time, as $1 \text{ ksec} > r/\sqrt{\frac{GM}{r}}$. Then, we obtain $r < 10 r_s$.

Figure 6.3 gives a schematic view of the absorption cloud envelop model for the emission/absorption structure of MCG-6-30-15. There is the blocker in the core of the low-ionized cloud which blocks the incoming X-rays completely. The partial absorber surrounds the core, and still outer cloud envelop corresponds to the low-ionized warm absorber. The size of low-ionized clouds is $\sim 10^{14}$ cm.

¹Using $r_s = 2GM/c^2$ and $V = \sqrt{GM/r}$, we obtain $r = (c^2/2V^2)r_s$. Since $V \sim 10^9$ cm/sec, $r \sim 10^3 r_s$.

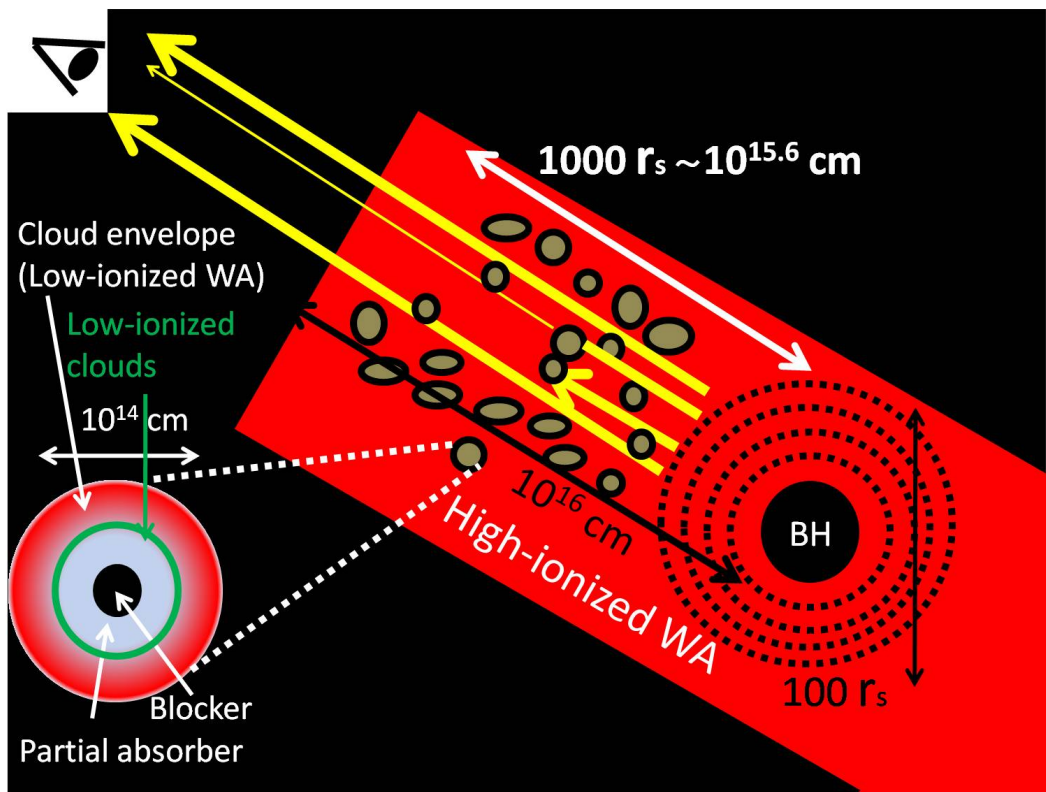


Figure 6.3: A schematic explanation of the absorbing cloud envelop model for MCG-6-30-15 and structure of the low-ionized cloud and the cloud envelope.

Chapter 7

Conclusion

We have analyzed Suzaku, RXTE, and Chandra data of MCG-6-30-15 in order to study its spectral variation and to construct a physical model to explain that. Our main conclusions are summarized below:

1. We have found a clear correlation between the 6 – 10 keV flux and the spectral ratio of 0.5 – 3.0 keV / 6.0 – 10 keV (or 2 – 4 keV / 6.0 – 10 keV) for over 14 years in the Suzaku and RXTE data. Also, using Chandra HETG data, we have found that Mg and Si absorption line equivalent widths varied with X-ray intensities. Both the continuum spectral variation and change of the absorption line equivalent widths are explained by change of the ionization degree of a photoionized warm absorber ($\log \xi = 1.2 \sim 3$, $N_H \sim 3.7 \times 10^{21} \text{ cm}^{-2}$) responding to the incoming flux change.
2. We have shown that the observed energy spectra and spectral variation can be explained by such a spectral model that includes a narrow and weak fluorescent iron emission line (EW ~ 20 eV), a cold disk reflection with $\Omega/2\pi = 0.3$ responsible for the narrow emission line, a direct power-law component, a heavily absorbed power-law component by an ionized matter with the same photon-index, and two warm absorbers with different ionization states. The ionized iron K-edge of the heavily absorbed component and spectral curvature due to the warm absorbers can explain most of the seemingly broad “disk line” spectral feature.
3. The observed spectral variations can be described by change of only the three spectral parameters, normalization of the direct power-law component, that of the heavily absorbed power-law component, and ionization degree of the low-ionized warm absorber. We have found that normalizations of the direct power-law component and the heavily absorbed power-law component are strongly anti-correlated, and that normalization of the direct power-law component and ionization degree of the low-ionized warm absorber are correlated.
4. In order to explain the observed anti-correlation and correlation between the spectral parameters, we propose an “absorbing cloud envelope model” that X-ray spectral variation of MCG-6-30-15 is primarily caused by partial absorption by numerous clouds having internal structures with different ionization degrees, which are on the line of sight of an extended X-ray source.
5. We have shown that general relativistic interpretation of the seemingly broad iron emission line feature in MCG-6-30-15 is not observationally established. Therefore, the claim that

MCG-6-30-15 is a Kerr BH with nearly extreme rotation (e.g., Miniutti et al. 2007), based on the observed iron line broadening, is not robust.

Appendix A

Spectral Models

In this appendix, we summarize the spectral models we used for spectral fitting in this thesis.

phabs

A photo electric absorption using cross-sections set by the `xsect` command. The relative abundances are set by the `abund` command.

$$M(E) = \exp(-par1\sigma(E)) \quad (\text{A.1})$$

Where, $\sigma(E)$ is the photo-electric cross-section (Not including Thomson scattering).

- `par1` is equivalent hydrogen column (in units of 10^{22} atoms/cm²)

cutoff power-law

A power-law with high energy exponential cutoff.

$$A(E) = K(E/1keV)^{-par1} \exp(-E/par2) \quad (\text{A.2})$$

where, `par1` is a power-law photon index, `par2` is e-folding energy of exponential cutoff (in keV), `K` is photons/s/cm²/keV at 1 keV.

pextrav

Exponentially cutoff power-law spectrum reflected from neutral material (Magdziarz & Zdziarski 1995). The output spectrum is the sum of the cutoff power-law and the reflection component. The reflection component alone can be obtained for `rel_refl` < 0. Then the actual reflection normalization is `|rel_refl|`. The metal and iron abundance are variable with respect to those defined by the command “`abund`”. The opacities are from Balucinska & McCammon (1994). H and He are assumed to be fully ionized.

- `par1` is γ , power-law photon index.
- `par2` is E_{cut} , cutoff energy in keV (if E_{cut} is 0, there is no cutoff).
- `par3` is `rel_refl`, scaling factor for reflection; `rel_refl` is 1 for isotropic source above the disk.
- `par4` is redshift.
- `par5` is abundance of elements heavier than He relative to that defined by “`abund`”.
- `par6` is iron abundance relative to that defined by “`abund`”.

- `par7` is cosine of the disk inclination angle.
- `K` is photon flux at 1 keV (photons/s/cm²/keV) of the power-law component in the observed frame.

gaussian

A simple gaussian line profile. If the width is ≤ 0 , then it is treated as a delta function.

$$A(E) = K \frac{1}{\sqrt{2\pi}\sigma} \exp\left(-\frac{(E - E_{line})^2}{2\sigma^2}\right) \quad (\text{A.3})$$

- E_{line} is line energy in keV.
- σ is line width in keV.
- `K` is total photons/s/cm² in the line.

Laor's disk line model

Line emission from accretion disk around a fast-rotating black hole (Laor 1991).

- Line energy in keV
- Power-law dependency of the emissivity on the disk radius R (scales as R^{-par2}).
- Inner disk radius (units of GM/c^2).
- Outer disk radius (units of GM/c^2).
- Disk inclination (degrees).
- Line flux in photons/cm²/s.

mtable

A multiplicative table model. The file name to be used should be given immediately after `mtable` in the model command. For example,

```
XSPEC> model mtable {miyakawa_model.fits} ...
```

uses `miyakawa_model.fits` as the input for the model.

XSTAR table model

XSTAR is a command-driven computer program for calculating physical conditions and emission spectra of photoionized gases. There are critical parameters.

- hydrogen column density in cm⁻². The range is $10^{20} - 10^{25}$ cm⁻².
- logarithmic of the ionization parameter, `rlogxi`. The range is 0.1 – 5.
- Redshift of the warm absorber.

Appendix B

Decomposition of the Variable Spectral Components

In this appendix, we show that variabilities of the spectral components composing the total spectrum can be, in principle, calculated from energy dependence of the observed variability, even without spectral fitting, making use of energy dependence of each spectral component.

As mentioned, we adopt the following partial absorption model:

$$F = W_H \{W_L(N_1 + W_2N_2)P + RN_RP + I_N\} \quad (\text{B.1})$$

Where P is the power-law function, W_H , W_L and W_2 are attenuation factors corresponding to the high-ionized warm absorber, low-ionized warm absorber, and partial absorber, respectively. N_1 and N_2 are direct power-law normalization and the absorbed power-law normalization, respectively. N_R and I_N are normalization of reflection component and normalization of narrow iron line, respectively. R is the reflection fraction. We omit the component of interstellar absorption which is not variable.

We could explain the observed spectral variation in various timescales with sole variations of N_1 , W_L , and N_2 , where N_1 and N_2 are significantly anti-correlated. This suggests that X-rays from the central source are partially absorbed, such that N_2 corresponds to the absorbed part and N_1 to the unabsorbed part. Consequently, we may introduce the “total normalization” N and the “covering fraction” α , so that $N_1 = (1 - \alpha)N$ and $N_2 = \alpha N$. Then Equation B.1, may be written as,

$$F = W_H \{W_L(1 - \alpha + W_2\alpha)NP + RN_RP + I_N\}. \quad (\text{B.2})$$

Where, W_2 drops zero rapidly in the vicinity of $\simeq 4$ keV, below which effect of W_L becomes significant. Also, W_H is invariable and I_N is so tiny that they hardly affect the spectral variabilities. Therefore, considering the spectral variability, we may consider the following function;

$$F = (W_L(1 - \alpha) + W_2\alpha)NP + RN_RP \quad (\text{B.3})$$

Note that the variable parameters are only N , α and W_L . Now, we calculate the variability from Equation B.3.

$$\delta F = (\delta W_L(1 - \alpha) - W_L\delta\alpha + W_2\delta\alpha)NP + (W_L(1 - \alpha) + W_2\alpha)P\delta N, \quad (\text{B.4})$$

so that we obtain,

$$\left(\frac{\delta F}{F}\right)^2 = \frac{((\delta W_L(1 - \alpha) - W_L\delta\alpha + W_2\delta\alpha)N + (W_L(1 - \alpha) + W_2\alpha)\delta N)^2}{((W_L(1 - \alpha) + W_2\alpha)N + RN_R)^2}. \quad (\text{B.5})$$

We may assume that W_L and N are independent, so are N and α . Hence, $\overline{\delta W_L \delta N} \sim 0$, $\overline{\delta \alpha \delta N} \sim 0$. Therefore,

$$\left(\frac{\delta F}{F}\right)^2 = A_{W-W} \left(\frac{\delta W_L}{W_L}\right)^2 + A_{\alpha-\alpha} \left(\frac{\delta \alpha}{\alpha}\right)^2 + A_{N-N} \left(\frac{\delta N}{N}\right)^2 + 2A_{w-\alpha} \left(\frac{\delta W_L}{W_L}\right) \left(\frac{\delta \alpha}{\alpha}\right). \quad (\text{B.6})$$

Where,

$$A_{w-w} = \frac{(1-\alpha)^2 W_L^2 N^2}{((W_L(1-\alpha) + W_2\alpha)N + RN_R)^2} \quad (\text{B.7})$$

$$A_{\alpha-\alpha} = \frac{(W_2 - W_L)^2 \alpha^2}{((W_L(1-\alpha) + W_2\alpha)N + RN_R)^2} \quad (\text{B.8})$$

$$A_{N-N} = \frac{(W_L(1-\alpha) + W_2\alpha)^2}{((W_L(1-\alpha) + W_2\alpha)N + RN_R)^2}. \quad (\text{B.9})$$

$$A_{w-\alpha} = \frac{(1-\alpha)(W_2 - W_L)\alpha W_L}{((W_L(1-\alpha) + W_2\alpha)N + RN_R)^2} \quad (\text{B.10})$$

Now, we investigate energy dependency of the variability of each parameter. First, variation of W_L hardly affects spectral changes above $\simeq 3$ keV. That is, $\delta W_L \simeq 0$ for $E \geq 3$ keV. As for $E > 10$ keV, $W_L \sim 1$, $W_2 \sim 1$, $R \sim 1$ because X-rays are hardly absorbed. In addition, W_2 and R are effectively 0 for $E \leq 4$ keV. Considering these properties, variabilities in each energy band may be written as follows;

For $E > 10$ keV,

$$\left(\frac{\delta F}{F}\right)_{(E>10\text{keV})}^2 = \frac{1}{\left(1 + \frac{N_R}{N}\right)^2} \left(\frac{\delta N}{N}\right)^2 \quad (\text{B.11})$$

For $3 \text{ keV} < E < 10 \text{ keV}$,

$$\left(\frac{\delta F}{F}\right)_{(3\text{keV}<E<10\text{keV})}^2 = A_{\alpha-\alpha} \left(\frac{\delta \alpha}{\alpha}\right)^2 + A_{N-N} \left(\frac{\delta N}{N}\right)^2 \quad (\text{B.12})$$

Especially for $3 \text{ keV} < E < 4 \text{ keV}$, $W_2 \simeq 0$ and $R \simeq 0$, so that,

$$\left(\frac{\delta F}{F}\right)_{(3\text{keV}<E<4\text{keV})}^2 = \frac{\alpha^2}{(1-\alpha)^2} \left(\frac{\delta \alpha}{\alpha}\right)^2 + \left(\frac{\delta N}{N}\right)^2 \quad (\text{B.13})$$

For $E < 3$ keV,

$$\left(\frac{\delta F}{F}\right)_{(E<3\text{keV})}^2 = \left(\frac{\delta W_L}{W_L}\right)^2 - 2\frac{\alpha}{1-\alpha} \left(\frac{\delta W_L}{W_L}\right) \left(\frac{\delta \alpha}{\alpha}\right) + \frac{\alpha^2}{(1-\alpha)^2} \left(\frac{\delta \alpha}{\alpha}\right)^2 + \left(\frac{\delta N}{N}\right)^2 \quad (\text{B.14})$$

Consequently,

$$\left(\frac{\delta N}{N}\right)^2 = \left(1 + \frac{N_R}{N}\right)^2 \left(\frac{\delta F}{F}\right)_{(E>10\text{keV})}^2, \quad (\text{B.15})$$

$$\frac{\alpha^2}{(1-\alpha)^2} \left(\frac{\delta \alpha}{\alpha}\right)^2 = \left(\frac{\delta F}{F}\right)_{(3\text{keV}<E<4\text{keV})}^2 - \left(1 + \frac{N_R}{N}\right)^2 \left(\frac{\delta F}{F}\right)_{(E>10\text{keV})}^2, \quad (\text{B.16})$$

$$\left(\frac{\delta W_L}{W_L}\right)^2 - 2\frac{\alpha}{1-\alpha} \left(\frac{\delta W_L}{W_L}\right) \left(\frac{\delta \alpha}{\alpha}\right) = \left(\frac{\delta F}{F}\right)_{(E<3\text{keV})}^2 - \left(\frac{\delta F}{F}\right)_{(3\text{keV}<E<4\text{keV})}^2. \quad (\text{B.17})$$

Hence, we may obtain variability of each spectral parameter (N, α, W_L) using the observed variability in $E > 10$ keV, $3 \text{ keV} < E < 4 \text{ keV}$ and $E < 3$ keV, from Equations B.15–B.17.

Appendix C

Robustness of the Spectral Variability Study with Method 2

In Section 5.6, we have made “bright” and “faint” spectra from two adjacent timebins, where time-bin widths are variable, and averaged all the bright and faint spectra respectively, to make a single bright spectrum and a faint spectrum for a given time interval. In this method, given photons may be counted either in the bright spectrum or faint spectrum, depending on rather arbitrary boundaries between the bright and faint intervals.

To check the robustness of Method 2 in order to study spectral variation, we repeated the same analysis in Section 5.6 by shifting one time-bin from the original binning. We chose 5,000, 10,000, 20,000, 40,000 sec, and 80,000 sec for the period T . As for 80,000 sec, the number of time-bins is only two for ID700007020 and ID700007030. Namely, we could not shift the time-bin. Hence, we used only ID 700007010 for 80,000 sec, which has 2 bins.

Figure C.1 shows the spectral ratios of the bright and faint spectra in case of shifting one time-bin to the original spectra for various timescales. As for 5,000 – 40,000 sec, the ratio is almost constant between 1–24 keV. Thus, choice of the bright-faint period boundaries hardly affects the study of spectral variation. There is difference at a confidence level of $\sim 1 \sigma$ between 24–42 keV. When T is 80,000 sec, the ratios of the bright and faint spectra are ≈ 0.88 – 0.96 and ≈ 0.98 – 1.06 , respectively. In terms of the variation amplitude, the value is affected by $\approx 10 \%$. This is the current limit of studying spectral variation in Method 2.

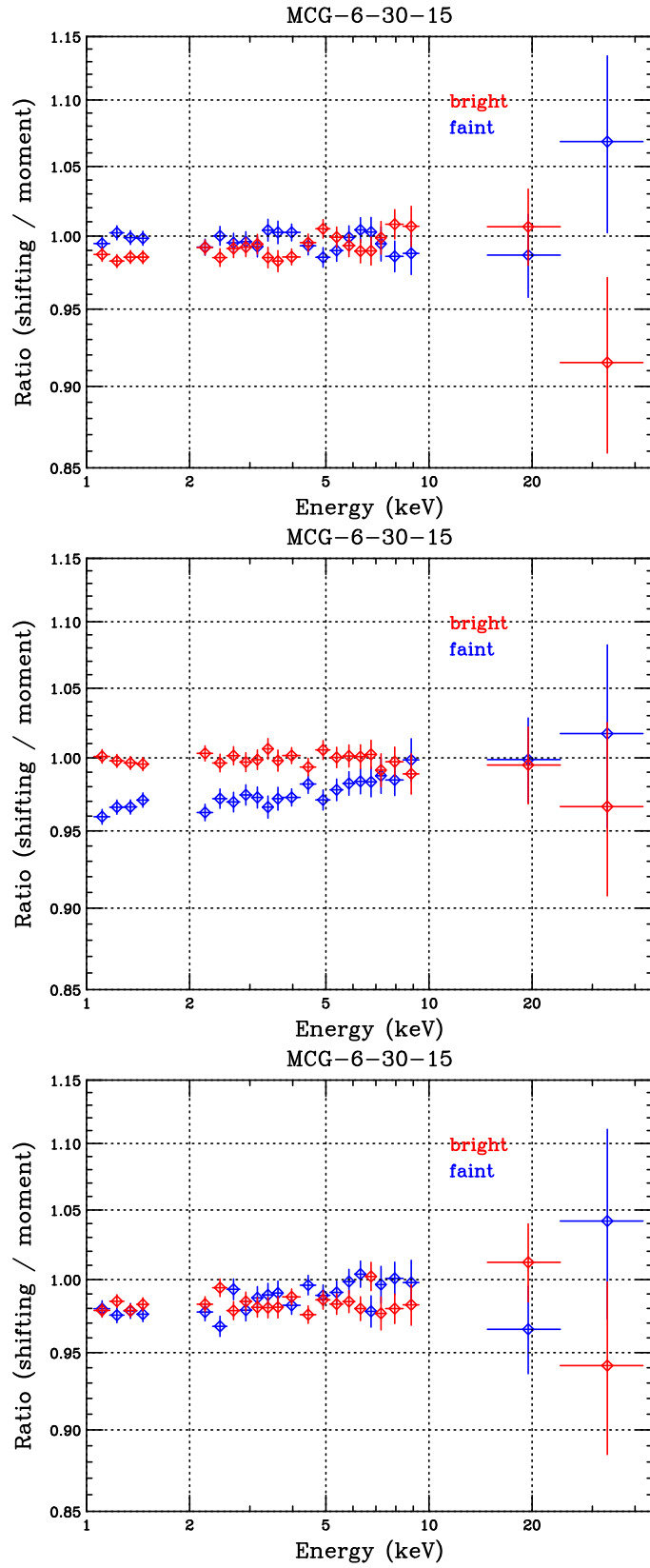


Figure C.1: Spectral ratios of the bright and faint spectra in case of shifting one time-bin to the original spectra. The cases for intervals of 5,000 sec, 10,000 and 20,000 sec, from top to bottom.

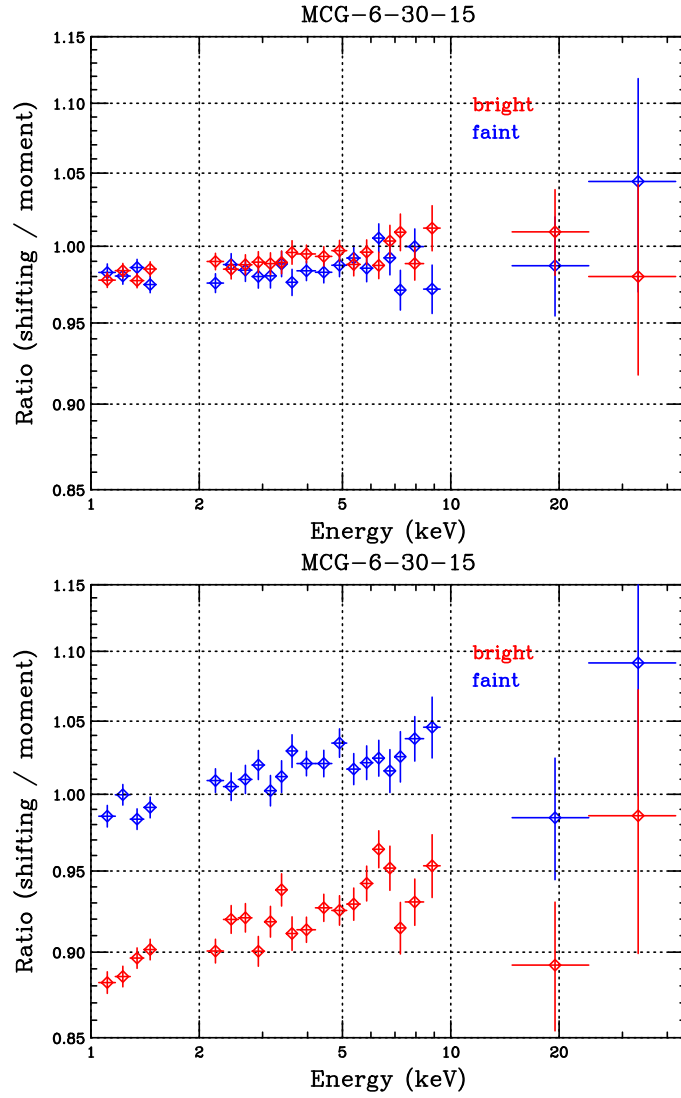


Figure C.1: (Continued) Spectral ratios of the bright and faint spectra in case of shifting one time-bin to the original spectra. The cases for intervals 40,000 sec and 80,000 sec for top and bottom, respectively.

Bibliography

- [1] Anders, E. & Ebihara, M. 1982, *Geochim Cosmochim Acta*, 46, 2363
- [2] Antonucci, R. 1993, *ARA&A*, 31, 473
- [3] Antonucci, R.R. J., & Miller, J. S. 1985, *ApJ*, 297, 621
- [4] Arnaud, K. 1996, *Astronomical Data Analysis Software & Systems V*, A.S.P., Conference Series, 101, 17
- [5] Awaki, H., Koyama, K., Kunieda, H., & Tawara, Y. 1990, *Nature*, 346, 544
- [6] Awaki, H., Koyama, K., Inoue, H., & Halpern, J. P. 1991, *PASJ*, 43, 195
- [7] Baade, W., & Minkowski, R. 1954, *ApJ*, 119, 206
- [8] Blandford, D., Netzer, H., & Woltjer, L. 1991, *Active Galactic Nuclei: Saas Fee Advanced Course 20*
- [9] Boldt, E. 1987, *Observational Cosmology*, 124, 611
- [10] Bolton, J. G., Stanley, G. J., & Slee, O. B. 1954, *Australian Journal of Physics*, 7, 110
- [11] Balucinska-Church, M., & McCammon, D. 1992, *ApJ*, 400, 699
- [12] Burke, B. E., Gregory, J. A., Loomis, A. H., Lesser, M., Bautz, M. W., Kissel, S. E., Rathman, D. D., Osgood, R. M., Cooper, M. J., Lind, T. A., & Ricker, G. R. 2004, *IEEE Transaction on Unclear Science*, 51, 2322
- [13] Dahari, O., & De Robertis, M. M. 1988, *ApJS*, 67, 249
- [14] de Rosa, A., Piro, L., Perola, G.C., Capalbi, M., Cappi, M., Grandi, P., Maraschi, L., & Petrucci, P.O., 2007, *A&A*, 463, 903
- [15] di Matteo, T. 1998, *MNRAS*, 299, L15
- [16] di Matteo, T., Celotti, A., & Fabian, A. C. 1999, *MNRAS*, 304, 809
- [17] Dove, J. B., Wilms, J., Maisack, M., & Begelman, M. C. 1997, *ApJ*, 487, 759
- [18] Ebisawa, K., Ueda, Y., Inoue, H., Tanaka, Y., & White, N. E. 1996, *ApJ*, 467, 419
- [19] Fabian, A. C., Rees, M. J., Stella, L., & White, N. E. 1989, *MNRAS*, 238, 729
- [20] Fabian, A. C., Nandra, K., Celotti, A., Rees, M. J., Grove, J. E., & Johnson, W. N. 1993, *ApJL*, 416, L57

- [21] Fabian, A. C., Kunieda, H., Inoue, S., Matsuoka, M., Mihara, T., Miyamoto, S., Otani, C., Ricker, G., Tanaka, Y., Yamauchi, M., & Yaqoob, T. 1994, PASJ, 46, L59
- [22] Fabian, A. C., et al. 2002, MNRAS, 335,L1
- [23] Fath, E. A. 1909, Popular Astron., 17, 504
- [24] Fiore, F., Perola, G. C., Matsuoka, M., Yamauchi, M., & Piro, L. 1992, A&A, 262, 37
- [25] Fisher, K. B., Huchra, J. P., Strauss, M. A., Davis, M., Yahil, A., & Schlegel, D. 1995, ApJS, 100, 69
- [26] Galeev, A. A., Rosner, R., & Vaiana, G. S., 1979, ApJ, 229, 318
- [27] George, I. M. & Fabian, A. C. 1991, MNRAS, 249, 352
- [28] Gibson, R. R., Canizares, C. R., Marshall, H. L., Young, A. J., Lee, J. C. 2007, ApJ, 655, 749
- [29] Greenstein, J. L., & Matthews, T. A. 1963, AJ, 68, 279
- [30] Grevesse, N., Noels, A., & Sauval, A. 1996, in “Cosmic Abundances” ASP Conference Series, 99, S. Holt & G. Sonneborn, eds.
- [31] Guainazzi, M., et al. 1999, A&A, 341, L27
- [32] Guilbert, P. W., & Rees, M. J., 1988, MNRAS, 233, 475
- [33] Halpern, J. P. 1984, ApJ, 281, 90
- [34] Heckman, T. M., Blitz, L., Wilson, A. S., Armus, L., & Miley, G. K. 1989, ApJ, 342, 735
- [35] Inoue, H. 1989, ESASP, 296, 783
- [36] Inoue, H., & Matsumoto, C. 2003, PASJ, 55, 625
- [37] Ishida, M., Suzuki, K., & Someya, K. 2007, JX-ISAS-SUZAKU-MEMO-2007-11, 1
- [38] Iwasawa, K., et al. 1996, MNRAS, 282, 1038
- [39] Kallman, T. R., Palmeri, P., Bautista, M. A., Mendoza, C., & Krolik, J. H. 2004, ApJS, 155, 675
- [40] Kaspi, S., Smith, P. S., Netzer, H., Maoz, D., Jannuzi, B. T., Giveon, U. 2000, ApJ, 533, 631
- [41] Koratkar, A., & Blaes, O. 1999, PASP, 111, 1
- [42] Kokubun, M., et al. 2007, PASJ, 59, 53
- [43] Koyama, K., et al. 2007, PASJ, 59, S23
- [44] Kubota, A., Tanaka, Y., Makishima, K., Ueda, Y., Dotani, T., Inoue, H., & Yamaoka, K. 1998, PASJ, 50, 667
- [45] Laor, A. 1991, ApJ, 376, 90
- [46] Lawrence, A. 1987, PASP, 99, 309

- [47] Lee, J. C., Fabian, A. C., Brandt, W. N., Reynolds, C. S., & Iwasawa, K. 1999, MNRAS, 310, 973
- [48] Lee, J. C., et al. 2001, ApJ, 554, L13
- [49] Lehmann, I., et al. 2000, A&A, 354, 35
- [50] Lehmann, I., et al. 2001, A&A, 371, 833
- [51] Levine A. M., Bradt, H., Cui, W., Jernigan, J. G., Morgan, E. H., Remillard, R. A., Shirey, R. E., & Smith, D. A. 1996, ApJ, 469, L33
- [52] Liang, E. P. T., & Price, R. H. 1977, ApJ, 218, 247
- [53] Lightman, A. P., & White, T. R. 1988, ApJ, 335, 57
- [54] Liu, B. F., Mineshige, S., & Shibata, K. 2002, ApJL, 572, L173
- [55] Machida, M., Hayashi, M. R., & Matsumoto, R. 2000, ApJL, 532, L67
- [56] Magdziarz, P., & Zdziarski, A. A. 1995, MNRAS, 273, 837
- [57] Maisack, M., et al. 1993, ApJL, 407, L61
- [58] Makishima, K., Maejima, Y., Mitsuda, K., Bradt, H. V., Remillard, R. A., Tuohy, I. R., Hoshi, R., & Nakagawa, M. 1986, ApJ, 308, 635
- [59] Makishima, K., et al. 2000, ApJ, 535, 632
- [60] Matsuoka, M., Piro, L., Yamauchi, M., Murakami, T. 1990, ApJ, 361, 440
- [61] Matsumoto, C., Inoue, H., Fabian, A. C., & Iwasawa, K. 2003, PASJ, 55, 615
- [62] McHardy, I. M. 1990, In Proc. 23rd ESLAB Symp., ed J. Hunt, B. Battrick, p. 1111. Paris: Eur. Space Agency
- [63] Miller, J. S., & Goodrich, R. W. 1990, ApJ, 355, 456
- [64] Miller, K. A., Stone, J. M. 2000, ApJ, 534, 398
- [65] Miller, L., Turner, L. J. & Reeves, J. N. 2008, A&A, 483, 437
- [66] Miniutti, G., & Fabian, A. C. 2004, MNRAS, 349, 1435
- [67] Miniutti, G., et al. 2007, PASJ, 59, 315
- [68] Mitsuda, K., et al. 1984, PASJ, 36, 741
- [69] Mitsuda, K., et al. 2007, PASJ, 48, 211
- [70] Miyakawa, T., Ebisawa, K, Terashima, Y., Tsuchihashi, F., Inoue, H., & Życki, P. 2009, PASJ, 61,
- [71] Mushotzky, R. F. 1984, Advances in Space Research, 3, 157
- [72] Mushotzky, R. F., Done, C., & Pounds, K. A. 1993, ARA&A, 31, 717
- [73] Nandra, K., Pounds, K. A., Stewart, G. C. 1990, MNRAS, 242, 660

- [74] Nandra, K., Pounds, K. A., Stewart, G. C., George, I. M., Hayashida, K., Makino, F., & Ohashi, T. 1991, MNRAS, 248, 760
- [75] Nandra, K., & Pounds, K. A. 1992, Nature, 359, 215
- [76] Nandra, K., et al. 1993, MNRAS, 260, 504
- [77] Nandra, K., & Pounds, K. A. 1994, MNRAS, 268, 405
- [78] Nandra, K., O'Neill, P. M., George, I. M., & Reeves, J. N. 2007, MNRAS, 382, 194
- [79] Nelson, C. H. 2000, ApJL, 544, L91
- [80] Niedźwiecki, A., & Życki, P. T. 2008, MNRAS, 386, 759
- [81] Ogawara, Y., Doi, K., Matsuoka, M., Miyamoto, S., & Oda, M. 1977, Nature, 270, 154
- [82] Ogle, P.M, Marshall, H.L, Lee, J.C., and Canizares, C.R., 2000, ApJ, 545, L81
- [83] Osterbrock, T., et al. 1996, A&A, 309, 781
- [84] Ostriker, J. P., Weaver, R., Yahil, A., & McCray, R. 1976, ApJL, 208, L61
- [85] Otani, C., et al. 1996 PASJ, 48, 211O
- [86] Page, K. L., Schartel, N., Turner, M. J. L., & O'Brien, P. T. 2004, MNRAS, 352, 523
- [87] Pan, H. C., Stewart, G. C., & Pounds, K. A. 1990, MNRAS, 242, 177
- [88] Piro, L., Yamauchi, M., & Matsuoka, M. 1990, ApJL, 360, 652
- [89] Ponti, G., Cappi, M., Dadina, M., & Malaguti, G. 2004, A&A, 417, 451
- [90] Reynolds, C. S., Fabian, A. C., Nandra, K., Inoue, H., Kunieda, H., & Iwasawa, K. 1995, MNRAS, 277, 901
- [91] Reynolds, C. S. 1996, Ph.D. thesis, Univ. Cambridge
- [92] Reynolds, C. S., & Nowak, M. A. 2003, Phys. Rep., 377, 389
- [93] Rothschild, R. E., Blanco, P. R., Gruber, D. E., Heindl, W. A., MacDonald, D. R., Marsden, D. C., Pelling, M. R., Wayne, L. R. et al. 1998, ApJ, 496, 538
- [94] Rybicki G. B., & Lightman A. P. 1979, Radiative Processes in Astrophysics
- [95] Sako, M., et al. 2003, ApJ, 596, 114
- [96] Schmidt, M. 1963, Nature, 197, 1040
- [97] Schmidt, M., et al. 1998, A&A, 329, 495
- [98] Serlemitsos, P. J., et al. 2007, PASJ, 59, 9
- [99] Seyfert C. 1943, ApJ, 97, 28
- [100] Shakura, N. I., & Sunyaev, R. A. 1973, A&A, 24, 337
- [101] Shimura, T., Takahara, F. 1995, ApJ, 445, 780

- [102] Shull, J. M., & van Steenberg M. 1982, ApJS, 48, 95
- [103] Stern, B. E., Poutanen, J., Svensson, R., Sikora, M., & Begelman, M. C. 1995, ApJL, 449, L13
- [104] Streblyanska, A., Hasinger, G., Finoguenov, A., Barcons, X., Mateos, S., & Fabian, A. C. 2005, A&A, 432, 395
- [105] Sunyaev, R. A., & Truemper, J. 1979, Nature, 279, 506
- [106] Tadhunter, C., & Tsvetanov, Z. 1989, Nature, 341, 422
- [107] Takahashi, K., Inoue, H., & Dotani, T. 2002, PASJ, 54, 373
- [108] Takahashi, T., et al. 2007, PASJ, 59, 35
- [109] Tanaka, Y., et al. 1995, Nature, 375, 659
- [110] Thone, K. S., & Price, R. H. 1975, ApJL, 195, L101
- [111] Turner, T. J., & Pounds, K. A., 1989, MNRAS, 240, 833
- [112] Turner, T. J., Nandra, K., George, I. M., Fabian, A. C., & Pounds, K. A. 1993, ApJ, 419, 127
- [113] Turner, T. J., et al. 2002, ApJ, 568, 120
- [114] Turner, A. K., Fabian, A. C., Vaughan, S., & Lee, J. C. 2003, MNRAS, 346, 833
- [115] Turner, A. K., Fabian, A. C., Lee, J. C., & Vaughan, S. 2004, MNRAS, 353, 319
- [116] Vaughan, S., & Edelson, R. 2001, ApJ, 548, 694
- [117] Vaughan, S., & Fabian, A. C. 2004, MNRAS, 348, 1415
- [118] Wandel, A., Peterson, B. M., & Malkan, M. A. 1999, ApJ, 526, 579
- [119] Yaqoob, T. 1992, MNRAS, 258, 198
- [120] Yaqoob, T., & Padmanabhan, U. 2004, ApJ, 604, 63
- [121] Yaqoob, T. 2005, in Populations of High Energy Sources in Galaxies, ed. M. J. A. Meurs & G. Fabbiano (Cambridge: Cambridge Univ. Press), 461
- [122] Young, A. J., Lee, J. C., Fabian, A. C., Reynolds, C. S., Gibson, R. R., & Canizares, C. R. 2005, ApJ, 631, 733
- [123] Zdziarski, A. A., Johnson, W. N., Done C., Smith, D., & McNaron-Brown, K. 1995, ApJL, 438, L63